FACULTY
OF SCIENCES

Red-emitting Mn^{4+}-doped phosphors for efficient lighting

Heleen Sijbom

Supervisors: Prof. Dr. Philippe Smet, Prof. Dr. Dirk Poelman

A dissertation submitted to Ghent University in partial fulfilment of the requirements for the degree of Doctor of Science: Physics

Academic year: 2017 - 2018

GHENT
UNIVERSITY

Dankwoord

"Happiness can be found, even in the darkest of times,
if one only remembers to turn on the light."

— Albus Dumbledore in *Harry Potter and the Prisoner of Azkaban*
by J.K. Rowling

Aan een doctoraat werken doe je vaak alleen, maar ook niet helemaal. In de afgelopen jaren hebben er veel mensen direct en indirect een bijdrage geleverd aan mijn doctoraat. Vijf jaar geleden kwam ik als chemist binnen in S1 en sindsdien heb ik me er altijd thuis gevoeld. De laatste maanden voelde ik me misschien zelfs een beetje te veel thuis, toen ik regelmatig als allerlaatste het gebouw verliet. Een heel aantal gebroken middenvoetsbeentjes en heel veel HF-syntheses later, ligt er nu een doctoraat.

Philippe en Dirk, dankjewel om mij de kans te geven om me bij LumiLab aan te sluiten als chemist tussen alle fysici. Ik heb de afgelopen jaren veel geleerd en jullie hebben daar veel aan bijgedragen. Bedankt ook voor het vele naleeswerk, de grondige feedback en de inspiratie en motivatie om mijn fosforsyntheses te blijven verbeteren. Dirk, je optimisme en grapjes zorgen voor de goede sfeer in LumiLab, bedankt daarvoor. Philippe, bedankt voor al je wetenschappelijk inzicht en je passie voor wetenschapscommunicatie die ook mijn onderzoek veel beter gemaakt hebben.

Ondanks dat ons bureau op de derde verdieping soms wel heel ver weg lijkt, was het er gezellig en dankzij het extra kacheltje zelfs warm in de winter. Dankjewel Anthony, Koen, Katrien, Lisa en Simon voor jullie fijne gezelschap de afgelopen jaren. Alle LumiLab-collega's hebben bijgedragen aan de fijne sfeer op het werk en vooruitgang in het onderzoek. Andreas, Ang and Jiaren, thanks for all your happy hello's in the corridor. David, bedankt voor je hulp bij het maken van fosforlaagjes en het OSM practicum, dat de studenten er niet altijd veel van begrepen lag zeker niet aan jou. Jonas, je bijna onuitputtelijke kennis is inspirerend, bedankt voor al je inzichten in energieniveaus en al je hulp bij berekeningen. Katleen, bedankt voor alle tripjes naar Grenoble en de metingen die je daar ook op mijn poeders deed. Lisa, bedankt voor de vele fijne gesprekken waarbij ik omgekeerd aan mijn bureau zat en veel succes met het alleen opboksen tegen alle mannen in LumiLab. Olivier, bedankt voor alle bestellingen als ik weer eens HF of KF nodig had omdat mijn syntheses niet zo'n hoog rendement hadden. Robin, als nieuwste doctoraatsstudent wens ik jou veel plezier en succes, ook zonder SB-beurs kun je een doctoraat halen. Simon, bedankt dat ik het fototoestel altijd mocht gebruiken en voor je bereidwilligheid om te helpen bij allerhande problemen.

Het leuke aan een SBO-project is dat je er niet helemaal alleen aan werkt, getuige de al dan niet regelmatige LumiCoR-meetings. Koen, je voorzag de eerste jaren van het LumiCoR-project van veel goede raad en inspirerende ontwerpen. Reinert, ondanks dat jouw werk vooral bestond uit het afbreken van mijn fosforpoeders, heeft onze samenwerking en jouw XRD-kennis geleid tot veel nieuwe inzichten en een verbetering van de fluoridesynthese, bedankt daarvoor!

Ook de andere S1 collega's hebben een bijdrage geleverd aan mijn doctoraat door de goede werksfeer, de interessante gesprekken in de keuken, technische hulp, XRD-metingen, veiligheidsadvies en vegetarische opties bij de barbecue. Dankjewel daarvoor! De juryleden wil ik tenslotte bedanken voor het nalezen van mijn doctoraat, dankzij jullie feedback is het boekje nog beter geworden.

Hoewel een doctoraat zich voornamelijk op de unief afspeelt, hebben ook daarbuiten veel mensen er een indirecte invloed op gehad. Papa en mama, dankjewel om mij altijd te steunen en mij kansen te geven. Zelfs toen ik als 17-jarige besloot dat ik in het buitenland wilde studeren, kon dat gewoon. Groningen was verder weg dan Gent, dus België was niet zo ver, was mijn redenatie. Achteraf gezien was Groningen dichterbij jullie geweest, maar dat had niemand voorzien en met de digitale communicatie van tegenwoordig is ver weg altijd relatief. Mariëtte, lieve grote kleine zus, je bent altijd bereid om te helpen en je bent echt een geweldige zus! Dankzij je doorzettingsvermogen heb je een mooie toekomst voor je.

Als de stress of frustraties hoog opliepen, of gewoon voor een gezellig etentje of een kopje thee, kon ik altijd bij mijn vriendinnen terecht. Offline of online, jullie waren er altijd voor mij. Loes, bedankt om al zo lang zo dichtbij mij te staan, bedankt voor alle woensdagavonden en voor alle veel te lange gesprekken aan de rotonde waar onze wegen naar huis splitsen. Jouw doctoraat komt er ook wel! Mieke, ik kan me geen betere klasgenoot en kotgenoot inbeelden, ik kon altijd bij je terecht met vragen en problemen en ik ben enorm blij met onze vriendschap die inmiddels al 10 jaar duurt. Merci voor alles en op naar nog minstens 10 jaar met vele babbels en etentjes op woensdagavond. Manon, bedankt voor alle gezellige etentjes en voor je advies in alle mogelijke Engelse taalkwesties die ik tegenkwam, dankzij jou staan er zeker minder taalfouten in mijn doctoraat. Marre, ik bewonder je zelfverzekerdheid en doorzettingsvermogen en ik ben heel vereerd om de meter van Midas te zijn, ooit vertel ik hem alles over ledverlichting. Marjolein, je passie voor Ottolenghi en ander lekker eten werkt aanstekelijk, bedankt voor de inspiratie voor de verzameling kookboeken in mijn kast waardoor ik zo veel lekker eten kan maken. Zonder HPO was ik nooit in België beland en als ik zie waar ik nu sta ben ik daar alle forummers dankbaar voor.

Gelukkig was er naast het werk ook tijd voor ontspanning, waar ik mijn hoofd even kon leegmaken en mijn energie kwijt kon. Lieve Goe Folkers, bedankt voor de vele fijne woensdagavonden, op de dansvloer, op de bank als ik weer eens mijn voet gebroken had en op café achteraf. Jullie zijn als een warme familie in Gent voor mij, waarbij ik altijd terecht kan voor steun en goede raad. Coro Maín is de laatste vijf jaar al mijn vaste afspraak op zondagavond. Lieve koorvrienden, er is geen betere afsluiting van het weekend dan een avondje zingen en daarna op café met de zotte bende die ons koor soms is.

Als laatste wil ik ook Tony bedanken voor zijn substantiële bijdrage aan mijn doctoraat. Er zijn heel wat chocoladerepen gesneuveld, maar als je dan toch veel chocolade eet kan die maar beter heel lekker, fair trade en slaafvrij zijn.

Gent, januari 2018
Heleen Sijbom

Contents

Part I

Introduction

1

Luminescence

The term *Luminescenz* was first used in 1888 by Eilhardt Wiedermann [1]. Luminescence is defined as “cold light”, where light is generated in a nonthermal way, by materials that convert energy to photons. This phenomenon is in contrast to incandescence, where light is emitted due to a very high body temperature, such as the thermal radiation from objects such as the sun or a glowing hot piece of metal. Several types of luminescence are defined, depending on the used source of excitation energy [2, 3]. These include the following:

- Photoluminescence (PL)
  In photoluminescent materials, luminescence is induced by incoming light. High-energy photons are absorbed and converted to photons with typically a lower energy. The light is emitted nano- to microseconds after the excitation process. When light is trapped in the material and emitted even after seconds or hours, this is called persistent luminescence.

- Cathodoluminescence (CL)
  A cathodoluminescent material is excited by an electron beam, for example in a cathode ray tube (CRT) found in old television screens.

- Electroluminescence
  An electroluminescent material is excited by an electric current or an electric field. A light-emitting diode (LED) chip emits light by electroluminescence.

- Chemiluminescence
  Chemiluminescent materials emit light originating from a chemical reaction, of which the reaction between luminol and hydrogen peroxide in presence of a metal catalyst is the best known.

- Bioluminescence
  Bioluminescence is luminescence induced by a biochemical reaction; the luciferase-catalyzed oxidation of luciferine causes the luminescence of fireflies.

- Radioluminescence
  Radioluminescence originates from excitation of the luminescent material by ionizing radiation such as X-rays or γ-rays. Radioluminescent paint was used on watch dials, mainly before the health hazards of radioactivity were well known.

- Thermoluminescence
  Thermoluminescence is thermally induced luminescence, but it is distinct from black-body radiation, as it can be induced upon mild heating. Thermoluminescent materials emit light using energy that was previously absorbed or “trapped” from exciting light or from an ionizing radiation source.

- Mechanoluminescence
  Mechanoluminescence is caused by a mechanical force on a solid. This class of luminescence includes fractoluminescence induced by fractions, piezoluminescence induced by pressure, triboluminescence induced by rubbing and sonoluminescence induced by sound waves.

The materials that were investigated in this work are photoluminescent materials emitting visible light. Inorganic luminescent materials are often called phosphors, from the Greek $\Phi\omega\sigma\phi\acute{o}\rho o\varsigma$ meaning “light bearer”. Although the chemical element phosphorus (P) has the same etymological origin, the presence of P in phosphor materials is not mandatory and in fact rather uncommon. The phosphor material typically consists of a host lat-

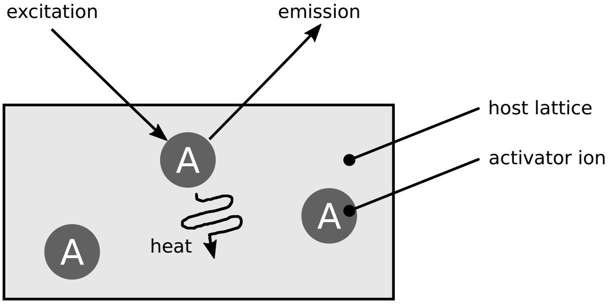

Figure 1.1: Schematic representation of a photoluminescent material where the activator absorbs the excitation energy and transforms it to emitted photons and lattice vibrations. Figure adapted from [3].

tice and a luminescent center, also called activator or dopant (figure 1.1). The dopant is an impurity ion, substituting up to a few percent of the host lattice ions.

During the photoluminescence process, a high-energy photon is absorbed by the activator, which is promoted to an excited state. A transition from the excited state to the ground state leads to the emission of light. Not every ion in the excited state will show luminescence, since nonradiative transitions such as multi-phonon relaxation, energy transfer or ionization compete with the radiative emission. Although the excitation and emission characteristics of the phosphor are mainly determined by the impurity ions, the host lattice also influences the luminescence.

Various types of impurity ions, including transition-metal ions and rare-earth ions, can be applied in phosphors and their different transitions can be studied according to the corresponding energy diagrams. The $4f^n$–$4f^n$ transitions and $4f^n$–$4f^{n-1}5d$ transitions are the common luminescent transitions in rare-earth-doped phosphor materials. Since this work focuses on Mn^{4+} luminescence, only the $3d^n$–$3d^n$ transitions present in transition-metal ions are discussed here.

1.1 Configurational coordinate model

The configurational coordinate (CC) model is used to describe the interaction between the impurity ion and the surrounding host lattice [2, 3]. The impurity ion and the surrounding atoms or ligands can be seen as a localized center, where the influence of more distant atoms in the lat-

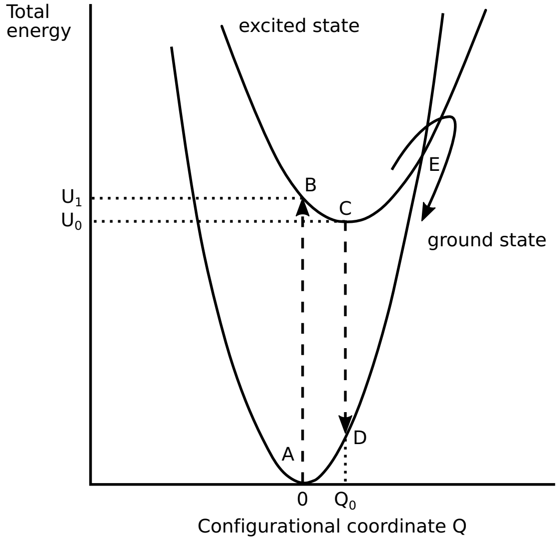

Figure 1.2: Configurational coordinate diagram adapted from [2]. The two parabolas depict the ground state and the excited state. The arrows connecting points A-E are explained in the text.

tice is neglected. A CC diagram (figure 1.2) shows the potential energy curve of an absorbing center as a function of a configurational coordinate. These curves portray the sum of the electron energy and the ion energy of the localized center in either the ground state or in an excited state. For a diatomic molecule, the adiabatic potential changes as a function of the interatomic distance. Similarly, a polyatomic molecule or our localized center can be approximated by a single configurational coordinate in the one-dimensional CC model.

In this model, only a fully symmetric vibrational mode (breathing mode) is assumed. In a symmetrical stretching mode, the central metal ion is at rest and the surrounding ions (ligands) move in phase, away from the central ion and back to it. In the CC diagram, this mode reduces to a plot of the energy as a function of the metal–ligand distance relative to the equilibrium position of the ground state, hereby neglecting all other possible vibrations. The bonding force between the dopant and the nearest neighbor is given by Hooke's law. When Q is the deviation from the equilibrium position, the energy of the ground state is given by equation 1.1, while the total energy of the excited state is given by equation 1.2. Here, K is the force constant of the chemical bond, Q_0 is the interatomic distance at the equilibrium of the excited state, U_0 is the total energy at $Q = Q_0$ and the subscripts $_g$ and $_e$ denote the ground state and the excited state respectively.

$$U_g = K_g \frac{Q^2}{2} \tag{1.1}$$

$$U_e = K_e \frac{(Q - Q_0)^2}{2} + U_0 \tag{1.2}$$

The CC model is a simplification of the polyatomic system, but it can be used to explain several effects of the luminescent process of a doped host crystal, such as the Stokes shift, the width of excitation and emission bands and the thermal quenching of luminescence.

1.2 Electronic transitions

The transitions between the ground state and the excited state are electronic transitions and the absorption of a photon is represented by a vertical line on the CC diagram. According to the Franck–Condon principle, the nucleus stays approximately in the same position during the excitation and emission processes. This is plausible since the nucleus is significantly heavier than an electron.

At 0 K, the excitation process starts with absorption of energy inducing a transition from the equilibrium position of the ground state (point A in figure 1.2), moving vertically on the diagram to a non-equilibrium position on the edge of the excited-state parabola (point B). Since the probability of losing energy by lattice vibrations is higher than the probability of light emission, a nuclear relaxation occurs to the highest probable, equilibrium position of the excited state (C). The excess energy is released to the surroundings by vibrations. For this, the nucleus moves over Q_0 to a new position so that the interatomic distance equals the equilibrium distance of the excited state.

In a classical, non-vibrational model, at higher temperatures including room temperature (rt), the electronic state can oscillate along the parabolic curve around the equilibrium position up to thermal energy kT. The amplitude of this oscillation causes a broadening of the excitation band, because not only the most probable transition, starting from point A can take place. Vertical transitions starting from lower or higher Q values can also occur, although these transitions are less probable.

Not only the dopant ion can absorb the excitation energy, the host lattice can also absorb energy, which can be transferred to the impurity ion. Semiconductors absorb energies larger than their band gap and form free charge carriers (electrons and holes) that can recombine and transfer energy to the dopant ion.

From point C on the CC diagram, the equilibrium position of the excited state, the system can return to the ground state with radiative emission. For this emitting transition, the same selection rules apply as for the exciting transition, so only vertical transitions are allowed, moving from point C to point D. In contrast to absorption, emission can happen spontaneously even in absence of radiation. Because of the vertical transition, the center reaches a higher vibrational level of the ground state (D), after which relaxation occurs to the lowest, most probable vibrational level of the ground state.

Although the vertical transitions from A to B and from C to D are possible in the CC diagram, there is a limit on possible transitions between energy levels. Two selection rules that limit the possible excited states to which transitions are possible have to be considered. The spin selection rule only allows electronic transitions between levels with the same spin state (ΔS= 0). The parity selection rule only allows electronic transitions that induce a change in parity. Relaxation of the selection rules, due to vibrational coupling can cause forbidden transitions to occur, albeit with a low probability.

1.3 Phonon interactions

Considering an equal force constant for the ground state and the excited state the two parabolas have the same shape. From quantum mechanics, the considered harmonic oscillator gives discrete energy levels in the CC parabolas, which can be calculated according to equation 1.3.

$$E_{\upsilon} = (\upsilon + \frac{1}{2})h\nu \tag{1.3}$$

Here the integer $\upsilon = 0, 1, 2, \ldots$ and ν is the oscillator frequency. From the wave functions, the probability distribution is known, with the highest probability of finding the system at Q = 0 or at the edges of the parabola for higher values of υ. From this discrete energy difference between vibrational levels, we get equation 1.4 with phonon energy $h\nu$ and Huang–Rys parameter S. The Huang–Rys parameter equals the average number of phonons emitted after one optical transition and it is used as a measure of the electron–phonon interaction. The Stokes shift, the energy difference between the maximum of the lowest excitation band and the emission band of a phosphor, is related to the change in interatomic distance during relaxation and is given by equation 1.5.

$$\frac{1}{2}K(Q_0)^2 = Sh\nu \tag{1.4}$$

$$\Delta E_s = k(R_0' - R_0)^2 = 2Sh\nu \tag{1.5}$$

Three cases are distinguished for the electron–phonon interaction: a weak-coupling regime for S<1, a strong-coupling regime for S>5 and an intermediate coupling regime in between those values. For a weak-coupling electron–phonon interaction, at 0 K the emission spectrum consists of a single line, the zero-phonon line (ZPL). When the phonon energy $h\nu$ is equal for both the ground state and the excited state, the excitation and emission band form a mirror image around the ZPL. At temperature T (T >0 K), every vibrational state reachable with thermal energy kT can act as the initial state for the absorption process, resulting in line emission spectra. Each of these vibrational states contributes to the transition with a probability corresponding to the population density of the state.

The simple picture of an excitation-emission process can be seen starting with an absorption process without changing the dopant-ligand distance, followed by an expansion of the host lattice to the equilibrium distance of the excited state $Q = Q_0$. Emission occurs, again without changing the distance, after which a contraction over Q_0 results in reaching the equilibrium distance of the ground state. However, distortions of the excited states are not included in this simplified view. Coupling with all possible vibrational modes can influence the emission spectrum, showing a broad emission spectrum instead of separate emission lines. The host lattice can also influence the shape of the emission spectrum. A rigid environment limits the value of Q_0 and S, so a smaller Stokes shift and vibrational structure can be observed.

The selection rules mainly influence the lifetime of the excited state. Allowed transitions have a short lifetime, in the ns to µs range, while forbidden transitions are slower with a lifetime in the ms range.

For a simple two-level system, with a ground state and an excited state, the population of the excited state decreases according to equation 1.6.

$$\frac{dN_e}{dt} = -N_e P_{eg} \tag{1.6}$$

Here, N_e is the number of ions in the excited state and P_{eg} is the transition probability for spontaneous emission from the excited state to the ground state. The population of the excited state as a function of time is given by equation 1.7 with radiative decay time τ.

$$N_e(t) = N_e(0)e^{-P_{eg}t} = N_e(0)e^{-t/\tau} \tag{1.7}$$

1.4 Crystal field splitting

The crystal field (CF) is another factor influencing the properties of a host lattice for a certain dopant ion. The CF is the electric field at the site of the dopant ion, influenced by the surrounding ions and it is responsible for the splitting of optical transitions. Uneven symmetry causes a crystal field that can lift the parity selection rule.

In a free ion, the five 3d orbitals have an equal energy, they are degenerated. In an octahedrally-coordinated crystal surrounding, the fivefold degenerate orbitals split into triply degenerate t_2 orbitals and doubly degenerate e orbitals. The t_2 orbitals have a lower energy, because the orbital lobes are pointing in between the octahedral ligands. In the higher energy state e, the orbitals are pointing towards the octahedral ligands.

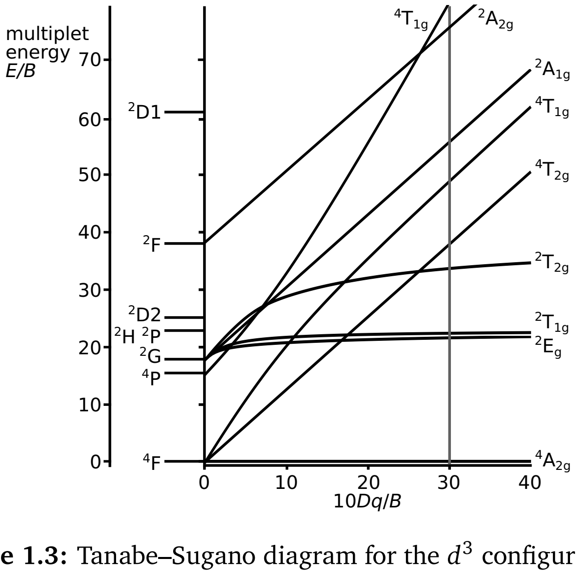

Figure 1.3: Tanabe–Sugano diagram for the d^3 configuration.

For a weak crystal field, where the crystal field energy is small compared to the configuration interaction, the energy levels are determined by total angular momentum quantum numbers L and S, expressed as ^{2S+1}L. The corresponding energy levels for a 3d^3 ion are given on the left vertical axis of figure 1.3, where $10Dq/B$ equals zero. $10Dq$ is the crystal field splitting parameter, a measure for the energy difference between the d orbitals, which equals zero for a free ion. B is a Racah parameter that characterizes the electrostatic repulsion of the electrons. The ratio $10Dq/B$ is used as a measure of the field strength in a metal complex. With an increasing crystal field, the levels split from these are represented by $^{2S+1}\Gamma$, with Γ the reduced representation, for which the degeneracy is 1 for A_1 and A_2, 2 for E and 3 for T_1 and T_2. The corresponding energy levels for a $3d^3$ ion are labeled on the right of figure 1.3.

The luminescence of d^3 ions such as Mn^{4+} consists of line emission from the $^2E \rightarrow {}^4A_2$ transition, from the lowest excited state ^2E to the $^4A_2$ ground state. These transition have a life time in the ms range, since both the parity and the spin selection rule are involved: there is no change in parity but there is a change in spin quantum number from $\frac{1}{2}$ to $\frac{3}{2}$. Vibronic transitions can increase the number of visible emission lines. Due to the high charge of Mn^{4+}, the ligands are close, resulting in a high value for $10Dq/B$, so the ^2E level will always be the emitting level. This is in contrast to the isoelectronic Cr^{3+}, where both line emission from the $^2E \rightarrow {}^4A_2$ transition ($10Dq/B > 18$) and broad band emission from the $^4T_2 \rightarrow {}^4A_2$ transition ($10Dq/B < 18$) can occur.

Although the transitions involved in excitation and emission occur in the impurity ion, the optical properties can vary extensively. The surrounding ligands are changed when changing the host lattice, which can influence both excitation and emission properties. Increasing covalency of the host lattice increases the orbital size, which reduces the interaction between electrons. Together with an increase in covalency, the difference in electronegativity between the dopant and the ligands is reduced. By this, the energy levels shift regarding to the free ion energies and by this the transitions involved in emission will shift to a lower energy. In this work, all phosphors contain Mn^{4+} as the luminescent center and the spectroscopic properties of this ion will be discussed in more detail in chapter 3. According to the spin selection rule, in 3d^3 ions optical absorption will occur dominantly from the ground level $^4A_2$ to the spin quartet states $^4T_2$, $^4T_1$ (^4F) and $^4T_1$ (^4P).

1.5 Nonradiative transitions

Nonradiative transitions are the alternative for a radiative, emitting transition from the excited state to the ground state. As these nonradiative transitions compete with the radiative transitions, they can reduce the high light output that was aimed for. When after absorption, the excited state reaches the intersection between the parabolas of the ground state and the excited state (point E in figure 1.2), it is possible to relax to the ground state nonradiatively. The electron in the excited state can cross the intersection when thermal energy is high enough. This way, all absorbed energy is dissipated as heat and is known as thermal quenching of the luminescence.

When the Huang–Rys parameter $S = 0$, the parabolas are parallel and will therefore never cross, but nonradiative transitions are still possible. A nonradiative return to the ground state is more probable when the energy difference is less than 5 times the highest vibrational mode of the surroundings. In this way, a few high-energy vibrations can be excited, resulting in the nonradiative multi-phonon emission [3].

The CC diagram can be expanded by adding a third parabola (figure 1.4), which originates from a different configuration of the activator ion. The absorption occurs towards the highest parabola, through an allowed transition which is more probable than absorption of towards the second parabola through a forbidden transition. From here, the system relaxes to the excited state of the second parabola, from which the emitting transition to the ground state can take place. This is the process involved in Mn^{4+} luminescence. The allowed $^4A_2 \rightarrow {}^4T_2$ (or $^4T_1$) transition is excited, followed by a relaxation to the ^2E excited state, followed by line emission back to the $^4A_2$ ground state.

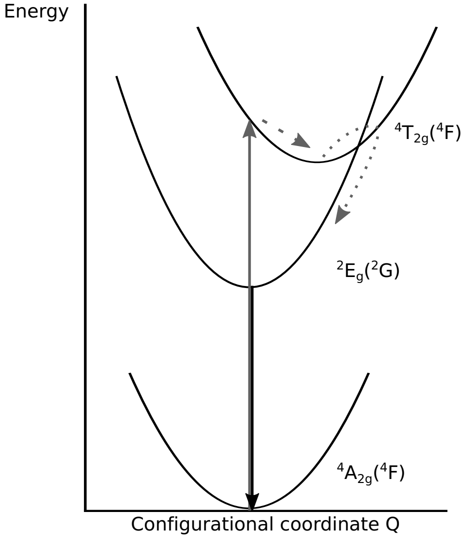

Figure 1.4: Configurational coordinate diagram expanded with a third parabola whichs originates from a different configuration of the activator ion.

2

White LEDs: the lighting of the future

Light-emitting diodes (LEDs) are coming up as a main source of lighting and as a backlight in displays of smartphones, laptops and televisions. Nevertheless, this evolution only happened in the past decades, since the development of the bright blue LED chip, that forms the basis of modern white LEDs. The importance of white LEDs (wLEDs) was recognized with awarding the 2014 Nobel Prize in Physics for the invention of efficient blue LEDs, which have enabled bright and energy-saving white light sources [4]. In this chapter, the flourishing of LEDs is addressed with a short overview of lighting through the years, the development of white LEDs and the further improvement into efficient warm-white LEDs.

2.1 Evolution in lighting

Artificial light has simplified human life over the last centuries. Incandescent lamps have lit the 20th century, but as they convert more than 90% of the electrical energy into heat, thus less than 10% in light, more efficient light sources have come up. Figure 2.1 gives an overview of different

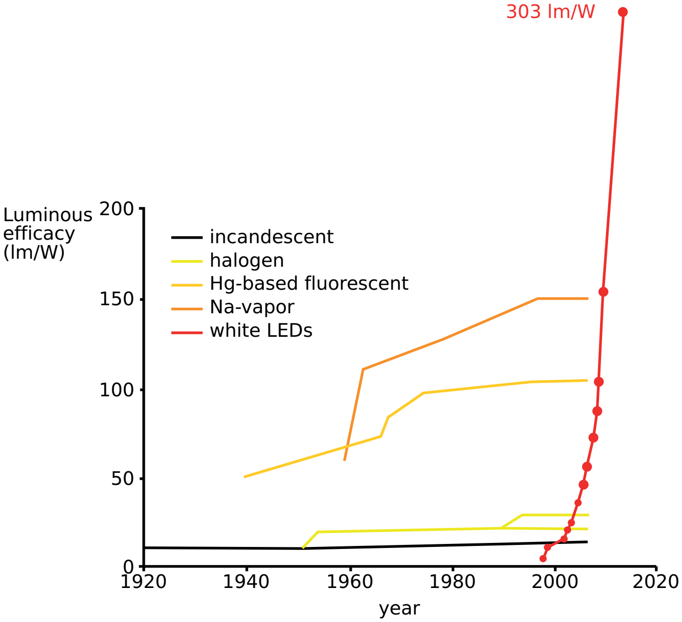

Figure 2.1: The history of the luminous efficacy in incandescent, halogen, fluorescent and sodium-vapor lamps and white LEDs, adapted from [5].

light sources that have been developed in the past century and their efficiency. Halogen lamps have the same working principle as incandescent lamps, which is a heated metal filament emitting black-body radiation. In the halogen atmosphere present in the bulb, a redeposition of evaporated tungsten is possible, elongating the lifetime of the halogen lamp and allowing to heat the filament to slightly higher temperatures. Fluorescent lighting, applied as both fluorescent tube lamps and compact fluorescent lamps (CFL), is more efficient than the black-body radiators. Here, the ultra-violet (UV) emission from excited Hg vapor excites the phosphors that are coated on the inside of the tubes, resulting in bright white light. Although CFL and tube lamps are widely applied, their light is not perceived as very pleasant. LEDs are even more efficient and will be the light sources of the 21st century. Research to the optimal materials for LEDs should lead to highly efficient, pleasant, bright warm-white LEDs, that can be applied in various consumer applications.

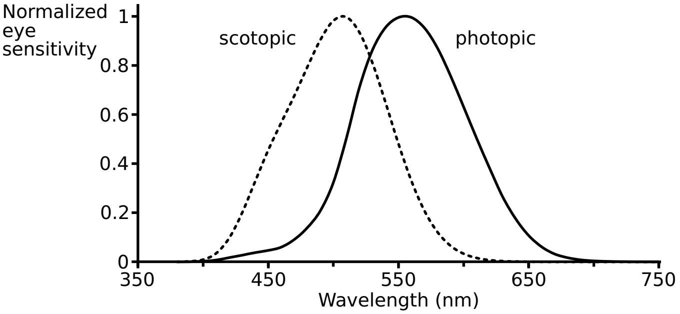

Figure 2.2: Normalized spectral eye sensitivity curves for photopic vision V(λ) (full line) and scotopic vision V'(λ) (dashed line), as specified by the CIE [6].

2.1.1 Quantifying lighting quality

Historically, incandescent light bulbs were qualified by the electric power consumption in W. When CFL came on the market, a lower power resulted in a similar light output, so both the CFL power and the comparable incandescent power were displayed. With LEDs, the power used by the lamp, compared to that of an equally bright incandescence lamp, was reduced even further.

Besides the output power, the color temperature is an important measure to qualify the light output of lamps. The correlated color temperature (CCT) is the temperature in K of a hypothetical black-body radiator that has the same color impression as the lamp of which the CCT is determined. On the CIE 1931 (x,y) diagram, published by the Commision Internationale de l'Éclairage in 1931, the Planckian locus (black line in figure 2.3) shows the relation between the CIE (x,y) coordinates and the CCT value. The sun has a color temperature of 3000–6500 K, depending on the time of day, weather or season. Higher CCT values are experienced as cold, blueish light, while lower CCT values are experienced as warm-white light. Warm-white LEDs have a CCT value of 2700–3000 K, while blueish white LEDs have a CCT of 4000–4500 K [2].

The luminous efficiency of the radiation (LER) describes how bright the light emission is perceived by the human eye. A theoretical maximum value of 683 $\mathrm{lm\,W^{-1}}$ is set for monochromatic green emission at 550 nm, where the eye sensitivity peaks (full line in figure 2.2). For white light, which includes blue and red light as well, the LER is significantly lower,

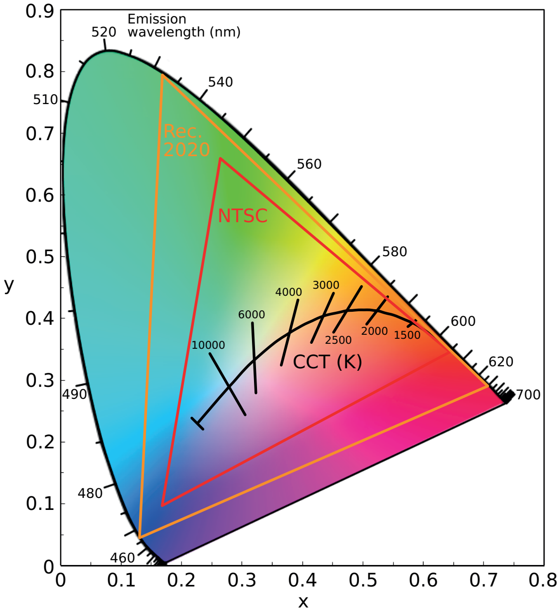

Figure 2.3: CIE 1931 (x,y) diagram with the Planckian locus (black), NTSC color gamut (red) and Rec. 2020 color gamut (orange). The monochromatic emission wavelengths are labeled around the horseshoe diagram.

with a maximum around 350 lm W^{-1}. Obtaining a high LER is a trade-off with color quality, since the human eye is not equally sensitive over the entire visible wavelength range.

A wide variation of white and colored light is possible and the distinct color is specified by the color coordinates on the CIE 1931 diagram (figure 2.3). Although updates have been proposed for the diagram, such as the CIE 1976 (L^*, u^*, v^*,) color space, the CIE 1931 (x,y) chromaticity diagram is still often used. Color gamuts are depicted by triangles with red, green and blue (RGB) corner points, where all colors within the triangle can be formed with the RGB light source. The NTSC color gamut, set by the National Television System Committee has long been the standard for display applications, but larger color gamuts such as the Rec. 2020 set by the International Telecommunication Union are used now for ultra-high definition televisions [7]. For lighting applications, the white light of the LED is qualified by the (x,y) color coordinates of the white point. The distance of the color point of the lamp to the white point on the Planckian locus D_{uv} is calculated in the CIE (u,v) space. CCT values of white light only correspond with the locus, so the D_{uv} value has to be minimized for white light. For display applications, the white point is often supplemented with the color gamut as a percentage of the NTSC or Rec. 2020 color gamut, defined as the area of the triangle.

Although a certain white point can be qualified using the color coordinates, many possible LED and phosphor combinations can reach the same point on the CIE diagram. The different colors that are contributing to the white spectrum can be reflected on colored objects, resulting in colors that can be observed by the human eye. To quantify the way in which colors are represented by lamps, the color rendering index (CRI) was introduced by the CIE. The CRI is a value up to 100 that quantifies the way in which the tested light source renders selected colored objects, compared to a black-body radiator at the same color temperature. The general color rendering index R_a is calculated using eight test color samples and is mostly referenced as the “CRI” value. The metric of the CRI is far from ideal, since the number of test samples is limited and their colors are rather dull, while it is important that bright vivid colors should also be perceived in a correct way. High CRI values can also be obtained for very high or low CCT values, since the test light source is always compared to a black-body radiator has the same imperfect CCT. For CCT values above 5000 K, a standard daylight spectrum of the same CCT, derived from the D65 standard illuminant is used as a reference source. Several improvements of the CRI and alternative indexes have been proposed, but the CRI is still the only one in general use, even on the consumer market [8].

2.2 White LEDs

An LED is a semiconductor chip that emits photons upon recombination of holes and electrons over a p-n junction. The wavelength of the emitted photon corresponds to the direct band-gap energy of the semiconductor material. This electroluminescent process results in a narrow emission band, with nearly monochromatic emission. Depending on the semiconductor used, the LED emission can vary from the UV to the near infrared (IR) region. Since white light consists of the entire visible spectrum, it cannot be obtained by a single LED chip. Three approaches are possible to use LED chips as a light source to form white LEDs (figure 2.4). On the one hand, three or more LED colors can be combined, while on the other hand, phosphors can be used to convert excitation light from either a UV LED or a blue LED [9].

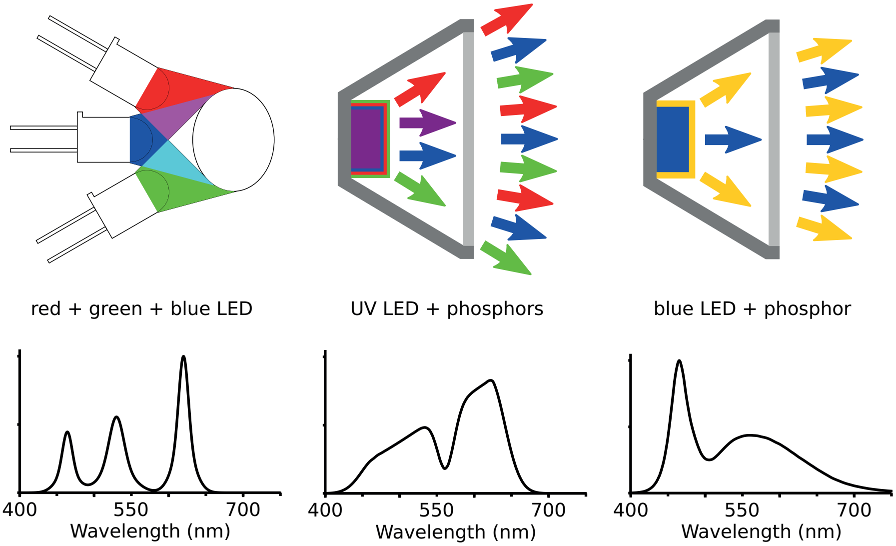

Figure 2.4: Three methods of generating white light from LEDs, schematic drawings (top) and emission spectra (bottom): red, green and blue LEDs (left); UV LED light converted by red, green and blue phosphors (center); phosphor-converted LED consisting of a blue LED and a yellow phosphor (right).

2.2.1 RGB LEDs

Combining red, green and blue LED chips (right in figure 2.4) results in white light, as can be seen in displays. By changing the relative intensity of the three colors, all colors within the RGB triangle on the CIE diagram can be produced. White light with a CRI of 50-70 can be obtained from a RGB LED, while a higher efficiency and color rendering can be obtained when an amber LED is added to the mixture [10]. An advantage of this approach is that no energy is lost by conversion to lower wavelengths, as always occurs when phosphors are used. RGB LEDs are mainly applicable in displays, where the light source is viewed directly and color rendering is not applicable. For lighting applications RGB leds are not the most obvious, apart from specific uses where color rendering is less important such as atmospheric lighting. Smart lighting, in which the emission color and the light intensity can be adapted by the user, is only possible with a combination of different LED chips. Nevertheless, the efficiency of green LED chips is rather low and bright green light can be more easily be obtained with a blue LED chip and a green phosphor. Since the various colored LED chips have a different aging rate, complex electronics with feedback mechanisms are needed for a stable color rendering over the lifetime of the white LED. Dimming the light while maintaining the emission color can be difficult, since current or temperature-dependent color shifts can occur.

2.2.2 Phosphor-converted wLEDs

In contrast to the RGB approach, in phosphor-converted white LEDs (pc-wLEDs), only one LED chip is used, with an emission wavelength in either the UV or the blue region. Phosphor materials are used to convert the high-energy photons to a lower energy, which corresponds to a longer wavelength. In this way, the complete visual spectrum can be covered, creating white light. Most wLEDs that are currently available are based on this phosphor conversion principle. Inevitably, energy is lost during the phosphor conversion, related to the Stokes shift on the one hand, and to imperfect conversion quantified as the internal quantum efficiency on the other hand.

With UV LEDs, at least two phosphor materials are needed to convert all LED light (360–410 nm) to white light. A high absorption by the phosphors is critical with a UV pumping LED, since transmitted UV light does not improve the white light output. UV light can also be harmful, so the unconverted UV light has to be filtered away.

When a blue pumping LED is used, at least one phosphor material is needed to create white light. A typical pc-wLED consists of an InGaN LED chip emitting blue light (420–480 nm) and the yellow $Y_3Al_5O_{12}$:Ce^{3+} (YAG:Ce) phosphor. Other phosphor combinations with green and red phosphors are also possible, all of which are covered by the research field of LED phosphors. Six performance requirements were proposed for phosphors for wLEDs [8]:

1. The emission spectrum of the phosphor should reach pure white emission when combined with an LED and other phosphors, reaching a specific color temperature, color rendering or color gamut. Different requirements are set for lighting and displays.

2. The excitation spectrum of the phosphor should match the excitation source, either blue or UV light and should not overlap with the emission spectrum.

3. The emission and excitation properties should be stable up to the elevated temperature reached by LEDs in operation.
4. A high internal quantum efficiency, close to unity, should be reached to reduce the energy losess by the conversion process.
5. The phosphor material should be chemically stable, to reach the proposed lifetime of 50 000 h.
6. A linear response of emission intensity is required upon excitation, reducing saturation effects even at high photon fluxes.

Only when these conditions are simultaneously fulfilled, a phosphor can be considered as a valid candidate for wLED applications. YAG:Ce has a broad yellow emission band, due to the 5d–4f transition in Ce^{3+}, with a broad excitation band around 460 nm. The phosphor has proven to be stable over a long time and thermal quenching and saturation is limited for the Ce^{3+} emission, ratifying the employment of YAG:Ce in pc-wLEDs. Unfortunately, the color rendering of a YAG:Ce pc-wLED is limited, especially in the red wavelength region. Nevertheless, the combination of a blue LED and YAG:Ce is the perfect work horse for high efficient white light in applications where color rendering is not crucial, such as street lights, car headlights and flashlights.

2.3 Red phosphors for warm-white LEDs

Addition of red light to the classic blue and yellow pc-wLED improves the color rendering quality of the white LED, lowering the CCT to warm white light and increasing the CRI. The number of suitable red phosphor materials that are available is limited, which opens opportunities for research into efficient red phosphors. Sulfide phosphors such as $CaS:Eu^{2+}$ and $SrS:Eu^{2+}$ have been suggested for LED applications, but show a moderately low chemical stability even when coated with Al_2O_3 [11]. Eu-doped nitrides such as $Sr_2Si_5N_8:Eu^{2+}$ and $CaAlSiN_3:Eu^{2+}$ have a better stability, but the broad emission band can extend in the deep red wavelength region [12, 13].

As can be seen in the eye sensitivity curve (figure 2.2), the human perception of red-emitting phosphors is limited by the low eye sensitivity at high wavelengths. Above 650 nm, the eye sensitivity is only 10% of the maximum sensitivity at 555 nm. Therefore, it is important for red phosphors to increase the emission intensity at shorter red wavelengths (620–630 nm) and to limit the emission intensity at longer wavelengths (>650 nm). In this way, a high LER can be obtained for a warm-white LED. This work will focus on Mn^{4+}-doped phosphors for warm-white LEDs. Chapter 3 will focus on Mn^{4+} as a dopant, which, depending on the host, can show emission at both shorter and longer red wavelengths.

2.4 Remote phosphor LEDs

In a remote phosphor setup, the phosphor is placed on a distance from the LED chip instead of directly on the LED chip. The operating temperature of the LED chip can reach 150–200 °C, and increasing the distance between the phosphor and the LED chip reduces the heat transfer to the phosphor material. This will reduce the influence of thermal quenching in the phosphor. In the phosphor layer, heat is additionally generated due to the energy difference between the incoming photons and the emitted photons, which is the Stokes loss and because the internal quantum efficiency is lower than 100 %. In the remote phosphor setup, an increased phosphor area will lower the optical flux density, which lowers the influence of the Stokes losses and scattering losses. More phosphor material is needed when the phosphor is deposited in a separate layer, which specifies the need for cheap materials that are easily made in a large scale synthesis.

In high-brightness applications, high excitation fluxes are used, which increases the probability of saturation of the emission. In a remote-phosphor setup, the optical flux density is lower because a larger phosphor area is used, so saturation effects are reduced. This allows for the use of phosphors with a longer luminescence lifetime (in the ms range).

Apart from the thermal properties, the remote phosphor setup can be advantageous from a design perspective. Although the remote phosphor setup is somewhat bigger than an on-chip phosphor-converted wLED, the emitted light is more diffuse, which is preferable for general lighting. The remote phosphor setup also offers a more homogeneous light output with stable colors due to initial averaging in the phosphor layer, which is needed for display backlights.

Although advantageous thermal effects can be expected, in smaller remote phosphor LED designs where a high light output is expected, the temperature in these layers increase up to 150 °C [14]. Besides thermal quenching of the phosphor, degradation of the encapsulant can reduce the total light output of the LED at increased operating temperatures. Therefore, proper heat management is also needed for remote phosphor LEDs [15]. The use of perforated, thermally conducting heatsinks can reduce the temperature of the phosphor layer [16]. A temperature reduction of 50 °C could be obtained with a perforated aluminum heatsink compared to a insulating heatsink, of which 15 °C was contributed by active cooling with a fan. The obtained maximum phosphor temperature in this setup was 75–78 °C, dependent on the heatsink configuration. At these temperatures thermal quenching is limited and stable encapsulants can be found. An experimental example of remote phosphor LEDs will be discussed in chapter 13.

3

Transition-metal dopants: Mn^{4+}

Most phosphor research in the last decade was focussed on rare-earth dopants. On the one hand, Ce^{3+} is the dopant of the go-to LED phosphor YAG:Ce. On the other hand, Eu is a multifunctional dopant with both Eu^{2+} and Eu^{3+} used in applications, such as $SrGa_2S_4$:Eu^{2+} as a green LED phosphor [17] and Eu^{3+}-doped scheelites that can be used as a thermographic sensor [18]. Another example of a widely-used rare-earth-doped phosphor is the characteristic glow-in-the-dark phosphor $SrAl_2O_4$:Eu^{2+},Dy^{3+} [19]. Although widely used, rare-earth elements have some drawbacks, as they are rather expensive to purify and the supply can be interrupted for geopolitical reasons. This paves the way for transition-metal dopants, such as Mn, to take over at least part of the phosphor market. In this chapter, the spectroscopic properties of Mn^{4+} will be discussed, to explore the possibilities of Mn^{4+}-doped phosphors. No extensive calculations of spectroscopic parameters were performed in this work, the overview in this chapter is based on a comprehensive literature review.

3.1 Spectroscopic parameters

Manganese is a transition metal with electron configuration [Ar] $3d^5$ $4s^2$, with many possible oxidation states, of which 7+, 4+, 2+ and 0 are the most common ones. Mn^{4+} can show luminescence due to $3d^3$–$3d^3$ transitions. The $3d^3$ electron configuration of Mn^{4+} results in 120 possible distributions of the three electrons over the ten available single-particle states of the 3d shell. The electronic Coulomb repulsion gives rise to a splitting of the 120-fold degenerate configuration in eight LS terms that can be found for the free Mn^{4+} ion, the magnitude of this splitting is characterized by the Racah parameters B and C [20]. These terms are further split by the crystal field (CF), characterized by so-called CF parameters [20]. The symmetry of the CF dictates the number of required parameters and the remaining degeneracies of the electronic energy levels. For an octahedral crystal field, only one CF parameter, $10Dq$, is required and the splitting is described by the Tanabe–Sugano diagram (figure 3.1(a)). Due to its high effective positive charge, Mn^{4+} experiences a large charge difference density, as specified by the high value of $10Dq/B$. In this case, the emitting level has ^2E_g symmetry, resulting in a sharp emission line of the spin-forbidden transition towards the $^4A_{2g}$ ground state. Two broad absorption bands are present from the spin-allowed $^4A_{2g} \rightarrow {}^4T_{2g}(^4F)$ and $^4A_{2g} \rightarrow {}^4T_{1g}(^4F)$ transitions [21]. The third spin-allowed absorption band, from the $^4A_{2g} \rightarrow {}^4T_{2g}(^4P)$ transition is located at higher energies and can overlap with host-lattice absorption or ligand–Mn^{4+} charge transfer [22]. The width of the excitation bands is explained by the strength of the electron-vibrational interaction between the electronic states of Mn^{4+} ions and crystal-lattice vibrations [22, 23]. The emitting transition, $^2E_g \rightarrow {}^4A_{2g}$, corresponds to a mere spin-flip of a single electron, showing a small electron–phonon coupling and hence an emission spectrum featuring a zero-phonon line (ZPL) along with a few Stokes and anti-Stokes lines.

Different hosts can be compared according to their spectroscopic parameters. These can be obtained by a tedious fitting procedure involving different terms in an effective Hamiltonian. The values given in this chapter are taken from literature or calculated from transition energies given in literature. Next to the common Racah parameters B and C and the CF parameters, additional interactions are sometimes accounted for. These can include low symmetry components of the crystal field or the 3d spin-orbit coupling. The Trees parameters α and β are known to improve the correspondence between experimental and calculated spectra as they correct in an effective way for the single configurational description of the formalism. In the case of Mn^{4+}, care should be taken to avoid overparameterization as only a few experimental energies are available. As can be seen in figure 3.1, it is designated to use the $^2E_g \rightarrow {}^4A_{2g}$ zero-phonon line for the CF fit, while band maxima are better used for the $^4A_{2g} \rightarrow {}^4T_{2g}(^4F)$ and $^4A_{2g} \rightarrow {}^4T_{1g}(^4F)$ transitions. The reason for this is the different offsets between the minima of the energy state parabolas. A CF Hamiltonian does not account for electron-vibrational coupling and represents only one geometry of the luminescent center, corresponding to a fixed Q-value in figure 3.1(b). CF calculations on K_2SiF_6:Mn^{4+}, including the effect of tetragonal and trigonal deformations on the energy levels were performed by Jonas Joos [24, 25].

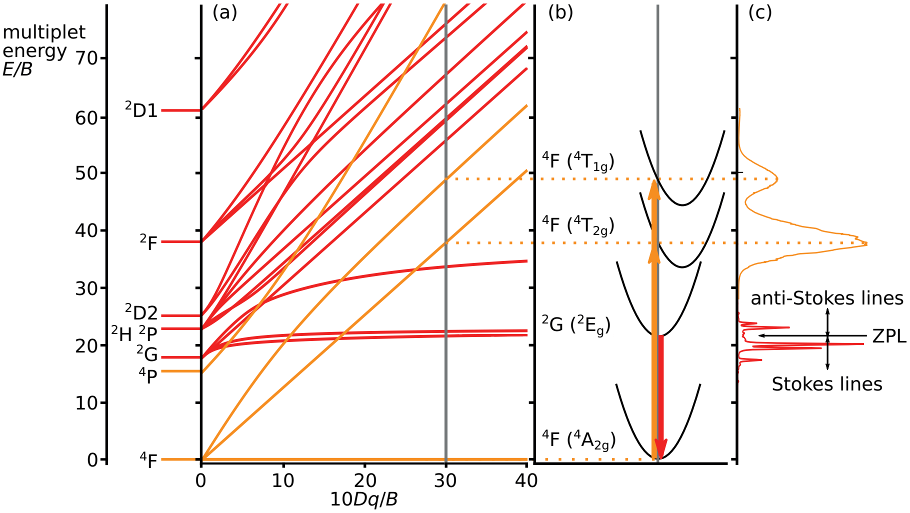

Figure 3.1: Illustration of how the emission and excitation spectrum are governed by the electronic structure of the octahedral $[MnF_6]^{2-}$ center. (a) Tanabe–Sugano diagram for a $3d^3$ system in the octahedral symmetry, showing how the free-ion terms (shown in the extreme left part of the figure) split in the crystal field. Orange lines indicate spin quartets, red lines indicate spin doublets. This diagram indicates the energies of the spectroscopic transitions. The gray vertical line corresponds to the case of Mn^{4+} in K_2SiF_6. (b) Simplified configurational coordinate diagram showing the potential energy parabolas that play a role in the radiative transitions. This diagram qualitatively indicates the spectral shape for the different transitions. (c) Room temperature excitation (orange line) and emission (red line) spectrum of K_2SiF_6:Mn^{4+}. The approximate location of the zero-phonon line (ZPL) is indicated.

3.2 Calculating the Racah parameters

Racah parameters can be calculated from experimental data, but here some equations derived in literature are given to be able to compare data without the need for lenghty calculations. Within the effective Hamiltonian formalism, numerically fitting is certainly the most practical approach, providing freedom in selecting which interactions are taken into account. If the Hamiltonian is however restricted to the octahedral crystal field and when only the Coulomb interaction (characterized by B and C) is taken into account, a simpler approach is possible where analytical formulas relate the parameters B, C and $10Dq$ to transition energies. The ratio $10Dq/B$, as used in the Tanabe–Sugano diagram, is often directly obtained from the location of the $^4\mathrm{T}_{2g}(^4\mathrm{F})$ level. The value of B can be obtained in addition from the location of a second energy level. The full Hamiltonian is block diagonal according to the irreducible representations of the octahedral point group O_h. Diagonalization of the 2×2 submatrix, corresponding to $^4\mathrm{T}_{1g}$, directly yields the energies of the $^4\mathrm{T}_{1g}(^4\mathrm{F})$ (lowest eigenvalue) and $^4\mathrm{T}_{1g}(^4\mathrm{P})$ levels. Subtracting the energy of $^4\mathrm{T}_{2g}(^4\mathrm{F})$, which constitutes a 1×1 block, yields equation 3.1, derived in [26].

$$\frac{B}{Dq} = \frac{(\Delta E/Dq)^2 - 10\,(\Delta E/Dq)}{15\left(\frac{\Delta E}{Dq} - 8\right)} \tag{3.1}$$

with

$$\Delta E = E[^4\mathrm{T}_{1g}(^4\mathrm{F})] - E[^4\mathrm{T}_{2g}(^4\mathrm{F})] \tag{3.2}$$

In addition, the B/C ratio is often kept fixed, to reduce the number of parameters. An approximate way to determine C is also provided in [26] and requires the location of a third energy level.

$$\frac{C}{Dq} \approx 0.328\frac{\Delta E'}{Dq} - 2.59\frac{B}{Dq} + 0.59\left(\frac{B}{Dq}\right)^2 \tag{3.3}$$

with

$$\Delta E' = E[^2\mathrm{E}_g(^2\mathrm{G})] - E[^4\mathrm{A}_{2g}(^4\mathrm{F})] \tag{3.4}$$

The obtained C value deviates up to a few tens of wavenumbers from the exact diagonalization of the Hamiltonian containing the octahedral crystal field and the 3d–3d Coulomb repulsion. Crystal field strengths $10Dq$ and Racah parameters B, C were empirically determined for Mn^{4+} in many host compounds. The value of $10Dq$ for Mn^{4+} is known to vary from

18 180 cm^{-1} in $SrTiO_3$ [27], to 24 000 cm^{-1} in $\frac{7}{2}\,MgO\cdot\frac{1}{2}\,MgF_2\cdot GeO_2$, a fluorogermanate host, in which the octahedral symmetry is slightly distorted due to the Jahn–Teller effect [28]. The location of the emitting ^2E_g state, and hence the color of the luminescence is largely independent of $10Dq$, as evidenced by the flat line in the Tanabe–Sugano diagram (figure 3.1(a)) [22, 27, 28]. Still, the position of the ZPL of the emitting $^2E_g \rightarrow {}^4A_{2g}$ transition can vary depending on the host from 16 207 cm^{-1} in Na_2SiF_6 to 13 827 cm^{-1} in $SrTiO_3$ [22, 27, 29]. This variation is primarily determined by the values of the Racah parameters B and C. When Mn^{4+} is incorporated in a crystal or molecule, the Racah parameters are reduced with respect to the free ion values $B_0 = 1160\,cm^{-1}$ and $C_0 = 4303\,cm^{-1}$ [30]. This reduction is commonly referred to as the nephelauxetic effect, a term first introduced by Schäffer and Jørgensen who introduced a nephelauxetic parameter β (equation 3.5) to quantify the effect [31, 32].

$$\beta = \frac{B}{B_0} \tag{3.5}$$

Values for this parameter were derived based on spectroscopy of the 3d ions Mn^{2+}, Ni^{2+}, Fe^{3+}, Cr^{3+} and Co^{3+}, the 4d ion Rh^{3+} and the 5d ion Ir^{3+} in various host compounds including halides. A series was found, the nephelauxetic series, ordering ligands according to a decreasing β value. Fluorides feature a limited nephelauxetic effect, corresponding to a β value close to unity while for oxides and other compounds, β decreases. This effect becomes more important for more easily polarizable ligands or, alternatively, for ligands that feature a smaller electronegativity, yielding more covalent chemical bonds, with elements such as chlorine, sulfur and iodine. The same effect plays a role in the spectroscopy of Mn^{4+} for which the emission color can be tuned due to the nephelauxetic effect from saturated red for fluorides such as K_2SiF_6, to deep red and near-infrared for oxides. Besides several oxide and fluoride compounds, Mn^{4+} is only suspected to be stabilized in two nitride compounds, GaN:Mn^{4+} and AlN:Mn^{4+} [33, 34], and in organic molecular complexes [35]. When incorporated in these nitrides, Mn^{4+} has a tetrahedral symmetry, resulting in $^4T_2(F) \rightarrow {}^4T_1(F)$ as the emitting transition [33], so equations 3.1 and 3.3 cannot be applied to these compounds. Based on a thorough literature survey of Mn^{4+} spectra, Brik and Srivastava altered Jørgensen's nephelauxetic parameter to equation 3.6 including both Racah parameters B and C simultaneously [23, 36].

$$\beta_1 = \sqrt{\left(\frac{B}{B_0}\right)^2 + \left(\frac{C}{C_0}\right)^2} \tag{3.6}$$

A linear dependence of β_1 on the $^2E_g \rightarrow {}^4A_{2g}$ transition energy is found in figure 3.2 and can be regarded as a further simplification of equation 3.3. A similar trend is found for Cr^{3+}, another $3d^3$ ion [37].

3.2.1 Spectroscopic parameters of K_2SiF_6:Mn^{4+}

All spectroscopic parameters for K_2SiF_6:Mn^{4+} reported in literature are summarized in table 3.1 and the corresponding data points are indicated in figure 3.2. When the Racah parameters were not available, they were calculated from the energy levels given in table 3.2 according to equations 3.1 and 3.3.

Table 3.1: Spectroscopic parameters for K_2SiF_6:Mn^{4+}.

Dq (cm^{-1})	B (cm^{-1})	C (cm^{-1})	Dq/B	Ref.
1980				[38]
1980[1]	375	4350	5.28	[39]
[1]	580	3860		[39]
	605	3806		[40]
	770	3435		[22]
2030	770	3470	2.64	[21, 41]
2159				[42]
2160				[38]
2179				[24]
2197[2]	599	3750	3.67	[23]
2212				[43]
2390[3]	770	3435	3.10	[23]
2500[4]				[44]
2800[5]				[44]

[1] ZPL from [42]

[2] Spectra from [38]

[3] Spectra from [21]

[4] Calculated with lattice relaxation

[5] Calculated without lattice relaxation

Table 3.2: Values of zero-phonon lines for optical relevant d-d transitions in K_2SiF_6:Mn^{4+} from experiments and empirical calculations.

$^2E_{2g} \rightarrow$ $^4A_{2g}$ (eV)	$^4A_{2g} \rightarrow$ $^4T_{2g}(^4F)$ (eV)	$^4A_{2g} \rightarrow$ $^4T_{1g}(^4F)$ (eV)	$^4A_{2g} \rightarrow$ $^4T_{1g}(^4P)$ (eV)	Method	Ref.
1.02				DFT-PBE calculation	[45]
1.29				DFT-HSE06 calculation	[45]
1.968				Based on experimental spectrum of [38]	[23]
1.989				Experimental (rt)	[46]
1.993				Experimental, after compression > 9 kbar	[47]
1.993	2.52	3.09	4.38	Franck–Condon fit (300 K)	[42]
1.995	2.45	2.94		Franck–Condon fit (300 K)	[48]
1.995	2.73	3.53	5.77	CF calculation, experimental (rt)	[40]
1.995				Experimental (20 K, rt)	[49, 50, 51]
1.996	2.52	3.09		Experimental (20 K, 300 K, rt)	[21, 41, 52]
1.998	2.67	3.38		Experimental (10 K)	[24]
1.998	2.68	3.20	4.48	Franck–Condon fit (20 K)	[38, 42]
1.999				Experimental (20 K, 90 K)	[43, 21]
2.003				Experimental (rt)	[53]
2.004	2.62	3.43		CF calculation	[24]
2.88	3.88	6.20		CF calculation	[22]

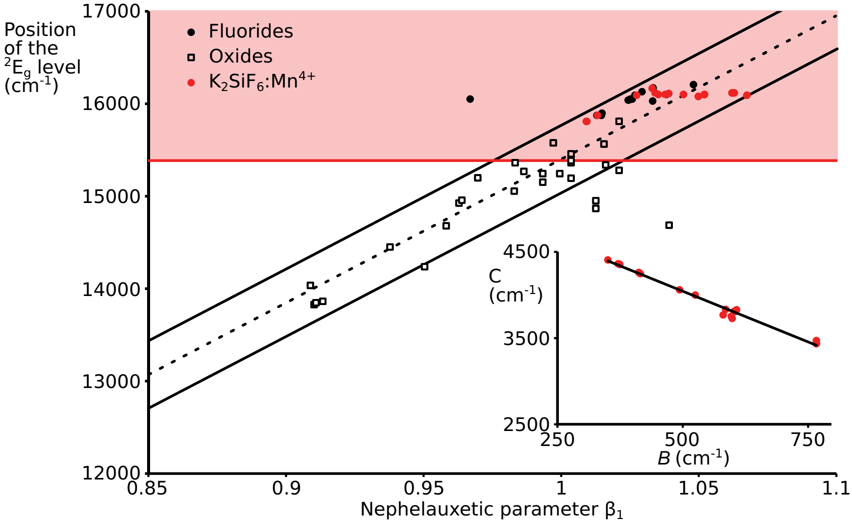

Figure 3.2: Dependence of energy of the Mn^{4+} ^2E_g level on the new nephelauxetic ratio β_1 for fluoride hosts and oxide hosts and reported values for $K_2SiF_6:Mn^{4+}$, adapted from [36]. The shaded red area corresponds to a peak wavelength < 650 nm, the given linear fit is $-142.83 + 15544.02\beta_1$, with $\pm\sigma = 365\,cm^{-1}$. Inset: The reported values of the Racah parameters B and C for $K_2SiF_6:Mn^{4+}$, which were used to calculate the nephelauxetic parameter β_1, show a linear correlation. The given linear fit is $5179.5 - 2.256B$.

The location of the energy levels of $K_2SiF_6:Mn^{4+}$ has been determined using experimental spectra, Franck–Condon fits and CF calculations, but the obtained values vary. In general, values from CF calculations are at higher energies than the experimental values. The B value of $K_2SiF_6:Mn^{4+}$ varies from 351–770 cm^{-1}, where the lower values originate from experimental ZPL energies and the higher ones come from CF calculated energies. The value of 770 cm^{-1} is most often referred to [24, 21, 23, 36] and corresponds only with the CF calculated energy levels by Brik and Srivastava [22], according to equations 3.1 and 3.3. Other publications use a value for the ZPL of the $^4A_{2g} \rightarrow {}^4T_{1g}(^4F)$ transition that is up to 7500 cm^{-1} lower, causing the variation of B to 375 cm^{-1}. Such a wide distribution of the location of the ZPL is remarkable, and has consequences for other spectroscopic parameters. The $10Dq/B$ ratio, which shows the position of the transitions in the Tanabe–Sugano diagram, is between 26.4 and 58.1, due to the large variation in B. The C value varies from 3433–4405 cm^{-1}, with lower values from CF calculated energies and higher values from experimental ZPL energies. When the $^2E_{2g} \longrightarrow {}^4A_{2g}$ ZPL is observed in experimental spectra of K_2SiF_6:Mn^{4+}, often at lower temperatures (10–90 K), it is located at 1.99–2.003 eV. Although various data are cross-referenced, the calculated parameters often differ, which can be caused by the choice for ZPL or centered energy values for the excitation bands. When equations 3.1 and 3.3 are applied to the CF-calculated energy levels by Brik and Srivastava [22], the obtained $10Dq/B$ ratio is 30.2 with $C = 3440\,\mathrm{cm}^{-1}$. Despite the different values for energy levels that are used in calculations, a clear linear correlation is found if all the empirical B and C values that are found for K_2SiF_6:Mn^{4+} are compared, as can be seen in the inset of figure 3.2. For the different B and C values, a rather constant β_1 of 1.039 ± 0.018 is found, favoring the use of a single β_1 parameter.

3.2.2 First principles calculations of K_2SiF_6:Mn^{4+}

The previous calculations were empirical, based on experimental photoluminescence spectra, typically measured at low temperature. On the other hand, it is possible to obtain information on structural, electronic and optical properties from so-called first principles methods. Novita et al. calculated transition energies starting from DV-Xα molecular orbitals that were combined in many-body states [54]. Correlation effects were introduced by a method described in [55]. The obtained results are promising, describing the influence of the host compound in a qualitative correct way and yielding ZPL energies that are 308 meV, 170 meV and 450 meV different from the experimental values at 10 K [24].

Density functional theory (DFT) was applied to the study of K_2SiF_6 and K_2SiF_6:Mn^{4+} at local density approximation (LDA) level [37, 40], generalized gradient approximation (GGA) level [37, 40, 45] or with a hybrid functional [45]. Ground state geometries were found that are in line with experimental results. Calculated energies of the direct band gap of K_2SiF_6 amount to 8.092 eV (LDA) [37] and 7.588 eV (GGA), with the corresponding electronic band structure given in figure 3.3(c) [37]. The experimental determination of band gaps above 5 eV is not straightforward, due to absorption of the setup. The only published experimental band gap is 5.6 eV [21], which seems underestimated since DFT calculations usually underestimate band gap values. The Kohn-Sham density of states (DOS) for K_2SiF_6:Mn^{4+} is shown in figure 3.3. The top of the valence band is mainly composed of F-2p orbitals while the conduction band bottom is composed

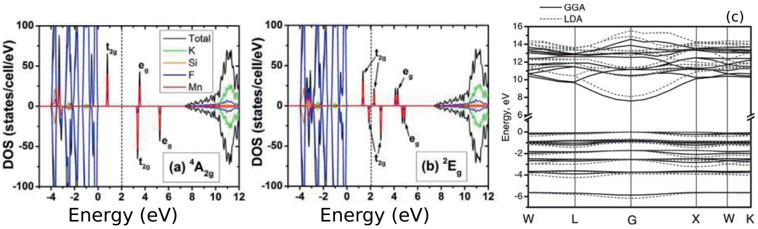

Figure 3.3: The Kohn-Sham density of states (DOS) for K_2SiF_6:Mn^{4+} calculated using DFT-PBE, ground state t_{2g}^3 ($^4A_{2g}$) (a) and excited state $t_{2g}^2e_g^1$ (^2E_g) (b). Reproduced from [45] with permission from The Royal Society of Chemistry. (c) The calculated band structure of K_2SiF_6. The GGA- and LDA-calculated electronic bands are shown by the solid and dotted lines, respectively. The Fermi level is set at zero energy. The coordinates of the special points of the Brillouin zone are (in terms of the reciprocal lattice unit vectors): W(1/2, 1/4, 3/4); L(1/2, 1/2, 1/2); G(0,0,0); X(1/2, 0, 1/2); K(3/8, 3/8, 3/4). Reprinted with permission from [37]. Copyright 2012, The Electrochemical Society.

of Si and K orbitals. Upon adding the Mn dopant to the supercell, Kohn-Sham single particle levels with symmetry labels t_{2g} and e_g are introduced in the band gap. These levels correspond to molecular orbitals composed of Mn-3d and F-2p character, indicating the existence of Mn-F hybridization [45].

Even though the use of DFT is essentially limited to ground state properties, the nature of the emitting transition in Mn^{4+}-doped phosphors allows to estimate the energy of the ZPL by means of Δ-SCF (self-consistent field), which is forcing the system into an alternative occupation of single-particle levels. The difference in total energy between the t_{2g}^3 (corresponding to the ground state $^4A_{2g}$ (^4F)) and $t_{2g}^2e_g^1$ (corresponding to the emitting level ^2E_g (^2G)) occupations of the Mn-3d shell were reported in literature [45]. This technique yields ZPL energies that are systematically too low, 1.02 eV and 1.29 eV in the case of K_2SiF_6:Mn^{4+} using the PBE and a HSE06 functional respectively.

3.3 Conclusion

The systematic behavior of energy levels as a function of the covalence of the chemical bond, empirically encoded in the parameter β or β_1, is found, paving the way for a semi-empirical method to predict the emission color of Mn^{4+}-doped phosphors [45]. A small Jahn–Teller distortion towards a tetragonal symmetry was shown in the DOS of the excited ^2E_g state in figure 3.3. Such a small deformation of the octahedral complex of the $[MnF_6]^{2-}$ defect clusters can change the energy level degeneracy, which can influence the luminescence behavior.

4

Phosphor evaluation techniques

Several analytical methods are used to evaluate the quality of a phosphor synthesis and to characterize the properties of the obtained phosphor material. In this chapter, an overview is given of the techniques and equipment used for the characterization of structural, electronic and luminescent properties of phosphor materials.

4.1 Structural properties

Structural characterization of phosphors is used to identify the material after synthesis and to confirm the crystallinity of the phases. Since the dopant is only present in low concentrations (typically 1–2 %), the influence of the dopant on the structural properties is limited. Therefore, reference data of undoped host materials can be used in structural determination.

4.1.1 X-ray diffraction

X-ray diffraction (XRD) is an analytical technique that is used to study crystal structures. Monochromatic X-rays from the Cu Kα source in the diffractometer are elastically scattered from the sample. On the randomly

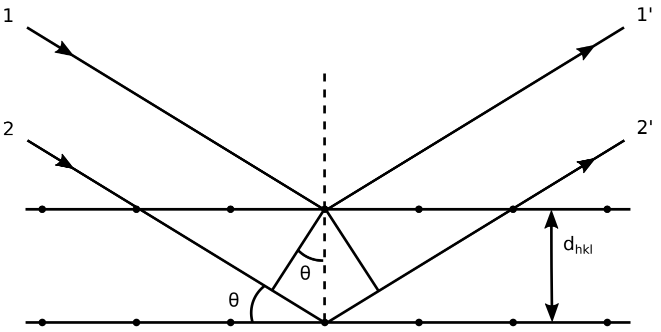

Figure 4.1: Schematic representation of Bragg's law, where constructive interference is found from reflections on parallel crystal planes.

oriented crystallites in powder samples, constructive interference occurs on parallel crystal faces when the incoming X-rays have the same angle θ as the scattered X-rays (figure 4.1). This relation is given by Bragg's law (equation 4.1), with d_{hkl} the distance between two parallel crystal planes, n the order of the diffraction and λ the wavelength of the X-rays.

$$2d_{hkl}sin\theta = n\lambda \tag{4.1}$$

A Siemens D5000 diffractometer (40 kV, 40 mA) was used to measure powder diffraction patterns in a $\theta/2\theta$ geometry, where the X-ray source is fixed and the table holding the sample moves over an angle θ, while the detector moves around the powder sample on an arc specified by the angle 2θ.

The obtained diffraction patterns can be compared to reference patterns to characterize the obtained crystal structure and to identify crystalline defects that are present in the sample. The width of the diffraction peaks is determined by the crystallite size, with broader peaks for smaller crystallites. If a dopant induces a large shift in the crystal lattice, it can influence the diffraction patterns.

4.1.2 SEM-EDX

A scanning electron microscope (SEM) uses a high-energy electron beam to analyze surfaces (figure 4.2). A higher resolution can be obtained compared to an optical microscope, since the wavelength of the electron beam is shorter than that of visible light. An instrumental resolution of 1–5 nm is obtained, limited by the spot size of the electron beam.

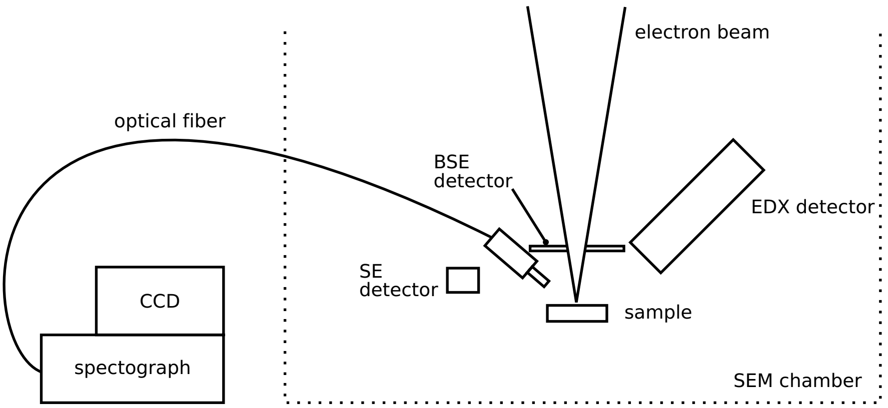

Figure 4.2: Schematic representation of the scanning electron microscope (SEM) with the detectors for secondary electrons (SE), backscattered electrons (BSE), energy-dispersive X-rays (EDX) and cathodoluminescence (CL).

The SEM measurements were performed using a Hitachi S-3400 N SEM. Electrons are emitted by a tungsten filament, accelerated in the direction of the sample by the anode and focused by lenses. The electron beam scans the sample row after row, similar to how a CRT television displays an image.

From the interaction of the primary electron beam with the sample, several types of secondary particles and photons with different energies are emitted. These include secondary electrons, backscattered electrons, characteristic X-rays and photons. While the sample surface is scanned, images of the sample can be formed by detecting the secondary particles emitted from every point.

Secondary electrons (SE) have a fairly low energy ($<50\,\mathrm{eV}$) and are emitted close to the incoming electron beam. They are deflected towards the SE detector positioned on the side by its electric field. Since secondary electrons are created close to the surface, the created image gives topographical information at a high resolution.

Backscattered electrons (BSE) are elastically scattered by the atoms in the sample. They have a higher energy than secondary electrons and are therefore hardly bent by the electric field of the SE detector. The BSE detector is placed above the sample, around the incoming electron beam. Since the scattering increases for heavier atoms, the intensity of the BSE is related to the chemical composition of the sample. In an image from the

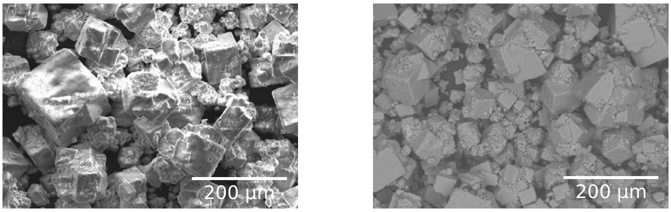

Figure 4.3: SEM image of a $K_2SiF_6:Mn^{4+}$ phosphor powder made using the SE detector (left) and the BSE detector (right). The white glow on the SE image is caused by charging of the phosphor powder by electrons.

BSE detector, heavier elements are depicted lighter (white) while lighter elements (such as carbon tape used to attach the sample) are depicted darker (black).

The information obtained from SE and BSE is complementary as can be seen in figure 4.3. In phosphor research, BSE images are mostly used, because they can also be obtained at a slightly lower vacuum (25 Pa). Measurements using the SE detector are possible at higher vacuum (<1 Pa), but result in charging of the sample, interfering with the image formed. These charges can be removed from the sample by sputtering of a conductive layer of gold (which will block any luminescence) or by introduction of air molecules by lowering the vacuum.

The high-energy incident electrons can excite a core electron of the atoms in the sample. The hole that is left is rapidly filled by an electron from a higher-lying shell, creating characteristic X-rays. With energy-dispersive X-ray spectroscopy (EDX), the different characteristic X-rays can be resolved and a map can be made of the distribution of various chemical elements over the sample.

4.2 Luminescent properties

The structural properties mainly yield information on the host material. Due to the low dopant concentration, the influence of the dopant on the host material can not always be determined using structural analytical techniques. Luminescence measurements focus on the influence on the dopant ion, since the pure host material mostly does not show any luminescence.

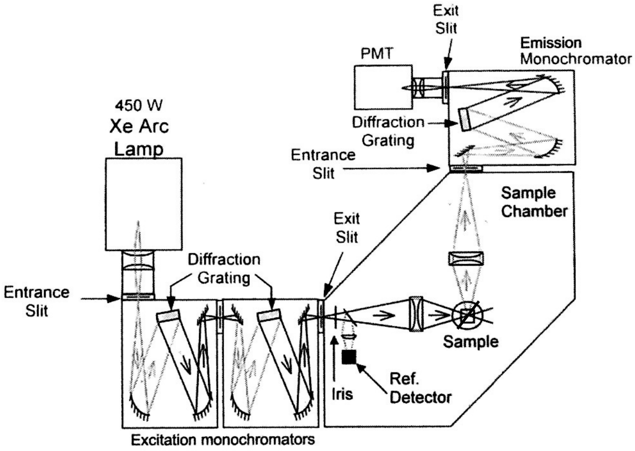

Figure 4.4: Schematic representation of the photoluminescence spectrometer.

4.2.1 Photoluminescence spectroscopy

Photoluminescence spectroscopy is the main analytical technique for luminescence characterization, which can be tuned to a wide variation of measurements.

Excitation and emission spectra To measure an emission spectrum, a fixed excitation wavelength is set and the emission intensity is recorded as a function of the wavelength. Confirming the Stokes shift, the excitation wavelength is always shorter than the emission wavelength. To measure an excitation spectrum, a fixed emission wavelength is set at which the emission intensity is recorded.

Excitation and emission spectra are measured using the Edinburgh Instruments FS920 photoluminescence spectrometer (figure 4.4). A high-pressure 450 W xenon arc lamp is used as a light source. The excitation wavelength is selected using a double excitation monochromator, where the second monochromator is used to improve the wavelength resolution and to remove stray light. The monochromatic light is focused on the tilted sample positioned under 45°. The emission light passes through another monochromator towards the Hamamatsu 928 photomultiplier tube. Colored glass filters are placed between the sample and the emission monochromator to block any excitation light, to prevent saturation of the detector with second order diffractions. The measurements are corrected for variation in detector sensitivity using a calibration file. Spectral features related to the xenon arc lamp, which can show in excitation spectra have been smoothed.

Thermal quenching Measuring emission spectra as a function of temperature yields information about the thermal quenching of the phosphor. Thermal quenching measurements were performed using a lab-built setup with an Anton Paar TTK 450 heating-cooling stage in a vacuum chamber. The stage can be heated up to 500 K by a resistor and cooled to 210 K with a liquid nitrogen flow. The vacuum chamber is connected to a spectrophotometer equipped with a monochromator (Princeton Instruments Acton SP2300) and a camera (Princeton Instruments ProEM 1600) using an optical fiber. A 5 mm LED is used as excitation source, which is also coupled to the vacuum chamber using an optical fiber. The thermal quenching temperature, at which the integrated emission intensity is halved compared to the initial emission intensity, is around 520 K for commercial YAG:Ce, which is above the typical working temperature for LEDs [56].

Time-resolved photoluminescence Time-resolved photoluminescence measurements are used to study the decay dynamics of the phosphor. In Mn^{4+}-doped phosphors, the excited state has a lifetime in the millisecond range, so the measurements have to be performed within this time frame. An Andor Technology DH720 intensified charge-coupled device (ICCD) is used as a detector. Coupled to a 0.5 m monochromator, the ICCD can collect a full emission spectrum at once. Since reading out the ICCD takes longer than the luminescence lifetime, a full decay profile can not be measured in one measurement. Therefore, a pulsed excitation source is used and a variable delay between the excitation pulse and the opening of the electronic shutter of the ICCD is programmed. In this way, the emission spectrum is sampled with an increasing duration after the excitation pulse, from which the decay profile can be reconstructed (figure 4.5). The decay time is determined from the measurements by fitting it to one or two exponential functions. A typical R^2 of 0.99 was accepted as a good fit.

Several excitation sources are available for time-resolved photoluminescence measurements. A pulsed nitrogen laser (337 nm) can be used, together with a photodiode to synchronize the laser pulse and the ICCD. A blue 445 nm 600 mW laser diode or a 5 mm LED can be used together with a wavegenerator to pulse the excitation and to synchronize the excitation

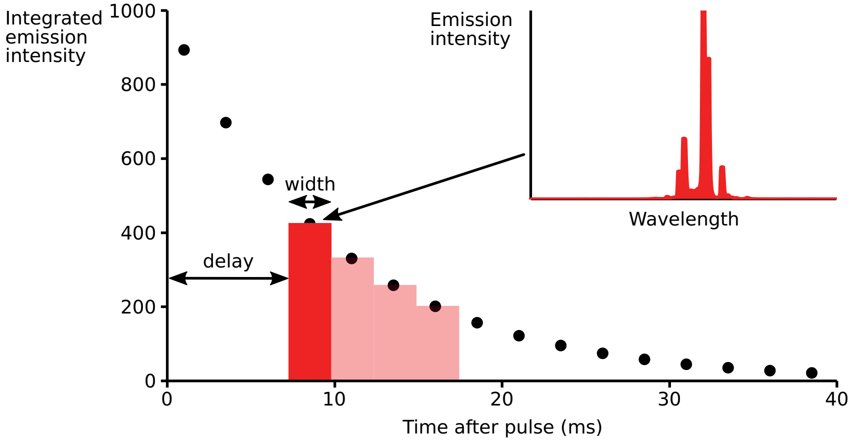

Figure 4.5: Principle of decay measurements, where sampling the emission spectrum on different times results in a profile of the luminescence lifetime.

pulse with the ICCD. Temperature-dependent decay times can be measured using an Oxford Instruments OptistatCF cryostat with transparant windows. Liquid nitrogen is used as a cooling liquid, enabling measurements in the 75–475 K temperature range.

4.2.2 Quantum efficiency

The quantum efficiency (QE) is an important measure to asses the quality of a phosphor and its application potential. In this work, the QE is often used as a quality measure to asses the different synthesis methods and to find the optimal synthesis conditions. A lab-built QE setup with a Spectralon-coated integrating sphere (figure 4.6) was validated using standard samples measured in different labs [57].

The powder phosphor sample is mounted in the sphere from the bottom, while excitation light is focused on the sample from the top of the sphere. Either a 5 mm LED (395 nm or 450 nm) or a xenon arc lamp with a monochromator (selected wavelength 450 nm) is used as excitation light and coupled to the sphere using an optical fiber. The emission light from the sample and the reflected excitation light are scattered from the powder sample in all directions. In the integrating sphere, the light scatters multiple times on the coating until light is collected on the right side of the sphere. An optical fiber couples the sphere to the spectrophotometer equipped with a monochromator (Princeton Instruments Acton SP2300)

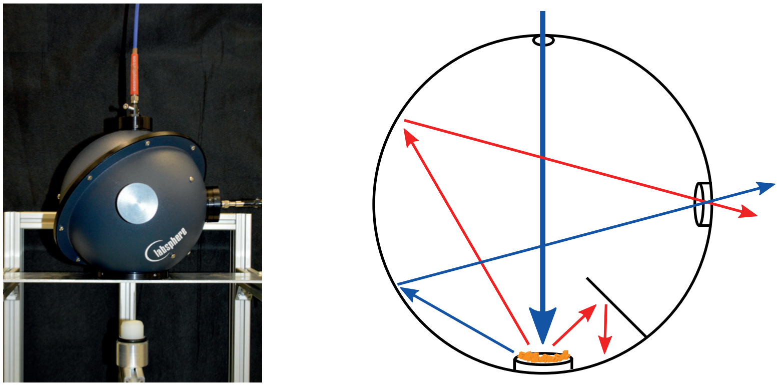

Figure 4.6: Integrating sphere used for quantum efficiency measurements.

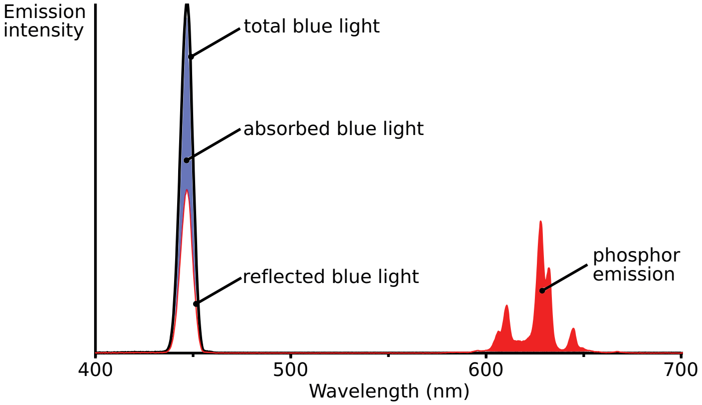

Figure 4.7: Calculation of quantum efficiencies from two spectra. One spectrum (red) is measured on the phosphor ($K_2SiF_6:Mn^{4+}$ in this case), resulting in reflected blue and emitted phosphor light. The second spectrum (black) is measured on Al_2O_3 as a reference for the reflected blue light.

and a camera (Princeton Instruments ProEM 1600). A baffle in between the powder sample and the detector fiber prevents the direct detection of reflected or emitted light (figure 4.6).

Two measurements are needed to calculate quantum efficiencies, one on the phosphor sample and another on a white reference sample (Al_2O_3) that reflects all excitation light. From this, both the internal and external quantum efficiency can be calculated by integrating the suitable ranges in the measured spectra. In the reference spectrum, $N_{ex,w}$ is the integral of the blue light reflected on the reference sample. In the phosphor spectrum, the same range is used to calculate the amount of blue light reflected by the phosphor N_{ex}. The emission spectrum of the phosphor is integrated to obtain the number of emitted photons N_{em} as is illustrated in figure 4.7. The external QE (EQE) is defined as the ratio of the number of emitted photons to the number of incident photons, while the internal QE (IQE) considers only absorbed photons. The absorption considers the amount of absorbed photons and is the ratio between the EQE and the IQE.

$$\mathrm{EQE} = \frac{N_{em}}{N_{ex,w}} \quad \mathrm{IQE} = \frac{N_{em}}{N_{ex,w} - N_{ex}} \quad A = \frac{N_{ex,w} - N_{ex}}{N_{ex,w}} = \frac{\mathrm{EQE}}{\mathrm{IQE}} \tag{4.2}$$

The QE is wavelength dependent, since absorption and the excitation probability can differ for different wavelengths. As a measure for phosphor performance in pc-wLEDs, the main focus lies on quantum efficiencies at excitation wavelengths in either the UV region (395 nm) or in the blue region (450 nm and 455 nm). Although the QE can be higher at other wavelengths, the application potential is evaluated at the relevant wavelengths for pc-wLEDs. The emission spectra are corrected for the variation in detector sensitivity at different wavelengths using a calibration file. This calibration file has been calculated using broad band benchmark phosphors. Therefore, an absolute error of at least 5% should still be taken into account for quantum efficiency measurements. Nevertheless, when materials with a similar emission spectrum are measured, the obtained values can be compared relatively independent of the calibration.

Not only powder samples can be evaluated in the QE setup, phosphor layers can also be measured in a remote phosphor setup. For this, the powder sample holder is replaced by a blue high-power LED in a white light-mixing cup. The flux density of the blue high-power LED used for the measurements of quantum efficiencies of phosphor layers is around $14\,\mathrm{W\,cm^{-1}}$ at the chip level. When a phosphor plate is put on top of the mixing cup, a remote phosphor LED is formed. In this way, the performance of the phosphor layer, including absorption and quantum efficiencies and the spectrum of the pc-wLED can be evaluated.

The absorption of a phosphor layer depends on several properties, both related to the phosphor itself and to the incorporation in a binder. On the one hand, absorption is an intrinsic property related to the transition that is involved. In $\mathrm{Eu^{2+}}$, a high absorption strength is found for the parity-allowed 4f–5d transition. In $\mathrm{Mn^{4+}}$, the absorption strength is rather low, since the involved 3d–3d transitions are parity-forbidden. To increase the absorption of the phosphor, more dopant ions can be added, provided that concentration quenching at high dopant concentrations can be limited. This optimization of the dopant concentration can positively influence both IQE and the absorption. On the other hand, in an LED application, the absorption of blue light in the phosphor layer can be increased by increasing the amount of phosphor powder, although this is limited by an increase in scattering losses. These scattering losses can be reduced by using an appropriate binder with a refractive index similar to the phosphor material. In this way, the absorption can be improved compared to the properties of the phosphor powder, which also improves the EQE.

4.2.3 SEM-CL

In addition to photoluminescence, luminescence measurements can also be performed using the SEM. The electron beam can excite valence electrons, create electron-hole pairs and produce secondary electrons, which results in cathodoluminescence (CL). For photoluminescent samples, the CL light is often very similar to the PL light, although other emission bands can be found since the excitation energy is not limited to a fixed wavelength. The CL light is collected using an optical fiber and detected using a spectrophotometer equipped with a monochromator (Princeton Instruments Acton SP2300) and a camera (Princeton Instruments ProEM 1600). Mapping the CL output yields the local emission spectrum and emission intensity, which can be linked to the chemical composition with a simultaneous EDX map.

4.2.4 Diffuse transmission spectroscopy

The transmission of (semi)transparent phosphor layers is measured using diffuse transmission in an integrating sphere in a Varian Cary 500 spectrophotometer. A polymer layer without phosphor is used as a reference. From these transmission measurements, the absorption of the phosphor layer is determined in the 200–800 nm wavelength range. Diffuse reflectance spectroscopy (DRS) on phosphor powders can similarly be measured in the same setup, using white $BaSO_4$ as a reference.

4.3 Chemical properties

Besides the luminescent properties, some other chemical properties of the phosphor are measured to evaluate its application potential or to determine the valence state of the dopant.

4.3.1 Chemical stability

A long lifetime of 50 000 h is required for pc-wLEDs, which implies the need for a stable emission during this lifetime. Since waiting for 50 000 h to evaluate a material will take too long, more extreme conditions are needed to speed up the degradation process. Phosphors can degrade chemically under influence of heat, water or air or they can degrade physically under influence of radiation of the UV or blue pumping LED.

Accelerated aging tests are performed in a climate chamber (Memmert HCP 108), where a constant atmosphere at high temperature and high humidity (HTHH) is created at typically 80 °C and 80 % relative humidity (RH). The degradation of the phosphor as a function of time at HTHH can be followed using XRD and QE measurements.

Photodegradation can be induced by LED illumination inside the climate chamber or by illumination with a blue 445 nm 600 mW laser diode. With the laser, both stability and saturation measurements can be performed by increasing the excitation power and measuring the emission intensity in situ. Using a FLIR A35sc thermal infrared (IR) camera, the sample temperatures can be measured as a function of excitation power.

4.3.2 XAS

With X-ray absorption spectroscopy (XAS) the local environment of a selected chemical element can be studied. XAS yields information on the first coordination shells and on the valence state of dopant ions. XAS measurements are performed with highly energetic synchrotron radiation, in our case in the European Synchotron Radiation Facility (ESRF) in Grenoble, France. The data analysis of XAS measurements was performed by Katleen Korthout.

A deeply bound electron is excited by selecting the characteristic X-ray energy for the chosen element and a core-hole is formed. In X-ray absorption near edge structure (XANES) spectroscopy, the excitation occurs near the absorption edge and the excited electron occupies the lowest unoccupied orbitals of the atom. The energy of these orbitals yields information of the valence state of the ion.

When higher X-ray energies are used, in extended X-ray absorption fine structure (EXAFS), the excited electron gets ionized and behaves as a photo-electron. The fine structure due to the scattering of the photo-electron yields information on the coordination of the excited atom.

Part II

Phosphors: synthesis and characterization

5

Solid state synthesis of Mn^{4+}-doped aluminates

Phosphors are typically produced using solid-state synthesis methods, in which starting materials such as metal oxides, nitrides or fluorides are mixed together in powder form and are subjected to a heat treatment at high temperature for several hours. Solid state synthesis, sometimes nicknamed 'shake and bake', is a rather straightforward synthesis method, which is worth exploring for every phosphor material, given suitable solid precursor materials and a safe reactive atmosphere can be used. Wet-chemical synthesis methods including sol-gel synthesis, hydrothermal synthesis and precipitation synthesis, can be advantageous due to better precursor mixing, but they are more labor-intensive and typically require a final heating step. In the case of Mn^{4+}-doped phosphors, the solid-state synthesis method has only been applied to oxide hosts. Solid-state synthesis methods for fluorides have been applied to lanthanide-containing fluorides such as $NaYF_4$ [58], but have not yet been successful for Mn^{4+}-doped fluorides.

Red-emitting Mn^{4+}-doped oxides can be found in a wide variety of host materials, including simple oxide lattices like Al_2O_3 and MgO [36]. Alkaline-earth magnesium hexaaluminates are a more complex host class than the simple oxides, but $BaMgAl_{10}O_{17}:Eu^{2+}$ (BAM:Eu) is a well-known example, as it is used as a blue-emitting phosphor in fluorescent lighting [2]. BAM:Eu has been codoped with Mn^{2+} to cover both the blue and the green emission region [59], but BAM can also be doped with Mn^{4+}. Similar lattices can be formed when other alkaline-earth ions are used, where Ba is replaced by Ca or Sr, leading to the so-called CAM and SAM hosts. In this chapter, the properties of Mn doping in these aluminate hosts and their possible application in pc-wLEDs are discussed. The materials were selected based on their accessible synthesis method and promising red emission.

5.1 $(Ca,Sr,Ba)MgAl_{10}O_{17}:Mn^{4+}$

$CaMgAl_{10}O_{17}:Mn^{4+}$, $SrMgAl_{10}O_{17}:Mn^{4+}$ and $BaMgAl_{10}O_{17}:Mn^{4+}$ phosphor samples were prepared with a Mn concentration of 0.12%. Dopant concentrations in phosphors are given as atomic percentages of the atom it replaces, which is Al in this case. A dopant concentration of 0.12% thus results in the chemical composition $(Ca,Sr,Ba)MgAl_{9.988}Mn_{0.012}O_{17}$. The doping of Mn^{4+} is expected at the octahedral Al^{3+} site in the $[AlO_6]$ chains (figure 5.1) [60] because of the similar ionic radius of Mn^{4+} (53 pm) and Al^{3+} (53.5 pm). Meanwhile, the larger Mn^{2+} (66 pm) can also be stabilized in this lattice at the Mg^{2+} site (57 pm), which is substituting a tetrahedrally coordinated Al^{3+} in $[AlO_4]$ chains [61] (figure 5.1). The crystal structure of the hexaaluminates belongs to the hexagonal $P6_3/mmc$ space group and it consists of spinel-type $MgAl_{10}O_{16}$ blocks stacked in the c direction with intermediate metal oxide conduction layers.

Two types of structures can be distinguished, the magnetoplumbite structure and the β-alumina structure. The difference between those structures is the ordering within the conduction plane, as can be seen in figure 5.2. The magnetoplumbite conduction plane consists of face-sharing AlO_6 octahedra, 12-fold coordinated alkaline-earth ions and 5-fold coordinated Al ions. The β-alumina conduction plane consists of corner-sharing AlO_4 tetrahedra and a 9-fold coordinated alkaline-earth ion. Both SAM and BAM form β-alumina hexaaluminates, while CAM forms the more compact magnetoplumbite structure, because of the smaller Ca cations [62]. The β-alumina hexaaluminate structure facilitates the incorporation of Mg in the lattice, because the positively charged conduction layer compensates for the valence deficiency created by the replacement of Al by Mg in the spinel block [63].

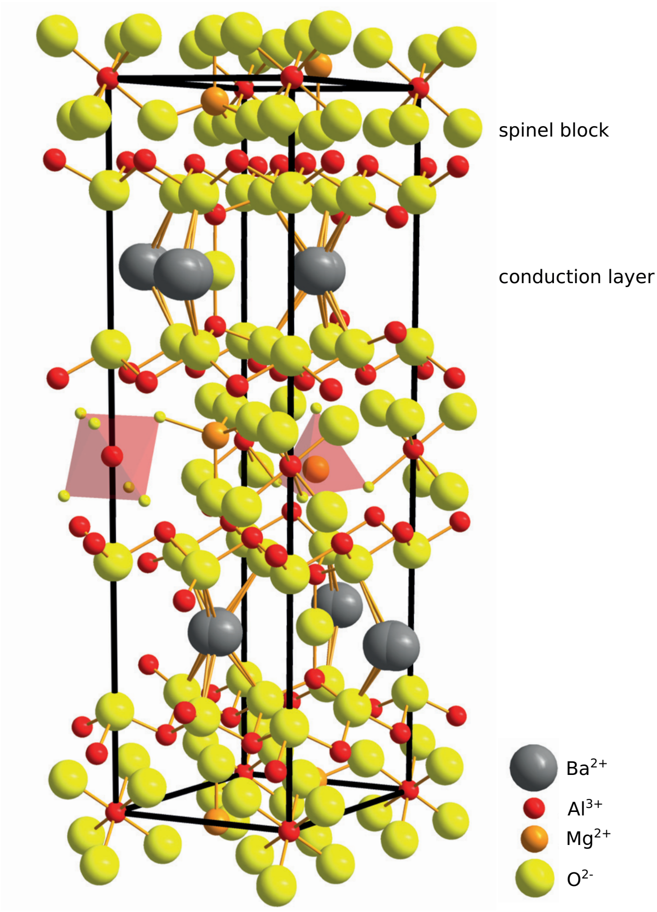

Figure 5.1: Crystal structure of $BaMgAl_{10}O_{17}$, with a magnetoplumbite type conduction layer of BaO. Al atoms are present in AlO_6 octahedra and AlO_4 tetrahedra.

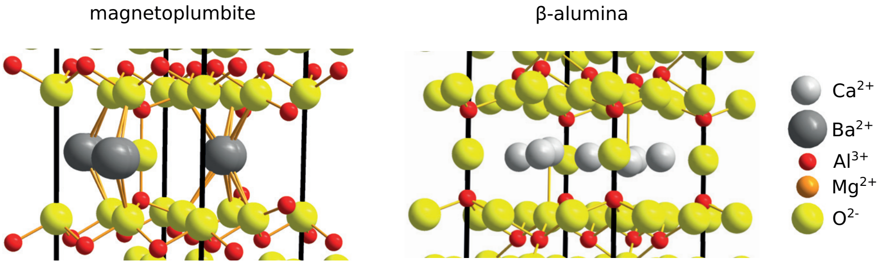

Figure 5.2: Schematic representation of the conduction planes of the magnetoplumbite-type ($BaMgAl_{10}O_{17}$) and of the β-alumina-type ($CaMgAl_{10}O_{17}$).

5.1.1 Synthesis

$CaMgAl_{10}O_{17}$:Mn^{4+} (CAM:Mn), $SrMgAl_{10}O_{17}$:Mn^{4+} (SAM:Mn) and $BaMgAl_{10}O_{17}$:Mn^{4+} (BAM:Mn) powders were prepared using a solid state synthesis method. Stoichiometric amounts of Al_2O_3 (Alfa Aesar, 99.99%), MgO (Alfa Aesar, 99.95%) and $MnCO_3$ (Alfa Aesar, 99.9%) were weighed and mixed in a mortar with the corresponding alkaline-earth precursors, either $CaCO_3$ (Alfa Aesar, 99.95%), $SrCO_3$ (Alfa Aesar, 99.99%) or $BaCO_3$ (Alfa Aesar, 99.95%), and put into an alumina crucible. The powders were heated in a tube furnace in air. This heat treatment occurred in two steps, during 3 h at 800 °C and 6 h at 1400 °C with intermediate grinding [64]. The powders were allowed to cool naturally, both in between and after the heating stages.

The X-ray diffraction patterns of SAM:Mn and BAM:Mn in figure 5.3 show that $MgAl_2O_4$, some Al_2O_3 and other unidentified crystalline impurities were present besides the SAM or BAM phase that was aimed for. The XRD pattern of CAM:Mn show a high fraction of $MgAl_2O_4$, typical for the limited incorporation of Mg in the magnetoplumbite hexaaluminates. Some smaller diffraction lines in the pattern of CAM:Mn can ei-

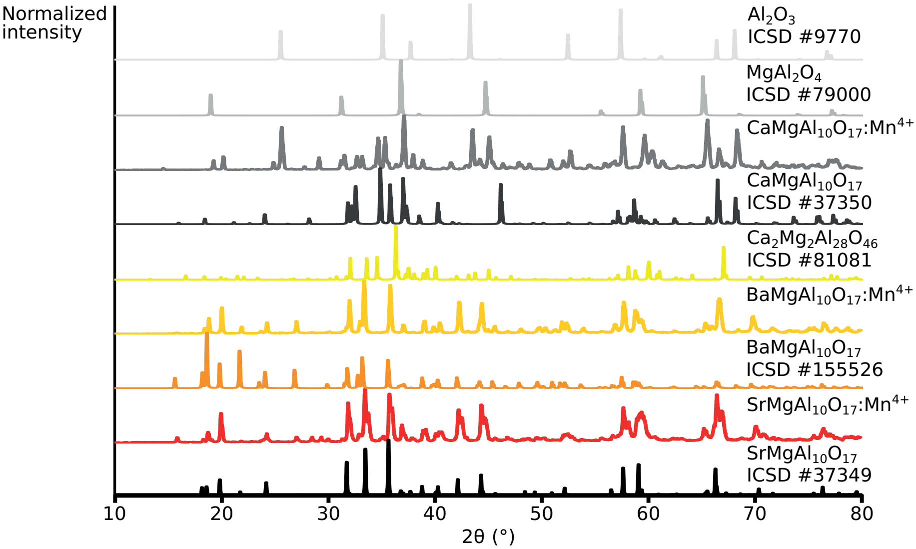

Figure 5.3: XRD patterns for SAM:Mn, BAM:Mn and CAM:Mn compared with reference patterns from the Inorganic Crystal Structure Database of the corresponding hexaaluminate, Al_2O_3 and $MgAl_2O_4$.

ther be $CaMgAl_{10}O_{17}$ or $Ca_2Mg_2Al_{28}O_{46}$. Although from the XRD measurements no pure $CaMgAl_{10}O_{17}$ phase can be identified, the sample will be referenced to as CAM:Mn. A low fraction of $MgAl_2O_4$ was found in the β-alumina hexaaluminates SAM:Mn and BAM:Mn. The incorporated Mn dopant caused no significant shift in the diffraction peaks.

5.1.2 Results

Upon excitation at 395 nm, all three powders show a broad red emission band (left part of figure 5.4). The most intense peak is found around 655–660 nm in SAM:Mn and CAM:Mn. This coincides with the Mn^{4+} emission in SAM around 660 nm reported in literature [60, 65]. The most intense peak of BAM:Mn is found at 678 nm, where an emission band is also found for SAM:Mn and CAM:Mn. For BAM:Mn^{4+}, the main emission band is also expected at 660 nm, and the lower intense broad emission band around 660 nm looks similar to the Mn^{4+} emission reported in literature [66]. A third intense emission peak is found at 693 nm in both BAM:Mn and CAM:Mn. The same emission bands are found upon excitation at 455 nm, together with an emission band around 515 nm which is caused by Mn^{2+} incorporation, as can be seen in the right part of figure 5.4.

From the decay measurements, a bi-exponential fit is found, with a decay time of the red emission in SAM:Mn of 0.67 ms and 0.24 ms (figure 5.5). This is in the same range as literature values for Mn^{4+} emission in SAM [65] although only mono-exponential decay profiles are reported

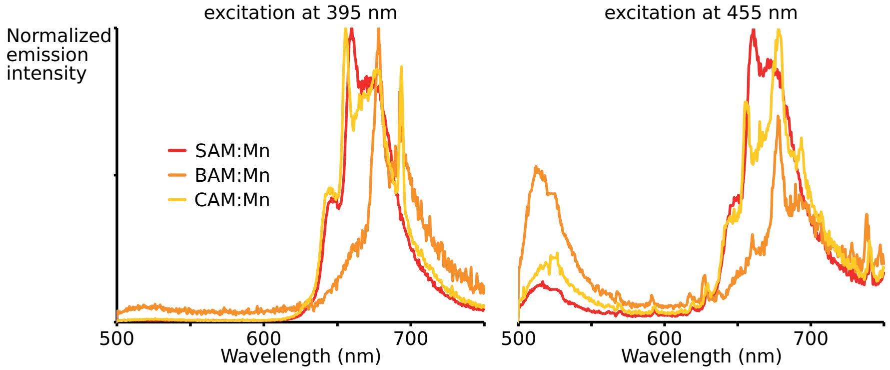

Figure 5.4: Normalized photoluminescence spectra of SAM:Mn (red), BAM:Mn (orange) and CAM:Mn (yellow) with a doping concentration of 0.12%. The excitation wavelength is 395 nm (left) or 455 nm (right).

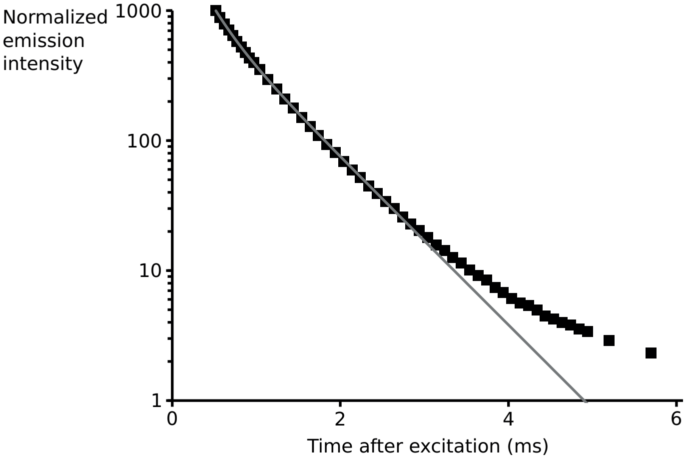

Figure 5.5: Luminescence decay profile of the red emission in SAM:Mn (black squares) and an bi-exponential fit (gray line) with decay times of 0.67 ms and 0.24 ms. A delay of 0.5 ms is set at the start of the measurement to remove the emission tail of the excitation LED.

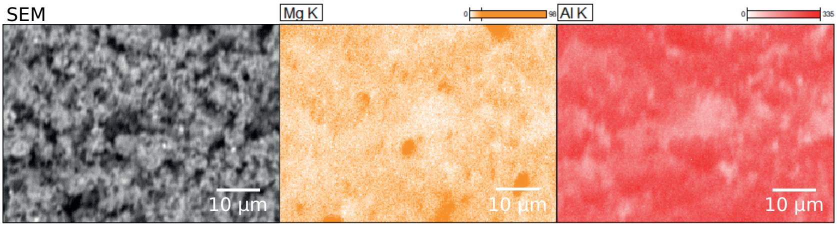

Figure 5.6: SEM-EDX maps of SAM:Mn, with a BSE SEM image and elemental distributions of Al and Mg. Other elements were distributed homogeneously.

in literature. The IQE at 395 nm excitation is 21% for SAM:Mn, 13% for BAM:Mn and only 10% for CAM:Mn. Since the absorption of the powders is low (10–15%), the EQE ends up at only 1–3%. The broad green emission band present upon excitation at 455 nm has a decay time of 5.2 ms in SAM:Mn. In BAM:Mn, the emission intensity of the green emission band is even of the same order as that of the red emission band.

In SEM-EDX, no Al rich phases could be localized, but the distribution of Mg over the sample was not fully homogeneous in SAM:Mn and CAM:Mn (figure 5.6), which is consistent with the presence of $MgAl_2O_4$ in these samples. From EDX measurements, the Mn concentration relative to the Al concentration was 0.20%, 0.79% and 0.29% for CAM:Mn, SAM:Mn and BAM:Mn respectively, while the dopant concentration in the synthesis was only 0.12%. The higher detected dopant concentration can be caused by a reduced incorporation of Al in the crystal structure but it can also be influenced by the somewhat limited detection at low element concentrations.

5.1.3 Discussion

The broad emission spectrum obtained from the Mn-doped aluminates (figure 5.4) has several contributions. In the short wavelength range, up to 560 nm, there is a green emission band with a maximum at 514 nm, 516 nm and 519 nm for BAM:Mn, SAM:Mn and CAM:Mn respectively. The broad emission is caused by the $^4T_1 \longrightarrow {}^6A_1$ transition in Mn^{2+} ions. In SAM and BAM, Mn^{2+} is known to substitute Mg^{2+} ions, resulting in an emission band around 515 nm [61, 59]. Mn^{2+} can also be incorporated in $MgAl_2O_4$, resulting in an emission band around 520 nm [67]. The incorporation of Mn^{2+}, besides the Mn^{4+} which was aimed for, is possible since the Mn in the precursor is divalent and can be incorporated as such before it is oxidized to Mn^{4+}.

The red emission band at 620–750 nm is more intense than the green emission band in SAM:Mn and CAM:Mn. Several peaks can be identified, with the most intense one at 660 nm in SAM:Mn and at 655.5 nm in CAM:Mn due to the ZPL of the $^2E_g \longrightarrow {}^4A_{2g}$ transition of Mn^{4+} in the aluminate host [60]. As discussed in chapter 1, this transition is parity- and spin-forbidden but the parity selection rule can be relaxed by a distortion of the local symmetry. In the hexaaluminates, Mn^{4+} can be stabilized in an Al^{3+} site in an $[AlO_6]$ octahedral chain, destroying the local lattice symmetry. Therefore, the ZPL emission is stronger than the phonon sideband. The sideband is an electric dipole transition induced by the ν_3 (stretching) and ν_4 (bending) vibrational modes, which relaxes the parity selection rule [64, 68]. The broad vibrational sideband at longer wavelengths, above 670 nm, is most clearly present in SAM:Mn [65].

A second strong emission peak emerges at 678 nm, which is the most intense emission band of BAM:Mn upon excitation at 395 nm and the most intense emission band of CAM:Mn upon excitation at 455 nm. This peak is another ZPL of the $^2E_g \longrightarrow {}^4A_{2g}$ transition, but of Mn^{4+} in an Al_2O_3 host [69]. The two emission bands overlap, which makes it difficult to quantify the purity of the hexaaluminate. When the ZPL of the hexaaluminate emission is compared to the ZPL of Al_2O_3:Mn, the contribution of

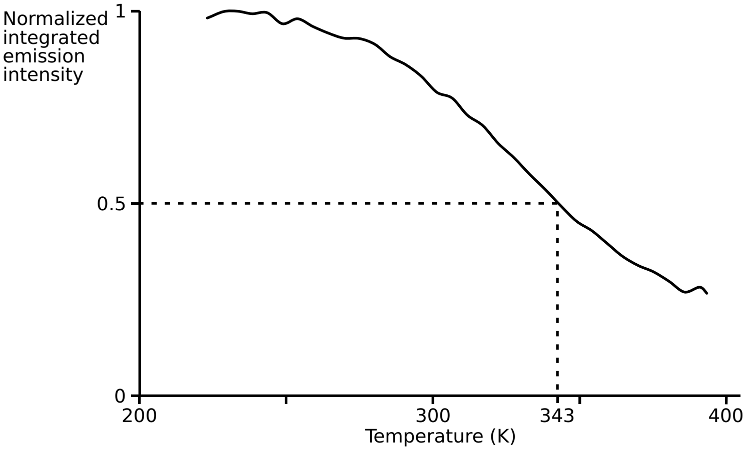

Figure 5.7: Thermal quenching profile of $SrMgAl_{10}O_{17}$:Mn^{4+}, integrated emission intensity at 625–725 nm upon LED excitation at 450 nm.

the Al_2O_3:Mn emission can be estimated as 68% for BAM:Mn and 58% for CAM:Mn. Since the intensity of the ZPL can be influenced by crystal symmetry, the crystallinity of the hexaaluminate could also influence the ZPL emission intensity, but at least an estimate can be calculated from this comparison. In SAM:Mn, the ZPL of Al_2O_3:Mn is not exceeding the vibronic sideband of SAM:Mn. Al_2O_3:Mn^{4+} can be regarded as a red phosphor in itself with its emission band around 678 nm. The emission intensity at 678 nm, where the ZPL of Al_2O_3:Mn is expected, contributes to 46% of the total emission intensity of the ZPLs. These contributions can be somewhat overestimated, since both vibronic sidebands of hexaaluminate Mn^{4+} emission and Al_2O_3:Mn^{4+} can contribute to the total emission at 678 nm. The XRD results already showed that Al_2O_3 is still present in the magnesium aluminates and Mn^{4+} can also be stabilized in Al_2O_3. Again, besides the ZPL emission, a vibronic sideband is present at a 600 cm^{-1} distance of the ZPL, peaking at 695 nm. The last part of the broad red emission band, in the 620–650 nm range is due to the anti-Stokes vibronic sidebands and is therefore less intense than the ZPL emission. As a function of temperature, the luminescent performance of the red emission band is not optimal. Thermal quenching sets in from 260 K with a quenching temperature $T_{1/2}$ of 343 K in the 0.12%-doped SAM:Mn (figure 5.7).

An excitation spectrum with an intense peak around 450 nm is found for the green Mn^{2+} emission around 515 nm (left part of figure 5.8), but our focus lies on the broad Mn^{4+} emission band. In the excitation spec-

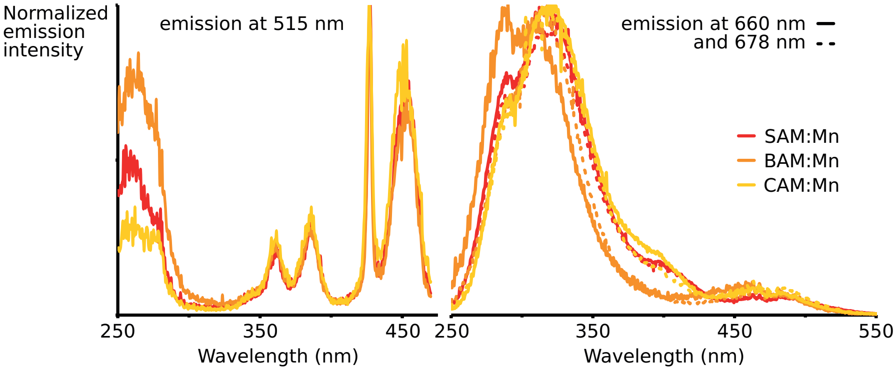

Figure 5.8: Normalized photoluminescence excitation spectrum of SAM:Mn (red), BAM:Mn (orange) and CAM:Mn (yellow) for the green Mn^{2+} emission around 515 nm (left) and the red Mn^{4+} emission at 660 nm (full line) and 678 nm (dotted line) (right).

trum in the right part of figure 5.8, several broad bands overlap in the 260–450 nm range, due to the presence of two emitting host lattices in each of the hexaaluminates. In BAM:Mn (full orange line in the right part of figure 5.8), two overlapping bands are seen peaking at 290 nm and 310 nm. In SAM:Mn and CAM:Mn, the main excitation band is found around 320 nm while the main excitation band for the 660 nm emission in BAM:Mn is found around 290 nm. An $O^{2-} \rightarrow Mn^{4+}$ charge transfer transition is present at 290 nm for Al_2O_3 and peaking at 320 nm for the hexaaluminates. The second excitation band is due to the spin-allowed $^4A_{2g} \longrightarrow {}^4T_{1g}$ transition at 397 nm with a sideband at 414 nm from the the $^4A_{2g} \longrightarrow {}^4T_{1g}$ transition in Al_2O_3. The third excitation band is due to the the spin-allowed $^4A_{2g} \longrightarrow {}^4T_{2g}$ transition at 470 nm without a clear Al_2O_3 sideband. Unfortunately, this last excitation band in the visible range is the least intense, which resulted in lower quantum efficiencies obtained at 455 nm excitation compared to 395 nm excitation. Although emission bands can be distinguished originating from either Al_2O_3:Mn (678 nm) or the Mn-doped hexaaluminates (660 nm), the excitation spectra of these peaks are quite similar, due to overlapping broad excitation bands.

Higher external quantum efficiencies can be expected at shorter excitation wavelengths, since the maximum of the excitation band is found around 330 nm. For LED applications however, shorter excitation wavelengths are not favorable because they induce a large Stokes shift and a high absorption is needed to remove the UV emission from the pc-wLED.

On the emission side, red emission within the eye sensitivity limit is needed and a stable emission is required within the operating range of the wLED. For this, the Mn-doped aluminates show some promising features, with strong ZPL emission and broad parity allowed sidebands. Nevertheless, the green Mn^{2+} emission and the Al_2O_3:Mn^{4+} emission at longer wavelengths should be avoided. SAM:Mn seems the most promising of the alkaline-earth aluminates, even though the LER is only 86 lm W^{-1}, with the highest obtained IQE and with a smaller contribution of the green Mn^{2+} emission when compared to BAM:Mn and CAM:Mn. The contribution of Al_2O_3 to the emission is lower compared to the other hexaaluminates, with a contribution to the IQE lower than 46%. Optimization of synthesis parameters could improve the purity of both the host lattice and the valence state of Mn. To optimize the emission spectrum of SAM:Mn, in a next step the synthesis was tuned using an excess Al_2O_3.

5.2 $SrMgAl_xO_{17\pm\delta}$:Mn^{4+}

Although the presence of Al_2O_3:Mn^{4+} emission in the alkaline-earth aluminates was not aimed for, introducing an excess of Al_2O_3 can improve the luminescent properties of these aluminate phosphors. In the so-called $SrMgAl_xO_{17\pm\delta}$:Mn^{4+}, for $x > 10$, two crystalline phases coexist as a mixture [64]. Both $SrMgAl_{10}O_{17}$ (SAM) and Al_2O_3 are present, with the amount of Al_2O_3 increasing with increasing x. For $x = 30$, in $SrMgAl_{30}O_{17\pm\delta}$ (SMA), the two crystalline phases occur in a 1:10 ratio, with a 10-fold excess of Al_2O_3. Although this phosphor is a mix of two phosphors, SAM:Mn and Al_2O_3:Mn, the mixed phosphor is noted as SMA:Mn. The dopant incorporation in this composite phosphor can be determined from the PL emission. Al_2O_3:Mn^{4+} shows two emission bands peaking at 678 nm and 695 nm at low intensities, while the emission peaks of $SrMgAl_{10}O_{17}$:Mn^{4+} (SAM:Mn) at 643 nm, 657 nm and 670 nm [64]. The influence of Bi and Ce as codopants is explored to improve the luminescent properties using energy transfer.

5.2.1 Synthesis

$SrMgAl_{30}O_{17\pm\delta}$:$Mn^{4+}$ powders were prepared using solid state synthesis with a variation of Mn concentration and with Bi or Ce as a codopant. A similar weight of $MnCO_3$ was added to the precursor mixture compared to the synthesis of SAM:Mn. Since Mn is replacing Al in the crystal structure, the dopant concentration is calculated relative to the amount of Al. In $SrMgAl_30O_{17\pm\delta}$:Mn^{4+}, the Al concentration is three times the amount of SAM:Mn, which results in a relatively low dopant concentration. Samples were made with a Mn concentration of 0.02 %, 0.04 % and 0.06 %, of which the 0.04%-doped sample contains the same amount of $MnCO_3$ as the 0.12%-doped sample of SAM:Mn, so the three Mn-doped samples correspond with the chemical compositions $SrMgAl_{29.994}Mn_{0.006}O_{17\pm\delta}$, $SrMgAl_{29.988}Mn_{0.012}O_{17\pm\delta}$ and $SrMgAl_{29.982}Mn_{0.018}O_{17\pm\delta}$ respectively.

These dopant concentrations are rather low, a dopant concentration of at least 1% is more often found in phosphor samples. Samples with a Mn concentration of 0.04% were codoped with either Bi or Ce. Although it is not clear where these ions will be incorporated in the host lattice, the dopant concentration is calculated relative to the amount of Al. Although this leads to low dopant concentrations, it is easier to compare with the Mn concentration. The codopant concentrations were 0.01 %, 0.02 %, 0.04 % and 0.08 % of Bi or 0.02 % and 0.04 % of Ce.

Stoichiometric amounts of $SrCO_3$ (Alfa Aesar, 99.99%), Al_2O_3 (Alfa Aesar, 99.99%), MgO (Alfa Aesar, 99.95%) and $MnCO_3$ (Alfa Aesar, 99.9%) were weighed and mixed in an mortar, possibly with Bi_2O_3 (Alfa Aesar, 99.975%) or CeO_2 (Aldrich, 99.9%) as a codopant, and put into an alumina crucible. The powders were heated in a tube furnace in air. This heat treatment occurred in two steps, during 3 h at 800 °C and 6 h at 1400 °C with intermediate grinding. The powders were allowed to cool naturally, both in between and after the heating stages. The X-ray diffraction patterns of the synthesized powders in figure 5.9 showed a mixed phase of $SrMgAl_{10}O_{17}$ and Al_2O_3. The $MgAl_2O_4$ phase, that was found in CAM:Mn (figure 5.3) was not found in the SMA:Mn powders. No influence from the (co)dopants is found in the XRD patterns.

5.2.2 Results

A broad, red emission band is found in all samples upon excitation at 395 nm and 455 nm (figure 5.10). The peak wavelength of the phosphor emission was 659 nm from the $SrMgAl_{10}O_{17}$:Mn^{4+} phase or 678 nm from the Al_2O_3:Mn^{4+} phase respectively. Similar to the decay profile of SAM:Mn, a bi-exponential decay is found for the red emission in SMA:Mn with a decay time of 0.77 ms and 0.28 ms (figure 5.12, black-gray), which is comparable to the decay time in SAM:Mn. No difference is found in

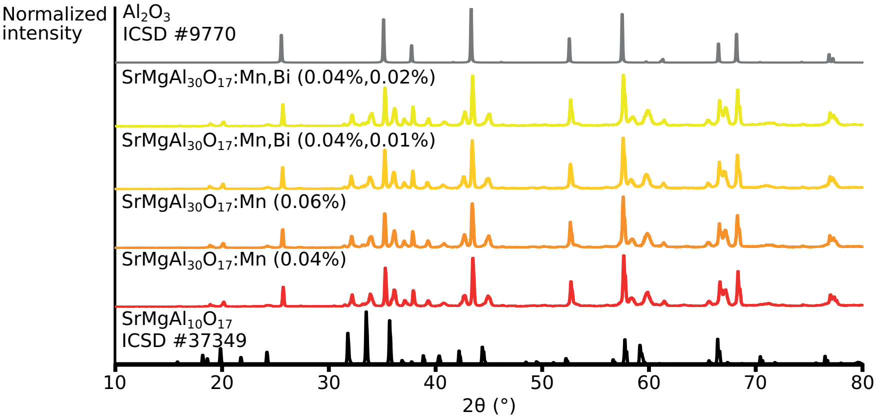

Figure 5.9: XRD patterns for SMA:Mn and SMA:Mn,Bi in several dopant concentrations, compared with the reference patterns of $SrMgAl_{10}O_{17}$ and Al_2O_3.

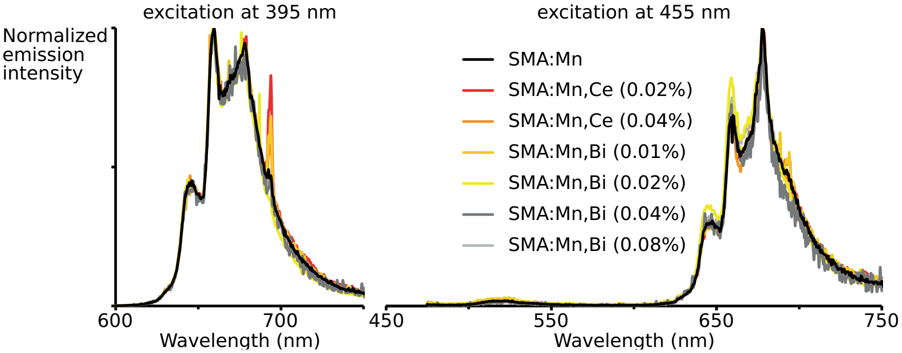

Figure 5.10: Normalized photoluminescence spectra of SMA:Mn (black), SMA:Mn,Ce (red-orange) and SMA:Mn,Bi (yellow-gray) in several codopant concentrations. The Mn concentration is 0.04 % for all samples. The excitation wavelength is 395 nm (left) or 455 nm (right).

decay time between the emission originating from SAM:Mn and the emission originating from Al_2O_3:Mn^{4+}. No explanation could be found for the bi-exponential decay, since it was found in both host materials.

A broad-band excitation spectrum (figure 5.11) is found around 335 nm for emission at both 659 nm and 678 nm. The main excitation band is slightly blueshifted to a maximum intensity at 320 nm for the sample codoped with 0.01% Bi and for the excitation spectrum following 678 nm emission of the sample codoped with 0.04% Bi. Since only the first, most intense band is shifted, it is caused by a change in the charge transfer

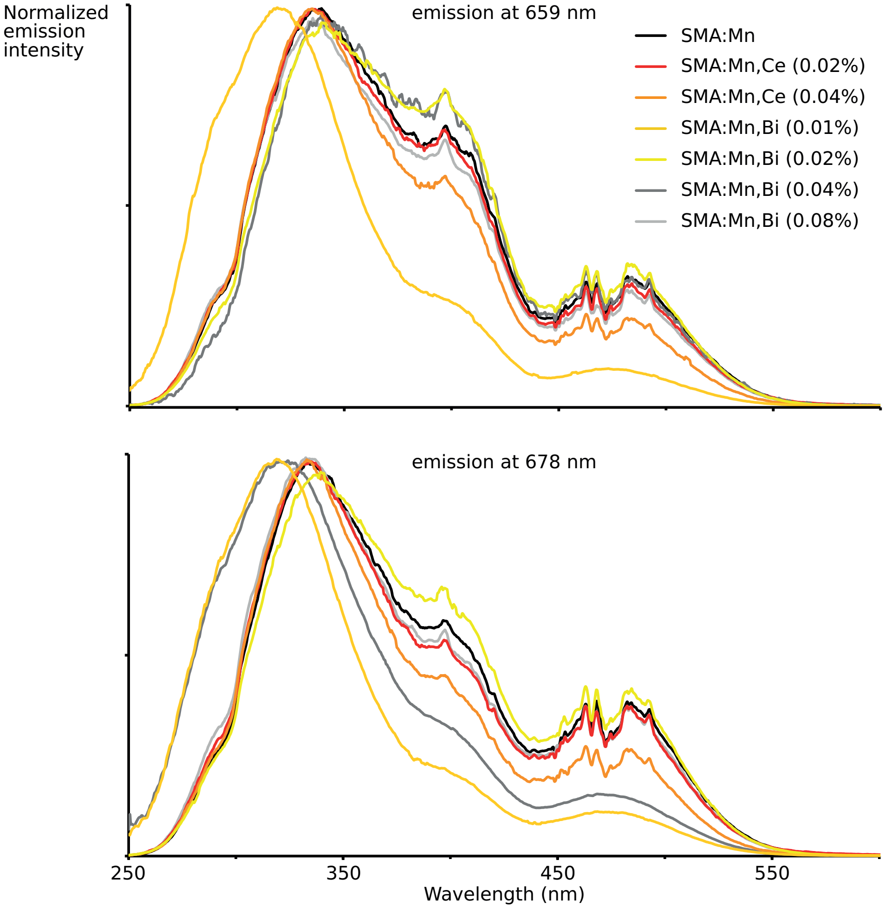

Figure 5.11: Normalized photoluminescence excitation spectra of SMA:Mn (black), SMA:Mn,Ce (red-orange) and SMA:Mn,Bi (yellow-gray) in several dopant concentrations for the red Mn^{4+} emission at 659 nm (top) and 678 nm (bottom). The small spectral features in the 450–500 nm wavelength range are caused by the detector.

band, which does not influence the emission upon excitation of the spin-allowed transitions. Upon excitation at 455 nm a minor emission band around 525 nm pops up. The higher red to green emission ratio in SMA:Mn compared to SAM:Mn shows a better control of the 4+ valence state of Mn. Compared to the powder synthesized as single phase SAM:Mn, the total emission intensity is higher in SMA:Mn due to the increased Al_2O_3:Mn^{4+} emission band at 678 nm. The highest IQE value (table 5.1) was found

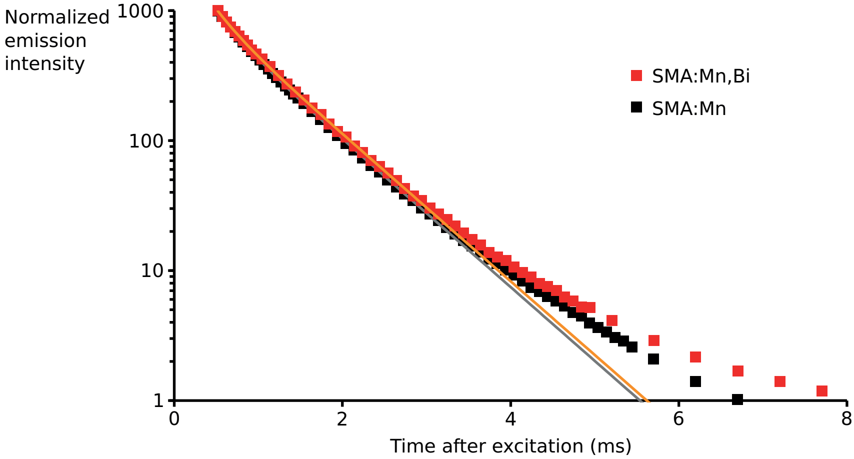

Figure 5.12: Decay profiles of the red emission (610–766 nm) of SMA:Mn (black-gray) and SMA:Mn,Bi (red-orange). A bi-exponential function is fitted to the data points, resulting in decay times of 0.77 ms and 0.28 ms for SMA:Mn and 0.76 ms and 0.25 ms for SMA:Mn,Bi.

Table 5.1: Influence of dopant concentration on the quantum efficiency of $SrMgAl_{30}O_{17\pm\delta}:Mn^{4+}$

Dopant concentration	EQE	IQE	Absorption
0.02%	4.4%	22%	0.20
0.04%	3.8%	26%	0.15
0.06%	5.0%	25%	0.20

for a Mn concentration of 0.04 %. Although the QE values of the other Mn concentrations are within the typical error of QE measurements, the 0.04% dopant concentration was selected for further codoping.

Codoping with Bi or Ce did not influence the location of the excitation and emission bands. SAM:Ce^{3+} shows a narrow emission band at 390 nm from host–exciton recombination at Sr–O groups and a broad emission band at 450 nm from 4f–5d transition in Ce^{3+} [70]. Luminescence from $Al_2O_3:Ce^{3+}$ has only been found originating from cathodoluminescence or radioluminescence using synchrotron radiation with an emission band around 450 nm [71]. Some benefits of Ce^{3+} codoping on Mn^{4+} emission have been shown in literature in BaO-Al_2O_3 and CaO-Al_2O_3 hosts [72]. Bi^{3+} has been used as a codopant in similar hosts such as $CaAl_{12}O_{19}:Mn^{4+}$ [73]. Although codoping can reduce Mn^{4+} to Mn^{2+} which is not preferred,

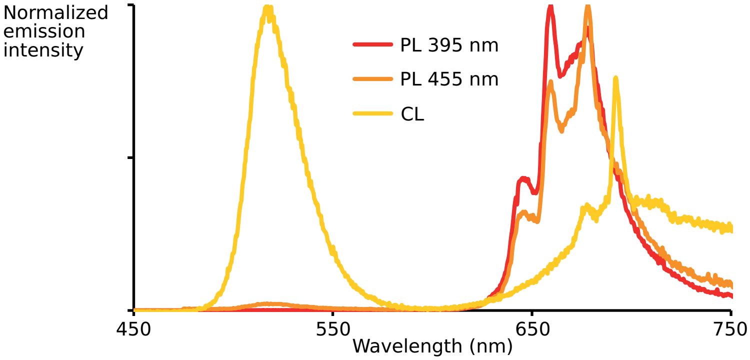

Figure 5.13: Normalized photoluminescence spectra (excitation at 395 nm (red) or 455 nm (orange)) and cathodoluminescence spectrum (yellow) of a 0.04%-doped SMA:Mn phosphor.

this effect is limited at low Bi^{3+} concentrations. Bi^{3+} luminescence in SAM or Al_2O_3 hosts has not yet been reported. A more intense peak at 694 nm emerges in the samples codoped with 0.3% Bi or 0.6% Ce, together with a more intense Mn^{2+} emission band (figure 5.10).

The composite phosphor with different hosts and dopants can be an interesting subject for combined SEM-EDX-CL measurement, either by measuring the CL while the scanning the sample during the measurement of an EDX map or by measuring the CL emission at a certain point. A homogeneous CL emission was found for the different codoped SMA:Mn,(Bi,Ce) samples, with an emission spectrum similar to that found in PL, where the green Mn^{2+} band is the most intense emission band (figure 5.13). The broad red emission band found in PL emission has a lower intensity in CL compared to the green emission band and the sharp peak at 692 nm is also present in CL. As a function of temperature, the luminescent performance is suboptimal. The integrated emission intensity increases from 244 K to 263 K and the initial integrated emission intensity was reached again at 281 K, where thermal quenching sets in. The quenching temperature $T_{1/2}$ is 319 K for the 0.12%-doped SMA:Mn (red line in figure 5.14). When the two different phases present in SMA:Mn are compared, lower quenching temperatures are found. The emission intensity of the SAM:Mn phase (orange line in figure 5.14), integrated over the 655–665 nm wavelength region, starts decreasing from 200 K with only a slight increase up to 258 K and a quenching temperature $T_{1/2}$ of 305 K. The increase in emission intensity is more clearly found in the Al_2O_3:Mn phase (yellow line in

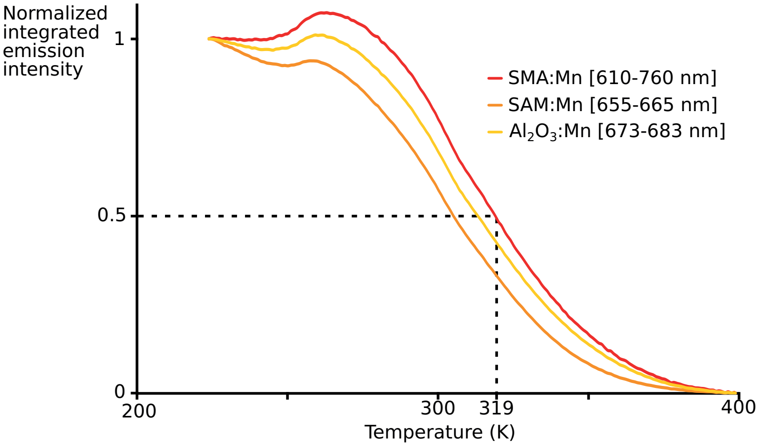

Figure 5.14: Thermal quenching profile of $SrMgAl_{30}O_{17\pm\delta}$:$Mn^{4+}$, integrated emission intensity at 610–760 nm upon LED excitation at 450 nm.

figure 5.14), integrated over the 673–683 nm wavelength region, with an increase from 250 nm up to 262 nm and a thermal quenching temperature $T_{1/2}$ of 313 K.

Decay times can also be used to distinguish different phases and energy transfer between different dopants. The decay times of the red emission (0.77 ms and 0.28 ms) of SMA:Mn is similar to the decay times of 0.67 ms and 0.24 ms found for the red emission of SAM:Mn. Codoping SMA with Bi has no significant influence on the decay time, since decay times of 0.76 ms and 0.25 ms were found for SMA:Mn,Bi (figure 5.12, red-orange). Therefore, no energy transfer model can be deduced from the decay measurements.

A higher IQE (21–64%) was found with Bi or Ce codopants, compared to 22–26% for a single Mn dopant (table 5.2). With an absorption of only 6–23%, even though the IQE can be reasonably high, the EQE in SMA:Mn,Bi and SMA:Mn,Ce samples does not exceed 12%. The EQE of the single doped SMA:Mn is 4–5%, depending on the dopant concentration (table 5.1). The quantum efficiency values do not follow any trend as a function of codopant concentration. Improved quantum efficiencies are only found for a Ce concentration of 0.02% and for a Bi concentration of 0.04%. The relative error on quantum efficiency measurements can be up to 5%, which is of the same order of magnitude as the possible influence of the codopants in most samples. Variations in quantum efficiency can therefore also be caused by improved crystallinity or by improved Mn

Table 5.2: Influence of codopant concentration on the quantum efficiency of $SrMgAl_{30}O_{17\pm\delta}$:$Mn^{4+}$,($Bi^{3+}$,$Ce^{3+}$)

codopant	concentration	EQE	IQE	Absorption
		3.8%	26%	0.15
Ce	0.02%	10%	59%	0.17
Ce	0.04%	3.2%	21%	0.16
Bi	0.01%	5.5%	55%	0.10
Bi	0.02%	5.1%	23%	0.23
Bi	0.04%	12%	64%	0.19
Bi	0.08%	3.3%	55%	0.06

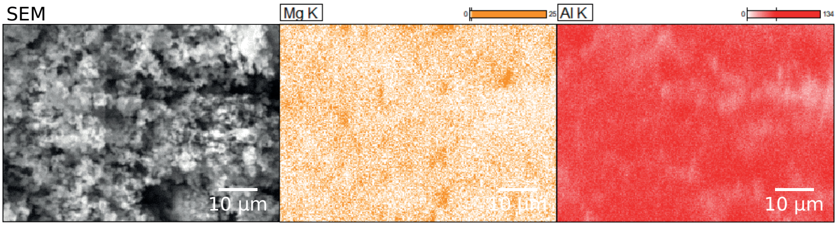

Figure 5.15: SEM-EDX maps of SMA:Mn, with a BSE SEM image and elemental distributions of Al and Mg. Other elements were distributed homogeneously.

incorporation during the synthesis rather than energy transfer from the codopants. The codopants can support the Mn incorporation by slightly changing the crystal lattice, possibly enlarging the lattice sites that can incorporate Mn.

In SEM-EDX (figure 5.15), the distribution of Mg was not fully homogeneous, although it was more homogeneous than the samples of SAM:Mn without an excess of Al_2O_3 (figure 5.6). Although a large Al_2O_3 excess is present in the phosphor, no concentrated Al was localized in the EDX map, so the Al_2O_3 phase and the SAM phase are mixed homogeneously on the submicron scale measured in the SEM. The detected Mn concentration was always higher than the concentration that was aimed for, from 0.06% to 0.15% while the inital Mn content was 0.02–0.06%. Although the concentration of the codopant was higher than the Mn concentration, up to 0.08%, it was still rather low so neither Bi nor Ce could be detected using EDX. If the codopant was incorporated in the host, detection could be expected for Ce that does not form volatile compounds during the synthesis.

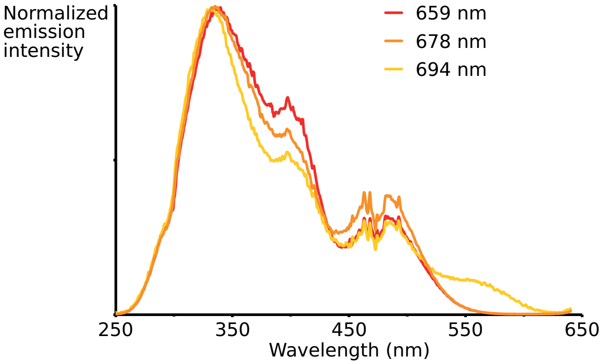

Figure 5.16: Normalized photoluminescence excitation spectrum of 0.04%-doped SMA:Mn, measured at the emission wavelengths 659 nm (red), 678 nm (orange) and 694 nm (yellow).

5.2.3 Discussion

The most intense Al_2O_3:Mn^{4+} emission (at 678 nm) is found upon 450 nm excitation. When the emission at 694 nm is probed (figure 5.16), the excitation spectrum of Al_2O_3:Mn^{4+} shows three bands. Two of them, the $O^{2-} \longrightarrow Mn^{4+}$ charge-transfer band at 300 nm and the spin-allowed $^4A_{2g} \longrightarrow {}^4T_{1g}$ transition at 414 nm, were already visible in the spectra of SAM:Mn that contained Al_2O_3:Mn^{4+}. The third band, due to the spin-allowed $^4A_{2g} \longrightarrow {}^4T_{2g}$ transition is present in some of the spectra with an excess Al_2O_3:Mn^{4+} at 565 nm. Although the Al_2O_3:Mn^{4+} excitation spectrum is more compatible with blue excitation LEDs than the excitation spectrum of SAM:Mn^{4+}, it is not optimal. In wLEDs, a yellow emission band is present, due to YAG:Ce or other yellow phosphors. The third absorption band of Al_2O_3:Mn^{4+} overlaps with such yellow emission, causing reabsorption of the converted photons. This reabsorption can improve the absorption of the pc-wLED, but it can also reduce the total conversion efficiency of the wLED if the IQE of the yellow phosphor is lower than 100 %.

The dopant concentration is rather low in all samples, with a Mn concentration of 0.02–0.06 % in SMA:Mn compared to 0.12 % in SAM:Mn. Compared to SAM:Mn, higher internal quantum efficiencies are obtained in the SMA:Mn phosphor even though the dopant concentration is lower in SMA:Mn. Since the absorption is still low, even when a high IQE is reached, the EQE is too low to use in applications. This could be improved by increasing the dopant concentration. Another drawback of this phosphor is the thermal quenching, which is far below the typical operating temperature of wLEDs (400–450 K), at which the emission is almost fully quenched. An increase in dopant concentration will not improve the thermal quenching behavior, since a higher dopant concentration increases the probability of nonradiative transitions.

Since neither of the codopants can be detected in EDX and no significant influence of the codopants is seen in the luminescence spectrum, it is possible that Bi and Ce have not been incorporated in the SAM lattice. Since the codopant concentration is only 0.01–0.04 %, the influence could be negligible. On the other hand, somewhat higher quantum efficiencies are obtained in the codoped samples. From the obtained results is it not clear if this is due to incorporated codopants or due to a better incorporation of the Mn dopant in a higher crystalline host with less defects, as can occur when a flux is added to a precursor mixture in solid state synthesis to increase the performance of the phosphor.

5.3 Conclusion

Although a broad red emission spectrum can be found in magnesium hexaaluminates including SAM:Mn, BAM:Mn, CAM:Mn, SMA:Mn and the codoped SMA:Mn,Bi, it has some drawbacks which prohibit it from application in white LEDs. The excitation spectrum has three bands around 323 nm, 397 nm and 468 nm, with a low absorption at 455 nm. The increased $Al_2O_3:Mn^{4+}$ emission in SMA:Mn increases the absorption of the emission by a blue LED chip at 455 nm, since an excitation band is present at 414 nm, but the $Al_2O_3:Mn^{4+}$ excitation band at 565 nm causes reabsorption of yellow phosphor emission in pc-wLEDs. UV-wLEDs with an excitation at 395 nm are an option, but the external quantum efficiency is still rather low in our samples, due to the low dopant concentrations.

Further optimization of the synthesis, including a higher dopant concentration, longer heat treatments or the use of flux materials, can improve the QE. The thermal quenching behavior is poor, with fully quenched emission in the typical operating range of wLEDs. Apart from the low QE and poor thermal quenching, the eye-sensitivity limit reduces the total efficiency for wLED applications. The broad emission band spans from 630–750 nm, while eye-sensitivity is limited above 650 nm. Therefore, the quest on red phosphors for LED applications shifted from oxides to fluorides. Other applications besides wLEDs can be found for the broad band red emission, like LED grow lights for horticulture applications. LED lamps applied in the cultivation of flowers, fruits and vegetables have been developed with different colors for different growing requirements, including deep red and far red emission range [74, 75].

6

Etching synthesis of K_2SiF_6:Mn^{4+}

When the manganese-doped potassium fluorosilicate K_2SiF_6:Mn^{4+} was first introduced as a possible red phosphor by Adachi and Takahashi in 2008 [76], they used a synthesis based on the etching of Si wafers with HF in the presence of $KMnO_4$. The formation of fluorosilicates, outside the framework of phosphor synthesis, has previously been reported as a sideproduct of electroless etching of silicon in HF-based solutions. Electroless etching is an electrochemical oxidation without an external potential, using strong oxidants such as $KMnO_4$, in contrast to anodic etching, where an external potential is applied on the electrolyte. With electroless silicon etching, the objective is to form porous silicon layers, but when the etchant is composed of HF and $KMnO_4$, K_2SiF_6 is formed on the surface of the silicon substrate [77]. Although Mn doping is not mentioned in this context, it is possible to form K_2SiF_6:Mn^{4+} in this etching solution, as will be seen in this chapter.

All common synthesis methods for Mn^{4+}-doped fluorides use aqueous or anhydrous HF or even elemental F_2 as a fluorine source [78]. A HF-free synthesis would strongly decrease the safety hazards associated to the current synthesis methods. As a first step in the direction of a HF-free synthesis of K_2SiF_6:Mn^{4+}, an ionic-liquid synthesis has been explored for the K_2SiF_6 host, but has not yet resulted in a phosphor synthesis [79]. Since the fluorine ions are a crucial part of the crystal lattice and because of their sensitivity to oxidation and hydrolysis, acidic environments and a fluorine excess seem necessary synthesis conditions. Even solution synthesis methods that claim to be HF free, produce HF in situ [80].

Although precautions have to be taken when using HF, it can be handled safely using the right protective equipment and avoiding glass labware. Possible synthesis methods using HF include etching, precipitation, cocrystallization and coprecipitation and they will be discussed in detail in the following chapters. A schematic overview of the four main synthesis methods is given in figure 6.1. An overview table of the four main synthesis methods (table 10.2) is included at the end of chapter 10. A literature review on the different synthesis methods for K_2SiF_6:Mn^{4+}, including overview tables of phosphor properties, was published in [81]:

K_2SiF_6:Mn^{4+} as a red phosphor for displays and warm-white LEDs: a review of properties and perspectives
Heleen F. Sijbom, Reinert Verstraete, Jonas J. Joos, Dirk Poelman and Philippe F. Smet
Optical Materials Express, **7** (9) 3332-3365 (2017)

6.1 Method

The etching solution consisted of 25% HF (40%, Sigma-Aldrich) and 0.19 M $KMnO_4$ (98%, Alfa Aesar) [76]. The Si wafers were degreased in isopropanol (99.7%, Fiers) in an ultrasound bath for 5 min and rinsed with deionized water. Si wafers cut into 1.5–3 cm^2 rectangular pieces were used as a Si source. After the wafer was put into the etchant, 0.2 mL of H_2O_2 (35%, Sigma-Aldrich) was added to the solution to get a concentration of 0.5 mM. The wafer was left in the etchant for 10 minutes, after which it was removed with plastic tweezers, rinsed with deionized water and dried in air overnight. The etching solution was filtered and the precipitate was washed with ethanol (96%, Fiers) and dried in air.

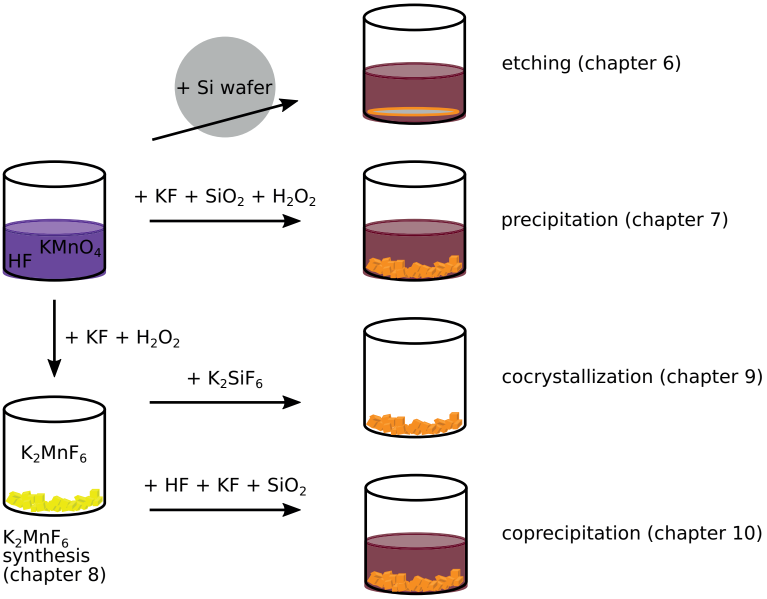

Figure 6.1: Schematic overview of the main possible methods for synthesis of K_2SiF_6:Mn^{4+}.

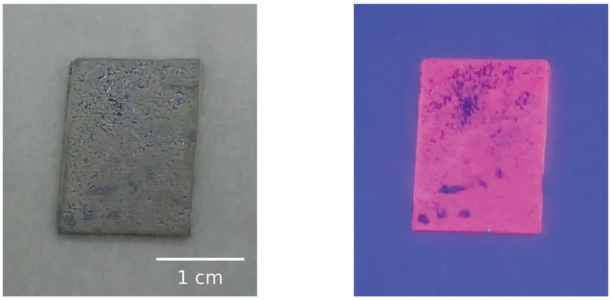

Figure 6.2: Si wafer (1.2 cm by 2 cm) etched in 25% HF and 0.19 M $KMnO_4$, in day light (left) and under UV illumination at 365 nm (right)

This synthesis produced Si wafers with a white to yellow precipitate attached to it (figure 6.2) and a yellow to orange phosphor powder was filtrated from the etchant. The etchant had a dark purple color throughout the synthesis, showing that Mn is available in the form of $KMnO_4$ during the etching. Alternative Si sources such as crushed quartz schist [41] or powdered silica glass [52] were explored in literature. In the presence of H_2O_2, the chemical reaction of the formation of K_2SiF_6:Mn^{4+} can be represented by equation 6.1. In this redox reaction, MnO_2 can form as a side product in the Mn reduction, especially since no other potassium source is present besides $KMnO_4$. The formed MnO_2 can precipitate from the solution or can be deposited on the wafer surface.

$$\begin{aligned}(1-x)\,\mathrm{Si}\,(s) + 2\,\mathrm{KMnO_4}\,(aq) + 6\,\mathrm{HF}\,(aq) + (1+2x)\,\mathrm{H_2O_2}\,(aq) &\longrightarrow \\ \mathrm{K_2Si_{1-x}Mn_xF_6}\,(s) + (2-x)\,\mathrm{MnO_2}\,(s) + (4+2x)\,\mathrm{H_2O}\,(l) + (1+2x)\,\mathrm{O_2}\,(g)\end{aligned} \tag{6.1}$$

The etching of Si with $KMnO_4$ in HF can also occur without H_2O_2 present, but the yield is lower when it is compared with the synthesis where H_2O_2 is added. Several manganese oxide phases can be formed in this slow redox reaction. The chemical reaction of the formation of K_2SiF_6:Mn^{4+} in a solution of $KMnO_4$ in HF can be represented by equation 6.2.

$$\begin{aligned}(2-2x)\,\mathrm{Si}\,(s) + 4\,\mathrm{KMnO_4}\,(aq) + 12\,\mathrm{HF}\,(aq) \longrightarrow 2\,\mathrm{K_2Si_{1-x}Mn_xF_6}\,(s) + \\ 2x\,\mathrm{MnO_2}\,(s) + (2-2x)\,\mathrm{Mn_2O_3}\,(s) + 6\,\mathrm{H_2O}\,(l) + (2+x)\,\mathrm{O_2}\,(g)\end{aligned} \tag{6.2}$$

To optimize the performance of the etching synthesis, various etching solutions were used with a HF concentration of 2–22.6 M, a $KMnO_4$ concentration of 6–304 mM and a KF concentration of 0–1.5 M. The obtained etched wafers were evaluated under a UV lamp of 365 nm and the obtained powder samples were evaluated using quantum efficiency measurements.

6.2 Results

Both powders and stained Si wafers were obtained from the synthesis. The powders were analyzed in more detail compared to the wafers, since powder based analysis methods are more widespread in phosphor evaluation.

6.2.1 Structural

K_2SiF_6 has a cubic crystal structure with space group $Fm\bar{3}m$ and a lattice constant $a = 8.13\,\text{Å}$ (figure 6.3). Therefore, a simple X-ray diffraction pattern is expected for K_2SiF_6. Four main diffraction lines are expected at 18.9° (111), 31.1° (220), 38.3° (222) and 44.5° (400) when using Cu $K\alpha$ radiation. All the reflections in the measured XRD pattern coincide perfectly with the reference pattern of K_2SiF_6 (figure 6.4). Cubic K_2SiF_6:Mn^{4+}

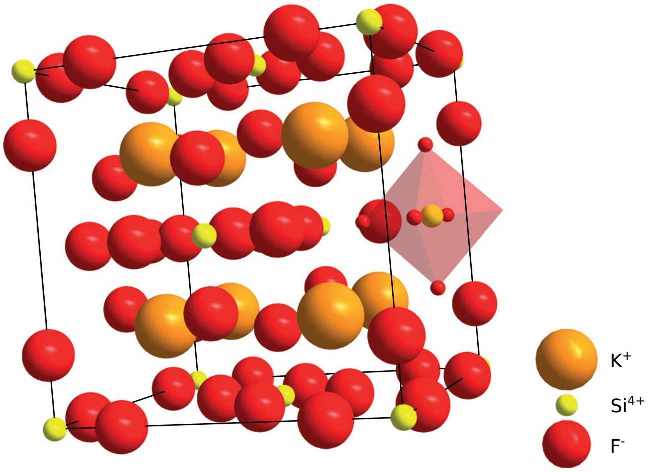

Figure 6.3: Cubic crystal structure of K_2SiF_6, showing an octahedrally coordinated Si atom.

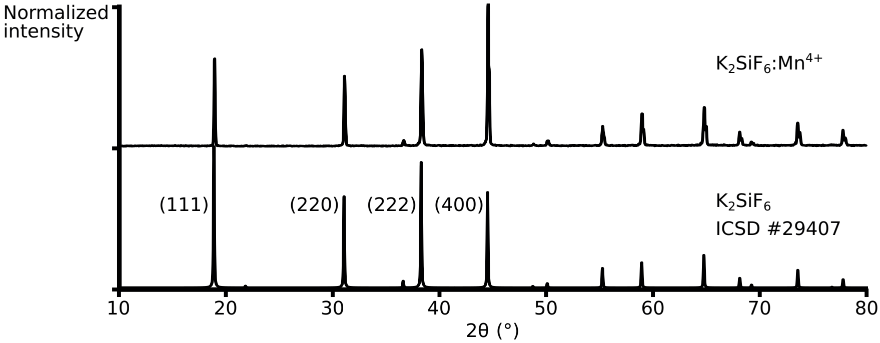

Figure 6.4: XRD pattern of a K_2SiF_6:Mn^{4+} phosphor powder (top) synthesized using an etching synthesis with a dopant concentration of 8.3%, compared with a reference pattern of K_2SiF_6 (bottom).

is thermodynamically more stable than the hexagonal phase, with calculated formation enthalpies of $-5.653\,22 \times 10^3$ eV for the cubic phase and $-5.653\,11 \times 10^3$ eV for the hexagonal phase, leading to a difference of 110 meV per unit cell [51].

Introducing a dopant into a host crystal can lead to small alterations of the crystal structure, especially when the dopant ion has a different ionic radius than the ion it replaces. In K_2SiF_6:Mn^{4+}, the Mn–F distance is expected to be larger than the Si–F distance since the ionic radius of Mn^{4+}

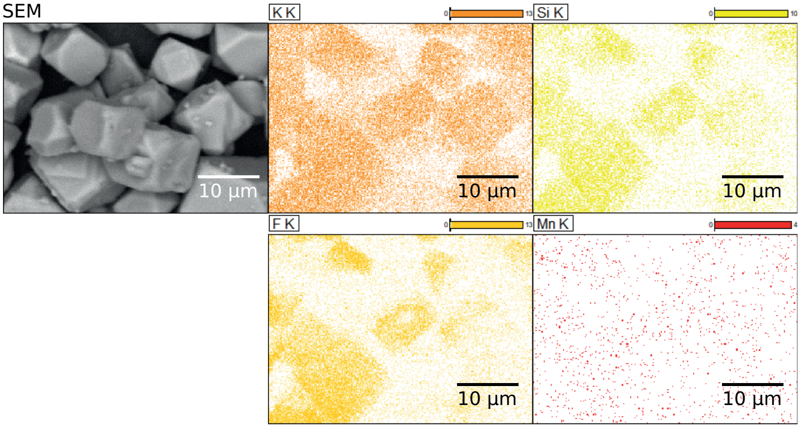

Figure 6.5: SEM picture and EDX maps of a K_2SiF_6:Mn^{4+} phosphor powder made using an etching synthesis.

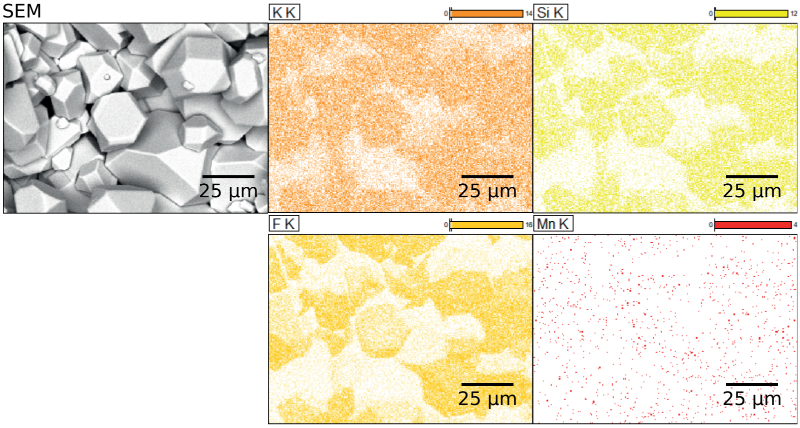

Figure 6.6: SEM picture and EDX maps of a K_2SiF_6:Mn^{4+} phosphor adsorbed to a Si wafer made using an etching synthesis.

(53 pm) is larger than that of Si^{4+} (40 pm). Although there is a lattice expansion when introducing the Mn dopant, no effect of this lattice expansion is seen in the diffraction patterns for low doping concentrations, when comparing the XRD pattern of K_2SiF_6:Mn^{4+} with the K_2SiF_6 reference pattern.

The phosphor particles from an etching synthesis are relatively big, 5–10 µm (truncated) cubes, as can be seen in the SEM image in figure 6.5. According to the EDX map, Mn is homogeneously distributed over the particles with a dopant concentration of 8.3% of the amount of Si present.

The phosphor adsorbed to the wafer is equally homogeneous (figure 6.6) but with a lower dopant concentration of 5.6%. Although Mn is available throughout the synthesis due to the excess of $KMnO_4$, the incorporation of Mn in K_2SiF_6 is favored in the powder compared to the material adsorbed to the wafer surface. This difference in Mn concentration between the precipitated powder phosphor and the adsorbed phosphor explains the difference in body color, with a darker orange color found for the precipitated powder phosphor and white to yellow body color for the adsorbed phosphor.

6.2.2 Luminescence

The photoluminescence spectra in figure 6.7 show narrow emission bands due to the $^2E_g \rightarrow {}^4A_{2g}$ spin-forbidden transitions in Mn^{4+}. When the emission is measured at a nm resolution the pattern consists of 5–6 lines. The main vibronic modes coupled to the $^2E_g \rightarrow {}^4A_{2g}$ transition are the antisymmetric $\nu_3(T_{1u})$, $\nu_4(T_{1u})$ and $\nu_6(T_{2u})$. The ν_6 Stokes line at 630 nm is the most intense, followed by the ν_4 Stokes line at 634 nm. The ν_6 and ν_4 anti-Stokes lines at 612 nm and 608 nm and the ν_3 Stokes line at 647 nm are less intense, but still reach over 10% of the emission intensity at 630 nm [47]. Lower intense lines are also found, such as the ν_3 anti-Stokes line at 597 nm and some minor emission bands at 618 nm, 621 nm,

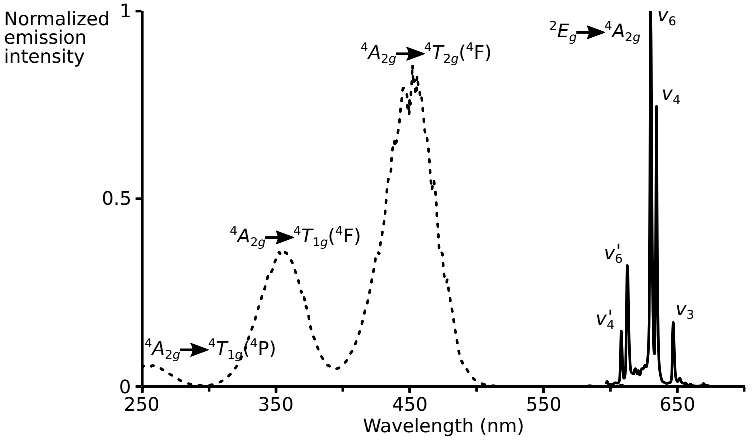

Figure 6.7: Normalized excitation spectrum (dotted line) and emission spectrum (full line) of K_2SiF_6:Mn^{4+} made using an etching synthesis.

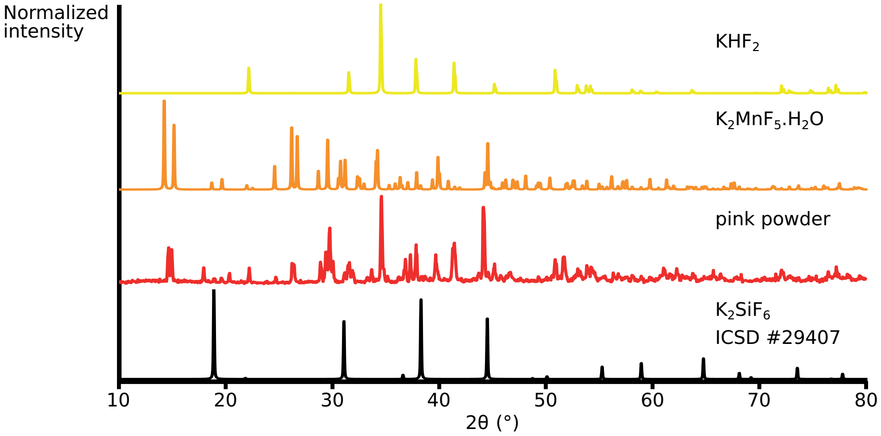

Figure 6.8: XRD pattern of the pink powder obtained from an etching synthesis with KF and $KMnO_4$ as etchant, compared to the reference patterns of K_2SiF_6, $K_2MnF_5 \cdot H_2O$ and KHF_2.

651 nm, 660 nm and 670 nm. The ZPL for the $^2E_g \rightarrow {}^4A_{2g}$ transition is located between 619 and 630 nm, but is usually not present in the emission spectrum due to the cubic crystal symmetry of K_2SiF_6:Mn^{4+}.

Three broad excitation bands are present corresponding to the $^4A_{2g} \rightarrow {}^4T_{1g}(^4P)$, $^4A_{2g} \rightarrow {}^4T_{1g}(^4F)$ and $^4A_{2g} \rightarrow {}^4T_{2g}(^4F)$ spin-allowed transitions. The main excitation band is centered around 450 nm, which is ideal for blue-LED excitation at 440–460 nm. A second, less intense excitation band is centered around 350 nm. The third excitation band at shorter wavelengths, around 240–260 nm is rarely reported, since it can be hidden by charge-transfer transitions or host–lattice absorption. The intensity of this UV excitation band is rather low compared to the other excitation bands and most reported spectra only start at 300 nm.

The high Mn concentration leads to a good absorption of blue light, up to 59% at 450 nm for a precipitated powder from an etching synthesis. With a high IQE of 69%, the EQE of 40% is reasonably high for an optimal etchant of 14 M HF, 0.19 M $KMnO_4$ and added H_2O_2 (table 6.1). When KF was added to the etching solution, a pink powder was formed which showed no luminescence. From the XRD reflection pattern, it was identified as the hydrated fluoride $K_2MnF_5 \cdot H_2O$ mixed with KHF_2 and only a minor fraction of K_2SiF_6 in the pattern (figure 6.8).

Table 6.1: Influence of synthesis conditions on a phosphor sample from the etching synthesis. Unless specified otherwise, 0.2 mL H_2O_2 was added to the etchant after the Si wafer was added.

synthesis conditions	IQE	EQE	Absorption
0.19 M $KMnO_4$, 14 M HF (optimal)	69%	40%	0.59
0.19 M $KMnO_4$, 22.6 M HF	61%	31%	0.51
0.15 M $KMnO_4$, 6 M HF, no H_2O_2	41%	20%	0.49
0.20 M $KMnO_4$, 6 M HF, no H_2O_2	39%	22%	0.58
0.25 M $KMnO_4$, 6 M HF, no H_2O_2	14%	9%	0.66
0.30 M $KMnO_4$, 14 M, no H_2O_2	65%	10%	0.15
0.037 M $KMnO_4$, 6 M HF	33%	11%	0.33

Somewhat lower quantum efficiencies were obtained when the synthesis conditions were further varied (table 6.1). Increasing the HF concentration from 14 M to 22.6 M leads to a drop in IQE to 61% and a reduced EQE value of 31% with an absorption of 51%. In a 6 M HF solution, etching wafers with 0.15 M, 0.2 M and 0.25 M $KMnO_4$ without H_2O_2 present resulted in IQE values of 41 %, 39 % and 14 % and EQE values of 20 %, 22 % and 9 %. With increasing $KMnO_4$ concentrations, the IQE drops, but due to an increase in absorption from 49% to 66%, the EQE increases to 22% at 0.2 M $KMnO_4$. With an increased $KMnO_4$ concentration of 0.3 M without addition of H_2O_2, a high IQE of 65% has been reached, but because of the low absorption of 15%, the EQE only reaches 10%. At low $KMnO_4$ and HF concentrations (0.037 M and 6 M respectively), formation of K_2SiF_6:Mn^{4+} is possible, but the obtained quantum efficiencies are only 33% internally and 11% externally, so higher precursor concentrations are preferred.

6.3 Discussion

The results of the etching synthesis of K_2SiF_6:Mn^{4+} are very promising and show the possibilities of Mn^{4+}-doped fluoride phosphors for warm-white LEDs. The line emission at 630 nm is perceived as saturated red and the eye sensitivity is still quite high in this wavelength range, which is beneficial for lighting applications. No excitation bands are present at wavelengths above 500 nm, which prevents reabsorption of yellow and green phosphor emission in a pc-wLED. The emission around 630 nm is a benefit of fluoride hosts when compared to oxide hosts, which have a lower lying ^2E_g level and therefore a longer emission wavelength up to deep red and near infrared. As discussed in chapter 5, Mn^{4+}-doped oxides have a broad UV excitation band which is not fully compatible with pc-wLED excitation at 395 nm or at 455 nm. Furthermore, in the hexaaluminates an excitation band is present around 565 nm in Al_2O_3:Mn^{4+}, which overlaps with the emission band of YAG:Ce.

The etching synthesis results in a pure phosphor powder with large particles and a high external quantum efficiency up to 40 %, which are equal to QE values obtained in literature [82]. The main drawback of the synthesis is the low synthesis yield. The phosphor forms on the surface of the Si wafer, passivating the surface and reducing the possibility for further phosphor formation. Part of the formed phosphor dissociates from the Si wafer after which it can be recovered by filtering the etching solution. The rest of the formed phosphor can be scratched of the wafer surface, which is rather cumbersome. Furthermore, the incorporation of Mn cannot be controlled during the etching synthesis. In the etching solution, the Mn concentration of 0.19 M is rather high, compared to other synthesis methods that will be discussed further on. In precipitation synthesis, the subject of chapter 7, an 8% Mn dopant concentration is present in the synthesis solution, which equals a concentration of 0.04 M. The dopant concentration of the etching synthesis is harder to calculate since Si is available as a 1.5–3 cm^2 wafer, but not all Si in the wafer is available for etching and phosphor forms mainly at the wafer edges and at scratches as can be seen from the SEM image in figure 6.9. Using powder Si instead of wafers could improve the available reactive surface, but this has not been tested nor reported in literature. At a 0.19 M Mn concentration, a dopant concentration of 8.3% is obtained as detected in EDX.

Although the presence of only a single potassium source can induce the formation of manganese oxides, adding KF to the etchant did not improve the phosphor quality, as it resulted in the pink powder that mainly contained $K_2MnF_5 \cdot H_2O$ and KHF_2 (figure 6.8). From the XRD patterns, it can be seen that only a small amount of K_2SiF_6 is formed. In literature, the addition of KHF_2 in various concentrations resulted in a mixture of K_2SiF_6:Mn^{4+} and K_2MnF_6, but only after three days of etching [38]. Variation of the HF or $KMnO_4$ concentration also lowered the quantum efficiency, while the addition of H_2O_2 to the etchant did improve the phosphor quality. In literature, the same etching solution of 14 M HF and 0.19 M $KMnO_4$ is most often used [21, 42, 76, 82], which confirms our variations.

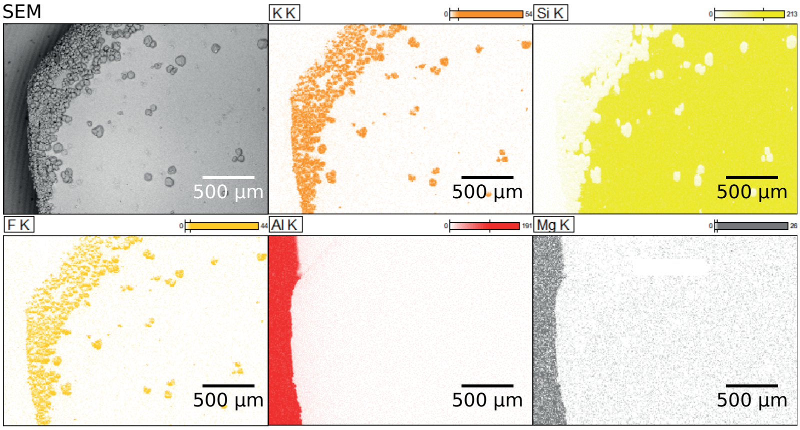

Figure 6.9: SEM picture and EDX maps of K_2SiF_6:Mn^{4+} formed on the edge of a Si wafer using an etching synthesis. Mg and Al were detected from the SEM sample holder. Si is present in the same areas as K and F, proving the formation of K_2SiF_6 adsorbed on the wafer, but the Si signal in the wafer is much higher. The Mn concentration was too low to be detected using EDX, but CL light emission proved the incorporation of Mn^{4+} in K_2SiF_6.

The addition of MnF_2 lead to an improved emission intensity [48], but other variations of the etchant, including the addition of H_2O_2 have not been reported.

6.4 Conclusion

K_2SiF_6:Mn^{4+} is a very promising red phosphor with line emission around 630 nm and an excitation band around 450 nm which is perfectly suited for blue LED excitation. The obtained quantum efficiencies are reasonably high at an EQE of 40% and are nearly suitable for LED applications. The major drawback of the etching synthesis is the limited access to Si in the synthesis, which lowers the possible synthesis yield. As $KMnO_4$ acts as both the potassium and manganese source, the potassium source is limited, but addition of KF to the etchant did not improve the phosphor formation but rather formed KHF_2 and $K_2MnF_5 \cdot H_2O$. If K_2SiF_6:Mn^{4+} grows up to applications, more efficient synthesis routes are needed, which will be discussed in the coming chapters.

7

Precipitation synthesis of $K_2SiF_6:Mn^{4+}$

The synthesis methods in the previous chapters consumed at least some solid precursors. Dissolving precursor materials prior to the synthesis can increase the reaction rate and improve phosphor synthesis due to enhanced molecular mixing in solution. It is possible to form a powder $K_2SiF_6:Mn^{4+}$ phosphor using a simple precipitation synthesis in HF solution. The results in this chapter were published in:

Luminescent behavior of the $K_2SiF_6:Mn^{4+}$ red phosphor at high fluxes and at the microscopic level
Heleen F. Sijbom, Jonas J. Joos, Lisa I. D. J. Martin, Koen Van den Eeckhout, Dirk Poelman and Philippe F. Smet
ECS Journal of Solid State Science and Technology, **5** (1) R3040-R3048 (2016)

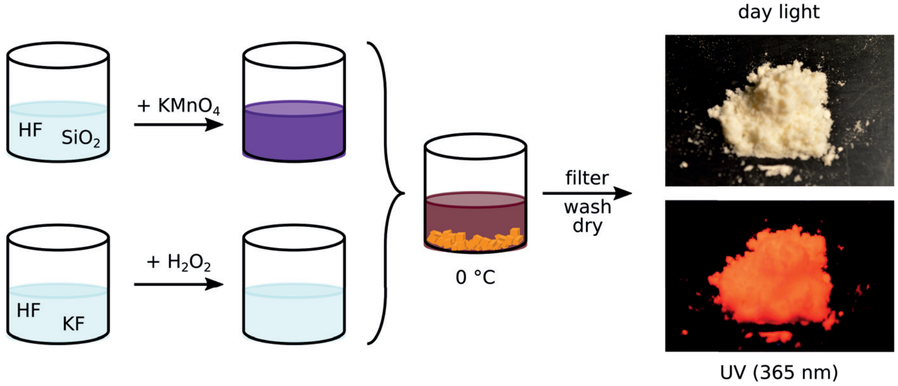

Figure 7.1: Schematic illustration of a simple precipitation synthesis of K_2SiF_6:Mn^{4+} at 0 °C. Appearance of K_2SiF_6:Mn^{4+} under day light and UV illumination at 365 nm (right).

7.1 Method

The phosphor particles were synthesized by solution synthesis in 40% HF (Sigma-Aldrich), according to the procedure as described by Nguyen et al [83]. SiO_2 (99.5%, Alfa Aesar) is dissolved in HF at room temperature. $KMnO_4$ (98%, Alfa Aesar) is added to this solution, such that a dopant concentration of 8% is present. In a separate solution, KF (99%, Alfa Aesar) is dissolved in HF and 35% H_2O_2 (Sigma-Aldrich) is added. The two solutions are mixed in an ice bath, after which the phosphor particles precipitate. The precipitate is filtered, washed with 20% HF and ethanol (96%, Fiers) subsequently and dried at room temperature in air, resulting in a light-yellow powder. The synthesis process is illustrated in figure 7.1.

In the precipitation synthesis, a yellow precipitate of K_2SiF_6:Mn^{4+} is formed upon a redox reaction of $KMnO_4$, SiO_2 and KF at room temperature or in an ice bath. Addition of H_2O_2 or mild heating (50 °C) of the solution can speed up the redox reaction that turns the solution from purple to colorless and forms the precipitate. Alternatively, the precipitate can be formed by addition of acetone as a nonsolvent. In the presence of H_2O_2, the chemical reaction of the formation of K_2SiF_6:Mn^{4+} can be represented by reaction 7.1, while the formation of K_2SiF_6:Mn^{4+} in absence of H_2O_2 can be represented by reaction 7.2.

$$\begin{aligned}(2-2x)\,\mathrm{SiO_2}\,(\mathrm{aq}) + 2x\,\mathrm{KMnO_4}\,(\mathrm{aq}) + (4-2x)\,\mathrm{KF}\,(\mathrm{aq}) +\\ (8+2x)\,\mathrm{HF}\,(\mathrm{aq}) + 3x\,\mathrm{H_2O_2}\,(\mathrm{aq}) \longrightarrow\\ 2\,\mathrm{K_2Si_{1-\mathit{x}}Mn_{\mathit{x}}F_6}\,(\mathrm{s}) + (4+4x)\,\mathrm{H_2O}\,(\mathrm{l}) + 3x\,\mathrm{O_2}\,(\mathrm{g})\end{aligned} \tag{7.1}$$

$$\begin{aligned}(4-4x)\,\mathrm{SiO_2}\,(\mathrm{aq}) + (4x)\,\mathrm{KMnO_4}\,(\mathrm{aq}) +\\ (8-4x)\,\mathrm{KF}\,(\mathrm{aq}) + (16+4x)\,\mathrm{HF}\,(\mathrm{aq}) \longrightarrow\\ 4\,\mathrm{K_2Si_{1-\mathit{x}}Mn_{\mathit{x}}F_6}\,(\mathrm{s}) + (8+2x)\,\mathrm{H_2O}\,(\mathrm{l}) + 3x\,\mathrm{O_2}\,(\mathrm{g})\end{aligned} \tag{7.2}$$

Variations in the synthesis conditions were applied to find the optimal parameters resulting in a phosphor with a high optical absorption and high IQE. Phosphor samples were prepared with a SiO_2 concentration of 0.24–0.52 M, a $KMnO_4$ concentration of 0.03–0.36 M and a KF concentration of 0–1.60 M. KF could be added to the solution of SiO_2 and $KMnO_4$ either in powder form or as a solution in HF. H_2O_2 was not always added to the synthesis solution. Other ways to speed up the redox reaction were variating the synthesis temperature from an ice bath over room temperature to a 50 °C hot water bath. Efforts were done to reduce the temperature of the ice bath used for precipitation even further by using salted ice cubes.

When H_2O_2 is added, the reaction time can be determined by the color change of the reduction of $KMnO_4$ and therefore can depend on the H_2O_2 addition rate. Without H_2O_2, this color change has not been observed and the reaction is stopped after a set amount of time between 5 min and 5 h. The reaction is stopped by decantation and filtering of the solution. Since purple $KMnO_4$ is still present in this solution, the filtrate is thoroughly washed with water and ethanol until all the purple color, typical for Mn^{7+}, is cleared away.

Due to the limited solubility of K_2SiF_6 and K_2MnF_6 in HF, the phosphor precipitates spontaneously from the synthesis solution. The use of an ice bath in the synthesis influences the solubility besides slightly slowing down the reaction rate to prevent excess reduction. Alternatively, precipitation was induced using acetone as a nonsolvent or by using a centrifuge as an alternative for the filtration step. Bubbling the reaction mixture with N_2 was tried to prevent incorporation of O_2 formed during the synthesis.

In literature, several post-synthesis treatments including coatings and F_2 annealing have been reported that improve the chemical stability of K_2SiF_6:Mn^{4+}. An undoped K_2SiF_6 coating on a commercially available

K_2SiF_6:Mn^{4+} powder showed that the coating protected against hydrolysis of surface groups, since the body color darkening at HTHH conditions was reduced [84]. An alkyl phosphate coating also improved the stability of K_2SiF_6:Mn^{4+}, both when immersed in water for 60 min and for 30 days at HTHH conditions [53]. Samples that were treated with a H_2SiF_6/K_2SiF_6 solution, either with or without F_2 annealing, showed the best balance of properties after aging at HTHH conditions and subjection to high-flux light conditions. The annealing especially improved resistance against laser damage, which also showed in the control samples [85, 86]. In this work, the thermal stability was evaluated by heating the powder in air to 200 °C and 300 °C for 3 h. Inorganic coatings were applied on the phosphor powders using a precipitation coating with SiO_2 or K_2SiF_6.

For the SiO_2 coating, 0.2 mL tetraethyl orthosilicate (99%, Aldrich) is added to a suspension of phosphor particles in ethanol and water. The pH is adapted to 9 using a solution of NaOH (98%, Sigma-Aldrich) in water. The solution is stirred at 35–60 °C for 35 min, after which the precipitate is filtrated and dried at 50 °C in air, possibly with an additional annealing step at 350 °C. For the K_2SiF_6 coating, a 0.09 M solution of K_2SiF_6 in HF is added to the phosphor powder, after which the mixture is evaporated in a hot water bath at 70 °C overnight.

7.2 Results

The luminescent and structural properties of the yellow phosphor powder were investigated. Special attention was given to the luminescent properties at high excitation intensities and on the microscopic level.

7.2.1 Structural characterization

All the reflections in the measured XRD pattern can be assigned to the standard pattern of K_2SiF_6 (cubic space group $Fm\bar{3}m$) as can be seen in figure 7.2. Although Mn^{4+} doping introduces a larger ion (53 pm) in the lattice site of Si^{4+} (40 pm), no significant shift of the reflections caused by the doping is observed. The cubic crystal structure is also clear from the SEM picture in figure 7.3 (left), where cubic and octahedral particles with a diameter of 2–10 µm can be seen. Truncation of cubic particles leads to truncated cubes, cuboctahedrons and octahedral crystals. This truncation can be beneficial for the luminescence output of the particles,

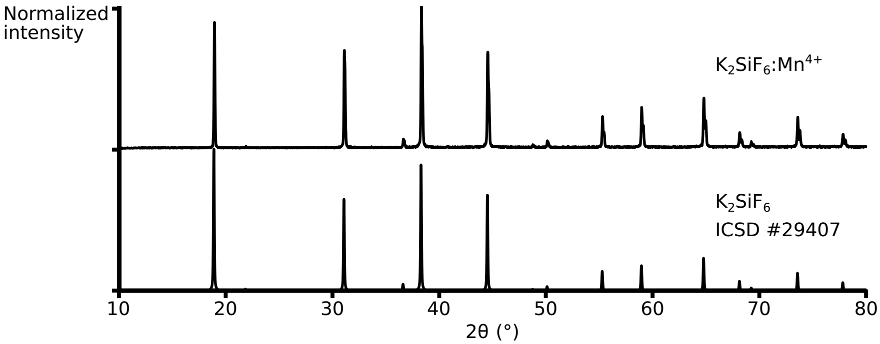

Figure 7.2: XRD pattern of the red phosphor K_2SiF_6:Mn^{4+} synthesized by precipitation synthesis with a dopant concentration of 1.5% (top), compared with the reference pattern for K_2SiF_6 (bottom).

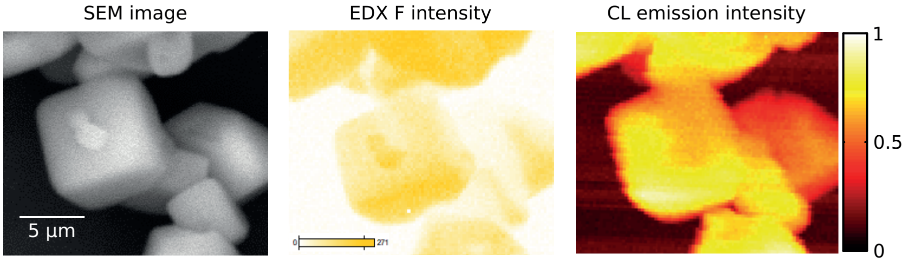

Figure 7.3: SEM image (left), F Kα EDX map (center) and cathodoluminescence map of K_2SiF_6:Mn^{4+} particles made using a precipitation synthesis. The EDX detector is located at the center bottom of the figure, while the optical fiber for CL emission is located at the center top of the figure, which can explain some shading effects.

as will be explained later. EDX analysis shows a homogeneous elemental distribution of K, Si, F and Mn. No clusters of Mn are observed, so the doping is homogeneous over the particles within the detection limit of EDX. The dopant concentration is 1.5 ± 0.3% of the amount of Si in EDX analysis. In the precursor solutions, the Mn concentration is 8% of the Si concentration, so the incorporation of Mn in the phosphor crystals during the synthesis is limited.

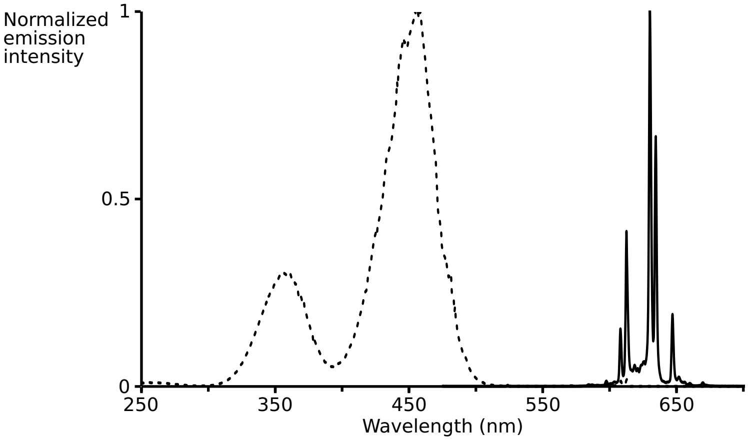

Figure 7.4: Normalized photoluminescence excitation spectrum (dotted line), upon monitoring emission at 630 nm and emission spectrum (full line), upon monitoring excitation at 455 nm of K_2SiF_6:Mn^{4+} made using a precipitation synthesis.

7.2.2 Luminescence

The photoluminescence spectra in figure 7.4 show narrow emission bands due to the $^2E_g \longrightarrow {}^4A_{2g}$ spin-forbidden d–d transitions in Mn^{4+}. Two broad excitation bands are present corresponding to the $^4A_{2g} \longrightarrow {}^4T_{2g}$ and $^4A_{2g} \longrightarrow {}^4T_{1g}$ spin-allowed transitions. The IQE is 46% and about 25% of the incident photons at 450 nm are absorbed by the phosphor, which limits the EQE to 12%. Although the absorption did not change, a higher IQE of 51% and a similar EQE of 12% could be obtained when the synthesis solution was bubbled through with N_2 gas, possibly reducing the incorporation of O_2.

The SEM picture in figure 7.3 shows the representative particles selected for CL and EDX maps. The CL map shows a preferential location of the light output on certain edges of the cubic particle, with the optical fiber located at the bottom for this image. Rotating the particle with respect to the light-collecting optical fiber leads to essentially the same spatial emission pattern. The light outcoupling is maximal at the lower crystal edge (figure 7.3, white and yellow corners in CL map), while excitation with the electron beam in the center of the top surface of the particle leads to lower CL emission intensity, independent of the location of the optical fiber (figure 7.3, orange center in CL map). The elemental distribution found EDX was homogeneous, the intensity variation in the F Kα EDX map (fig-

Figure 7.5: Body color of K_2SiF_6:Mn^{4+} from a precipitation synthesis at 0 °C without (left) and with bubbling through N_2 (right) during the synthesis.

ure 7.3, center) is caused by shading, since the EDX detector is located at the bottom of the image. As the low-energy F Kα X-rays have a short attenuation length in the K_2SiF_6 lattice, geometrical aspects influence the relative number of detected X-rays.

For these symmetrically shaped particles, it can be expected that total internal reflection plays an important role in the light outcoupling behavior, especially when the particles are measured in vacuum, leading to a significant difference in refractive index at the faces of the crystals. The longer optical-path length will lower the external quantum efficiency as defects other than Mn^{4+}, which can be unintentionally present, might reabsorb the light and nonradiatively dissipate the energy. When K_2SiF_6 (refractive index of 1.34) is embedded in an epoxy or silicone binder material, the outcoupling from the phosphor particles can be improved. Phosphor layers with several polymers were made and will be discussed in chapter 13.

Since O_2 is formed during the synthesis (reaction 7.1) it could possibly form oxide compounds instead of the fluoride compounds that are aimed for. Bubbling N_2 through the synthesis solution could slightly improve the IQE compared to the same precursor solutions mixed in an air atmosphere, from 46% to 51%. Nevertheless, the absorption and EQE are equal at 0.25 and 12%, which shows that the increase in IQE is not very noticeable. The body color is negatively influenced by the N_2 atmosphere, since the powder precipitated without N_2 is slightly more yellow (figure 7.5). This is confirmed in the dopant concentration found in EDX, which is 1.5% without N_2 and only 0.59% with N_2. Possibly, the agitation caused by the N_2 gas disturbed the stability of the $[MnF_6]^{2-}$ complex in the solution, which lowers the incorporation of Mn^{4+} in K_2SiF_6:Mn^{4+}.

Other variations in the synthesis conditions, such as different concentrations of SiO_2, $KMnO_4$, KF and synthesis temperatures, did not have sufficient positive influence on the luminescence properties. An increase of the $KMnO_4$ concentration in the synthesis solution did not increase the dopant concentration incorporated in the phosphor. For a 13–29 % Mn concentration in the solution, a dopant concentration of 0.12–1.2 % was detected in EDX and quantum efficiencies for these phosphors were lower compared to the optimal 1.5% dopant concentration, with an EQE of 0.14–6.4 % and an IQE of 0.3–38 % with absorption between 15 % and 69 %. The optimal precursor concentrations were 0.5 M SiO_2, 0.036 M $KMnO_4$ and 1.47 M KF, for which the highest quantum efficiencies were obtained and the optimal 1.5% dopant concentration was found.

Lowering the synthesis temperature using salted ice cubes resulted in a similarly light-orange body color, but lower quantum efficiencies and absorption values. The lower synthesis temperature resulted in either an absorption value of 0.13 or an IQE of 27%, resulting in EQE values of 7–8 % while an EQE of 12% was obtained for the same precursor concentrations precipitating at 0 °C. The results of a precipitation synthesis at 50 °C were even worse, with EQE values of 0.38–3.7 % and a light-pink to light-brown body color. The optimal synthesis temperature was 0 °C, resulting in a light-orange phosphor powder with an EQE of 12 %.

The post-synthesis treatments can have some positive influence, but the effect is still limited. A heat treatment at 200 °C and 300 °C (table 7.1) did slightly improve the IQE, but since it was already low to start with, the influence is not that significant. The SiO_2 coating on a powder phosphor sample resulted in a decrease in IQE from 46% to 7% when the coating was applied on the phosphor after drying. The SiO_2 precursor formed particles of SiO_2 mixed with K_2SiF_6:Mn^{4+} particles, as can be seen from the SEM image in figure 7.6. A stable IQE of 19% was obtained when the coating was applied directly after the synthesis, after separating the phosphor by filtration but without an intermediate drying step. In literature, SiO_2 coatings have not been applied on fluoride phosphors, but SiO_2 coatings showed to improve the water resistance and thermal stability of Eu-doped phosphors [87].

On the other hand, the K_2SiF_6 coating resulted in a slight decrease in IQE when applied directly after the synthesis, but an increase in IQE from 53% to 66% was found when a dried phosphor was coated with K_2SiF_6. The phosphor particles were small (1–5 µm) and clearly cubic before coating (left part of figure 7.7). After coating, the particles were somewhat bigger, more clustered and more rounded of, showing the cubic particles less clearly (right part of figure 7.7). With an absorption of 31%, the EQE of the coated phosphor was 20%, compared to 12% of the uncoated phosphor. In literature, the influence of the coating on the initial QE is not

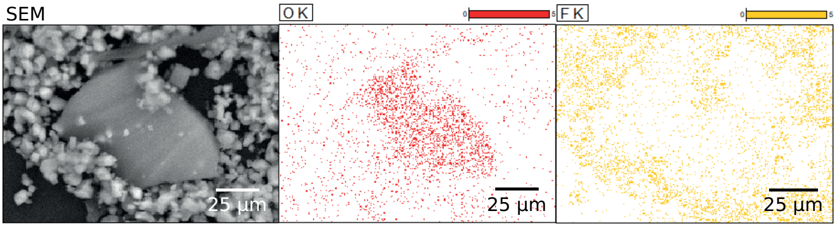

Figure 7.6: SEM image and EDX maps of K_2SiF_6:Mn^{4+} after applying a coating of SiO_2, showing a big SiO_2 particle surrounded by K_2SiF_6:Mn^{4+} phosphor particles.

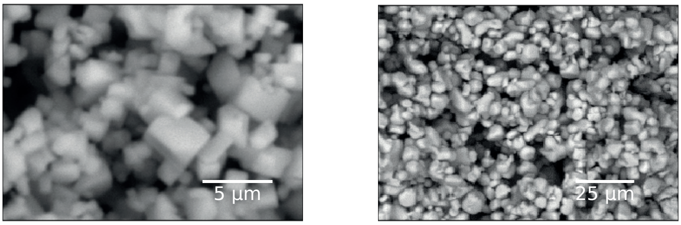

Figure 7.7: SEM image of K_2SiF_6:Mn^{4+} particles synthesized by a precipitation synthesis before (left) and after coating with undoped K_2SiF_6 (right).

discussed, but the K_2SiF_6 coating improves the stability in HTHH conditions, inducing a loss in QE of only 5% after 48 h, compared to a 33% loss for an uncoated phosphor sample [88]. Quantum efficiencies should be higher for practical applications, but the increase in IQE due to the coating is already a positive effect, especially if the coating is beneficial for the chemical stability, which will be discussed in chapter 9.

Table 7.1: Influence of a post-synthesis heat treatment on a phosphor sample from the precipitation synthesis.

sample	IQE	EQE	Absorption
untreated	4.1%	0.70%	0.17
3 h at 200 °C	7.6%	1.4%	0.19
3 h at 300 °C	5.8%	1.2%	0.20

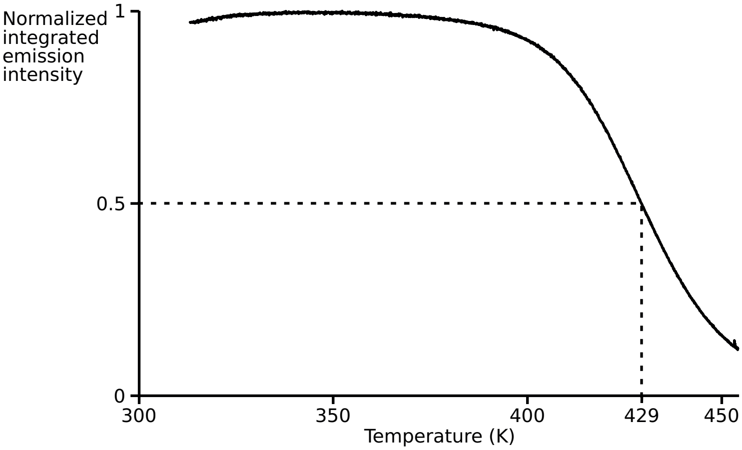

Figure 7.8: Normalized integrated emission intensity of K_2SiF_6:Mn^{4+} made using a precipitation synthesis, as a function of temperature upon LED excitation at 450 nm.

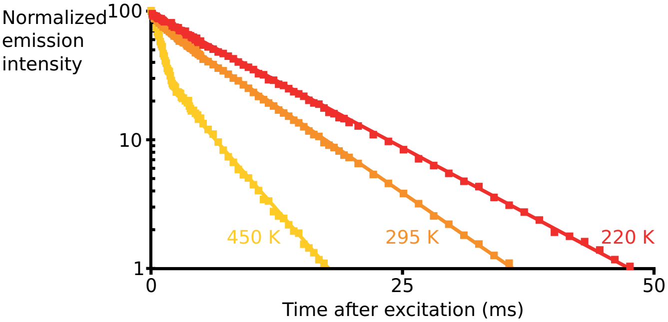

Figure 7.9: Decay profile measurements (squares) and fit (lines) of the luminescence intensity of K_2SiF_6:Mn^{4+} made using a precipitation synthesis at 450 K (yellow), 295 K (orange) and 220 K (red).

7.2.3 Thermal properties

Both the luminescent emission intensity and the luminescent lifetime were measured as a function of temperature. From the thermal-quenching measurements up to 450 K the characteristic temperature $T_{1/2}$, for which the emission intensity is halved compared to the intensity at low temperature, is determined at 429 K. As can be seen in figure 7.8, the emission intensity remains stable until 400 K, which is within the 400–450 K operating temperature of LED chips. At 450 K, the emission intensity is lowered to 16% of the initial emission intensity.

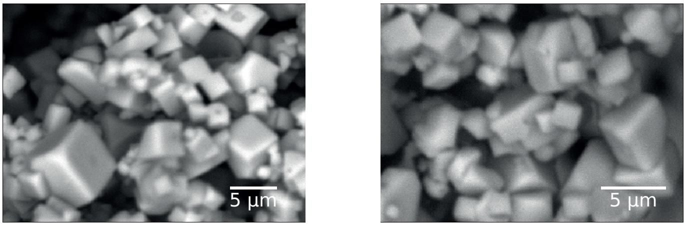

Figure 7.10: SEM image of K_2SiF_6:Mn^{4+} phosphor particles made using a precipitation synthesis before (left) and after heating to 300 °C for 3 h (right).

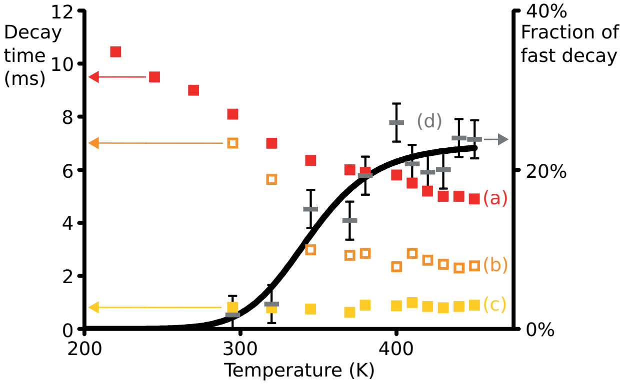

Figure 7.11: Decay time (a-c) (boxes) and fraction of decay component (d) (bars, the full line is a guide to the eye) as a function of temperature of K_2SiF_6:Mn^{4+} made using a precipitation synthesis. With increasing temperature, a second, faster decay component (c) emerges. The effective decay time (b) (open boxes) is calculated as a weighted average of the two components (a) and (c).

Heat treatment of the phosphor powder at 473 K in air left the luminescent properties intact, while heat treatment at 673 K caused a color change of the powder from light-yellow to brown and almost entirely destroyed the luminescence, with a remaining EQE around 1%. In SEM, some particles still seem to be intact, but on other particles, structural changes from cubic crystals to rough shapes are detected (figure 7.10). This is in agreement with the decomposition starting at 638 K as reported in literature [89].

The luminescent-lifetime measurements in figure 7.9 show a mono-exponential decay at 220 K with a decay time $\tau = 10.5$ ms. With increasing temperature (from 295–450 K), fitting to a bi-exponential decay is required since a second, faster decay component emerges. The time constant

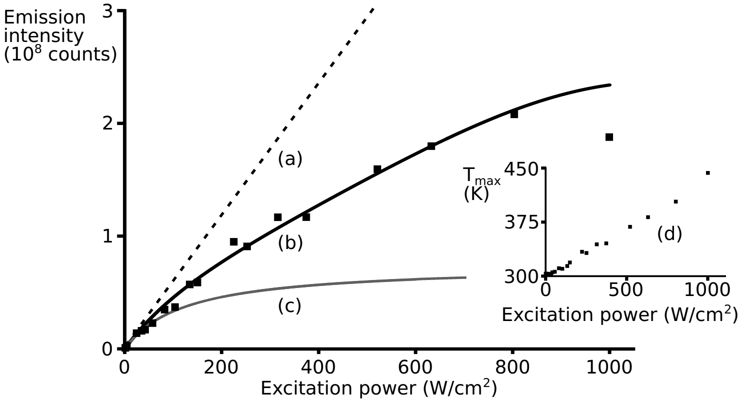

Figure 7.12: Saturation of K_2SiF_6:Mn^{4+} made using a precipitation synthesis at high laser power (445 nm): measurements (dots), simulation of saturation with temperature-dependent decay time (b) (black line), simulation of saturation with fixed decay time (c) (gray) and simulation of linear response (a) (dotted line); and sample temperature at the laser spot (d) (inset).

of the slow component decreases with increasing temperature, reaching $\tau = 8.1$ ms at room temperature and $\tau = 4.9$ ms at 450 K (figure 7.11). This behavior is consistent with a drop in the overall decay time from 15–7 ms at 20–300 K which was reported earlier [38]. Our results show that the drop in decay time continues further with increasing temperature, although thermal quenching only starts above 400 K.

The second, faster component, has a decay time from 0.63–1.0 ms at 295–450 K. The fraction of the total emission assigned to the fast component increases from 2–3% at 295–320 K to 15% at 345 K and 24% at 450 K. An effective decay time is calculated as a weighted average of the two decay components. The majority of the emission, 76% at 450 K, takes place following the slower, spin-forbidden $^2E_g \longrightarrow {}^4A_{2g}$ transition and no extra peaks are observed in the emission spectrum with increasing temperature.

In other phosphor samples, precipitated in a salted ice bath below 0 °C, a bi-exponential decay component is also present at room temperature. The major, slow decay component has a decay time of 7.4–8.0 ms and the faster decay component has a decay time of 1.5 ms.

7.2.4 Saturation behavior

When this work was published [24], the occurrence of light-induced degradation in K_2SiF_6:Mn^{4+} was reported in literature, but at high laser power, both saturation and degradation of the phosphor occur. In another report, the combination of a blue LED and HTHH conditions caused a drop of 23% of the total luminous flux in a wLED with β-SiAlON:Eu^{2+} and K_2SiF_6:Mn^{4+} as phosphors [90]. The saturation behavior, which is the sublinear response of the emission for increasing excitation intensity, of YAG:Ce is rather limited, and intrinsically better than K_2SiF_6:Mn^{4+}, due to the faster (ns) decay of Ce^{3+} emission. The measured emission intensity of this saturation experiment is plotted as a function of excitation power in figure 7.12. The expected linear response of the emission intensity to increasing excitation power, when no saturation occurs, is shown as a dotted line. At about 40 W/cm^2 the sublinear response becomes appreciable, which puts an upper limit on the incident excitation flux.

$$I_{em} = IQE.I_{exc}.A.[N_0/(I_{exc}A.\tau(T) - I_{exc}AP_{ESA}.\tau(T) + N_0)] \qquad (7.3)$$

The emission intensity can be fitted according to equation 7.3. The equation was composed to incorporate all factors contributing to the (saturated) emission intensity. In this equation, IQE is the internal quantum efficiency of the phosphor, I_{exc} is the excitation intensity (increasing with increasing laser power), A is the absorption probability of the phosphor (decreasing with increasing laser power because of the slow decay of Mn^{4+}), N_0 is the number of Mn ions exposed to the laser spot, $\tau(T)$ is the effective decay time, which is a function of the sample temperature and P_{ESA} is the probability of excited-state absorption. The first term ($IQE.I_{exc}.A$) covers the loss of excitation photons due to an internal quantum efficiency less than 100%, specifying how many ions get to the excited state. The fraction considers the number of radiative transitions from the excited state (the effective emission), reduced by the number of excited-state absorptions (causing saturation). The absorption probability A and the probability for excited-state absorption P_{ESA}, were varied to calculate the emission intensity as a function of excitation power. The parameters were optimized using least-squares minimization.

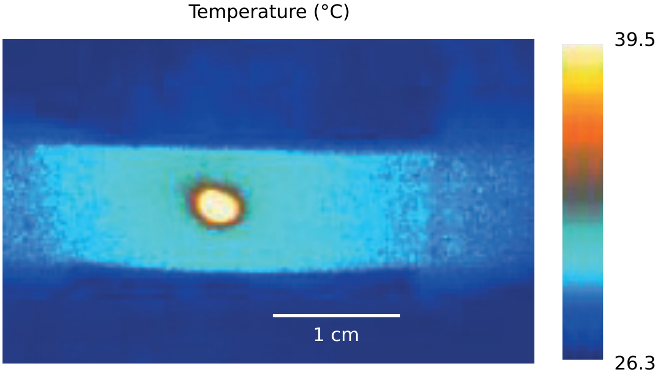

Figure 7.13: Thermographic image of the phosphor sample saturated with the laser spot at 63% of the full laser intensity.

The rise in temperature of the phosphor powder with increasing laser intensities was estimated using an IR camera. At low laser power, the sample temperature is 300 K, close to the ambient temperature. The last data point (at 440 K) of the emission intensity is excluded from the fit, as thermal quenching takes place and some irreversible degradation sets in.

The temperature dependency of the effective decay time is specifically included in the simulation, because an obvious temperature increase is caused by the high laser flux, due to nonradiative transitions and Stokes losses following the absorption of blue photons. The temperature increase of the sample around the laser spot is visible on the thermographic image in figure 7.13. The effect of this is visible when the simulated emission intensity with a fixed decay time is compared to the data points, as found at room temperature. Here, saturation sets in earlier, because less Mn ions are available for excitation due to the longer lifetime of the emitting state. With increasing excitation power, the absorption probability decreases, because a large fraction of the Mn ions are in the excited state, making less ions available from excitation from the ground state (ground-state depletion). The same process occurs at high light fluxes in phosphors doped with Mn^{2+} [91]. In this situation, the excited ions will eventually give light emission, but no further absorption of blue photons is possible.

Another saturation mechanism is possible, when an ion in the excited state absorbs another blue photon, followed by a nonradiative transition to the ground state [92]. This excited-state absorption results in no emission from two absorbed blue photons. The probability for excited-state absorption was varied in the simulation, but its contribution turned out to be zero, so the saturation behavior of K_2SiF_6:Mn^{4+} can be adequately explained without including excited-state absorption [24]. However, pump–probe absorption spectroscopy should be performed to assess the extent of excited-state absorption in this phosphor.

7.3 Discussion

The excitation and emission spectrum of the phosphor powders produced by precipitation synthesis are equal to those of the phosphors produced by etching (figure 7.4). Nevertheless, the obtained quantum efficiency is lower, reaching an IQE of 46% and an EQE of only 12% due to an absorption of 25%, compared to an EQE of 46% for etching synthesis. Somewhat higher values are obtained due to improved synthesis conditions, reaching to an IQE of 51% and an EQE of 12% when N_2 was bubbled through. However, the increase in quantum efficiency is nearly unnoticable and less Mn is incorporated according to the EDX measurements so working in an environment that is low in oxygen only has a limited influence. Further improvement of the IQE is realistic since values up to 69% and 88% have been reached for the etching synthesis (chapter 6) and coprecipitation synthesis (chapter 10) respectively. One of the reasons for the lower IQE could be heterogeneous outcoupling of emission light in the truncated corners of the cubic phosphor particles. On the other hand, an improved IQE is expected in more perfect crystal structures, since defects in the crystal structure can increase the nonradiative transition probabilities.

The thermal quenching behavior of K_2SiF_6:Mn^{4+} is very promising for LED applications with a stable emission up to 400 K and a quenching temperature of 430 K. Unfortunately, a bi-exponential decay emerges at increased temperatures. Crystal field calculations by Jonas Joos suggested that a tetragonal compression of the coordination polyhedron of Mn^{4+} can be responsible for this, when a certain fraction of the Mn^{4+} dopants are incorporated in close vicinity of another point defect. Defects present after the precipitation synthesis can cause the bi-exponential decay that is found with increasing temperatures.

Saturation that occurs at high excitation power cannot be fully relieved by the decreasing decay time at higher temperatures, but the decrease in absorption probability is less severe compared to the case of a fixed decay time due to a decrease in decay time down to 2.3 ms at 800 W/cm^2.

The sublinear response to the emission intensity starts to appear at an excitation power of 40 W/cm^2, where 11% of the available Mn ions are in the excited state.

These results show that the studied phosphor might be useful for low-power white LEDs, but not for high-power applications, where the long decay time of the phosphor leads to saturation effects. For the latter application, a remote phosphor approach can be used: by increasing the distance between the exciting LED and the phosphor, both the thermal load and the optical load on the phosphor are strongly reduced. This approach will be further discussed in chapter 13.

7.4 Conclusion

$K_2SiF_6:Mn^{4+}$ shows red line emission around 630 nm with a main excitation band around 455 nm, ideal for blue LED excitation. From the precipitation synthesis, an IQE of 46% is found, which can be somewhat improved to 51% by bubbling N_2 through the reaction solution, but the incorporated Mn concentration is lower in this case. A K_2SiF_6 coating can improve the internal quantum efficiency, while a SiO_2 coating decreases the internal quantum efficiency of the phosphor powders.

The incorporation of Mn into the host lattice still imposes difficulties. The dopant concentration is 1.5% of the Si ions, while the concentration is higher in the precursor solution, leading to a limited incorporation of Mn in the phosphor host during the synthesis. This effect of concentration quenching influenced by synthesis properties was also found by General Electric (GE) [93]. An increased Mn concentration in the precursor solution does not lead to an increase in dopant concentration. Since the phosphor spontaneously precipitates from the synthesis solution, controlling the dopant concentration during the synthesis is difficult.

At low temperatures (220 K), a mono-exponential decay is found, while a bi-exponential decay emerges with increasing temperature from 295–450 K. The decay time continues to decrease with increasing temperature up to 450 K, although thermal quenching only starts above 400 K. High incident fluxes cause both saturation of the emission and degradation of $K_2SiF_6:Mn^{4+}$. Above 40 W/cm^2, there is a sublinear response of the emission intensity to the excitation power, caused by ground-state depletion. Saturation cannot be fully relieved by the decreasing decay time at higher temperatures.

At the microscopic level, combined SEM-EDX-CL maps show a preferential location of the light output on certain edges of the cubic particles. Since total internal reflection plays an important role in the light outcoupling behavior of symmetrically shaped particles, it is within expectations that higher emission intensities are found at distortions of the cubic shape. Besides cubic particles, different types of truncated particle shapes are found.

8

K_2MnF_6 as a phosphor precursor

It is possible to stabilize Mn^{4+} in K_2SiF_6, as has been shown in chapter 6 on etching and in chapter 7 on precipitation synthesis, but the obtained dopant concentration and quantum efficiencies are relatively low. Mn has many possible oxidation states, of which 0, +2, +4 and +7 are the most common ones. In the K_2SiF_6:Mn^{4+} phosphor synthesis, a reduction of Mn^{7+} to Mn^{4+}, starting from $KMnO_4$ is performed. In a two-step synthesis, the reduction reaction is separated from the phosphor precipitation. Through this procedure, the purity of the phosphor synthesis can be increased, since the fluorine coordination of Mn can take place in a fluorine rich environment without preliminary precipitation as an oxide. As will be discussed in this chapter, the long-term stability of Mn^{4+} in fluorides is limited. K_2MnF_6 is not commercially available, so it has to be produced in-house to be used in a two-step phosphor synthesis. In this chapter, the delicate synthesis of K_2MnF_6, its properties and the stability issues will be discussed.

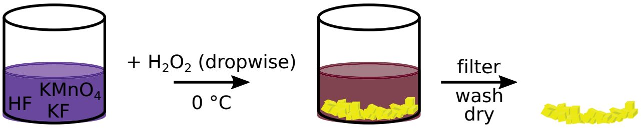

Figure 8.1: Schematic illustration of the precipitation synthesis of K_2MnF_6.

8.1 Synthesis

K_2MnF_6 is prepared according to the method of Bode and Bandte [94]. It crystallizes following a redox reaction in a solution of KHF_2 and $KMnO_4$ in 40% HF, which is illustrated in figure 8.1. For this purpose, 36 g KF (99.0%, Alfa Aesar) and 2 g $KMnO_4$ (98%, Alfa Aesar) were dissolved in 150 mL of 40% HF (Sigma-Aldrich). A 48-fold excess of KF is present as a potassium source but reducing the KF excess decreased the synthesis yield. The solution is magnetically stirred and cooled in an ice bath. To this solution, 2 mL H_2O_2 (Sigma-Aldrich, 35%) is added dropwise, with a new drop only added when the O_2 formation has decreased. Meanwhile, the dark purple solution gradually turns light-brown, over light-purple and dark brown, indicating the reduction of Mn^{7+} to Mn^{4+} and a golden-yellow precipitate forms. The addition rate of H_2O_2 has to be controlled to prevent both excess O_2 formation and excess reduction of Mn. The reaction solution is cooled to improve the precipitation of K_2MnF_6 and to slow down the redox reaction.

It is crucial to stop the reaction before excess Mn reduction, to Mn^{3+}, takes over. Although the $[MnF_6]^{2-}$ complex exists in aqueous solution, even in HF solution it can slowly decompose to dissolved Mn^{3+} or precipitated $MnO_2 \cdot xH_2O$ [95]. When no dark purple $KMnO_4$ is present any more and the solution is light-brown, the stirring is stopped. To obtain the precipitate, the solution is decanted, filtrated in a plastic funnel with filter paper, washed with 40% HF and acetone (99.5%, Fiers) and dried overnight in air. The decantation is crucial to stop the reaction in time, since exposure of the precipitate to the reaction solution can cause redissolving and further reduction of the precipitate. Washing the precipitate with HF reduces the presence of KHF_2 as a byproduct, while washing with acetone removes any HF residues. Washing with water is to be avoided, since K_2MnF_6 is hygroscopic and forms a black manganese oxide in contact with water.

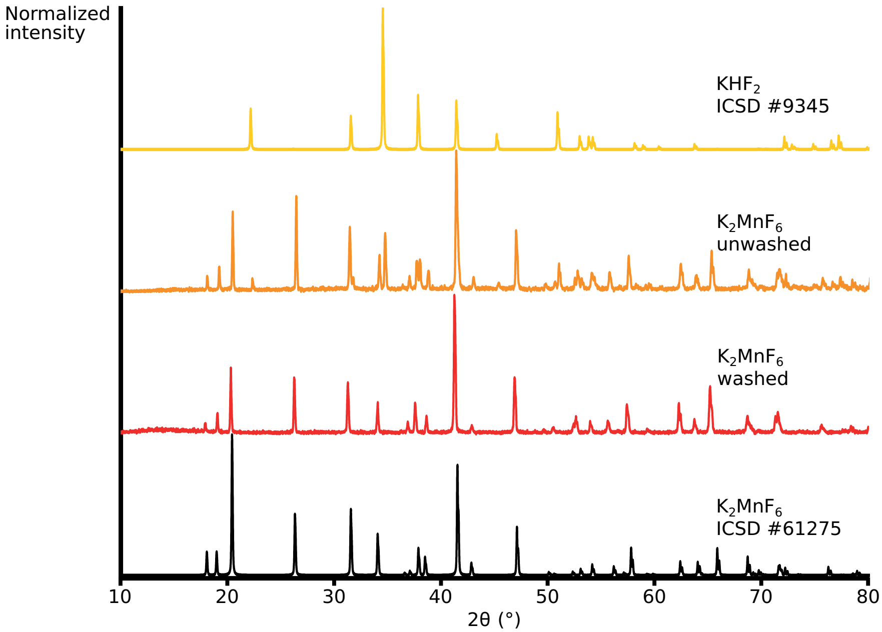

Figure 8.2: XRD patterns of K_2MnF_6 before (orange) and after washing with HF (red), compared with the reference patterns of KHF_2 (yellow) and the hexagonal phase of K_2MnF_6 (black).

The reduction reaction of $KMnO_4$ to K_2MnF_6 is sped up by the addition of H_2O_2, which is however not necessary for the formation of K_2MnF_6. In absence of H_2O_2, K_2MnF_6 is formed according to equation 8.1 [38], while in presence of H_2O_2, the reaction is given by equation 8.2 [96].

$$\begin{aligned}4\,KMnO_4\,(aq) + 4\,KHF_2\,(aq) + 16\,HF\,(aq) &\longrightarrow \\ 4\,K_2MnF_6\,(s) + 10\,H_2O\,(l) + 3\,O_2\,(g)\end{aligned} \tag{8.1}$$

$$\begin{aligned}2\,KMnO_4\,(aq) + 2\,KF\,(aq) + 10\,HF\,(aq) + 3\,H_2O_2\,(aq) &\longrightarrow \\ 2\,K_2MnF_6\,(s) + 8\,H_2O\,(l) + 3\,O_2\,(g)\end{aligned} \tag{8.2}$$

8.2 Results

The yellow K_2MnF_6 was formed from the solution synthesis with a yield of 32% of the initial amount of Mn. Considering the excess of KF present, the synthesis yield is fairly low, only 0.7% of the initial K concentration.

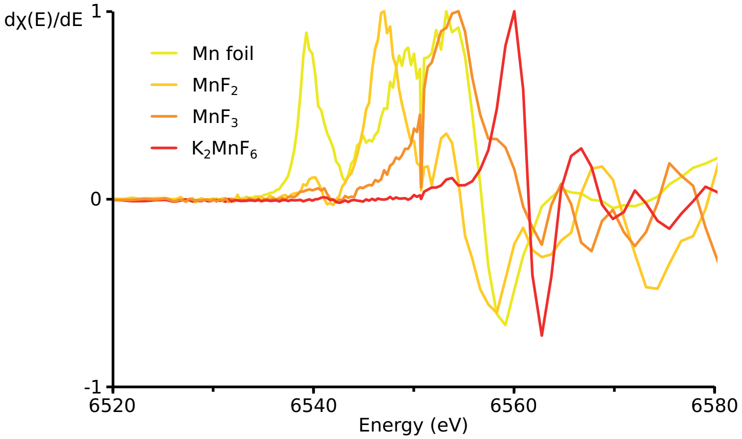

Figure 8.3: First derivative of XANES measurements of Mn foil (yellow), MnF_2 (ocher), MnF_3 (orange) and K_2MnF_6 (red).

From XRD measurements, it was found that KHF_2 initially showed up as a contaminant (figure 8.2 - unwashed K_2MnF_6). Using a lower (1:20) excess of KF reduced the presence of KHF_2, but did not fully remove it. Moreover, a lower synthesis yield was obtained with a reduced KF concentration. A post-synthesis washing procedure with HF was able to remove KHF_2 contamination. When this was handled, XRD measurements showed a pure hexagonal phase of K_2MnF_6 (figure 8.2 - washed K_2MnF_6).

XANES measurements by Katleen Korthout showed that in the K_2MnF_6 powder, 79% of the Mn was present as Mn^{4+}, while the other 21% was present as Mn^{3+}. The derivative curves in figure 8.3 show a contribution of the Mn^{3+} in the small band at 6554 eV while the main contribution of the spectrum comes from the Mn^{4+} band at 6560 eV. Diffuse reflectance spectroscopy (DRS) measurements performed by Reinert Verstraete (figure 8.4) also showed presence of some Mn^{3+} absorption besides the Mn^{4+} absorption. The 450 nm absorption band corresponding to Mn^{4+} in K_2MnF_6 is accompanied by an extra absorption at the longer wavelength side which is superposed on the sharp Mn^{4+} absorption lines around 620 nm. Comparison with the MnF_3 spectrum suggests that this broad absorption might be due to a fraction of the Mn ions that are in the 3+ valence state. This Mn^{3+} contaminant can be present as an amorphous phase, which does not show up in XRD but can influence the absorption

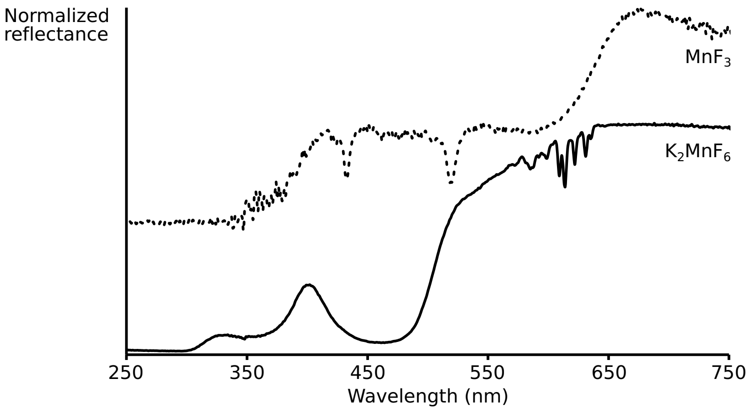

Figure 8.4: Normalized reflectance from diffuse reflectance measurements of K_2MnF_6 (full line) and the Mn^{3+} reference compound MnF_3 (dotted line), shifted for clarity.

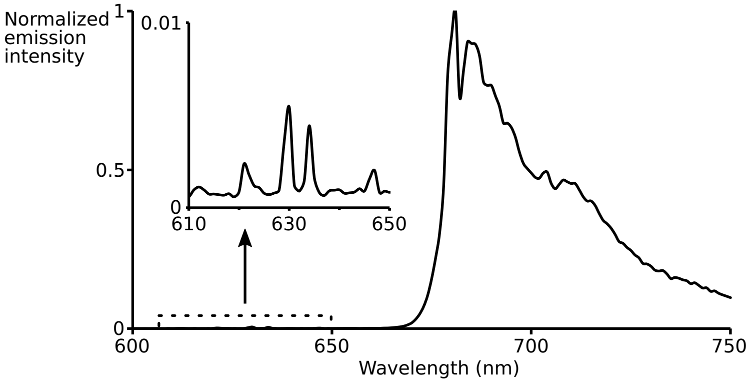

Figure 8.5: Normalized photoluminescence emission spectrum of K_2MnF_6 (excitation at 450 nm), measured at 75 K. Inset: blow-up of the 610–650 nm wavelength range.

of blue light. Since the $[MnF_6]^{2-}$ complex is not very stable, reduction to Mn^{3+} will reduce the presence of Mn^{4+} in the further phosphor synthesis, since no further oxidation step is included in the synthesis processes.

In photoluminescence measurements that were performed by Reinert Verstraete, a broad deep red emission band is found in K_2MnF_6 around 700 nm at 10–120 K upon excitation at 450 nm (figure 8.5). In literature, this band was attributed to the $^4T_{1g} \rightarrow {}^6A_{1g}$ transition of an octahedrally coordinated Mn^{2+} impurity in $KMnF_3$ [97] or to hydrolysis products of the $[MnF_6]^{2-}$ ion [98]. Since no Mn^{2+} was found in the XANES measurements, the presence of hydrolysis products like $[MnF_5(OH)]^{2-}$, $[MnF_4(OH)_2]^{2-}$ or the corresponding aqua-complexes, is more likely. The shape and location of the emission band are similar to that of Mn^{4+} in $LiTiO_3$:K^+,Mn^{4+}, confirming the (partial) oxygen coordination of the emitting center [99]. The decay time of the broad emission band is 0.23 ms at 90 K and shortened to 0.02 ms at 120 K. Other reports show slightly lower values of 0.20–0.005 ms in the same temperature range for K_2MnF_6 [38].

The broad band emission quenches above 120 K, while red peak emission is visible up to 390 K, with the maximum emission intensity at 630 nm. Although this emission is not thermally quenched, its intensity is rather low due to concentration quenching. The decay times of the emission around 630 nm are 8.88–3.51 ms at 240–390 K, which is slower than the broad band emission, but similar to K_2SiF_6:Mn^{4+} phosphor emission. Although the nature of the $3d^3$–$3d^3$ transition, emission from the spin-forbidden $^2E_g \rightarrow {}^4A_{2g}$ is the same as in K_2SiF_6:Mn^{4+} phosphors, the emission intensity of K_2MnF_6 is low. The yellow powder does absorb 94% of the blue light at 450 nm, but the quantum efficiency was too low to be measurable.

In SEM-EDX images, the K_2MnF_6 particles show to be 2–20 µm octahedrons with a homogeneous elemental distribution (figure 8.6). Si is detected by EDX, but only for 0.06 atomic percent (at%), which can be neglected compared to the 9.15 at% of Mn that is detected. Since rather big particles of 20 µm are also present, a solution based synthesis might be favored for incorporation of the $[MnF_6]^{2-}$ complex ion into the K_2SiF_6 host. On the other hand, redissolving K_2MnF_6 might degrade the $[MnF_6]^{2-}$ complex ion, since its stability is limited even in HF solution.

8.3 Stability

During phosphor synthesis, K_2MnF_6 is subjected to elevated temperatures in a HF environment. To evaluate the influence hereof, the temperature-induced degradation of a solution of K_2MnF_6 in HF was studied. K_2MnF_6 is dissolved in 40% HF resulting in a clear yellow solution. The solution is heated in a hot water bath in small temperature increments. When heating the water bath to 41 °C, the color of the solution changes from yellow to orange (figure 8.7). Precipitation of the orange solution with acetone as a nonsolvent results in a yellow precipitate that is light-brown when it is dried. An XRD measurement shows that besides K_2MnF_6 and KHF_2 that were already present in the starting material, $KMnF_4 \cdot H_2O$ is

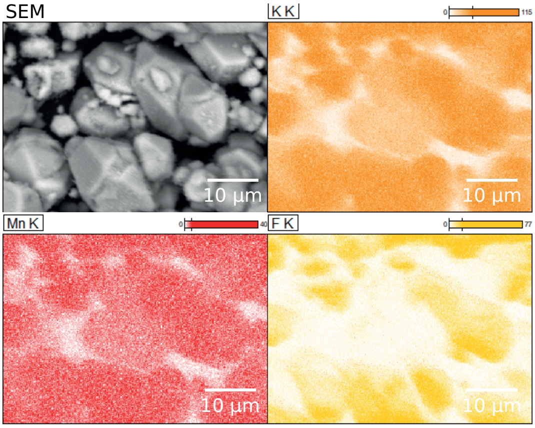

Figure 8.6: SEM image and EDX maps of K_2MnF_6.

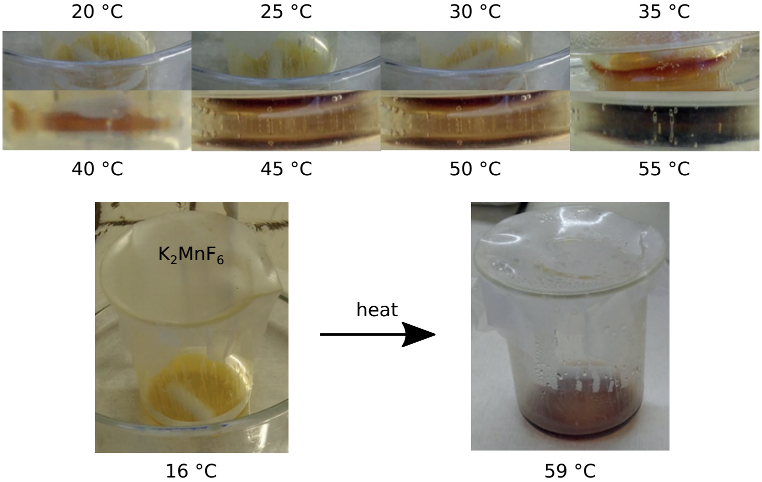

Figure 8.7: Degradation of K_2MnF_6 in a HF solution with increasing temperature of the hot water bath.

present in the precipitate. When the K_2MnF_6 solution is heated to even higher temperatures, the fraction of $KMnF_4 \cdot H_2O$ increases. When the hot water bath is slowly heated to 59 °C, the yellow solution has turned into dark brown-red (figure 8.7). An XRD measurement shows that the pink-brown powder precipitated from this solution consists mostly of $KMnF_4 \cdot H_2O$ together with some remaining K_2MnF_6 (figure 8.8).

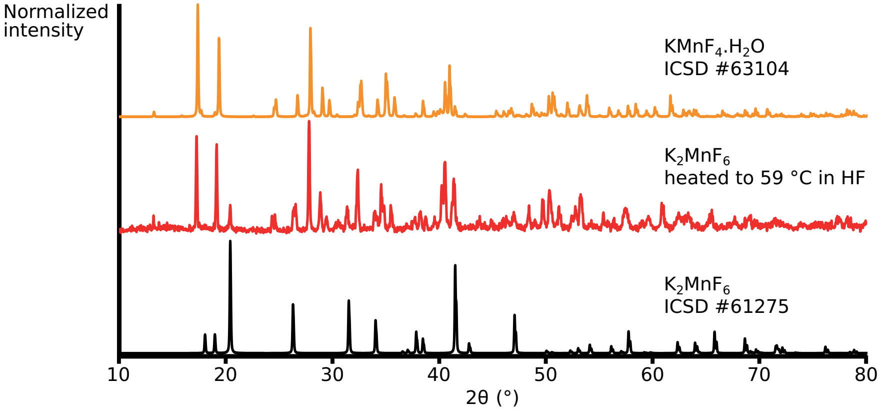

Figure 8.8: XRD spectrum of K_2MnF_6 after heating to 59 °C in a HF solution (red) compared with the reference spectra of K_2MnF_6 (black) and $KMnF_4 \cdot H_2O$ (orange).

Not only elevated temperature causes degradation of K_2MnF_6. When the yellow powder is stored in glass vials, over time a dark brown powder forms at the surface and the glass vial turns opaque. A SEM-EDX comparison of the brown and yellow particles shows degradation of the particle surface. The yellow powder consists of regular particles with surfaces without visible defects. The brown powder shows more small particles and the particles are less regular and the surfaces are less smooth. Using EDX, a large difference in Si and Mn concentration can be found. In the yellow K_2MnF_6 powder, only 0.1 at% of Si is detected and 8.9 at% of Mn is detected. In the degraded brown powder, 4.3 at% of Si is detected and 6.7 at% of Mn is detected. No Si was present during the synthesis, but the brown powder mainly forms around the walls of the glass recipient. Therefore, this degradation process is expected to be a reaction with the glass recipient in which the powder is stored. The lower detected Mn concentration is caused by the incorporation of Si from the glass in the powder, which reduces the relative presence of Mn. No secondary phase was found in the black and yellow powder using XRD measurements, so the contamination is suspected to be an amorphous manganese oxide or silicon oxide phase. The opaque glass is suspected to be caused by an etching reaction of the glass by HF residues. Storage of the yellow K_2MnF_6 in polypropylene vials prevents any visible degradation of the yellow powder.

More research on the degradation of K_2MnF_6 was done by Reinert Verstraete in the context of his Ph.D. work. Using in situ XRD measurements in air, argon and N_2, from room temperature up to 600 K several phases were identified that are involved in the degradation of K_2MnF_6. Hydration and hydrolysis reactions during the synthesis or in contact with water vapor can result in compounds such as $KMnF_4 \cdot H_2O$ and $KMnF_3/KF \cdot MnF_2$. The results of this stability study were published in [99].

8.4 Conclusion

Although the synthesis of K_2MnF_6 has a critical timing and a low yield, it is possible to synthesize enough K_2MnF_6 to use in a two-step synthesis of K_2SiF_6:Mn^{4+}. The formation of KHF_2 during the synthesis was inevitable and it is crucial to remove this by washing with HF. Although the XRD shows that a pure K_2MnF_6 phase is formed, amorphous Mn^{3+} is still present according to EXAFS and DRS measurements. The presence of Mn^{3+} can reduce the Mn^{4+} incorporation in K_2SiF_6:Mn^{4+} phosphor synthesis. The long-term stability of K_2MnF_6 remains an issue, but when the right washing procedure is applied and the powder is stored in polypropylene vials, the in-house produced K_2MnF_6 is stable enough and suitable to use in further phosphor synthesis.

9

Cocrystallization synthesis of K_2SiF_6:Mn^{4+}

The first synthesis of K_2SiF_6:Mn^{4+} was described by Paulusz in 1973 [43]. K_2SiF_6:Mn^{4+} was prepared by recrystallizing mixtures of K_2MnF_6 and the host-lattice material K_2SiF_6. In this chapter, the cocrystallization process will be discussed and the resulting phosphors will be evaluated. The used terminology of two-step synthesis methods of K_2SiF_6:Mn^{4+} is somewhat ambiguous. In literature, cation exchange is widely used for any synthesis involving an exchange of the host cation and Mn from K_2MnF_6 or even $KMnO_4$, which can be a cocrystallization or a coprecipitation synthesis.

In this work, a pure *cation-exchange* reaction is considered to take place in an undissolved fraction of K_2SiF_6, as was proven by Zhu et al. in a synthesis of K_2TiF_6:Mn^{4+} [100]. A *cocrystallization* synthesis of K_2SiF_6:Mn^{4+}, the subject of this chapter, includes all HF-solution based synthesis methods employing K_2SiF_6 and K_2MnF_6, independent of the amount of HF involved. *Coprecipitation* syntheses involve the formation of the host material, as will be discussed in chapter 10, in contrast to cocrystallization reactions where the host is already available. Although promising for

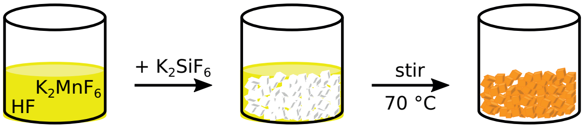

Figure 9.1: Schematic illustration of the cocrystallization synthesis where K_2SiF_6:Mn^{4+} is formed from K_2MnF_6 and K_2SiF_6 in a slurry.

K_2TiF_6:Mn^{4+}, no cation-exchange reactions have yet been reported for K_2SiF_6:Mn^{4+}. In this chapter, both cocrystallization in solution and cation-exchange reactions will be discussed.

9.1 Method

In literature, a cocrystallization synthesis of K_2SiF_6:Mn^{4+} is only reported twice. Paulusz recrystallized the fluorides from a solution of 40% HF, without specifying the concentrations [43]. Setlur et al. dissolved K_2SiF_6 and K_2MnF_6 in 70% HF with a Mn^{4+} concentration of 3–8 % [101]. In this cocrystallization synthesis, K_2MnF_6 is dissolved in 40% HF (Sigma-Aldrich) to concentration of 0.34 M. The solubility of K_2MnF_6 in 40% HF has not been reported in literature, but enough HF was added to form a clear yellow solution. To this solution, K_2SiF_6 (99%, Fluka) was added to a concentration of 12.4 M. When K_2MnF_6 is incorporated homogeneously, a dopant concentration of 2.7 % can be expected based on the used precursor concentrations. Since the solubility of K_2SiF_6 in 40% (22.6 M) HF is 0.087 M at room temperature [102], a large part of the added K_2SiF_6 is not dissolved and a slurry is formed. This slurry is heated in a hot water bath at 70 °C evaporating the 40% HF solvent overnight (figure 9.1).

Meanwhile, a cation exchange is supposed to take place, replacing some of the Si^{4+} ions in K_2SiF_6 by Mn^{4+} to form the doped K_2SiF_6:Mn^{4+}. Even though the solubility of K_2SiF_6 can increase with increasing temperature, the excess is large enough to never fully dissolve, so a cation-exchange reaction is expected in the undissolved fraction. The slurry was magnetically stirred during the evaporating and the stirring was stopped when all HF had evaporated. The obtained powders were washed with ethanol (96%, Fiers) and dried in air. Variations in the synthesis were introduced by applying ultrasound to the hot water bath instead of stirring and by lowering the temperature of the hot water bath to 60 °C.

To investigate the influence of the addition rate of K_2MnF_6 to K_2SiF_6 in the cocrystallization synthesis, the addition sequence was reversed. For this, K_2SiF_6 was mixed with a small volume of HF until a slurry was formed. The slurry is heated in a hot water bath to 70 °C. When this temperature is reached, a solution of K_2MnF_6 in HF is added dropwise while the slurry is stirred. After the first drops of the yellow solution are added, the slurry turns yellow. When more K_2MnF_6 is added, the slurry turns dark red. The slurry is evaporated while being stirred in the hot water bath, resulting in a pink phosphor material.

In an attempt to increase the dopant incorporation, lower (3.0 M) K_2SiF_6 concentrations were used in the synthesis, dissolving a larger fraction of K_2SiF_6. Here, a 0.20 mM K_2MnF_6 solution is dropwise added to a slurry of K_2SiF_6 in HF in a hot water bath at 70 °C. During the addition of K_2MnF_6, the white slurry first turns yellow and turns dark red afterwards. The mixed K_2MnF_6-K_2SiF_6 slurry is evaporated overnight in the hot water bath at 70 °C.

To reduce the surface effects of incorporated Mn ions, an undoped K_2SiF_6 coating was applied using a precipitation coating method. In the coating process, a 0.09 M saturated solution of K_2SiF_6 in HF was added to the phosphor powder, after which the mixture was evaporated overnight in a hot water bath at 70 °C. The coating thickness was varied by varying the phosphor to K_2SiF_6 ratio.

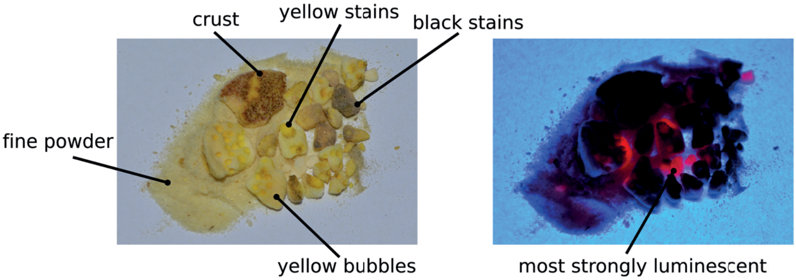

Figure 9.2: Heterogeneous K_2SiF_6:Mn^{4+} powder made using a cocrystallization synthesis, in daylight (left) and under 365 nm UV illumination (right).

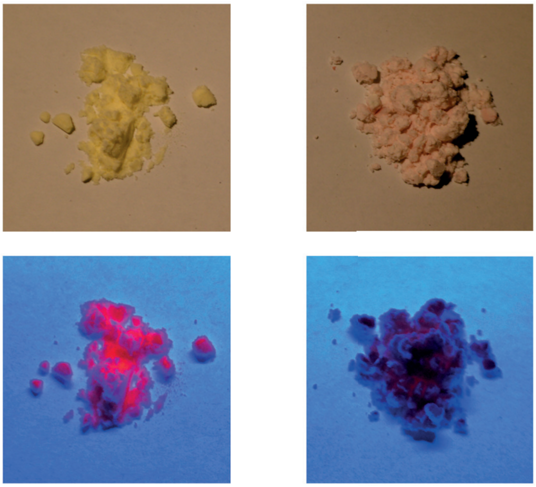

Figure 9.3: Yellow-orange (left) and pink (right) K_2SiF_6:Mn^{4+} from a cocrystallization synthesis in day light (top) and under UV illumination at 365 nm (bottom).

9.2 Results

Despite the stirring, the solids that remain after evaporation are very inhomogeneous (figure 9.2). Due to the very limited amount of liquid present, the magnetic stirring bar is not able to homogenize the mixture. When evaporation is performed in small batches ($<$ 5 mL), a black stained or dark red crust forms at the top of the beaker, which shows little luminescence under UV light. When the crust is removed, the underlying material is a pink or light-yellow condensed powder with lumps. The lumps show discolorations formed by bubbles during the evaporation process. Under UV light, a lower luminescence intensity is observed in the bubbles, possibly due to an inhomogeneous Mn distribution. Within the powder, bright yellow particles could be present as well as yellow-stained lumps and chunks that show luminescence under a UV lamp on one side and no luminescence on another side.

Switching the mixing order K_2SiF_6 and K_2MnF_6 resulted in more different textures in the obtained phosphor powder. Using ultrasound to homogenize the reaction mixture instead of stirring did not improve the homogeneity of the resulting powder and the bubble spots are still present. When the evaporation temperature was lowered from 70 °C to 60 °C, a ho-

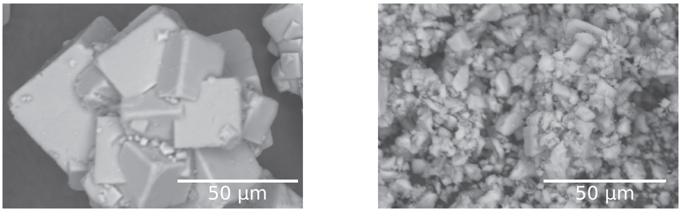

Figure 9.4: SEM images of K_2SiF_6 before (left) and after (right) ball milling in ethanol for 1 h at 300 rpm.

mogeneous light-pink powder formed with a dark pink crust (figure 9.3). In a large volume (11 mL) synthesis, homogeneous light-yellow powders could be obtained, with some big pink lumps in the crust.

9.2.1 Structural

Commercially available K_2SiF_6 is used for the cocrystallization synthesis. Before synthesis, the particles are cubic, showing fusion of cubic structures and having a particle size of 50–200 µm. After the synthesis, the particle size of the phosphor particles is typically 25–50 µm, so during the synthesis, the large K_2SiF_6 clusters are broken down while K_2MnF_6 is incorporated. To improve the dopant incorporation, K_2SiF_6 was ball-milled

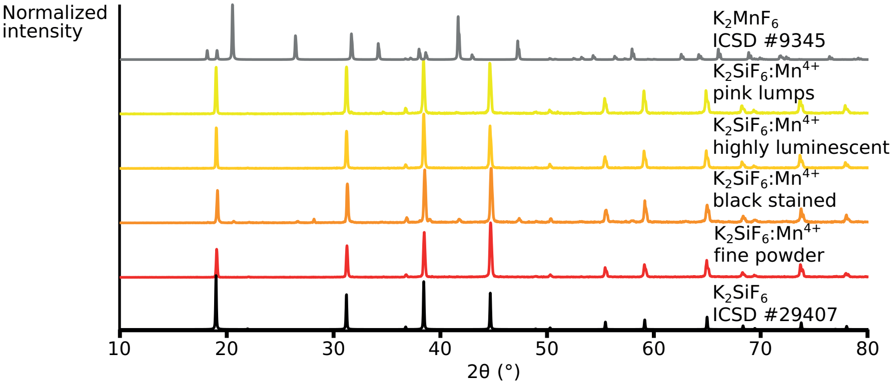

Figure 9.5: XRD patterns of several fractions from one cocrystallization synthesis batch (red-orange-ocher-yellow) with an intended dopant concentration of 2.6%, compared with reference patterns of K_2SiF_6 and K_2MnF_6 (black-gray).

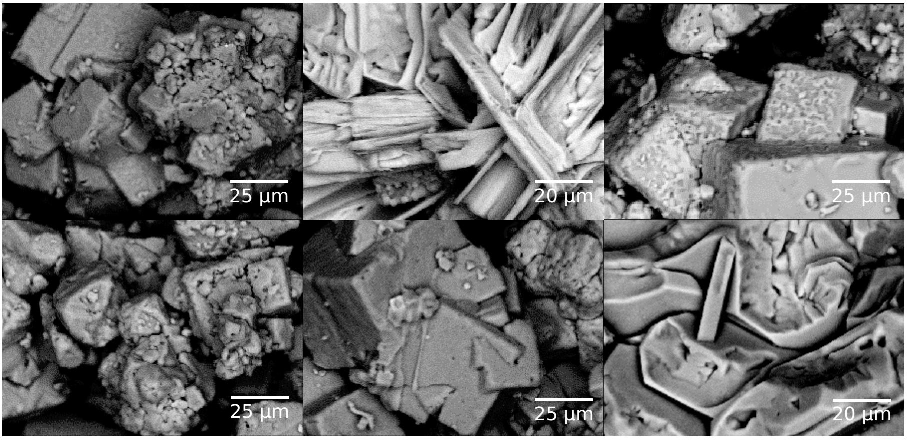

Figure 9.6: SEM images of several fractions from the same cocrystallization synthesis batch. Top, from left to right: fine powder, black stained crust, most strongly luminescent particles. Bottom, from left to right: yellow lumps, pink lumps, black-spotted lumps.

prior to the cocrystallization to obtain smaller particles. After milling, the K_2SiF_6 particles are irregularly shaped and have sizes between 2–20 µm (figure 9.4).

Several fractions from one synthesis batch, separated according to body color and luminescent intensity under a 365 nm UV lamp, were evaluated using XRD measurements (figure 9.5). In the fine powder found under the crust, single phase cubic K_2SiF_6 is found. In the black stained crust, both starting materials K_2SiF_6 and K_2MnF_6 are identified, leaving some minor unidentified peaks. The black stains cannot be explained with the crystalline phases found, since K_2SiF_6 has a white body color and K_2MnF_6 has a yellow body color, but the black stains can possibly be amorphous MnO_2. The lumps that were selected under the UV lamp for high luminescent intensity, was single phase K_2SiF_6. In the pink lumps, some small peaks of K_2MnF_6 could be identified besides K_2SiF_6. Hydrates such as $K_2MnF_5 \cdot H_2O$ could explain the pink body color, but those were not identified from the XRD pattern.

In SEM pictures (figure 9.6), some differences between the fractions can be seen. The fine powder shows some inhomogenity in elemental distribution, showing lighter particles that are rich in Mn, which could possibly be unreacted K_2MnF_6. The crust forms a more fibre-like structure instead of clusters of cubic crystals. With EDX, the presence of Si mainly

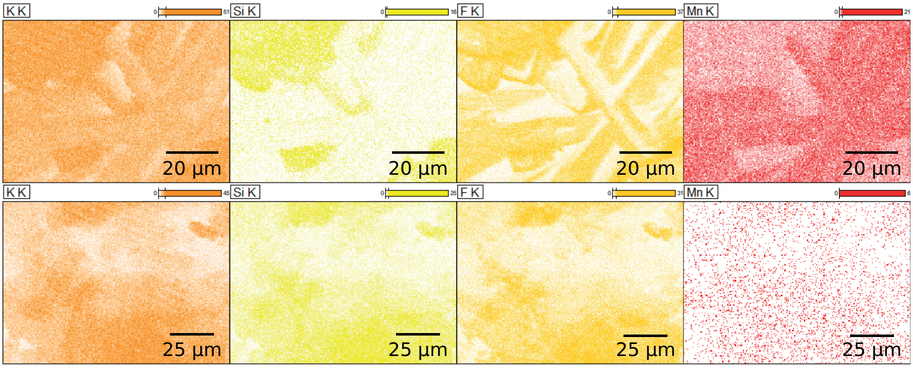

Figure 9.7: EDX maps of two fractions from the same cocrystallization synthesis batch, the black stained crust (top) and the most strongly luminescent particles (bottom). SEM images of the corresponding fractions are given in figure 9.6.

shows up in the phosphor-like particle clusters (figure 9.7, bottom), and less in the fibre-like structures (figure 9.7, top). The fibre-like structures are rich in K, Mn and F and could possibly be a hydrated potassium magnesium fluoride such as $KMnF_4 \cdot H_2O$, although this phase could not be identified in the XRD pattern. The surface of the most strongly luminescent particles is not as smooth as that of the fine powder, but the elemental distribution is homogeneous. The smaller yellow lumps look similar to the most strongly luminescent phase in the SEM images. The pink lumps show a smoother surface and homogeneous elemental distribution. In the lumps with black spots, the particles seem to been fused together. Some shading effect occurred in the EDX measurement of this sample, but the elemental distribution was homogeneous. From SEM-EDX, the dopant concentration shows to be 4 % in the fine powder and only 1.4 % in the most strongly luminescent phase. The pink lumps show weak luminescence with a similar dopant concentration, while a high Mn concentration and a low Si signal is found in the black lumps of the crust.

9.2.2 Luminescence

Despite the heterogeneity of the obtained powders, the red line emission around 630 nm was found in most powders upon excitation at 450 nm. No other emission lines were found, but some powders made in a cocrystallization synthesis showed no luminescence. The obtained quantum efficiencies are divergent, with an IQE of 4.7–67 %, an EQE of 2.4–26 % and

Table 9.1: Quantum efficiency and absorption values of different fractions of a single cocrystallization synthesis batch.

Fraction	IQE	EQE	absorption
fine powder	31%	16%	0.50
most strongly luminescent lumps	52%	29%	0.55
pink lumps	25%	15%	0.59

an absorption of 12–56 %. When the most strongly luminescent lumps were selected under the UV lamp, an IQE of 67% and an EQE of 29% were found compared to an IQE of 23% and an EQE of 13% for the light-yellow powder obtained from the same synthesis.

Switching the mixing order during the synthesis did not improve the homogeneity of the formed powder. When the most strongly luminescent lumps were selected under the UV lamp, an IQE of 52% and an EQE of 29% were found compared to an IQE of 31% and an EQE of 16% for the light-yellow powder obtained from the same synthesis (table 9.1). The particles with bright yellow spots showed a slightly lower quantum efficiency, with an IQE of 25% and an EQE of 15%. The yellow spots can be K_2MnF_6 residues that reduce the EQE by causing a strong absorption with very limited emission, as was seen in chapter 8. Reducing the temperature of the hot water bath to 60 °C resulted in light-pink powder that showed an absorption of 31% upon excitation at 450 nm, but no visible red emission was found.

With an IQE of 22% and an EQE of 11%, pink lumps selected from a heterogeneous phosphor sample had a lower quantum efficiency compared to the light-yellow powder obtained from the same sample, that reached an IQE of 55% and an EQE of 25%. The crust with black stains performed even worse with an IQE of 10% and an EQE of 7%. In general, low quantum efficiencies were found for the yellow and pink powders found under the dark crust. IQE values of 10–48 % and EQE values of 4–21 % were mostly obtained. Somewhat higher values were obtained with optimized synthesis conditions, with IQE values of 24–67 % and EQE values of 11–26 %.

From the dropwise cocrystallization synthesis, homogeneous light-pink powders were obtained. Increasing the volume of the synthesis improved the homogeneity of the obtained powders, reducing the surface defects during the evaporation phase. On the other hand, the discoloration from

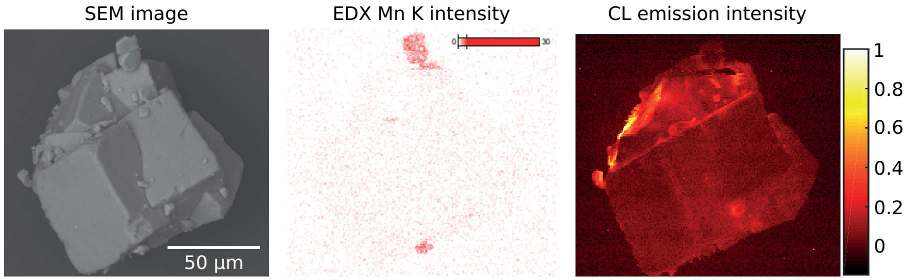

Figure 9.8: SEM image, EDX map of Mn and CL map of a phosphor particle synthesized using cocrystallization synthesis.

yellow to red during the synthesis, seemed to be irreversible and induced pink phosphor powders. The obtained quantum efficiencies were lower compared to the smaller volume synthesis, with IQE values of 16–77 % and an EQE of 12 %.

In the SEM-EDX-CL map in figure 9.8, a 100 µm particle of fused cubes shows a higher emission intensity from one side of the particle. A homogeneous dopant distribution is found, apart from two smaller (10 µm) particles fused to the bigger particle that are rich in Mn. Although some Si is also detected in these fused particles, these could be remaining K_2MnF_6 particles. The Mn rich spots do not coincide with the higher emission intensity, which can confirm the presence of K_2MnF_6 which has a very low emission intensity.

From the QE values in table 9.2, it can be concluded that a K_2SiF_6 coating can have a positive influence on the quantum efficiency, but a drop in IQE or EQE is also possible. Growing a K_2SiF_6 coating on the phosphor particles improved the IQE, from 28% without a coating to 66% with a coating of 1.2 µm. Intermediate IQE values were reached for thinner coatings. For the thickest coating, the EQE only increased a little, from 9% to 15%, due to a decrease in absorption from 33% to 23%. For another coating series, the IQE improved from 16% to 53% by growing a coating of only 0.2 µm. Likewise, the absorption dropped from 45% to 34%, resulting in an increase in EQE from 7% to 18%. Although the coating can improve the emission effiency of the phosphor, high initial quantum efficiencies are preferred. When a phosphor with an IQE of 38% and an EQE of 7% was coated with a 0.1 µm coating, the IQE increased only to 44% and the EQE remained stable at 7%.

Table 9.2: Influence of coating thickness of a K_2SiF_6 coating on the quantum efficiency

coating thickness (μm)	IQE	EQE	absorption
0	28%	9%	0.33
0.24	75%	19%	0.26
0.78	54%	13%	0.23
1.2	66%	15%	0.23
0	16%	7%	0.45
0.12	12%	5%	0.45
0.18	53%	18%	0.34
0	38%	7%	0.17
0.09	44%	7%	0.16
0.12	39%	6%	0.16

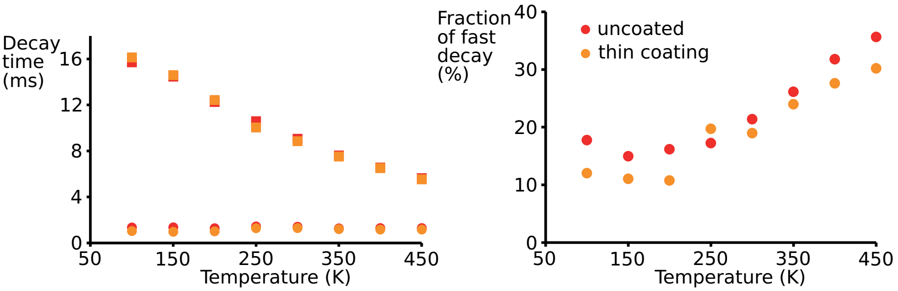

Figure 9.9: Decay times (left) with a slow component (squares) and a fast component (circles) in function of temperature of an uncoated $K_2SiF_6:Mn^{4+}$ phosphor powder (red) and $K_2SiF_6:Mn^{4+}$ phosphor powder coated with 0.2 μm of undoped K_2SiF_6 (orange). Fraction of fast decay time of uncoated (red) and coated (orange) $K_2SiF_6:Mn^{4+}$ phosphor powder in function of temperature (right).

In both the coated and uncoated phosphor sample, a bi-exponential decay behavior was found in the 100–450 K temperature range (figure 9.9). This second, faster decay component was also found in $K_2SiF_6:Mn^{4+}$ synthesized by a precipitation synthesis (figure 7.9). No difference was found between the decay times fitted to the decay profiles of uncoated and coated phosphor particles, with decay times of 16 ms at 100 K to 6 ms at 450 K. Though, after coating, the fraction of the second, faster decay component is lower compared to uncoated particles. This shows that coating improves the quality of the phosphor particles, since the faster decay component was attributed to a certain fraction of Mn^{4+} dopants that are incorporated in close vicinity of another point defect, which was discussed in chapter 7.

9.2.3 Stability

Introducing an undoped K_2SiF_6 coating on the phosphor particles reduced the absorption, but also slightly improved the overall quantum efficiency. From the volume of K_2SiF_6 solution added to the phosphor in the coating synthesis, the thickness of the coatings can be estimated as 0.2 µm on the thin coated sample and 1.2 µm on the thick coated sample. Before coating, the clustered phosphor particles had a diameter of 50 µm, so the coating resulted in a volume increase of 3 % and 15 % respectively.

To test the stability of the coated phosphor materials compared to that of the uncoated phosphor, they were subjected to a high temperature and high humidity (HTHH) environment in a climate chamber at 80 °C and 80% relative humidity by Reinert Verstraete. Both the uncoated and the coated phosphors degraded over time, but the IQE of the 0.2 µm-coated phosphor remained at 30% after 36 h at HTHH conditions, while the IQE of the uncoated phosphor dropped below 10% of the initial IQE. The IQE of the 1.2 µm-coated sample dropped to 20% after 36 h at HTHH conditions, performing worse than the thin coated sample. In the XRD patterns, no extra peaks emerged after aging in the climate chamber, the only difference was found in the intensity of the reflections.

9.2.4 EPR-measurements

In an attempt to learn more about the surroundings of the Mn^{4+} ions in the phosphor samples, electron paramagnetic resonance (EPR) measurements were performed by Jevgenij Kusakovskij on an uncoated phosphor sample and phosphor samples coated with 0.2 µm and 1.2 µm undoped K_2SiF_6. Mn^{2+} and Mn^{4+} are both EPR-active and result in similar hyperfine structures, but the difference between both can be determined from a difference in g value. EPR on K_2SiF_6:Mn^{4+} is only occasionally reported in literature. The six hyperfine components due to the $1/2 \rightarrow -1/2$ transition of Mn^{4+} with a d^3 configuration in X-band EPR were reported for a high dopant concentration in K_2SiF_6:Mn^{4+} [80].

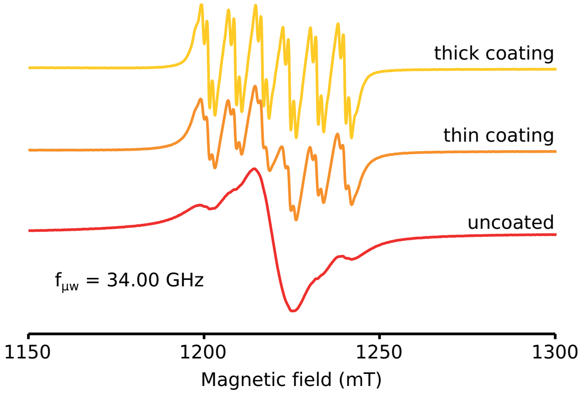

Figure 9.10: Q-band EPR spectrum of a K_2SiF_6:Mn^{4+} phosphor, with an 1.2 µm K_2SiF_6 coating (yellow), with an 0.2 µm K_2SiF_6 coating (orange) and uncoated (red).

Measurements were performed on both X-band and Q-band EPR, with analogous results. The Q-band spectra are shown in figure 9.10. The hyperfine structure of the $1/2 \rightarrow -1/2$ transition of Mn^{4+} is more apparent in the coated phosphor samples, which shows that more Mn–F interaction is created by applying the coating. When a thick coating is applied, the Mn concentration is lowered due to the addition of K_2SiF_6 to the powder. In this sample, the details of the hyperfine structure are the most resolved. The difference in peak resolving of the EPR spectrum between the uncoated and the coated sample is related to the Mn–Mn distance in the crystal lattice, so treating the phosphor at 70 °C in presence of HF and K_2SiF_6 influences the crystal structure of the phosphor in addition to the deposition of extra K_2SiF_6 on the phosphor material. These coating conditions are similar to the initial synthesis conditions of the cocrystallization synthesis, where either cation exchange or diffusion can improve the Mn distribution in the phosphor sample.

9.3 Discussion

Although the cation-exchange synthesis is promising, consuming far less HF compared to other synthesis methods, it has only been reported in one, widely cited publication for K_2TiF_6:Mn^{4+} [100], in $(NH_4)_2TiF_6$:Mn^{4+} and $(NH_4)_2SiF_6$:Mn^{4+} [103] and for the more exotic fluoride host K_2LiGeF_6:Mn^{4+} [104]. In our synthesis, we were able to produce K_2SiF_6:Mn^{4+} using a cation-exchange cocrystallization synthesis, but there were several drawbacks as it produced heterogeneous, discolored powders with low quantum efficiencies. This shows that cation exchange can also take place between Si^{4+} and Mn^{4+} in hexafluoride hosts, but not as effective as the reaction between K_2TiF_6 and K_2MnF_6. When Mn^{4+}, with an ionic radius of 53 pm, replaces Si^{4+} with an ionic radius of 40 pm, the lattice has to expand to accomodate Mn^{4+}. In K_2TiF_6 on the other hand, no lattice expansion needs to take place during the cation exchange. The Ti^{4+} ion has an ionic radius of 60.5 pm, so a lattice relaxation occurs when Mn^{4+} is incorporated in K_2TiF_6. Furthermore, the difference in ionic radius is only 7.5 pm between Ti^{4+} and Mn^{4+}, while the difference in ionic radius is 13 pm between Si^{4+} and Mn^{4+}. A smaller change in the lattice distances will be easier overcome, promoting the cation exchange reaction in the K_2TiF_6 host.

Although some high quantum efficiency values were found, manual selection of the most strongly luminescent lumps under a UV lamp was needed to obtain these powders. Apart from the selected particles, the major yellow powder fraction performs best. All other fractions found, including pink particles, yellow stained particles and black stained crusts, have lower quantum efficiencies. For practical applications, a homogeneous synthesis result is preferred, reducing cumbersome post-synthesis selection. The removal of a crust is sometimes unavoidable due to thermally induced surface effects and is also common for some solid state synthesis reactions. Upscaling of the synthesis improved the homogeneity of the powder formed under the crust in cocrystallization reactions.

Apart from variation in the synthesis properties, the quality of the used K_2MnF_6 can greatly influence the quality of the resulting phosphor. During the cocrystallization synthesis, a lot of pink powder and dark red crusts were synthesized, although K_2SiF_6:Mn^{4+} has an orange-yellow body color. When the white slurry turns yellow after addition of K_2MnF_6, $[MnF_6]^{2-}$ complex ions are still present, while when the solution turns red, some degradation of K_2MnF_6 has set in. As discussed in chapter 8, when K_2MnF_6 is heated in an HF solution, $KMnF_4 \cdot H_2O$ forms. During overnight evaporation at 70 °C, hydrate formation can occur even when only a small amount of HF is present. Comparing samples is also a little ambiguous, since different K_2MnF_6 samples, with possibly different purity and degree of degradation have often been used, since the production yield of K_2MnF_6

is low. Using pure K_2MnF_6 has probably been the most advantageous synthesis optimization, obtaining the highest quantum efficiency reached for cocrystallization synthesis.

Using smaller, ball-milled K_2SiF_6 particles had a positive effect on the quantum efficiency, but even higher quantum efficiencies were obtained with K_2SiF_6 used as such. Ball-milling reduces the particle size, but thereby destroys some of the crystallinity. More recrystallization has to occur during the synthesis, compared to big crystalline particles. Since these large particles are mostly used in cocrystallization synthesis, Mn is suspected to only incorporate in the outer layers of the host crystal. Unfortunately, due to the low dopant concentration and limited detector sensitivity, it has not been possible to quantify the penetration depth of Mn in a cocrystallization synthesis using SEM-EDX or X-ray photoelectron spectroscopy.

Using a larger volume synthesis seemed to have a positive effect, since no black crust (with high Mn concentration) formed in these syntheses. The samples were more homogeneous and did not show any bubble spots, but only low quantum efficiencies were achieved. Lowering the temperature of the hot water bath to 60 °C, to prevent the formation of MnO_2 as happens in XRD when heating the sample to higher temperatures [99], resulted in no emission from the resulting powder. Although temperatures of 70 °C and lower are known to induce degradation of K_2MnF_6, the heat is apparently needed to induce the cation exchange.

Applying a K_2SiF_6 coating somewhat increases the quantum efficiency of the phosphor material. Due to the heat treatment at 70 °C involved in the coating procedure, the homogeneous distribution of Mn ions over the lattice is improved by diffusion effects, improving the Mn–F interaction, as can be seen in EPR measurements.

9.4 Conclusion

Some cation-exchange reaction takes place when K_2MnF_6 and K_2SiF_6 are mixed, as we see phosphor formation when the two precursors are mixed with a little HF and heated up to 70 °C. Unfortunately, the difference in ionic radii hinders smooth cation exchange, resulting in interfering degradation processes and contaminated, low quality phosphor samples. The opportunities of this synthesis method can be seen in the most strongly luminescent lumps that can be selected post-synthesis under a UV lamp. These fractions reach high quantum efficiencies, but selecting and sorting them is not realistic. Therefore, creating the K_2SiF_6 host in situ, so that it can grow around dissolved $[MnF_6]^{2-}$ ions, seems to be more realistic to overcome the lattice expansion needed for dopant incorporation. Selection of the most strongly luminescent lumps from heterogeneous synthesis results is possible under a UV lamp, but cumbersome, so the aim is to find a way to make the phosphor synthesis itself more homogeneous.

In general, relatively low quantum efficiencies are found for the yellow and pink powders found under the dark crust. With the right synthesis conditions, IQE values of 55 % and EQE values of 25 % are reached using a cocrystallization synthesis, showing a performance of the same level as the precipitation synthesis, but still below the performance of an etching synthesis. The quality of K_2MnF_6 is important, on the one hand in controlling the dopant concentration, on the other hand to reduce the introduction of defects such as Mn^{3+} and hydrates like $K_2MnF_5 \cdot H_2O$.

Applying a K_2SiF_6 coating to the phosphor particles is beneficial in many aspects. Not only does the quantum efficiency improve, an improved long-term stability has also been found. The coating process improves the crystal structure as a whole, since more Mn–F interaction is detected in EPR and a lower fraction of bi-exponential decay is found in luminescence lifetime measurements.

10

Coprecipitation synthesis of K_2SiF_6:Mn^{4+}

The cocrystallization synthesis that was discussed in chapter 9 already showed the benefits of using K_2MnF_6 as the Mn source in K_2SiF_6:Mn^{4+} phosphor synthesis. Using a two-step synthesis, the reduction of Mn^{7+} and the fluorine coordination of Mn^{4+} can be isolated from the incorporation in the phosphor host. Although cocrystallization yields good results for K_2TiF_6:Mn^{4+}, the smaller K_2SiF_6 host is less prone to incorporate the slightly bigger $[MnF_6]^{2-}$ complex. In a coprecipitation synthesis, K_2MnF_6 is used as the Mn source, but the host is precipitated from other precursor materials. By forming the host lattice in situ, the lattice relaxation that is necessary to incorporate Mn^{4+} in K_2SiF_6 is facilitated.

10.1 Method

In general, the coprecipitation synthesis involves the precursors K_2MnF_6, SiO_2 (99.5%, Alfa Aesar) and KF (99%, Alfa Aesar), which are dissolved in 40% HF (Sigma-Aldrich) and mixed together (figure 10.1). The specific conditions of mixing order, mixing speed and reaction temperature

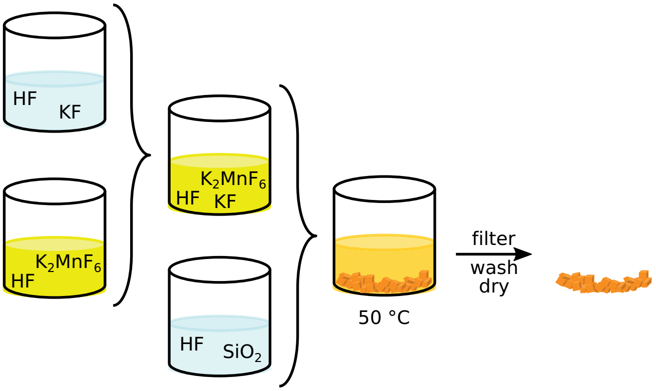

Figure 10.1: Schematic illustration of the coprecipitation synthesis.

as well as the post-synthesis treatments were varied to find the optimal synthesis conditions, resulting in a stable phosphor powder with a high internal quantum efficiency. Since K_2SiF_6 can precipitate from HF solution from the moment that KF and SiO_2 are mixed, it is crucial to separate these precursors before addition of K_2MnF_6. KF and K_2MnF_6 can be mixed in HF solution, although precipitation of K_2MnF_6 can occur due to the common ion effect [88]. Because K^+ is present in both KF and K_2MnF_6, the solubility of K_2MnF_6 is reduced when KF is added to the solution. Since K_2MnF_6 is not commercially available, it was synthesized in-house.

As discussed in chapter 9, the cocrystallization synthesis was performed at 70 °C, although thermally induced degradation of K_2MnF_6 is known to occur at these temperatures. In the cocrystallization synthesis, lowering the synthesis temperature to 60 °C did not prove to be advantageous, resulting in a discoloration to pink powder (figure 9.3). In contrast, in coprecipitation synthesis, the Mn^{4+}-doped K_2SiF_6 phosphor could be precipitated at 50 °C or even at room temperature without additional heating. Unlike the cation-exchange process involved in the cocrystallization synthesis, the precipitation of K_2SiF_6 and K_2MnF_6 from 40% HF solution is a spontaneous process. The chemical reaction for this precipitation reaction is given by reaction 10.1.

$$\begin{aligned} &(1-x)\,SiO_2\,(aq) + (2-2x)\,KF\,(aq) + \\ &x\,K_2MnF_6\,(aq) + (4-4x)\,HF\,(aq) \longrightarrow \\ &K_2Si_{1-x}Mn_xF_6\,(s) + (2-2x)\,H_2O\,(l) \end{aligned} \tag{10.1}$$

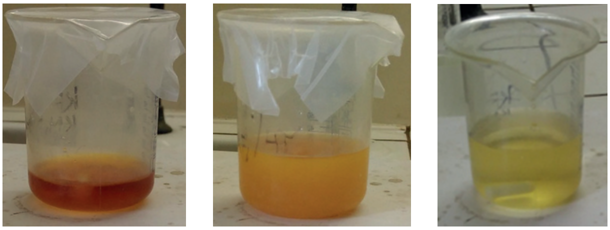

Figure 10.2: Different synthesis solutions from the coprecipitation synthesis. Orange solution of K_2MnF_6 in HF (left), precipitated orange solution of KF and K_2MnF_6 in HF (center) and a stable, clear yellow solution of KF and K_2MnF_6 in HF (right).

Because this precipitation reaction is spontaneous, K_2SiF_6 precipitates from HF solution when SiO_2 and KF are mixed. To incorporate K_2MnF_6 during the host precipitation, it must be added to the SiO_2 solution simultaneously with KF. In this way, preliminary K_2SiF_6 precipitation can be reduced, preventing incorporation of K_2MnF_6 by cation exchange only. When clear HF solutions of KF and K_2MnF_6 are mixed, both K_2MnF_6 and KHF_2 can precipitate from the solution (figure 10.2). The common ion effect lowers the solubility of K_2MnF_6 due to the increased K^+ concentration in the solution after addition of KF.

Not only concentration influences the stability of the KF-K_2MnF_6 solution. Stable mixed solutions of KF and K_2MnF_6 were made with K concentrations of 0.05–8.2 M, while other solutions with K concentrations of 2.0–8.2 M resulted in precipitates. Stable solutions can be obtained by stirring the KF solution and slowly adding the K_2MnF_6 solution dropwise. Both stable and precipitated KF-K_2MnF_6 solutions were used in coprecipitation synthesis. The formed precipitation can stay behind in the separatory funnel, which would lower the possible incorporated dopant concentration. When drop pipets are used to add the KF-K_2MnF_6 solution to the SiO_2 solution, there is no residue left, so all Mn is available to be incorporated in the phosphor, either by coprecipitation or by a cation-exchange reaction.

To find the optimal synthesis conditions, precursor solutions of SiO_2 (78 mM), KF (0.35 M) and K_2MnF_6 (3.6 mM) were mixed. 1 mL of SiO_2 solution was mixed with 3 mL, 5 mL and 8 mL of KF-K_2MnF_6 solution using syringes, which corresponds with a dopant concentration of 0.4 %, 0.6 % and 0.9 %. The solutions which were mixed at room temperature or in a hot water bath at 50 °C, were left to evaporate at room temperature or at 50 °C and were either stirred or not stirred during the mixing and evaporation. However, evaporation at room temperature is very slow, especially for the larger volume (9 mL) solutions. Therefore, after some rest at room temperature, these slurries were filtered, washed with acetone and dried in air to obtain the phosphor powders.

To enhance the optical absorption of the obtained phosphor, the concentration of K_2MnF_6 was increased. For this, SiO_2 was added to a beaker in a hot water bath at 50 °C, to which the KF-K_2MnF_6 solution was added dropwise using a syringe or a separatory funnel. The synthesis volumes were chosen in a way that the intended dopant concentration could be varied from 2.1 to 11 %. For a dopant concentration of 2%, synthesis conditions were further optimized in both the mixing and the treatment of the formed precipitate. After the precursors were all added, the precipitated solutions were further stirred at 50 °C for 0 h, 1 h, 3 h and 4 h, after which the suspension was either evaporated overnight at 35 °C or 50 °C or the solution was decanted, filtrated and the precipitate was washed with HF and acetone. To further optimize the precursor mixing, the two precursor solutions were added to separatory funnels and a dropwise synthesis was performed (figure 10.3). The SiO_2 solution and the KF-K_2MnF_6 solution were simultaneously added dropwise to a beaker in a hot water bath at 50 °C at drop rates of 24–100 min^{-1}.

The optimal K_2SiF_6:Mn^{4+} phosphor was found using a synthesis where 12.5 mL of a 39.9 mM solution of K_2MnF_6 in 40% HF was added dropwise to 25 mL of a 1.96 M solution of KF in 40% HF while stirring at room temperature, which formed a clear yellow solution without formation of a precipitate. A second, clear white precursor solution was prepared by dissolving SiO_2 in 37.5 mL 40% HF at room temperature to a concentration of 0.65 M. The precursor solutions were mixed in a beaker in a hot water bath at 50 °C, simultaneously dropping from a separatory funnel at a drop rate of 52 min^{-1} for the SiO_2 solution and 92 min^{-1} for the KF-K_2MnF_6 solution. When the precursor solutions were mixed, a light-yellow precipitate formed in the beaker. After stirring at 50 °C for 1 h, most of the supernatant was decanted, after which the suspension was filtrated, washed with acetone and left to dry in air overnight. Upscaling of this synthesis was possible up to a total synthesis volume of 200 mL, which was the volume limit of the separatory funnels.

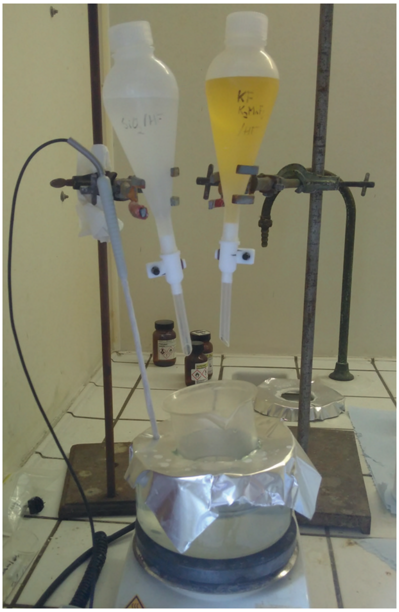

Figure 10.3: Synthesis setup for a coprecipitation synthesis with two separatory funnels for dropwise mixing. The left funnel contains SiO_2 in HF, the right funnel contains KF and K_2MnF_6 in HF.

An undoped K_2SiF_6 coating was applied using a precipitation coating method. Here, a 0.09 M saturated solution of K_2SiF_6 in HF was added to the phosphor powder, after which the mixture was evaporated overnight in a hot water bath at 50 °C. The coating thickness was varied by changing the phosphor to K_2SiF_6 ratio.

10.2 Results

The coprecipitation synthesis resulted in a light-yellow to orange phosphor powder. A yellow or orange crust was sometimes formed when the synthesis mixture was evaporated overnight. Stirring the mixture while evaporating prevents crust formation, though the total yield is somewhat lower due to splashing of the solution. When the precipitate was filtered, washed and dried, a homogeneous yellow-orange powder was obtained.

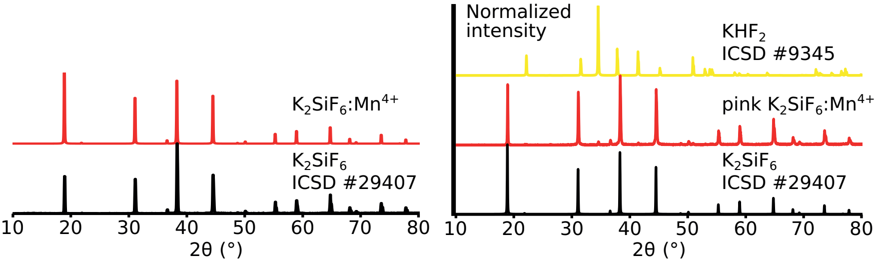

Figure 10.4: XRD patterns of an orange K_2SiF_6:Mn^{4+} phosphor powder with a dopant concentration of 2% (red line, left) and a pink K_2SiF_6:Mn^{4+} phosphor powder with a dopant concentration of 3% (red line, right) compared with reference patterns of K_2SiF_6 (black) and KHF_2 (yellow).

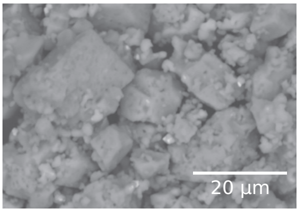

Figure 10.5: SEM image of K_2SiF_6:Mn^{4+} phosphor powder from a coprecipitation synthesis.

10.2.1 Structural

In the XRD patterns in figure 10.4, the phosphors show the four characteristic intense reflections of K_2SiF_6 together with the less intense K_2SiF_6 reflections. Even for pinkish phosphor powders that clearly contain some other phases, only XRD reflections of K_2SiF_6 and some KHF_2 are found, which does not explain the pink body color. In an SEM image, the phosphors show to be agglomerated (truncated) cubes of 5–10 µm (figure 10.5).

In a sample series of varying dopant concentration of 1.7–11 %, a homogeneous Mn distribution is found in all samples except for the samples of 4.8 % and 5.7 %. Remarkably, those two samples were made using a stable K_2MnF_6-KF precursor solution in contrast to the other samples in this series, where some precipitation occurred in the K_2MnF_6-KF solution. Two other samples were synthesized using a K_2MnF_6 solution that had turned red and these phosphor powders show a pink body color. The high absorption reached by one of these is probably caused by other Mn phases such as $KMnF_4 \cdot H_2O$, since the IQE is lower than for other powders with a

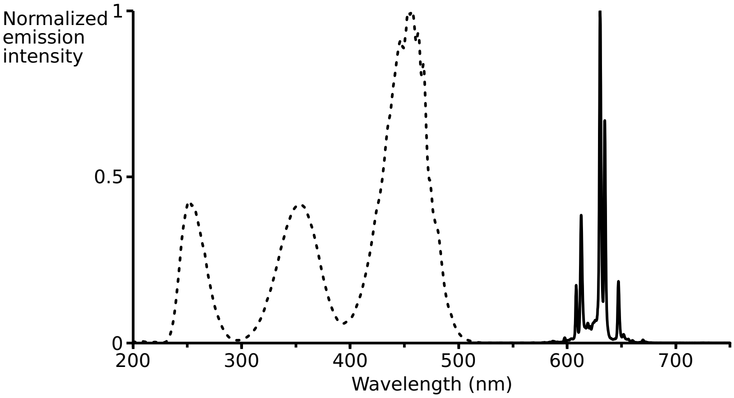

Figure 10.6: Normalized photoluminescence excitation spectrum (dotted line) (emission at 630 nm) and emission spectrum (full line) (excitation at 450 nm) of K_2SiF_6:Mn^{4+} synthesized using a coprecipitation synthesis.

yellow body color and a similar dopant concentration. The dopant concentration as found using EDX is 1.9–12.3 %, with the highest concentration found due to a heterogeneous Mn distribution. Reproducing the synthesis for an aimed dopant concentration of 2–2.5 % during the synthesis results in a dopant concentration of 0.81–3.7 % as measured by EDX.

10.2.2 Luminescence

Upon 450 nm excitation, bright red line emission shows around 630 nm (figure 10.6). The spectrum perfectly matches the emission spectrum found in other synthesis methods. The excitation spectrum clearly shows the three excitation bands, of which the band corresponding to the $^4A_{2g} \longrightarrow {}^4T_{1g}(^4P)$ transition (around 250 nm) is rarely reported. Here, the intensity of this UV excitation band is more intense compared to other synthesis methods.

Low emission intensities and low quantum efficiencies were found after the initial coprecipitation synthesis at room temperature or at 50 °C, due to the low dopant concentration. The measured IQE values exceeded 100%, which is physically impossible, but these values were obtained due to experimental errors when measuring relatively efficient phosphors with low absorption strength. Absorption ratios of 3–22 % were obtained for a Mn concentration of 0.35–3.0 %. A dopant concentration exceeding 2% showed little benefit, since a dopant concentration of 2.0–3.0 % resulted in a similar absorption of 20–22 %. Abnormally high IQE values of 64–

102 % are obtained for the samples synthesized at room temperature or 50 °C for Mn concentrations of 0.35–1.8 %. Since the absorption for these samples does not exceed 20%, the EQE values are 5–19 %, which is relatively low. Although the IQE values obtained for these samples are high, the phosphors do not perform very well. A high absorption is also needed to obtain a high emission intensity as well.

More realistic IQE values, with a better balance between absorption and emission intensity, were found when K_2MnF_6 and KF were added as separate solutions. For Mn concentrations of 0.52–6.7 %, IQE values of 10–45 % and EQE values of 1.9–6.3 %. In this sample series, where the precursor solutions are mixed at 50 °C and then stirred for 2 min, only a small spread on the absorption values is found, with values of 13–22 %, with an absorption of 20% reached from a dopant concentration of 2.0%.

Higher quantum efficencies were obtained when not only the Mn concentration but also the reaction time were increased. In one sample series the precursor solutions were mixed at 50 °C, stirred for 5 min and evaporated in a hot water bath at 50 °C overnight, instead of being filtered and washed directly. For dopant concentrations of 1.7–11 %, absorption values of 27–63 % were obtained. Even for similar dopant concentrations as in the previous sample series, for 1.7–2.0 %, higher absorption values of 27–38 % were obtained by increasing the reaction time. Together with the absorption, the quantum efficiency increased with increasing dopant concentration and reaction time, reaching IQE values of 27–67 % and EQE values of 14–25 %. As a function of dopant concentration, the absorption is stable around 46% for a dopant concentration of 3–7 %. The IQE peaks at 67% for a dopant concentration of 2%, while it is stable around 51% for a dopant concentration of 1.7–4.8 %. For higher dopant concentrations, the IQE drops to values below 40%. Reproducing the synthesis at a dopant concentration of 2% resulted in an IQE of (73 ± 4) %, and EQE of (26 ± 1) % and an absorption of (36 ± 2) %. Increasing the dopant concentration slightly to 2.5% did not increase the quantum efficiency, so the 2% concentration was kept for further syntheses. Finally, a bright yellow-orange phosphor powder was obtained with an IQE of 88%, an EQE of 45% and an absorption of 52%, which is close the the best values reported by General Electric [84].

When phosphor samples from a cocrystallization synthesis where coated with undoped K_2SiF_6, the quantum efficiency improved after the coating (table 9.2). With the coprecipitation synthesis, the initial quantum efficiency is already higher due to improved synthesis conditions but a thin

Table 10.1: Influence of a K_2SiF_6 coating on the quantum efficiency of phosphors from a coprecipitation synthesis.

coating thickness µm	IQE	EQE	absorption
0	27%	16%	0.57
0.2	48%	20%	0.43
0.6	32%	12%	0.38
1.2	8%	1%	0.12

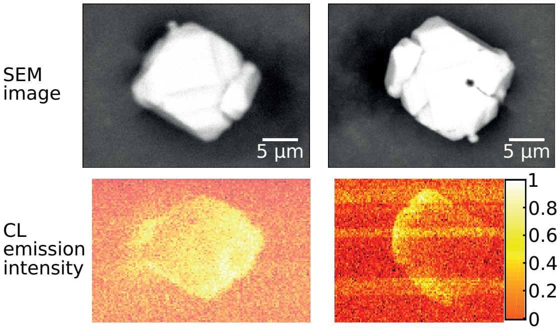

Figure 10.7: The SEM image (top) and CL map (bottom) of a single $K_2SiF_6:Mn^{4+}$ particle (right: rotated over 180°) shows a heterogeneous light outcoupling, even when the particle is rotated over 180°.

coating of 0.2 µm can still somewhat improve both the IQE and the EQE (table 10.1). A 0.6 µm coating improves the IQE a little, but due to the decrease in absorption, the EQE drops. For a thick coating of 1.2 µm, the luminescence intensity is even further diminished, resulting very low QE values. The drop in absorption is caused by the decrease in Mn^{4+} by the addition of an undoped K_2SiF_6 coating. The initial phosphor particles have a diameter of 10 µm, so a volume increase of 0.1 %, 0.3 % and 0.7 % is found for a coating thickness of 0.2 µm, 0.6 µm and 1.2 µm.

Although the Mn distribution is homogeneous in the EDX-map, the light emission is not. When observing a single cubic particle in SEM-CL (figure 10.7), a higher emission intensity is observed on the right side of the particle, where the integrated emission intensity of a selected region (9 pixels) is 2.7 times bigger than the emission intensity of a selected region on the left side of the particle. When the particle is rotated over 180°, the higher emission intensity moved along to the left side of the particle, with an equivalent intensity ratio of 2.7. This heterogeneous light emis-

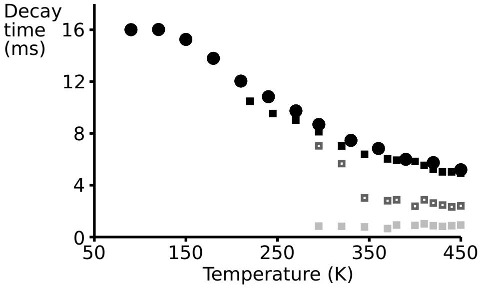

Figure 10.8: Decay time of K_2SiF_6:Mn^{4+} made using a coprecipitation synthesis as a function of temperature (black dots). The bi-exponential decay times of K_2SiF_6:Mn^{4+} made using a precipitation synthesis (figure 7.11) are portrayed in gray squares, with open squares for the effective decay time of this sample.

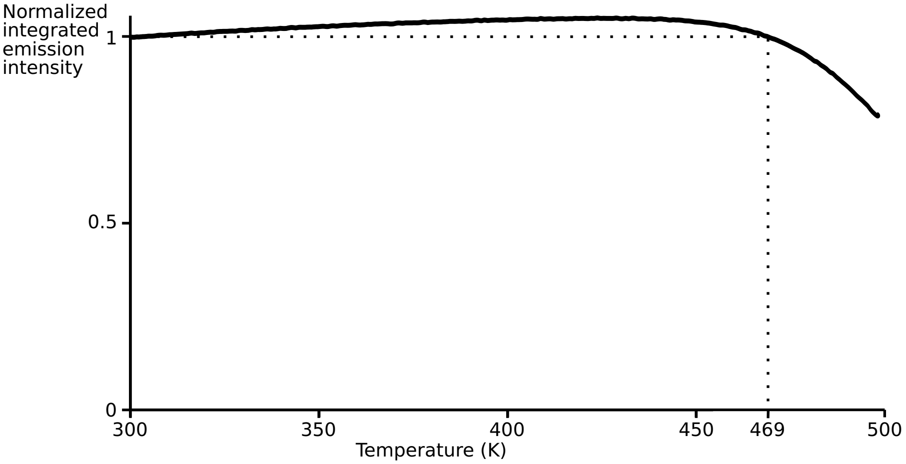

Figure 10.9: Thermal quenching profile of K_2SiF_6:Mn^{4+} made using a coprecipitation synthesis, integrated emission intensity at 590–690 nm upon excitation at 450 nm.

sion was also observed in the precipitation synthesis (figure 7.3). Due to internal reflections within the cubic particle, a preferential outcoupling of the light can be found.

In temperature-dependent luminescent lifetime measurements, a decay time of 16.3 ms was found at 90 K. With increasing temperature, the decay time decreased down to 5.2 ms at 450 K. Contrary to the phosphor synthesized with the precipitation synthesis, only a mono-exponential decay behavior was found (figure 10.8).

The thermal stability of the K_2SiF_6:Mn^{4+} synthesized by coprecipitation is substantially better compared to the precipitation synthesis. In the thermal quenching profile (figure 10.9), measured up to 500 K, the integrated emission intensity only drops to 79%. The thermal quenching temperature at which the emission intensity is halved compared to the intensity at low temperature could not be determined, but is $>$500 K, compared to 429 K for K_2SiF_6:Mn^{4+} synthesized using a precipitation synthesis, as was discussed in chapter 7. In literature, thermal quenching temperatures $T_{1/2}$ of 430–520 K are reported [24, 38, 43, 105].

In the 300–450 K temperature range, the integrated emission intensity increases further. When the separate emission peaks are considered, the intensity of the Stokes emission peaks (625–644 nm) decreases to 92% of its initial emission intensity in the 300–450 K temperature range, but this drop is compensated by a 22% increase of the anti-Stokes emission peaks (604–620 nm). The increase in emission intensity with temperature is often found in Mn^{4+}-doped fluoride phosphors [80, 100], caused by the combination of the expected peak broadening and the increase in peak intensity of the anti-Stokes emission lines. The nonradiative transition probability remains stable at 290–420 K, while the radiative transition probability increases. Therefore, the increase in emission intensity with increasing temperature should be attributed to enhanced phonon-assisted radiative transitions which increase the EQE. The stronger electron–phonon interaction at higher temperatures results in increased radiative transition probabilities for the spin- and parity-forbidden $^2E_g \rightarrow {}^4A_{2g}$ transition [46]. This is in contrast to other phosphors, where an increase in the nonradiative transition probability with increasing temperature reduces the emission intensity. In K_2SiF_6:Mn^{4+} the emission intensity only drops at temperatures above 450 K, reaching the initial emission intensity at 469 K.

10.2.3 Stability

The XRD pattern of the uncoated K_2SiF_6:Mn^{4+} phosphor sample (left part of figure 10.10) shows a small contribution of KHF_2 at 34° and a small contribution of K_2MnF_6 at 26° together with the main pattern of K_2SiF_6. When the phosphor was aged in a climate chamber for 20 h at 70 °C and 80% relative humidity, the signals of K_2MnF_6 and KHF_2 in the XRD pattern were reduced. In the humid atmosphere, the hygroscopic K_2MnF_6 will hydrolyze and KHF_2 can decompose into KF and HF.

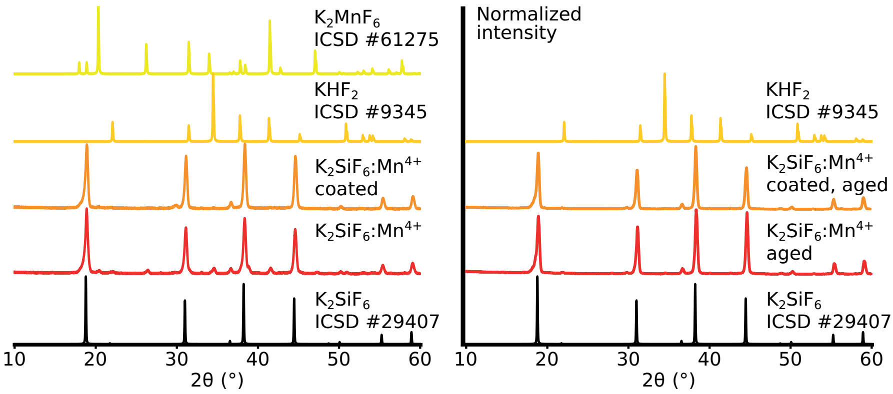

Figure 10.10: XRD patterns of the K_2SiF_6:Mn^{4+} phosphor synthesized using a coprecipitation synthesis with a dopant concentration of 10.8%, both uncoated (red) and with a 0.6 µm coating (orange), before (left) and after 20 h in the climate chamber at 70 °C and 80% relative humidity (right) compared with the reference patterns of K_2SiF_6 (black), KHF_2 (ocher) and K_2MnF_6 (yellow).

In the XRD pattern of the coated phosphor sample (right part of figure 10.10), only a small contribution of KHF_2 at 34° shows superposed on the pattern of K_2SiF_6. The coating process itself reduced the contamination of the phosphor sample with both K_2MnF_6 and KHF_2, which can happen through recrystallization in the HF solution at 50 °C. For the coated phosphor sample, aging in the climate chamber has no significant influence on the XRD pattern.

Diffuse reflectance measurements by Reinert Verstraete showed that both Mn^{3+} and Mn^{4+} absorption was present in the phosphor sample before and after the coating process (figure 10.11). After the aging procedure in the climate chamber, the characteristic Mn^{4+} absorption bands from K_2SiF_6:Mn^{4+} have almost vanished in the uncoated sample. In the DRS spectrum of the coated sample, the absorption bands are less pronounced but still present, which shows that the K_2SiF_6 coating can improve the chemical stability of the Mn^{4+}-doped K_2SiF_6.

10.3 Discussion

Initially, solutions were mixed using separatory funnels to find the optimal synthesis conditions with various Mn concentrations and mixing and evaporating at 20 °C, 50 °C and 70 °C. Since the set drop rate is hardly re-

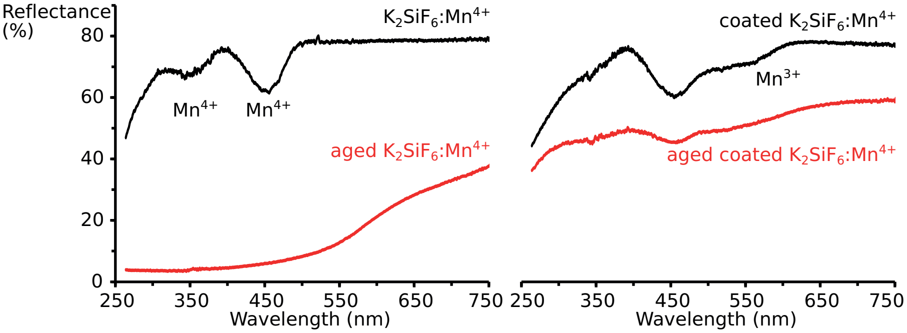

Figure 10.11: Diffuse reflectance measurements of both uncoated (left) and coated K_2SiF_6:Mn^{4+} phosphor samples (right) before (black) and after aging (red) for 20 h at 70 °C and 80% relative humidity.

producible using separatory funnels, syringes were preferred to control the amount of mixed precursor solutions. When the right concentrations and synthesis temperatures were found, separatory funnels were reintroduced. Using separatory funnels, larger synthesis volumes can easily be achieved. Furthermore, using the separatory funnels, the drop rate of both precursor solutions can be regulated, so the SiO_2 solution can be added simultaneously with the KF-K_2MnF_6 solution. When the SiO_2 solution is heated to 50 °C and the KF-K_2MnF_6 solution is added subsequently, KF and K_2MnF_6 react with an excess of SiO_2. When an excess of KF is present, relative to the aimed dopant concentration, more K_2SiF_6 can precipitate and lower the obtained dopant concentration. Although the initial KF concentration is matched to the SiO_2 concentration, a mixed KF-K_2MnF_6 solution is used in the synthesis. When the same mixed solution is used for a range of dopant concentrations, the KF excess increases with increasing dopant concentration. Adding the SiO_2 and the mixed KF-K_2MnF_6 solutions to a beaker simultaneously induces precipitation of doped K_2SiF_6:Mn^{4+} with the aimed dopant concentration, especially if the drop rates are equal. Since the precipitation occurs instantaneous, there is no need for a slow drop rate, as long as the precursors are mixed dropwise.

Stirring the solution for some time after the precursors are mixed is beneficial as can be seen when two samples were compared from the same synthesis batch. The first sample is isolated after all SiO_2 solution has run through and the second sample is isolated when more of the KF-K_2MnF_6 solution is added to the mixture. Higher quantum efficiencies are obtained for the second sample, proving that more crystalline K_2SiF_6:Mn^{4+}

is formed after the initial instant precipitation. When all $[MnF_6]^{2-}$ ions are incorporated into the precipitation, the highest possible dopant concentration is reached and the supernatant is colorless instead of yellow. When for equal solution volumes, the drop rate of the KF-K_2MnF_6 solution exceeds the drop rate of the SiO_2 a better dopant incorporation is obtained, since a small excess of K_2MnF_6 present will induce precipitation of K_2SiF_6:Mn^{4+} rather than preliminary precipitation of K_2SiF_6.

Compared to other synthesis methods, the dopant incorporation is substantially better using a coprecipitation synthesis. Fully homogeneous dopant incorporation can be achieved in a coprecipitation synthesis for the optimal 2% concentration, but also for higher concentrations up to 11%. The phosphor powders synthesized using coprecipitation show less defects, as can be seen from the mono-exponential decay behavior. After precipitation synthesis, a defect-induced bi-exponential decay was found at increased temperatures (figure 7.9), while a mono-exponential decay behavior is found after coprecipitation. The mono-exponential decay time of 16.3–5.2 ms (figure 10.8) follows the same trend as the slow component of the bi-exponential decay found with precipitation synthesis, which had a decay time of 10.5–4.9 ms in the 220–450 K temperature range. A somewhat heterogeneous light emission is found in SEM-CL, but this is not linked to a heterogeneous dopant distribution.

Further scaling of the synthesis volume, to an industrial scale, is possible using larger volume lab ware, with possibilities for a flow synthesis. A complicating limiting factor of the coprecipitation synthesis is the synthesis of K_2MnF_6. As discussed in chapter 8, this precursor is not available commercially, and the in-house synthesis is possible but only at a low yield, due to the large excess of KF present. Industrial upscaling of K_2MnF_6 should be the first priority in upscaling of the K_2SiF_6:Mn^{4+} synthesis.

An undoped K_2SiF_6 coating can improve the quantum efficiency in some instances and can improve the chemical stability of the K_2SiF_6:Mn^{4+} phosphor powder. On the other hand, improving the synthesis method to obtain pure phosphor powders without contamination of KHF_2 or K_2MnF_6 is even more beneficial. With the optimal synthesis conditions, higher QE values are obtained compared to the coated samples. In DRS measurements (figure 10.12), no contribution of Mn^{3+} can be found. Even after aging the sample in the climate chamber for 48 h at 70 °C and 80% relative humidity, no change in the reflectance spectrum was found, showing that the characteristic Mn^{4+} absorption of K_2SiF_6:Mn^{4+} is still present and the phosphor powder is chemically stable in this time frame.

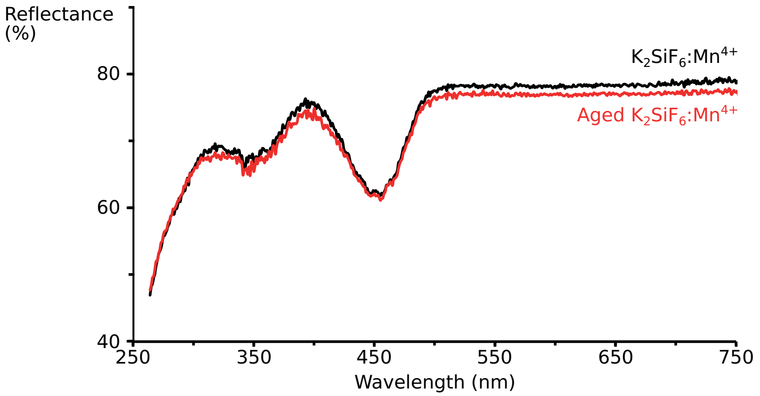

Figure 10.12: Diffuse reflectance measurement of a phosphor sample after optimization of the coprecipitation synthesis before (black) and after aging (red) for 48 h at 70 °C and 80% relative humidity.

The obtained quantum efficiencies exceed all the results obtained by other explored synthesis methods. Even the etching synthesis, which produced highly efficient phosphors, though at a low chemical yield, does not outperform the coprecipitation synthesis. The absorption of 52% for an optimal coprecipitation is in the same range as the absorption of 59% for an optimal etching synthesis, which can be the limit for an optimal doped K_2SiF_6 host. Somewhat higher absorptions have been reached, such as 63% for a dopant concentration of 3%, but with lower quantum efficiencies. Since the highest quantum efficiencies have been found for a 2% Mn concentration, concentration quenching can lower the efficiency of higher doped phosphor samples.

10.4 Conclusion

A bright yellow-orange $K_2SiF_6:Mn^{4+}$ phosphor powder is obtained from a coprecipitation synthesis. The optimal dopant concentration is found to be 2% and full homogeneous incorporation can be seen in SEM-EDX. The best obtained EQE is 45% with an absorption of 52% of the blue light at 450 nm. The coprecipitation synthesis was optimized until the resulting homogeneous powder, without any crust formation, had a high absorption and quantum efficiency. This was achieved when a stable mixed solution of KF-K_2MnF_6 in HF was dropped in a beaker in a hot water bath at 50 °C simultaneously with a solution of SiO_2. The drop rate of the SiO_2 solution is preferably slower than the drop rate of the KF-K_2MnF_6 solution to prevent preliminary precipitation of undoped K_2SiF_6. Precipitation of the doped K_2SiF_6:Mn^{4+} phosphor happens instantaneously, but further dopant incorporation is reached when the mixture is stirred in the hot water bath for 1 h, after which it is decanted and the precipitation is filtered, washed with acetone and dried in air.

Although the dopant distribution is homogeneous as found using EDX, the light emission in SEM-CL is slightly heterogeneous, with more emission intensity from one side of the particle. Over all, the phosphor powder contains few defects, since the defect-induced bi-exponential decay behavior that was present with other synthesis methods, has disappeared. A mono-exponential decay behavior is found with a decay time of 16.3–5.2 ms in the 90–450 K temperature range. The phosphor powder is chemically stable, even after aging for 20 h at 70 °C and 80% relative humidity.

Table 10.2: Overview table of the four main synthesis methods of K_2SiF_6:Mn^{4+}.

Synthesis method	Advantages and disadvantages	[Mn] (%)	Quantum efficiency (%)	Synthesis conditions
Etching (chapter 6)	+ one step synthesis - no control on dopant concentration - low yield	powder 8.3% wafer 2.9%	IQE 69% EQE 40% A 0.59	25% HF room temperature filtered, washed
Precipitation (chapter 7)	+ one step synthesis + relatively high yield - low dopant concentration - Mn^{3+} and hydrate impurities	1.5%	IQE 46% EQE 12% A 0.25	40% HF 0 °C filtered, washed
Cocrystallization (chapter 9)	- two step synthesis - highly heterogeneous	2.6%	IQE 47% EQE 21% A 0.45	40% HF 70 °C solvent evaporation
Coprecipitation (chapter 10)	+ high yield + control on dopant concentration + pure, stable - two step synthesis	2%	IQE 88% EQE 45% A 0.52	40% HF 50 °C filtered, washed

Part III

Applications

11

K_2SiF_6:Mn^{4+} for brighter red in displays

With its emission essentially situated at 600–650 nm, the red-emitting K_2SiF_6:Mn^{4+} phosphor can be applied in both LEDs for display backlights and in warm-white LEDs for lighting applications. Both types of application call for efficient red phosphors, but the required specifications are different. K_2SiF_6:Mn^{4+} is included as a possible red phosphor in several patents for LED applications, including LED televisions and edge-lit displays which demand a large color gamut and for silicon-resin sheets for illumination applications [106, 107, 108, 109, 110, 111, 112, 113, 114, 115, 116].

K_2SiF_6:Mn^{4+} has even been proposed for the use in head lamps for cars [111], although the saturation behavior of K_2SiF_6:Mn^{4+} at high excitation fluxes (figure 7.12) seems incompatible with the high-brightness requirements. Besides lighting applications, K_2SiF_6:Mn^{4+} has been proposed as a downshifting phosphor for solar cell applications [117] and its stable emission can be used for magnetic field sensing and calibration [118]. K_2SiF_6:Mn^{4+} has also been proposed as a temperature sensor, due to the linear dependence of the anti-Stokes to Stokes emission intensity ratio on temperature [46]. Nevertheless displays and general lighting are the two

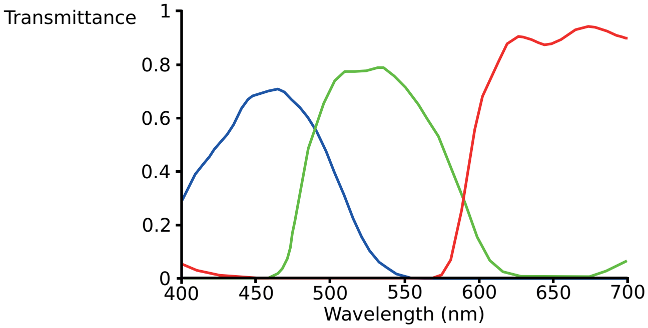

Figure 11.1: Transmission spectra of conventional RGB color filters, adapted from [119].

major applications of this red phosphor, justifying a more detailed discussion of the phosphor requirements for these applications. In this chapter, the requirements for display applications will be discussed, focussing on the opportunities for $K_2SiF_6:Mn^{4+}$.

11.1 Color gamut

Display applications require saturated colors to achieve the widest possible color gamut. To reach the Rec. 2020 standard, the primary RGB colors are ideally composed of monochromatic light located at respectively 630 nm, 532 nm and 467 nm [7]. Rec. 2020 improves the color gamut requirements compared to the 1953 National Television Standards Committee (NTSC) color gamut by 34% in the CIE (x,y) diagram (figure 2.3). When broad-emitting phosphors are used, narrow-band color filters are needed to obtain the mandatory nearly-monochromatic light. This reduces the total efficiency of the system, filtering away light from the phosphor emission, introducing a trade-off between color saturation and energy efficiency. The typical color filters used in displays are broader (figure 11.1), to reduce the losses, which in its turn influences the color gamut. The narrow emission spectrum of $K_2SiF_6:Mn^{4+}$ is an advantage for display applications, since less emission needs to be filtered out and the peak emission is located at the aimed position of 630 nm. In contrast to Eu^{2+}-doped nitride phosphors with a comparable peak wavelength, $K_2SiF_6:Mn^{4+}$ hardly contains emission beyond 650 nm, where the eye sensitivity steeply drops

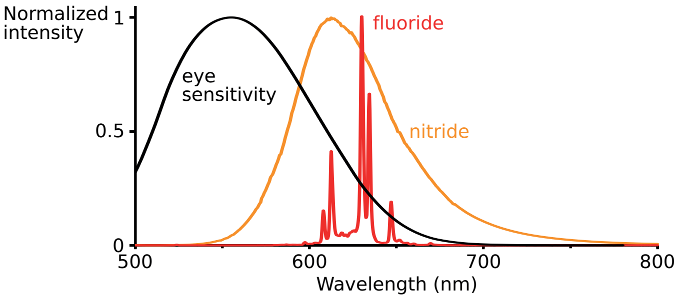

Figure 11.2: Emission spectrum of $K_2SiF_6:Mn^{4+}$ (red) compared to the emission spectrum of $CaAlSiN_3:Eu^{2+}$ (orange) and the eye sensitivity curve (black).

(figure 11.2). When $K_2SiF_6:Mn^{4+}$ is combined with a blue LED at 467 nm, only efficient, narrow green emission around 532 nm is needed to complete the full color gamut.

11.2 Phosphor combinations

Suitable narrow-band green phosphors are not yet available; the green phosphors β-SiAlON:Eu^{2+} and $SrGa_2S_4:Eu^{2+}$ both have a full width at half maximum (FWHM) of about 50 nm [17, 120], but color filters can be applied to obtain a more narrow green emission by cutting the tails of the emission band. Semiconductor nanocrystals (or quantum dots) are the main alternatives for display applications, thanks to their tunable and narrow emission [121]. Although the available quantum dots (QDs) were initially based on toxic CdS/CdSe core-shell QDs, cadmium-free QDs start to become available, such as InP or the lead halide perovskites [121, 122]. The wLED properties that are obtained when $K_2SiF_6:Mn^{4+}$ is combined with green phosphors or QDs and a blue LED chip are presented in table 11.1, aiming for a high color gamut. When ideal monochromatic RGB light is used according to the Rec. 2020 standard, the color gamut reaches up to 133.9% NTSC in the CIE 1931 color space. Combinations of $K_2SiF_6:Mn^{4+}$ and green phosphors or QDs reach color gamuts of 85–127 % NTSC in the CIE 1931 color space, as can be seen in table 11.1, with the highest value close to the ideal limit, using $CH_3NH_3PbBr_3/NaNO_3$ perovskite QDs. Interestingly, the current application of QDs is situated almost uniquely in display applications, characterized by less stringent conditions on temperature, flux and lifetime compared to general lighting. K_2SiF_6:Mn^{4+}, having similar application restrictions, is in the same playing field as the QDs.

Unfortunately, the performance of K_2SiF_6:Mn^{4+} alone cannot be quantified from these color gamuts, since the difference in color point for the different green QDs also influences the color gamut. Since the color gamuts are calculated in the CIE 1931 (x,y) color space, where the green area is larger compared to the CIE 1976 (u,v) color space, the influence of the green color point can be overestimated. Still, K_2SiF_6:Mn^{4+} can be qualified as a well-performing phosphor concerning the color points, when pc-wLEDs using K_2SiF_6:Mn^{4+} are compared to pc-wLEDs with the same green phosphor or QDs and a different red phosphor. For a pc-wLED using $SrGa_2S_4$:Eu^{2+} and K_2SiF_6:Mn^{4+}, color gamuts of 85–87 % NTSC are obtained. Lower color gamuts are obtained for pc-wLEDs with $SrGa_2S_4$:Eu^{2+} and $CaAlSiN_3$:Eu^{2+} (81 % NTSC) [123], or pc-wLEDs with $SrGa_2S_4$:Eu^{2+} and $Gd_2(MoO_4)_3$:Eu^{3+} phosphors (79 % NTSC) [124].

In display applications, red QDs will be the main competitors of the K_2SiF_6:Mn^{4+} phosphor, with CdSe/CdS based core-shell QDs as good options [121, 125]. It will be interesting to see how the competition between QDs and phosphors evolves in the coming years. While QDs offer superior, strongly tunable, narrow-band emission compared to the common broad-band emitting Eu^{2+} or Ce^{3+} phosphors, but their long-term (photo)stability currently limits their use in applications. Especially in display applications, where the driving current conditions are relatively benign and where their spectral properties are most beneficial, QDs are limited by their stability. The emergence of Mn^{4+}-doped red phosphors can be considered disruptive for the application of QDs, as they offer similar spectral properties as QDs, while maintaining basic properties of impurity-doped phosphors, such as a stable emission color and a stable intensity up to fairly high temperatures. The main disadvantages of Mn^{4+}-doped phosphors are the need for fluoride chemistry and often, similar to QDs, stability issues which have not yet been fully understood. Hence it is clear that the outcome of this competition is not a priori clear. For general lighting applications, characterized by much higher photon fluxes for extended durations, QDs cannot yet compete with impurity-doped bulk phosphors, although the currently developed approaches to allow their use in display applications can eventually pave the way for use in general lighting. Similarly, it will be interesting to see which share Mn^{4+}-doped phosphors will acquire in the market of general lighting, currently being solely occupied by Eu^{2+} and Ce^{3+}-doped phosphors.

11.3 Conclusion

The emission wavelength of K_2SiF_6:Mn^{4+} coincides with the ideal red color point at 630 nm for display applications. High color gamuts (up to 127% of the NTSC) can be reached when K_2SiF_6:Mn is combined with green perovskite quantum dots, which are close to the Rec. 2020 color gamut of 134% of NTSC. Higher color gamuts are reached using K_2SiF_6:Mn^{4+} compared to pc-wLEDs with different red phosphors, which shows that K_2SiF_6:Mn^{4+} is up to the challenge of ultra-high definition television and can improve the color gamut of smartphone screens. K_2SiF_6:Mn^{4+} has similar properties compared with red QDs, but if the stability can be controlled by an improved synthesis, the phosphor material might win the duel even in display applications.

Table 11.1: Lighting properties of K_2SiF_6:Mn^{4+} with green phosphors or QDs and a blue LED suited for displays

Phosphor or QDs	CCT (K)	CRI	CIE coordinates	Efficacy (lm/W)	K_2SiF_6:Mn (wt%)	phosphor (wt%)	% NTSC[1]	Ref.
β-SiAlON:Eu	4024	69	(0.37, 0.36)	67				[53]
β-SiAlON:Eu	8611		(0.28, 0.31)	91			86	[105]
β-SiAlON:Eu			(0.43, 0.19)	42.1			90	[90]
β-SiAlON:Eu							96	[126]
$SrGa_2S_4$:Eu			(0.35, 0.33)		38	62		[127]
$SrGa_2S_4$:Eu	5700			109	50	20	85	[128]
$SrGa_2S_4$:Eu	6800			104	50	15	87	[128]
$CH_3NH_3PbX_3$	5772		(0.33, 0.27)	48				[129]
$CH_3NH_3PbBr_3$/ $NaNO_3$		86.6	(0.28, 0.32)	22.39			127	[130]
$CH_3NH_3PbBr_3$ @POSS			(0.30, 0.33)	38				[131]
$CsPbBr_3$/ SDDA@PMMA							102	[120]
$CsPbBr_3$ @NH_4Br			(0.36,0.35)					[132]

---

[1] In the CIE 1931 color space

12

K_2SiF_6:Mn^{4+} in a pc-wLED

Although high color gamuts can be reached by combining K_2SiF_6:Mn^{4+} with green phosphors or QDs, these phosphor combinations cannot straightforwardly be transferred to lighting applications. Although the display solution of combining narrow-band red, green and blue components leads to white light and to a wide range of possible displayed colors, it falls short for lighting applications, where color rendering and color temperature are key factors. For example, narrow-RGB white LEDs lack yellow emission, hindering the optimal rendering of yellow objects. For lighting applications, a full coverage of the visible spectrum is desired to accurately render the color of objects, similar to a broad-emitting black-body radiating light source, such as the sun or an incandescent lamp. For energy-efficient lighting however, all invisible radiation, beyond the eye-sensitivity curve, should be omitted. Therefore, the combination of a blue LED with a broadband yellow phosphor and narrow red emission can be tailored to specific lighting specifications, such as the correlated color temperature (CCT) and the color rendering index (CRI). When K_2SiF_6:Mn^{4+} is combined with an LED (350–550 nm) and additional phosphors, CCT values of 2500–4500 K and CRI values of 70–95 can be reached [88].

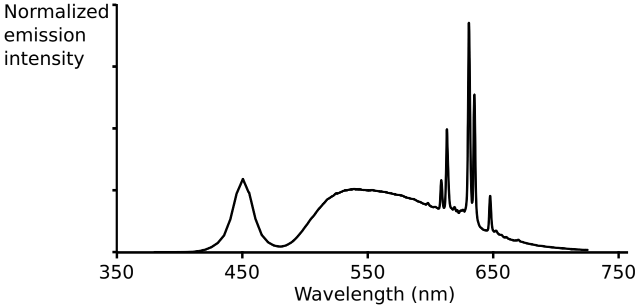

Figure 12.1: Simulated emission spectrum of a pc-wLED consisting of a blue LED chip and YAG:Ce and K_2SiF_6:Mn^{4+} as phosphor materials.

12.1 Method

YAG:Ce is a classic yellow LED phosphor with minimal emission in the red spectral region, making it ideally suited to be combined with the red-emitting K_2SiF_6:Mn^{4+}. The narrow red emission of K_2SiF_6:Mn^{4+} complements the broad yellow emission of YAG:Ce and the blue LED-chip emission of pc-wLEDs as can be seen in figure 12.1. Due to the large offset between the excitation and emission bands in the spectrum of K_2SiF_6:Mn^{4+} (figure 6.7), there is no reabsorption of YAG:Ce emission by the red phosphor. Therefore, the pc-wLED can be simulated by weighted addition of the emission spectra of a blue LED, YAG:Ce and K_2SiF_6:Mn^{4+}.

In figure 12.2, x is the K_2SiF_6:Mn^{4+} content, while $1-x$ is the YAG:Ce content in the total phosphor amount. The phosphor amount can be an actual weight percent (wt%) of phosphor added to the LED chip or a (simulated) ratio of converted photons. Here, the emission spectra are normalized on the number of emitted photons, implying an IQE of 100%. For each x, the D_{uv} value (the shortest distance of the LEDs color point to the blackbody locus in the CIELuv color space) is minimized by varying the ratio between the blue emission from the LED and the yellow and red emission from the phosphor blend to find an optimal white LED. By minimizing D_{uv}, the correlated color temperature is automatically fixed, since they are coupled in the Planckian locus. The total amount of phosphor used increases with a higher content of K_2SiF_6:Mn^{4+}, because more phosphor emission is needed to reach the blackbody locus at low color temperatures. The simulations of phosphor combinations for white LEDs were performed using the NIST-CQS software for a color quality scale published by the National Institute of Standards and Technology [133, 134, 135].

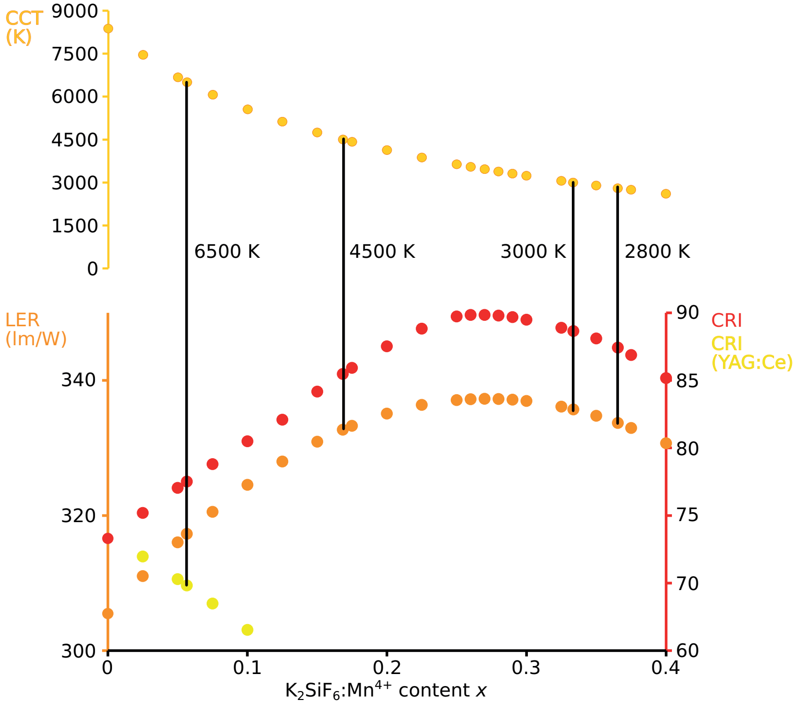

Figure 12.2: Range of correlated color temperature (CCT) (ocher, top), luminous efficiency of the radiation (LER) (orange) and color rendering index (CRI) (red) for a pc-wLED with YAG:Ce and $K_2SiF_6:Mn^{4+}$ phosphors in function of the phosphor ratio. CRI values (yellow) for a pc-wLED with YAG:Ce are projected on the x-axis for equal CCT values. The black lines are guides to the eye for a CCT of 6500 K, 4500 K, 3000 K and 2800 K.

12.2 Results

When increasing the amount of $K_2SiF_6:Mn^{4+}$ in the phosphor mixture, the CCT in figure 12.2 can be tuned from 8376 K for pure YAG:Ce to 2700 K for 61.7% YAG:Ce. Both the LER and the CRI in figure 12.2 reach a maximum value for $x = 0.27$. For $x > 0.6$, the values of both CRI and LER drop below the values of a YAG:Ce white LED. The addition of $K_2SiF_6:Mn^{4+}$ to YAG:Ce in a pc-wLED can improve the properties, but only within a specific range of phosphor combinations. It is important that in a wide range of CCT values (4750–2700 K), a sufficiently high CRI can be obtained (>80) while the LER remains above 320 lm W^{-1}, which is not the case when red phosphors with a much broader bandwidth are used. In that case, lowering the CCT results in a relatively larger spill of photons beyond 650 nm, where the eye sensitivity is low. The optimal combination of 73% YAG:Ce and 27% K_2SiF_6:Mn^{4+} in figure 12.1, results in a CCT of 3466 K, a CRI of 90 and a LER of 337 lm W^{-1}.

When only YAG:Ce is used in a pc-wLED, the range of available CCT values is lower. In figure 12.2, the CRI values for YAG:Ce are projected on the CCT values of a YAG:Ce–K_2SiF_6:Mn^{4+} pc-wLED, and they show a dramatic drop with decreasing color temperature. This shows the need for a red phosphor for warm-white light in YAG:Ce containing pc-wLEDs.

Apart from simulations, experimental pc-wLED setups have also been reported in literature to evaluate the properties of phosphor combinations. The lighting properties in table 12.1 are from experimental pc-wLED setups with YAG:Ce–K_2SiF_6:Mn^{4+} phosphors. The difference between the simulated data in figure 12.2 and the experimental data in table 12.1 is that perfect IQE values are assumed in simulations, while defect absorption and scattering effects can lower the QE and thereby also lower the luminescent output in experimental setups. In general, the values for CCT and CRI in table 12.1 are in accordance with the simulations in figure 12.2. These combinations are all best suited for lighting applications, aiming for efficient white light. The obtained CCT values reach from 2700 K (warm white) over 3900 K (cool white) to 5300 K (blue-white). This overview shows the broad possibilities with K_2SiF_6:Mn^{4+} upon combination with YAG:Ce. Comparing the efficacy for the different phosphor combinations is difficult, because the overall efficacy is largely determined by the electrical-to-optical conversion efficiency of the blue pumping LED. This is reflected in the efficacy values given in table 12.1, spanning 36.7–129.3 lm W^{-1}. For YAG:Ce combined with K_2SiF_6:Mn^{4+} a CRI value of 63.9–93 is obtained for the tested devices, with low CRI values obtained for high CCT values with a large D_{uv} values. For simulations, reaching a small D_{uv} is possible, resulting in a CRI value of 90-94 for an average phosphor amount of one-third of K_2SiF_6:Mn^{4+} and two-thirds of YAG:Ce [24, 141].

Although good lighting properties can be obtained using YAG:Ce, the red-emitting K_2SiF_6:Mn^{4+} can also be combined with other phosphors or QDs to improve the lighting properties even further. The lighting properties from experimental phosphor/QD–K_2SiF_6:Mn^{4+} pc-wLED setups or from simulations thereof are presented in table 12.2. LuAG:Ce is very similar to YAG:Ce, but substitution of the Y ion for Lu causes a blueshift of the Ce^{3+} emission, which allows to narrow the cyan gap [142]. Adding K_2SiF_6:Mn^{4+} will increase the wLED emission in the red region, but the blueshifted Ce^{3+} emission will be less intense in the orange region, result-

Table 12.1: Lighting properties of K_2SiF_6:Mn^{4+} with YAG:Ce and a blue LED suited for lighting.

CCT (K)	CRI	CIE coordinates	LER (lm/W)	Efficacy (lm/W)	K_2SiF_6:Mn (wt%)	YAG:Ce (wt%)	Ref.
5296[1]	63.9	(0.34, 0.40)		64.7			[111]
3840	67.6	(0.39, 0.42)		40			[80]
4470	78.7	(0.36, 0.36)		129.3			[136]
4492[2]	79.7	(0.36, 0.37)		36.7			[111]
2704	81.2			122			[51]
4205[3]	82.7	(0.38, 0.42)		64.2	6.25	20	[137]
6000[4]	86	(0.32, 0.31)					[138]
3519	87	(0.42, 0.42)		82			[53]
3900	89.9	(0.38, 0.33)		116			[139]
3510[5]	90.9	(0.40, 0.39)		81.56	22.22	5.56	[140]
3766[6]	93	(0.40, 0.41)		79			[53]

---

[1] K_2SiF_6:Mn^{4+} layer on top

[2] YAG:Ce layer on top

[3] Embedded in epoxy

[4] K_2SiF_6:Mn^{4+} with oleic acid coating

[5] Embedded in silicone

[6] K_2SiF_6:Mn^{4+} with alkyl coating

ing in lower CRI values for warm-white CCT values, compared to YAG:Ce. Red phosphors with a broader emission band like $Sr_2Si_5N_8$:Eu^{2+} profit more from the use of LuAG:Ce since the broad red emission covers the orange region [141]. The gap in the orange region can also be filled by adding (Sr,Ca)$AlSiN_3$:Eu^{2+} to the mix of LuAG:Ce and K_2SiF_6:Mn^{4+}, resulting in an CRI of 97 [142].

The CRI values are higher for the combination of the blue-emitting BAM:Eu^{2+} and the green-emitting $SrSi_2N_2O_2$:Eu^{2+} with K_2SiF_6:Mn^{4+} compared to the LuAG:Ce–K_2SiF_6:Mn^{4+} phosphor combination, but UV-LED excitation is necessary for BAM:Eu^{2+}, which severely worsens the overall electrical–optical efficiency of this wLED configuration [143]. Even though it is possible to excite K_2SiF_6:Mn^{4+} with UV light around 360 nm, excitation with blue light is more efficient due to the more intense excitation band in the blue region. Moreover, the choice for BAM:Eu^{2+} is not ideal, since its emission at 450 nm is efficiently absorbed by K_2SiF_6:Mn^{4+}, further reducing the total conversion efficiency if the IQE is <100%. High CRI values for pc-wLEDs containing K_2SiF_6:Mn^{4+} have been reported by GE without mentioning the composition of the yellow phosphor used in the phosphor blend [84, 144], and by using alkaline-earth silicate phosphors doped with Eu^{2+} [10].

The broadness and peak position of the red-emitting phosphor are more critical in the warm-white than in the cool-white LED from the viewpoint of optimizing human perception of color. The LER of Mn^{4+}-doped fluoride phosphors increases with the decrease of local symmetry, because the higher ZPL emission results in a slight blueshift of the total emission. The optimization of color rendition is a trade-off. For Mn^{4+}-doped fluoride phosphors with bandwidths smaller than 30 nm, the blueshifted color is better for energy efficiency while the redshifted color is beneficial for color rendition. Apart from a good color rendering and a high efficiency, a long lifetime is expected for pc-wLEDs, up to 50 000 h [145]. To reach this long lifetime, the phosphor has to remain stable during this lifetime.

12.3 Color stability

The color stability of a phosphor or a pc-wLED can be quantitatively described by the chromaticity shift (ΔE) defined in equation 12.1 [146].

$$\Delta E = \sqrt{\left(u'_f - u'_i\right)^2 + \left(v'_f - v'_i\right)^2 + \left(w'_f - w'_i\right)^2} \qquad (12.1)$$

Table 12.2: Lighting properties of $K_2SiF_6:Mn^{4+}$ with phosphors and a blue LED suited for lighting.

Phosphor	CCT (K)	CRI	LER (lm/W)	Efficacy (lm/W)	Amount of K_2SiF_6:Mn	Amount of phosphor	Ref.
LuAG:Ce	2700	64	314		0.51	0.43	[141]
LuAG:Ce	3000	67	315		0.47	0.45	[141]
LuAG:Ce	3000	60.9		92.4	1	5.1	[142]
LuAG:Ce + SCASN[7]		96.9		115.4	6	5.1:0.72	[142]
BAM:Eu^{2+} + $SrSi_2N_2O_2$:Eu[8]	2700	80	348		0.50	0.09:0.41	[141]
BAM:Eu^{2+} + $SrSi_2N_2O_2$:Eu[9]	3000	82	347		0.45	0.11:0.43	[141]
$La_3Si_6N_{11}$:Ce[10]	2686	87	222		31.7 wt%	4.4 wt%	[109]
?[11]	4000	>90		137			[84]
?	3750	95	325	125			[144]
M_nSiO_4:Eu + M_3SiO_5:Eu[12]	2700	94	328	107			[10]

---

[7] $(Sr,Ca)AlSiN_3:Eu^{2+}$

[8] UV LED 395 nm

[9] UV LED 395 nm

[10] In silicone resin, CIE (0.46, 0.41)

[11] Stable over 5000 h

[12] M = (Ba, Ca, Sr)

with

$$\begin{aligned} u' &= 4x/(3-2x+12y) \\ v' &= 9y/(3-2x+12y) \\ w' &= 1-u'-v' \end{aligned} \tag{12.2}$$

In these equations, u' and v' are the chromaticity coordinates in $u'v'$ uniform CIE 1976 color space, x and y are the chromaticity coordinates in the CIE 1931 color space, and i and f are referring to the initial and final CIE coordinates respectively [146].

The chromaticity shift can be used to quantify the influence of intrinsic LED parameters such as operating temperature or the operating current. It can also quantify the stability of the color point after aging the phosphor or LED in a climate chamber. When increasing the temperature from room temperature to 500 K a wLED composed of YAG:Ce and $K_2SiF_6:Mn^{4+}$ had a chromaticity shift of 0.031 (orange dots in figure 12.3). This shift is lower than the shift of 0.041 of a wLED composed of YAG:Ce and the commercial $(Ca,Sr)AlSiN_3:Eu^{2+}$ phosphor [80]. This shift can be caused by either thermal quenching or thermally induced degradation. Thermal quenching starts from 400 K in $K_2SiF_6:Mn^{4+}$, as was discussed in chapter 7, although an improved synthesis lead to a phosphor stable up to 469 K (chapter 10). The $K_2SiF_6:Mn^{4+}$ phosphor is stable in air to at least 473 K, as discussed in chapter 7, but can degrade at higher temperatures.

In a pc-wLED containing β-$SiAlON:Eu^{2+}$ and $K_2SiF_6:Mn^{4+}$ the influence of HTHH conditions is in the same order of magnitude as the temperature influence. For 0–1000 h at 85 °C and 85% relative humidity, the chromaticity shift increased to 0.038 after 1000 h (red squares in figure 12.3) [90]. The chromaticity shift is bigger compared to a pc-wLED with β-$SiAlON:Eu^{2+}$ and $CaAlSiN_3:Eu^{2+}$ and when both red phosphors are combined [90], showing that $K_2SiF_6:Mn^{4+}$ is less stable than $CaAlSiN_3:Eu^{2+}$ in this setup.

A pc-wLED at 2700 K with four components; a blue LED, a green and an amber Eu-doped silicate phosphor and $K_2SiF_6:Mn^{4+}$ shows a rather small chromaticity shift as a function of both temperature (20–120 °C) and applied current (250–1500 mA), as can be seen in figure 12.4 (yellow dots, red triangles) [10]. Since an increased current also increases the temperature of the LED chip, no distinction could be made between the influence of the temperature and the applied current. Other setups show similar behavior, in pc-wLEDs with a bilayered phosphor film containing

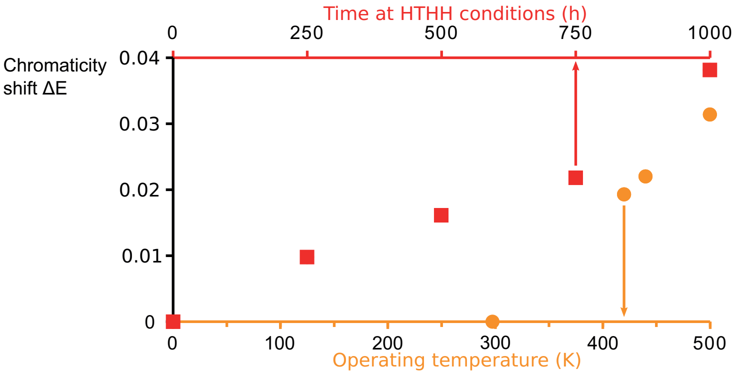

Figure 12.3: Influence of HTHH conditions (red) and operating temperature (orange) on the chromaticity shift ΔE for $K_2SiF_6:Mn^{4+}$ (combined with β-SiAlON:Eu^{2+} in HTHH conditions). Data from [80, 90].

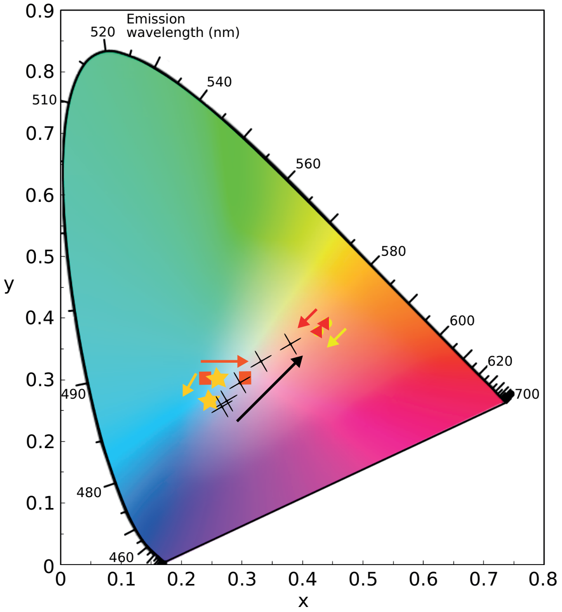

Figure 12.4: Chromaticity shift of a pc-wLED containing $K_2SiF_6:Mn^{4+}$ and green and amber Eu-doped silicates (yellow dots, red triangles) or $SrGa_2S_4:Eu^{2+}$ (orange squares, ocher stars) as a function of applied current (250–1500 mA for yellow dots, 10–180 mA for orange squares) and temperature (20–120 °C for red triangles and ocher stars), data obtained from [10, 128]. Influence of phosphor ratio YAG:Ce–$K_2SiF_6:Mn^{4+}$ (0–22.22 wt% for black crosses) on the position of the pc-wLED on the CIE diagram, data obtained from [140].

$K_2SiF_6:Mn^{4+}$ and $SrGa_2S_4:Eu^{2+}$ a larger chromaticity shift is seen under influence of applied current (10–180 mA) and temperature (20–120 °C) [128]. A blueshift is seen in figure 12.4 (orange squares, ocher stars) with both increasing current and temperature. A setup with a $K_2SiF_6:Mn^{4+}$ phosphor coated with oleic acid showed a distinct greenshift for a 60–140 mA current increase [138]. Post-synthesis treatments improve the color stability of $K_2SiF_6:Mn^{4+}$. Though no absolute CIE coordinates are published, it has been shown that the shift in CIE coordinate is smaller for $K_2SiF_6:Mn^{4+}$ that is annealed in a F_2 atmosphere. When $K_2SiF_6:Mn^{4+}$ is annealed in a F_2 atmosphere and afterwards coated with K_2SiF_6, the chromaticity shift is negligible, without a shift in the y coordinate and only a shift of 0.004 in the x coordinate [85]. This shows that the chromaticity shift of $K_2SiF_6:Mn^{4+}$ is influenced slightly by different properties of the pc-wLED, including driving current, operating temperature and aging effects, but that coatings can improve the stability and further reduce the chromaticity shift. The chromaticity shift is obviously smaller than the influence of the red and yellow phosphor ratio. The color point of the wLED on the CIE diagram can be changed from cold-white light to warm-white light depending on the YAG:Ce–$K_2SiF_6:Mn^{4+}$ ratio, as is shown in the experimental data sets (black crosses) in figure 12.4 [140]. On the other hand, stable color points have not been achieved for reasonable operating conditions such as temperatures up to 120 °C. Only phosphor samples that were annealed in a F_2 atmosphere obtain a relatively stable performance.

12.4 Conclusion

Because of the large Stokes shift in $K_2SiF_6:Mn^{4+}$, it can be combined with the broad-band emitting YAG:Ce to form a warm-white LED without reabsorption processes reducing the total efficiency. CCT values of 4750–2700 K can be obtained with a CRI values exceeding 80, using a varying amount of $K_2SiF_6:Mn^{4+}$. The combination of 73% YAG:Ce and 27% $K_2SiF_6:Mn^{4+}$ resulted in a pc-wLED with a CCT of 3466 K, a CRI of 90 and a LER of 337 lm W^{-1}. In literature, many phosphor combinations for pc-wLEDs are found which are applicable to lighting applications. YAG:Ce remains the main contestant to combine with $K_2SiF_6:Mn^{4+}$, but the somewhat shifted emission spectrum from LuAG:Ce is also a possible candidate, as well as Eu-doped silicate or oxynitride phosphors. The color stability of pc-wLEDs with $K_2SiF_6:Mn^{4+}$ is not as good as that of pc-wLEDS with β-

SiAlON:Eu^{2+} and $CaAlSiN_3$:Eu^{2+} phosphors. Only K_2SiF_6:Mn^{4+} annealed in a F_2 atmosphere is reported to have a relatively stable performance at elevated temperatures.

13

Remote phosphor applications of $K_2SiF_6:Mn^{4+}$

In pc-wLEDs, the phosphor material is most often deposited directly on the blue LED chip. In several applications, such as bicycle lights or smartphone flashlights, the yellow phosphor material is clearly visible (figure 13.1). In a remote phosphor setup, the phosphor layer is separated from the LED chip (figure 13.2). This can reduce the operating temperature of the phosphor because there is no direct heat transfer from the LED chip to the phosphor material. Saturation effects are also limited in remote phosphor setups, because the excitation flux is spread over a larger phosphor surface. Since more phosphor material is needed in a remote phosphor setup, cheap phosphors are preferred, which promotes Mn^{4+}-doped phosphors over rare-earth-doped phosphors.

For a lab scale coprecipitation synthesis, the estimated material cost for 10 g of $K_2SiF_6:Mn^{4+}$ with a dopant concentration of 2% is €14, of which K_2MnF_6 contributes to 30% of the costs and HF contributes to 60% of the costs. Different from solid state synthesis, no energy-consuming high-temperature synthesis is needed for fluoride phosphors. For small designs, the $K_2SiF_6:Mn^{4+}$ phosphor is cheap enough to include in a remote phos-

Figure 13.1: Smartphone with LED flashlight using a yellow phosphor.

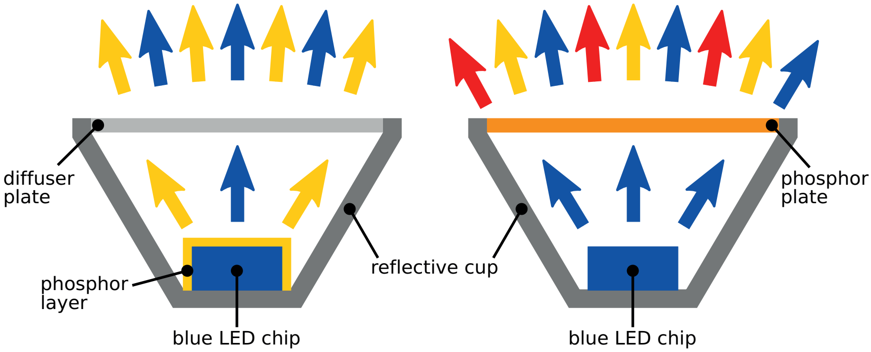

Figure 13.2: Schematic illustration of a classical wLED (left) and a remote phosphor setup (right).

phor layer, as circular layers with a diameter of 5 cm can be made with a phosphor cost of €1, for an absorption of the layer of 33% for an assumed IQE close to unity.

In the phosphor layers, the excitation light can be absorbed when it reaches a phosphor particle. After the blue light is converted to red (or yellow) light, the emitted light has to leave the layer. Unlike a powder phosphor, light from an incorporated phosphor has to pass several interfaces at which the light can be refracted or scattered. Although some refraction at a refractive boundary between the phosphor particle and its surroundings is inevitable, total internal reflection in a luminescent layer should be avoided. In a phosphor layer, scattering occurs a lot on the phosphor particles. When the absorption is low, more phosphor material is added to the layer, to the point that the emission light can be trapped in the phosphor layer due to the high scattering probability. Lowering the scattering effects by creating transparent layers can improve the light outcoupling in this case. For specific applications, such as luminescent solar concentrators, fully transparent phosphor layers are essential, to absorb the incoming light followed by outcoupling of the light on the edges of the layer, where solar cells are positioned. Perfect transparent absorbing phosphor layers have a single-crystal or ceramic-like behavior and the guided light in the phosphor layer has a relatively small étendue compared to the incident light.

The refractive index of K_2SiF_6 from literature is 1.34 at 590 nm [37]. Some influence of the Mn-doping on the refractive index is possible, but a refractive index of 1.34 was also reported for K_2SiF_6:Mn^{4+} [147]. To match the refractive index of the polymer to that of the phosphor, low-refractive index polymers are needed, such as the NOA polymers (Norland Products). The specific composition of the NOA polymers is withheld as a trade secret, but it consists of an aliphatic urethane acrylate and an acrylate monomer, which are crosslinked under influence of UV radiation. Refractive indexes as low as 1.33–1.36 are only obtained for perfluorinated polymers, containing only C-F bonds, C-C bonds and other heteroatoms. Of this material class, polytetrafluoroethylene (PTFE), best known by the brand name Teflon, is well known for its use as non-stick coating in cookware.

To explore the application of K_2SiF_6:Mn^{4+} as a red phosphor in remote phosphor pc-wLEDs, polymer layers containing K_2SiF_6:Mn^{4+} were prepared. By matching the refractive index of the phosphor and the polymer, semitransparent phosphor layers could be obtained in which the scattering effects are limited. The luminescence properties and application possibilities of the transparent phosphor layers are discussed in this chapter.

13.1 Experimental

The K_2SiF_6:Mn^{4+} phosphor used for the phosphor layers was synthesized using the optimized coprecipitation synthesis from chapter 10. The phosphor powder was slightly ground in a mortar before mixing with the polymer. Two variants of the low-refractive index UV adhesives of Norland Optical Adhesives (NOA), NOA 133 and NOA 136 (Norland Products) were mixed with phosphor powder to construct phosphor layers with a variation in refractive index and phosphor load. The polymers have a refractive index of 1.33 and 1.36 respectively. Intermediate refractive indexes can be formed by mixing the polymers.

A phosphor layer is made by weighing phosphor powder, after which the respective amounts of liquid NOA 133 and NOA 136 are added. The polymers and phosphor powder are mixed with a spatula until the powder is homogeneously mixed with the liquid polymer, in the meanwhile avoiding the creation of air bubbles. The phosphor-polymer mixture is deposited on a circular glass substrate with a diameter of 18 mm. A second glass substrate is put on the mixture and slightly pressed to spread the polymer mixture over the substrate and to form a uniform phosphor layer between the glass substrates. The substrates are exposed to a 365 nm fluorescent UV lamp for 5 h to induce UV curing of the polymer.

13.2 Results

Phosphor layers containing $K_2SiF_6:Mn^{4+}$ and NOA polymers were made with a varying refractive index and phosphor load.

13.2.1 Refractive index

For a phosphor load (mass fraction of phosphor to polymer) of 0.50 ± 0.01, the refractive index was varied to values of 1.338, 1.345, 1.352, 1.358 and 1.360. The refractive index was calculated according to the effective medium theory using to the Maxwell Garnett approximation. Phosphor layers with a lower refractive index could not be made with semitransparent properties, since the low viscous NOA 133 polymer ($\eta = 15\,\mathrm{mPa\,s}$) separates from the phosphor powder in the layers before curing. Mixing NOA 133 with the higher viscous NOA 136 ($\eta = 160\,\mathrm{mPa\,s}$) results in a workable surface tension, that makes uniform spreading of the layer over the substrate possible. Although air bubbles are avoided as much as possible, they are inevitable in the phosphor layers and impossible to remove between the two glass substrates, resulting in some scattering induced by air bubbles. The layers in figure 13.3 have an increasing refractive index from left to right. On the white background, not much difference can be seen between the layers and when text is portrayed on the white background, it is readable through the layers. On the black background, the slight heterogeneity in phosphor density is visible for the lowest three

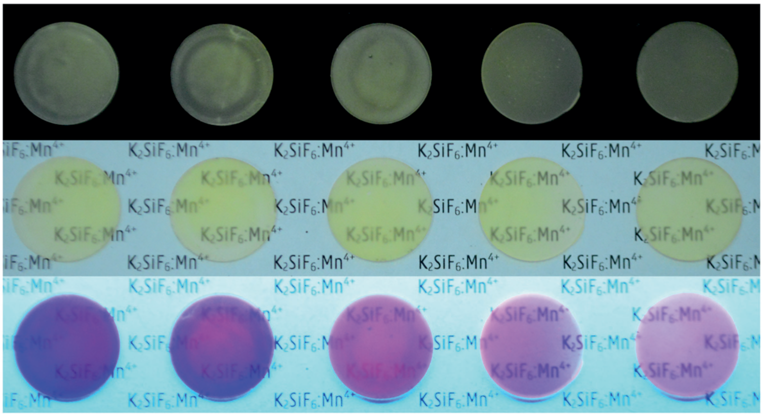

Figure 13.3: Phosphor polymer layers with an increase in refractive index of the polymer, from left to right 1.338, 1.345, 1.352, 1.358 and 1.360, displayed on a black background (top), on a white background (center) and under UV illumination at 365 nm (bottom).

Table 13.1: Quantum efficiency and absorption values of phosphor layers with a phosphor load of 0.50 and a variable refractive index n.

n	IQE	EQE	absorption
1.338	90%	35%	0.39
1.345	88%	36%	0.41
1.352	90%	42%	0.46
1.358	99%	35%	0.35
1.360	94%	35%	0.37

refractive-index values. For a refractive index of 1.338–1.352 , concentric circles show in the phosphor-polymer mixture and some scattering phosphor particles can be detected by visual inspection. The layers with a refractive index of 1.358 and 1.360 show a homogeneous surface with some small air bubbles in the 1.358-layer.

The quantum efficiencies (table 13.1) were measured using the integrating sphere setup discussed in chapter 4, using a high-power LED in a white light-mixing cup. The LED is a royal-blue LUXEON Rebel EX LED mounted on a 20 mm Star Saber with an emission wavelength of 453.3 nm. The QE is calculated comparing the emission spectra to a reference polymer layer with a refractive index of 1.360, containing no phosphor material. The absorption of the phosphor layer is the difference between the

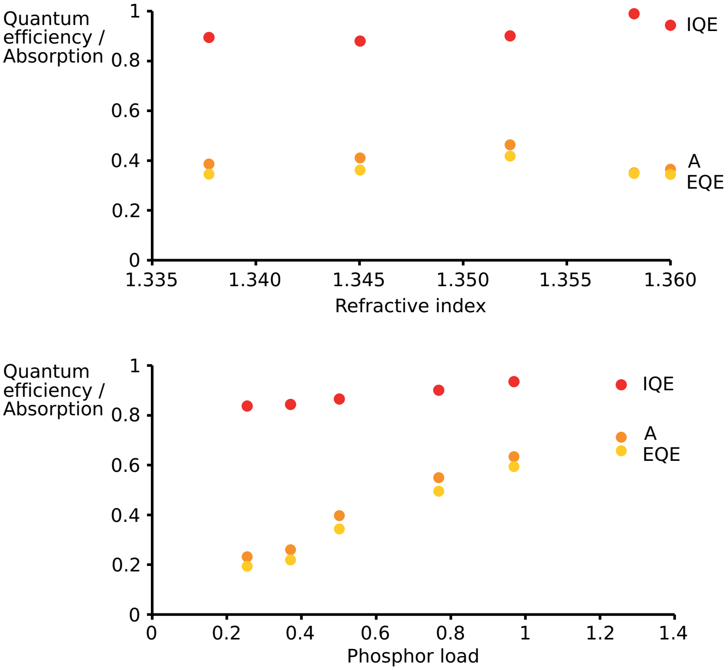

Figure 13.4: Quantum efficiency and absorption values for different phosphor layers, as a function of refractive index (top) and phosphor load (bottom).

emission intensity of the transmitted blue light of the reference layer and the phosphor layer. Somewhat different values were obtained for phosphor layers compared to the powder measurements, where an IQE of 88%, an EQE of 45% and an absorption of 52% were obtained for the phosphor used in the phosphor layers. The difference between the values is caused by the measurement setup, since powders are measured in reflection mode while the transparent layers are measured in transmission mode. Due to the reduced scattering, less blue light is absorbed during the transmission of the blue light, since the path length of the blue light is limited. In powder samples, multiple scattering events can increase the path length of the blue light, which explains the higher absorption and EQE found in the powder phosphor compared to the phosphor layers. A high emission intensity is obtained for both the powder phosphor and the phosphor layers. The higher IQE values can be caused by less scatter losses, emitted light that is scattered and absorbed by other centers, in the transparent layers compared to the powder sample.

The quantum efficiencies are quite stable as a function of the refractive index, averaging to an IQE of (92 ± 4) %, an EQE of (36 ± 3) % and an absorption of 0.40 ± 0.04 (figure 13.4, top). The reference layer had a refractive index of 1.360, even for layers with a different refractive index, which hardly affects the QE measurements. When the different layers were compared, the higher refractive indexes (1.358 and 1.360) were more transparent to the eye. In contrast, for the layers with a lower refractive index, the phosphor particles were still visible in the layers. From this refractive index variation, 1.360 was selected as the optimal refractive index to achieve a semitransparent K_2SiF_6:Mn^{4+} phosphor layer. This refractive index is somewhat higher than the refractive index of 1.34 that has been reported for K_2SiF_6, which can be an influence of the Mn doping.

13.2.2 Phosphor load

To study the absorption behavior of the K_2SiF_6:Mn^{4+} phosphor in the polymer layers, a series of phosphor layers with a different phosphor load were made. For this, 0.051 g, 0.075 g, 0.101 g, 0.150 g, 0.200 g and 0.250 g of phosphor was mixed with 0.195–0.206 g of NOA 136 liquid polymer, to create phosphor layers with a phosphor to polymer ratio (phosphor load) of 0.25, 0.37, 0.50, 0.77, 0.97 and 1.26. Higher phosphor loads are not possible for an equal amount (0.200 g) of polymer, since the viscosity of the phosphor-polymer mixture increases with higher phosphor amounts, until it is too high to form uniformly mixed phosphor-polymer layers. Introducing higher phosphor amounts is possible, by keeping a phosphor load around 1 and increasing the volumes of both the phosphor powder and the polymer. Due to the relatively high surface tension of NOA 136, a uniform layer forms on the glass substrate while the risk of overflowing the substrate is limited.

The phosphor layers in figure 13.5 have an increasing phosphor load from left to right. All layers are reasonably transparent, although the readability of text through the layer decreases with increasing phosphor load, as can be expected. Less light scattering is induced in lower loaded phosphor samples, since less phosphor particles are present, but the lower load also leads to a lower absorption.

The quantum efficiencies and absorption values (table 13.2) were calculated comparing the transmission spectra to a reference polymer layer with a refractive index of 1.360 and a phosphor load of 0. As expected, the absorption increases with increasing phosphor load, up to 71% for a

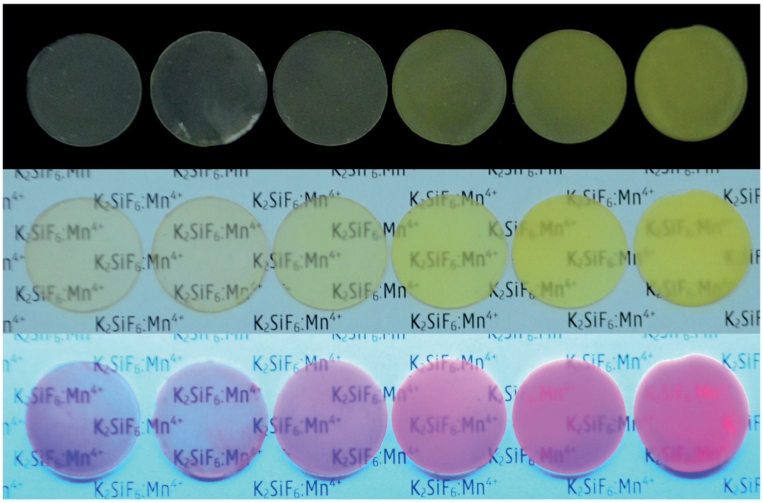

Figure 13.5: Phosphor polymer layers with an increase in phosphor load, from left to right 0.25, 0.37, 0.50, 0.77, 0.97 and 1.26, displayed on a black background (top), on a white background (center) and under UV illumination at 365 nm (bottom).

Table 13.2: Quantum efficiency and absorption values of phosphor layers with a refractive index of 1.360 and a variable phosphor load.

phosphor load	IQE	EQE	absorption
0.25	84%	19%	0.23
0.37	84%	22%	0.26
0.50	87%	34%	0.40
0.77	90%	50%	0.55
0.97	94%	59%	0.63
1.26	92%	66%	0.71

relative load of 1.26 (figure 13.4, bottom). High IQE values are found, that increase slightly with increasing phosphor load. Due to reasonably good refractive index matching, scatter losses can be reduced even for an increasing phosphor load, which results in an increase in IQE.

The diffuse transmission measurements (figure 13.6) show the d-d absorption band of Mn^{4+} around 450 nm. The transmission in the 500–800 nm wavelength range is determined by the scattering of light by the phosphor layers. For the unloaded phosphor layer, a transmission of 93% is

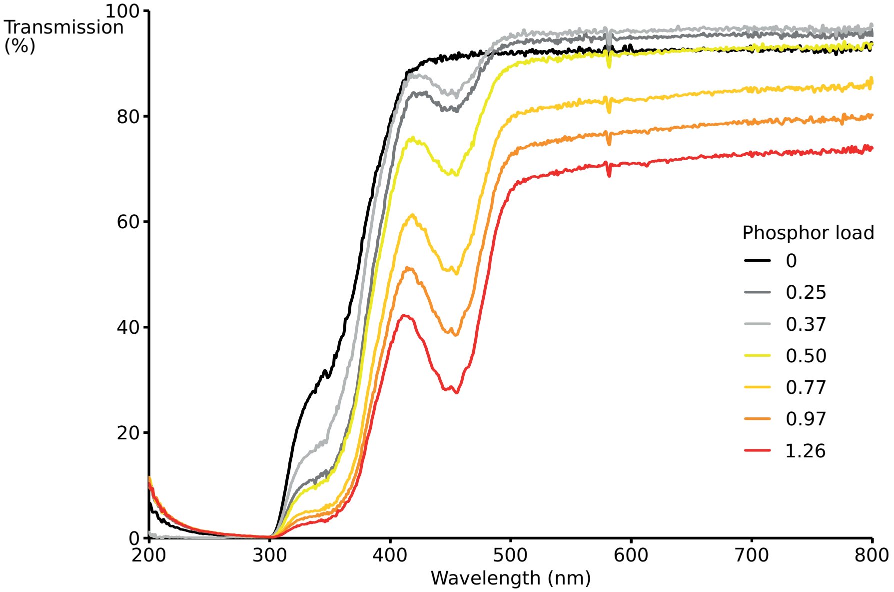

Figure 13.6: Diffuse transmission measurement of phosphor layers as a function of phosphor load.

reached. Somewhat higher values were reached for the low loaded layers, a transmission of 96% for the 0.25-loaded phosphor layer and a transmission of 95% for the 0.37-loaded phosphor layer. The higher transparency of the low loaded layers can be caused by small polymer stains that cause unwanted light scattering in the reference sample. For a low phosphor load, the blue light absorption is rather low (0.23–0.26) due to the low amount of phosphor powder present, but scattering is also low due to the good mixing and reasonably good refractive index matching of phosphor particles and polymer.

13.3 Kraton layers

To appreciate the performance of the phosphor layers containing the NOA polymers, it should be compared to a polymer with a different refractive index. Kraton FG1901X is a polymer used for phosphor layers and quantum dot layers [121]. The phosphor layers were prepared by David Van der Heggen by mixing the phosphor powder with a solution of 20 m% Kraton FG1901X in a mixed solvent of 3:1 toluene (VWR) and methyl ethyl ketone (99.5%, Fluka). The phosphor and polymer mixture was magnet-

Table 13.3: Quantum efficiencies and absorption values of phosphor layers containing Kraton polymer with a different phosphor load.

phosphor (mg)	IQE	EQE	absorption
56	58%	19%	0.32
66	62%	24%	0.39
powder	96%	32%	0.34

ically stirred, drop casted on a circular glass substrate with a diameter of 18 mm, after which the solvents are evaporated at room temperature. The refractive index of the Kraton FG polymer is 1.51 at 633 nm [148], which is significantly higher than the refractive index of the K_2SiF_6:Mn^{4+} phosphor powder. The difference between two different possible embedding materials, Kraton FG1901X and NOA 136, is seen in figure 13.7. For a similar phosphor weight, 56 mg and 51 mg for Kraton and NOA respectively, the transparency is greatly improved for the NOA polymer, which has a refractive index similar to that of K_2SiF_6:Mn^{4+}. The phosphor layer using the Kraton polymer in figure 13.7 includes a similar amount of phosphor as the 0.25-loaded phosphor layer, but the transmission of text is comparable to the 1.26-loaded phosphor layer.

The quantum efficiency values for two phosphor layers using the Kraton polymer are given in table 13.3. A glass substrate was used as a reference for blue emission peak. Compared to the quantum efficiency values of the layers with the NOA polymer (table 13.2), lower values are found for both the IQE and EQE. In the Kraton layers that are not very transparent, scattering losses cause a lower IQE. Although the initial EQE of the powder is a little lower compared to the powder used in NOA polymer layers, the drop in IQE is large compared to the NOA polymer layers, which show only a small drop in IQE for layers with a low load and an increase in IQE for layers with a high load. The absorption values of the Kraton layers are higher compared to NOA layers with a comparable phosphor load (0.25 and 0.37 respectively), so at least a similar IQE would be expected. The IQE values of the Kraton layers are lower than expected based on the NOA layers, which can be related to the higher scatter losses in the Kraton layers.

Increasing the number of materials used to form a remote phosphor layer also increases the number of boundaries at which refraction occurs. A glass substrate is used to support the liquid polymer-phosphor mixture

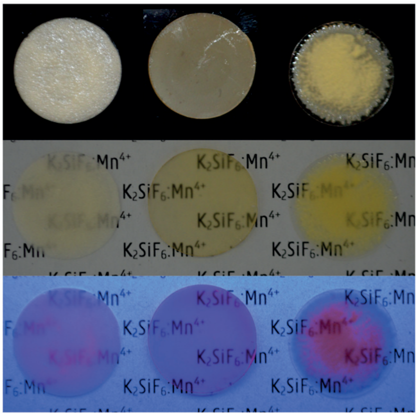

Figure 13.7: Three $K_2SiF_6:Mn^{4+}$ phosphor layers, with Kraton FG1901X (left), NOA 136 (center) and a mixture of NOA 136 and NOA 133 as embedding polymer (right), displayed on a black background (top), on a white background (center) and under UV illumination at 365 nm (bottom). The center polymer layer is embedded between two glass substrates, while the other polymer mixtures are deposited on a single glass substrate.

before it is hardened and to keep the circular shape. The glass substrate induces a smooth bottom surface, while a smooth top surface should be formed by the polymer-phosphor mixture. Using Kraton FG1901X, a rather smooth surface is formed, reducing scattering on the surface, although some heterogeneous phosphor density is visible upon UV illumination. Using the NOA polymer, a smooth surface cannot be formed on a glass substrate, because the surface tension of the polymer prevents full coverage of the substrate, as can be seen in the right layer in figure 13.7. To solve this, a second glass substrate was used on top of the polymer layer. With the polymer-phosphor mixture squeezed in between two glass substrates, a smooth, homogeneous phosphor layer can be formed covering the full substrate, as can be seen in the center layer in figure 13.7, but the polymer is not rigid enough to form a self-supporting phosphor layer.

13.4 Conclusion

Semitransparent phosphor layers could be made using the low-refractive index polymer NOA 136, with the optimal refractive index of 1.36. Layers with a phosphor load up to 1.26 were made, which were however not able to reach a 100% absorption of blue light. Practically, phosphor loads should be limited to one, to keep a viscous phosphor-polymer mixture to form layers. A higher phosphor amount can be deposited in a somewhat thicker layer keeping the phosphor load to 1. In this way, reaching a higher absorption than 71% can be possible. Lowering the scattering effects by creating transparent layers can improve the light outcoupling for phosphor layers where the large phosphor amount would otherwise induce high scatter losses. It has to be noted that $K_2SiF_6:Mn^{4+}$, with its low refractive index, forms an quite easy case for index matching with a polymer. Oxide and sulphide phosphors have a refractive index that can be much higher, even above 2, which makes it difficult to match their refractive index with an organic binder.

Summary: conclusions and perspectives

Efficient solid state lighting makes use of so-called phosphors to convert blue light to yellow, green or red. The workhorse of white LEDs contains a blue LED and a yellow phosphor, YAG:Ce, but the color rendering in the red wavelength region is not optimal. Addition of an efficient red phosphor to the mix increases the color rendering, the luminous efficacy and improves the obtained color temperature. Since the eye sensitivity is limited above 650 nm, phosphors should show bright red emission around 600–650 nm for lighting applications, while display applications require nearly monochromatic emission at 630 nm. Red emission is typical for Mn^{4+}-doped phosphors, both in fluorides and oxides. For lighting applications, fluoride hosts are needed because the limited nephelauxetic effect of fluorides cause saturated red emission (630 nm) for fluoride hosts such as K_2SiF_6, while oxide hosts show deep red to near-infrared emission.

The synthesis of Mn^{4+}-doped fluorides is not possible using the solid state synthesis that is typical for phosphors. Several wet chemical synthesis methods using concentrated (20–40 %) HF can be used to make $K_2SiF_6:Mn^{4+}$. Obtaining optimal synthesis conditions is vital, since possible formation of hydrates, oxides or Mn^{3+} and degradation of the formed fluorides can limit the efficiency of $K_2SiF_6:Mn^{4+}$. In this dissertation, some Mn^{4+}-doped oxides are explored, followed by a thorough evaluation of the four main synthesis methods of fluorides: etching, precipitation, cocrystallization and copreciptation. From this, the optimal synthesis conditions were found and the application potential of $K_2SiF_6:Mn^{4+}$ is discussed.

Conclusions

In chapter 5, hexaaluminate hosts including $BaMgAl_{10}O_{17}$ (BAM) and $SrMgAl_{10}O_{17}$ (SAM), were investigated as a phosphor when doped with Mn^{4+} ions. $CaMgAl_{10}O_{17}:Mn^{4+}$ (CAM:Mn) showed similar luminescent behavior, but it is difficult to make the pure phase. Adding excess Al_2O_3 in the solid state synthesis of SAM:Mn resulted in a mixed phosphor powder containing $SrMgAl_{10}O_{17}:Mn^{4+}$ and $Al_2O_3:Mn^{4+}$, denoted as SMA:Mn. A broad red emission band around 660 nm is found for Mn^{4+} in hexaaluminates while the Mn^{4+} emission in Al_2O_3 corresponds to a broad band around 678 nm. The excitation bands of both the hexaaluminates and the Al_2O_3 show high absorption in the UV region, while the absorption around 455 nm is rather low. Upon 455 nm excitation, a green emission band, corresponding with Mn^{2+} emission also emerges, showing a limited control over the valence state of Mn during the synthesis.

The thermal quenching behavior of SAM:Mn and SMA:Mn is similar and rather poor, with a quenching temperature $T_{1/2}$ of 343 K and 319 K respectively, which is far below the typical operating temperature of white LEDs (400–450 K), at which the emission is almost fully quenched. The external quantum efficiency (EQE) of the phosphor samples is very low ($<5\%$), which is mainly related to a low dopant concentration. The internal quantum efficiency (IQE), which is not influenced by a low absorption due to a limited number of absorbing centers, only reaches 26%, so improvements by a higher dopant concentration might be limited, let alone the thermal quenching would improve for a higher dopant concentration. Codoping SMA:Mn with a low concentration of Ce^{3+} or Bi^{3+} did improve the quantum efficiency up to 12% (external) and 64% (internal) respectively, although the codopant could not be detected using energy-dispersive X-ray spectroscopy (EDX). Apart from the low quantum efficiency and the poor thermal quenching, the eye-sensitivity limit further reduces the total efficiency for white LED applications. The broad emission band of all hexaaluminate phosphors spans from 630–750 nm, while the eye-sensitivity is limited above 650 nm, which limits the application potential in white LEDs, apart from deep red LEDs for agricultural applications.

To focus on red phosphors for warm-white LEDs, the shift from oxide to fluoride hosts was made. Chapters 6–10 focus on the fluoride host K_2SiF_6 and the different synthesis methods that can be used to make $K_2SiF_6:Mn^{4+}$ namely etching, precipitation, cocrystallization and coprecipitation. The fluoride $K_2SiF_6:Mn^{4+}$ is a very promising red phosphor with line emission around 630 nm and an excitation band around 450 nm which is perfectly suited for blue LED excitation.

$K_2SiF_6:Mn^{4+}$ can be obtained from **etching** Si wafers in an etching solution of $KMnO_4$ in HF, where H_2O_2 can speed up the redox reaction forming $K_2SiF_6:Mn^{4+}$. The quantum efficiencies obtained with an etching synthesis are reasonably high at an EQE of 40%. The major drawback of the etching synthesis is the limited access to Si in the synthesis, which lowers the possible synthesis yield and compromises control over the dopant concentration. As $KMnO_4$ acts as both the potassium and manganese source, the potassium source is limited, but addition of KF to the etchant did not improve the phosphor formation but rather formed KHF_2 and $K_2MnF_5 \cdot H_2O$.

In the **precipitation** synthesis, $K_2SiF_6:Mn^{4+}$ precipitates from a solution of $KMnO_4$, SiO_2 and KF in HF, where H_2O_2 is added to speed up the reaction. An IQE of 46% and an EQE of 12% are found, which is lower compared to the etching synthesis. The incorporation of Mn into the host lattice still imposes difficulties. The dopant concentration is 1.5% of the Si ions, while the concentration is higher in the precursor solution, leading to a limited incorporation of Mn in the phosphor host during the synthesis. An increased Mn concentration in the precursor solution does not lead to an increase in dopant concentration. Since the phosphor spontaneously precipitates from the synthesis solution, controlling the dopant concentration during the synthesis is difficult.

At low temperatures (220 K), a mono-exponential decay is found, while a bi-exponential decay emerges with increasing temperature from 295–450 K. The decay time continues to decrease with increasing temperature up to 450 K, although thermal quenching only starts above 400 K, with a thermal quenching temperature $T_{1/2}$ of 429 K. High incident fluxes cause both saturation of the emission and degradation of $K_2SiF_6:Mn^{4+}$. Above $40\,W/cm^2$, there is a sublinear response of the emission intensity to the excitation power, caused by ground-state depletion.

Cocrystallization is the process where K_2MnF_6 and K_2SiF_6 are mixed in a little HF and form the doped $K_2SiF_6:Mn^{4+}$ at 70 °C via a cation-exchange process. Unfortunately, the difference in ionic radii between Si^{4+} and Mn^{4+} hinders a smooth cation exchange, resulting in interfering degradation processes and contaminated, low quality phosphor samples. The opportunities of this synthesis method can be seen in the highly luminescent lumps that can be selected post-synthesis under a UV lamp.

These fractions reach high quantum efficiencies, but selecting and sorting them is not realistic. Therefore, creating the K_2SiF_6 host in situ, so that it can grow around dissolved $[MnF_6]^{2-}$ ions, seems to be more realistic to improve the dopant incorporation.

With the right synthesis conditions, IQE values of 47 % and EQE values of 21 % are reached, showing a somewhat better performance compared to the precipitation synthesis, but still below the performance of an etching synthesis. The purity of K_2MnF_6 is important, on the one hand in controlling the dopant concentration, on the other hand to reduce the introduction of defects such as Mn^{3+} and hydrates like $K_2MnF_5 \cdot H_2O$.

Applying a K_2SiF_6 coating to the phosphor particles is beneficial in many aspects. Not only does the quantum efficiency improve, an improved long-term stability has also been found. The coating process improves the crystal structure as a whole, since more Mn—F interaction is detected in EPR and a lower fraction of bi-exponential decay is found in luminescence lifetime measurements.

In a **coprecipitation** synthesis, $K_2SiF_6{:}Mn^{4+}$ precipitates from mixing solutions of SiO_2 in HF with a solution of KF and K_2MnF_6 in HF at 50 °C, resulting in a bright yellow-orange phosphor powder. The optimal dopant concentration is found to be 2% and full homogeneous incorporation can be found in SEM-EDX. From the optimal synthesis, an IQE of 88% and an EQE of 45% was obtained, which is close to the best values reported by General Electric. Precipitation of the doped $K_2SiF_6{:}Mn^{4+}$ phosphor happens instantaneously, but further dopant incorporation is reached when the mixture is stirred in the hot water bath for 1 h.

Over all, the phosphor powder contains few defects, since the defect-induced bi-exponential decay behavior that was present in phosphor samples from precipitation synthesis and from a cocrystallization synthesis, has disappeared. A mono-exponential decay behavior is found with a decay time of 16.3–5.2 ms in the 90–450 K temperature range. The phosphor powder is chemically stable, even after aging for 48 h at 70 °C and 80% relative humidity. The thermal stability is improved compared to the precipitation synthesis, with an increasing emission intensity up to 450 K and a thermal quenching temperature $T_{1/2}$ above 500 K.

Both the cocrystallization synthesis and the coprecipitation synthesis use K_2MnF_6 as a precursor. This fluoride is not very stable and not commercially available. The synthesis of K_2MnF_6 was discussed in chapter 8. Although it has a critical timing and a low yield, enough K_2MnF_6 could be synthesized to use in a two-step synthesis of $K_2SiF_6{:}Mn^{4+}$. The formation of KHF_2 during the synthesis was inevitable and it is crucial to remove this by washing with HF. Although the XRD shows that a pure K_2MnF_6 phase is formed, amorphous Mn^{3+} is still present according to X-ray absorption and diffuse reflectance measurements. The presence of Mn^{3+} can reduce the Mn^{4+} incorporation in K_2SiF_6:Mn^{4+} phosphor synthesis and can cause unwanted optical absorption near the blue excitation region.

The optimized K_2SiF_6:Mn^{4+} phosphor is suitable for various lighting applications. In chapter 11, the requirements for display applications are discussed. The emission wavelength of K_2SiF_6:Mn^{4+} coincides with the ideal red color point at 630 nm for display applications. High color gamuts can be reached when K_2SiF_6:Mn is combined with green perovskite quantum dots, which are close to the Rec. 2020 color gamut. Higher color gamuts are reached using K_2SiF_6:Mn^{4+} compared to pc-wLEDs with other red phosphors, which shows that K_2SiF_6:Mn^{4+} is up to the challenge of ultra-high definition television and can improve the color gamut of smartphone screens. K_2SiF_6:Mn^{4+} has similar properties compared with red QDs, but if the stability can be controlled by an improved synthesis, the phosphor material might win the duel in display applications.

The requirements for lighting applications are different compared to displays. The opportunities for K_2SiF_6:Mn^{4+} in warm-white LEDs for lighting applications are discussed in chapter 12. Because of the large Stokes shift in K_2SiF_6:Mn^{4+}, it can be combined with the broad-band emitting YAG:Ce to form a warm-white LED without reabsorption processes reducing the total efficiency. CCT values of 4750–2700 K can be obtained with a CRI values exceeding 80, using a varying amount of K_2SiF_6:Mn^{4+}. The combination of 73% YAG:Ce and 27% K_2SiF_6:Mn^{4+} resulted in a pc-wLED with a CCT of 3466 K, a CRI of 90 and a LER of 337 $\text{lm}\,\text{W}^{-1}$. In literature, many phosphor combinations for pc-wLEDs were found applicable to lighting applications. YAG:Ce remains the main contestant, but the somewhat shifted emission spectrum from LuAG:Ce is also a possible candidate, as well as Eu-doped silicate or oxynitride phosphors.

Remote phosphor applications require self-supporting phosphor layers with specific optical properties, which are discussed in chapter 13. Semi-transparent phosphor layers could be made using the low-refractive index polymer NOA 136, with the optimal refractive index of 1.36. An absorption of 71% was obtained for 250 mg phosphor in 199 mg polymer. Lowering the scattering effects by creating transparent layers can improve the light outcoupling for phosphor layers where the large phosphor amount would otherwise induce high scatter losses. K_2SiF_6:Mn^{4+}, with its low refractive index, forms an quite easy case for index matching with a polymer compared to oxide or sulphide phosphors.

Perspectives

Although oxide hosts doped with Mn^{4+} are not really suitable for warm white LEDs, other applications for broad-band red emission, such as LED grow lights for horticulture applications, can be a suitable application for the Mn^{4+}-doped hexaaluminates, after some further optimization of the efficiency and thermal stability. On the other hand, the application potential of K_2SiF_6:Mn^{4+} in warm-white LEDs is very high. The coprecipitation synthesis resulted in a phosphor with a high quantum efficiency that is stable even in high temperature and high humidity conditions. The long-term stability of K_2MnF_6 remains an issue, but with the right washing procedure and storage, the in-house produced K_2MnF_6 is stable enough and suitable to use in further phosphor synthesis.

The use of concentrated HF requires specific safety measures, both in personal protective equipment and in the use of plastic labware, but those difficulties can be overcome, even in industrial conditions. Since the fluorine ions are a crucial part of the crystal lattice and because of their sensitivity to oxidation and hydrolysis, acidic conditions and a fluorine excess seem to be necessary synthesis conditions. For now, the use of HF is therefore inevitable for the incorporation of Mn^{4+} in fluoride hosts. As a first step in the direction of a safer, HF-free synthesis, an ionic liquid synthesis of K_2SiF_6 host material has been reported in literature, but it has not yet resulted in the synthesis of a Mn^{4+}-doped phosphor. Further progress in the synthesis methods is mainly expected in post-processing, including coatings and annealing steps. Coating the phosphor particles with the undoped host material K_2SiF_6 has proven to be beneficial in terms of moisture stability and quantum efficiency. Annealing treatments have been proposed in literature, but the fluorine-containing atmosphere must be approached with caution, since it can easily form HF in contact with water.

Stable, efficient K_2SiF_6:Mn^{4+} can be applied in various light applications, including backlights for displays and general lighting. For displays, the opportunities of K_2SiF_6:Mn^{4+} are threatened by the development of stable, efficient, cheap, nontoxic quantum dots, which have a similar narrow emission band. For lighting applications, K_2SiF_6:Mn^{4+} is a suitable phosphor for warm-white LEDs, increasing the color rendering and efficacy of the white light. Remote phosphor setups with transparent phosphor layers form another promising application, which benefit from the low refractive index of K_2SiF_6 and allow for a relatively strong absorption of blue light, while limiting the scattering losses.

Samenvatting: conclusies en perspectieven

Efficiënte ledverlichting maakt gebruik van zogenaamde fosforen om blauw licht te converteren naar geel, groen of rood licht. De typische witte led bevat een blauwe ledchip en de gele fosfor YAG:Ce, maar hiervan is de kleurweergave in het rode spectrale bereik niet ideaal. Door een efficiënte rode fosfor toe te voegen aan de led verbetert de kleurweergave, het lichtrendement en de kleurtemperatuur. Aangezien de ooggevoeligheid beperkt is voorbij 650 nm, hebben rode fosforen idealiter een helderrode emissie tussen 600 nm en 650 nm voor verlichtingstoepassingen, terwijl er voor beeldschermtoepassingen gestreefd wordt naar een bijna monochromatische emissie bij 630 nm. Rode emissie is typisch voor Mn^{4+}-gedoteerde fosforen, zowel in fluoride- als in oxideroosters. Fluorideroosters zijn nodig voor verlichtingstoepassingen omdat het beperkte *nephelauxetic effect* voor fluorides zorgt voor een gesatureerde rode emissie bij fluorideroosters zoals K_2SiF_6:Mn^{4+}, terwijl oxideroosters een dieprode tot nabij-infrarode emissie vertonen.

De synthese van Mn^{4+}-gedoteerde fluorides gaat niet met de vastestofsynthese die typisch gebruikt wordt bij een fosforsynthese. Verschillende natchemische synthesemethoden met geconcentreerde (20–40 %) HF kunnen gebruikt worden om K_2SiF_6:Mn^{4+} te maken. Het bereiken van de optimale synthese-omstandigheden is cruciaal, aangezien de efficiëntie van het gevormde K_2SiF_6:Mn^{4+} beperkt wordt door de vorming van hydraten, oxides en Mn^{3+}, net als door degradatie van de gevormde fluorides. In dit proefschrift worden een aantal Mn^{4+}-gedoteerde oxides onderzocht, gevolgd door een grondige bespreking van de vier belangrijkste synthesemethoden voor fluorides: etsen, neerslag, cokristallistatie en coprecipitatie. Hieruit werden de optimale synthese-omstandigheden gevonden, waarna de toepassingsmogelijkheden voor K_2SiF_6:Mn^{4+} besproken worden.

Conclusies

In hoofdstuk 5 werden hexaaluminaatroosters zoals $BaMgAl_{10}O_{17}$ (BAM) and $SrMgAl_{10}O_{17}$ (SAM) onderzocht als fosfor waarbij ze gedoteerd worden met Mn^{4+}-ionen. $CaMgAl_{10}O_{17}$:Mn^{4+} (CAM:Mn) heeft een gelijkaardig luminescent gedrag, maar het is moeilijk om deze fase puur te maken. Door een overmaat van Al_2O_3 toe te voegen aan de vastestofsynthese van SAM:Mn ontstaat een gemengde fosfor die $SrMgAl_{10}O_{17}$:Mn^{4+} en Al_2O_3:Mn^{4+} bevat en beschreven wordt als SMA:Mn. Mn^{4+}-gedoteerde hexaaluminaten hebben een brede rode emissieband rond 660 nm, terwijl de Mn^{4+}-emissie in Al_2O_3 overeenkomt met een emissieband bij 678 nm. De excitatiebanden van de hexaaluminaten en Al_2O_3 hebben een sterke absorptie in het uv-bereik, terwijl de absorptie rond 450 nm redelijk zwak is. Bij excitatie bij 455 nm ontstaat een groene emissieband die overeenkomt met Mn^{2+}-emissie, wat aantoont dat er een beperkte controle is over de valentietoestand van Mn tijdens de synthese.

De thermische doving van SAM:Mn en SMA:Mn is gelijkaardig en eerder slecht, met een dooftemperatuur $T_{1/2}$ van respectievelijk 343 K en 319 K, wat veel lager is dan de typische werkingstemperatuur van witte leds (400–450 K), waar de emissie bijna volledig gedoofd is. De externe kwantumefficiëntie (EQE) van de fosforen is heel laag ($< 5\%$), wat voornamelijk komt door de lage dopantconcentratie. De interne kwantumefficiëntie (IQE) wordt niet beïnvloed door de lage absorptie bij weinig absorberende centra, maar is ook maar 26%, dus de verbetering bij een hogere dopantconcentratie zal beperkt zijn, laat staan dat de thermische doving verbetert. Toevoegen van een lage concentratie Ce^{3+} of Bi^{3+} aan SMA:Mn zorgde voor een verbetering van de kwantumefficiëntie tot 12% (extern) en 64% (intern), ondanks dat het bijdotant niet waargenomen kon worden met elementanalyse (EDX). Naast de lage kwantumefficiëntie en het snelle thermische doven zorgt ook de ooggevoeligheid voor een beperkte efficiëntie van witte leds met deze fosforen. De brede emissieband van alle hexaaluminaatfosforen ligt rond 630–750 nm terwijl de ooggevoeligheid beperkt is boven 650 nm. Dit beperkt de toepassingsmogelijkheden van Mn^{4+}-gedoteerde hexaaluminaatfosforen tot specifieke toepassingen zoals dieprode ledverlichting voor landbouwtoepassingen.

Om te kunnen streven naar rode fosforen voor warmwitte ledverlichting werd overgegaan van oxideroosters naar fluorideroosters. De hoofdstukken 6–10 behandelen het fluoriderooster K_2SiF_6 en de verschillende synthesemethoden die gebruikt kunnen worden om K_2SiF_6:Mn^{4+} te maken, namelijk etsen, neerslag, cokristallisatie en coprecipitatie. Het fluoride K_2SiF_6:Mn^{4+} is een veelbelovende rode fosfor met lijnemissie rond 630 nm en een excitatieband rond 450 nm die perfect beantwoordt aan de emissie van een blauwe led.

K_2SiF_6:Mn^{4+} kan gemaakt worden door een siliciumschijf te **etsen** in een oplossing van $KMnO_4$ in HF. Door H_2O_2 toe te voegen aan de etsvloeistof wordt de redoxreactie waarmee K_2SiF_6:Mn^{4+} gevormd wordt versneld. De kwantumefficiënties die behaald worden met een etssynthese zijn redelijk hoog, met een EQE van 40%. Het grootste nadeel aan de etssynthese is de beperkte beschikbaarheid van Si in de reactie, wat het syntheserendement verlaagt en de controle over de dopantconcentratie vermindert. Aangezien $KMnO_4$ in de reactie als bron dient voor zowel kalium als mangaan, is er relatief weinig kalium beschikbaar, maar het toevoegen van KF aan de etsvloeistof resulteerde in de vorming van KHF_2 en $K_2MnF_5 \cdot H_2O$, in plaats van een betere fosforvorming.

In een **neerslag**synthese slaat K_2SiF_6:Mn^{4+} neer uit een oplossing van $KMnO_4$, SiO_2 en KF in HF, waaraan H_2O_2 werd toegevoegd om de reactie te versnellen. Dit resulteert in een IQE van 46% en een EQE van 12%, wat lager is dan bij de etssynthese. De inbouw van Mn in het gastrooster vertoont nog altijd moeilijkheden. De dopantconcentratie in de fosfor is 1.5% van de Si-ionen, terwijl de concentratie in de precursoroplossing hoger is, dus de opname van Mn-ionen tijdens de synthese is beperkt. Aangezien de fosfor spontaan neerslaat uit de oplossing is het moeilijk om de dopantconcentratie te controleren.

K_2SiF_6:Mn^{4+} uit een neerslagsynthese vertoont een mono-exponentieel vervalgedrag bij lage temperatuur (220 K). Met toenemende temperaturen (295–450 K) wordt een bi-exponentieel vervalgedrag waargenomen. De vervaltijd neemt af met toenemende temperatuur tot 450 K, ondanks dat de thermische doving pas start boven 400 K met een dooftemperatuur $T_{1/2}$ van 429 K. Een hoge invallende flux veroorzaakt saturatie van de emissie en degradatie van K_2SiF_6:Mn^{4+}. Boven 40 W/cm^2 is er een niet-lineair verband tussen de emissie-intensiteit en het excitatievermogen dat veroorzaakt wordt door depletie van de grondtoestand.

Cokristallisatie is het proces waarbij K_2MnF_6 en K_2SiF_6 gemengd worden met een beetje HF en het gedoteerde K_2SiF_6:Mn^{4+} vormen bij 70 °C door een kationuitwisselingsproces. Het verschil in ionaire straal tussen Si^{4+} en Mn^{4+} verhindert echter een vlotte uitwisseling van kationen, wat leidt tot degradatieprocessen en verontreinigde, laagkwalitatieve fosforen. De mogelijkheden van deze synthesemethode zijn zichtbaar in de sterkst luminescente brokken die geselecteerd kunnen worden onder een uv-lamp. Deze fracties hebben een hoge kwantumefficiëntie, maar het handmatig selecteren en sorteren van de verschillende fracties is niet realistisch. Het zal daarom interessanter zijn om het K_2SiF_6-rooster in situ te maken, zodat het kan groeien rond de opgeloste $[MnF_6]^{2-}$-ionen.

Met de juiste synthese-omstandigheden worden met cokristallisatie kwantumefficiënties behaald van 47% (intern) en 21% (extern), wat iets beter is dan de neerslagsynthese maar slechter dan de etssynthese. De zuiverheid van K_2MnF_6 is belangrijk, aan de ene kant om de dopantconcentratie te kunnen controleren en aan de andere kant om het inbrengen van onzuiverheden zoals Mn^{3+} en hydraten zoals $K_2MnF_5 \cdot H_2O$ in het gastrooster te beperken.

Het aanbrengen van een ongedoteerde K_2SiF_6-laag op de fosfordeeltjes heeft verschillende voordelen, zoals het verbeteren van de kwantumefficiëntie en de langetermijnstabiliteit. Het aanbrengen van de deklaag verbetert de hele kristalstructuur, aangezien meer Mn–F interactie wordt waargenomen in metingen van de elektron paramagnetische resonantie en metingen van de luminescente levensduur tonen een lagere fractie van het bi-exponentieel verval.

In een **coprecipitatie**-synthese slaat K_2SiF_6:Mn^{4+} neer door het mengen van een oplossing van SiO_2 in HF met een oplossing van KF en K_2MnF_6 bij 50 °C, wat een helder oranjegeel fosforpoeder oplevert. De optimale dopantconcentratie was 2% en met EDX kan een volledige homogene inbouw worden gemeten. Met de optimale synthese wordt een IQE van 88% en een EQE van 45% behaald, wat dicht aanleunt tegen de beste waarden die vermeld worden door General Electric. De neerslagvorming van K_2SiF_6:Mn^{4+} gebeurt onmiddellijk, maar verdere dopantincorporatie kan plaatsvinden als het mengsel nog een uur geroerd wordt in het warmwaterbad.

Het fosforpoeder bevat weinig defecten waardoor het bi-exponentieel vervalgedrag, dat in de fosforen uit de neerslagsynthese en de cokristallisatie-synthese door defecten veroorzaakt werd, verdwenen is. De fosfor uit de coprecipitatie-synthese vertoont een mono-exponentieel vervalgedrag met een vervaltijd van 16.3–5.2 ms bij temperaturen van 90–450 K. Het fosforpoeder is chemisch stabiel, zelfs na een verouderingsproces van 48 h bij 70 °C en 80% relatieve vochtigheid. De thermische stabiliteit is verbeterd ten opzichte van de neerslagsynthese, met een toenemende emissie-intensiteit tot 450 K en een thermische dooftemperatuur $T_{1/2}$ groter dan 500 K.

K_2MnF_6 wordt als precursor gebruikt in de cokristallisatie-synthese en de coprecipitatie-synthese. Dit fluoride is niet zo stabiel en niet commercieel verkrijgbaar. De synthese van K_2MnF_6 werd besproken in hoofdstuk 8. Ondanks de cruciale timing en de lage opbrengst kon er genoeg K_2MnF_6 gemaakt worden om te gebruiken in een tweestapssynthese van K_2SiF_6:Mn^{4+}. Het was onvermijdelijk dat KHF_2 gevormd werd tijdens de synthese, dus is het cruciaal om dit te verwijderen door de neerslag te wassen met HF. Niettegenstaande een pure K_2MnF_6-fase geïdentificeerd kon worden met X-straal poederdiffractie, is er amorf Mn^{3+} aanwezig volgens de X-straalabsorptie en diffuse reflectie metingen. De aanwezigheid van Mn^{3+} kan de inbouw van Mn^{4+} tijdens een synthese van K_2SiF_6:Mn^{4+} verminderen en kan zorgen voor een ongewenste optische absorptie in de buurt van het blauwe excitatiebereik.

De geoptimaliseerde K_2SiF_6:Mn^{4+}-fosfor is geschikt voor verschillende verlichtingstoepassingen. In hoofdstuk 11 worden de vereisten van beeldschermtoepassingen besproken. De emissiegolflengte van K_2SiF_6:Mn^{4+} komt overeen met het ideale rode kleurpunt bij 630 nm voor beeldschermtoepassingen. Een groot kleurengamma, dat het Rec. 2020 kleurengamma benadert, kan bereikt worden door K_2SiF_6:Mn te combineren met groene perovskiet *quantum dots*. Door K_2SiF_6:Mn^{4+} te gebruiken kan een groter kleurengamma bereikt worden dan met andere rode fosforen, wat aantoont dat de fosfor geschikt is om te gebruiken in beeldschermen van televisies en smartphones. K_2SiF_6:Mn^{4+} heeft vergelijkbare eigenschappen als rode quantum dots, maar als de fosforen chemisch stabiel blijven kunnen ze het duel in de beeldschermtoepassingen mogelijk nog winnen.

De vereisten van verlichtingstoepassingen zijn anders dan die van beeldschermen. De kansen voor K_2SiF_6:Mn^{4+} in warmwitte ledverlichting worden besproken in hoofdstuk 12. Doordat K_2SiF_6:Mn^{4+} een grote Stokesverschuiving heeft kan deze fosfor gecombineerd worden met de brede emissieband van YAG:Ce om een warmwitte led te vormen waar geen herabsorptie in plaatsvindt die de totale efficiëntie vermindert. Kleurtemperaturen (CCT) van 4750–2700 K kunnen behaald worden met een kleurweergave-index (CRI) groter dan 80 door YAG:Ce te combineren met verschillende hoeveelheden $K_2SiF_6:Mn^{4+}$. De combinatie van 73% YAG:Ce en 27% $K_2SiF_6:Mn^{4+}$ leidt tot een witte led met een CCT van 3466 K, een CRI van 90 en een lichtrendement van 337 lm W^{-1}. In de literatuur werden veel fosforcombinaties beschreven die geschikt zijn voor verlichtingstoepassingen. YAG:Ce blijft de belangrijkste kandidaatfosfor, maar het lichtjes verschoven emissiespectrum van LuAG:Ce is een andere mogelijke kandidaat, net als Eu-gedoteerde silicaten of oxynitride-fosforen.

Voor *remote*-fosfortoepassingen zijn zelfstandige fosforlagen met specifieke optische eigenschappen nodig, die worden besproken in hoofdstuk 13. Half-transparante fosforlagen werden gemaakt met het NOA 136 polymeer met een lage brekingsindex van 1.36. Een fosforlaag met 250 mg fosfor in 199 mg polymeer absorbeert 71% van het blauwe licht. In transparante lagen ontstaan minder verstrooiingseffecten, waardoor de uitkoppeling van licht beter is in lagen met veel fosfor, waar het licht anders niet zou kunnen ontsnappen door veel verstrooiingsverliezen. Voor $K_2SiF_6:Mn^{4+}$ is het, door de lage brekingsindex, relatief eenvoudig om een polymeer te kiezen met een gelijke brekingsindex, terwijl oxide- of sulfidefosforen een veel hogere brekingsindex hebben.

Perspectieven

Ondanks dat Mn^{4+}-gedoteerde oxideroosters niet zo geschikt zijn voor warmwitte ledverlichting, zijn andere toepassingen zoals groeilampen wel nog mogelijk voor de breedbandige rode emissie, al is er nog wat optimalisatie nodig van de kwantumefficiëntie en de thermische stabiliteit. Voor $K_2SiF_6:Mn^{4+}$ is het toepassingspotentieel in warmwitte leds juist weer heel groot. De coprecipitatie-synthese leverde een fosfor op met een hoge kwantumefficiëntie die stabiel is, zelfs bij hoge temperatuur en/of hoge luchtvochtigheid. De langetermijnstabiliteit van K_2MnF_6 blijft een aandachtspunt, maar met de juiste wasprocedure en verpakking is de zelfgemaakte K_2MnF_6 stabiel genoeg en geschikt om te gebruiken in verdere fosforsynthese.

Specifieke veiligheidsmaatregelen zijn nodig bij het gebruik van geconcentreerde HF, zowel in persoonlijke beschermingsmiddelen als in het gebruik van plastic laboratoriummateriaal, maar dit is haalbaar, zelfs in industriële omstandigheden. De zure omgeving en de overmaat aan fluor lijken noodzakelijke synthese-omstandigheden aangezien de fluorionen een cruciaal deel vormen van het kristalrooster en omdat de fluorcomplexen gevoelig zijn voor oxidatie en hydrolyse. Tot nu toe is het gebruik van HF onvermijdelijk voor de inbouw van Mn^{4+} in fluoriderooster. Als eerste stap in de richting van een veiligere synthese zonder HF werd een synthese van K_2SiF_6 in een ionische vloeistof beschreven in de literatuur, maar dat heeft nog niet geleid tot de synthese van een Mn^{4+}-gedoteerde fosfor. Verdere ontwikkelingen in de synthesemethoden worden vooral verwacht in nabehandelingen zoals deklagen en thermische behandelingen. Het aanbrengen van een laag ongedoteerd K_2SiF_6 op de fosfordeeltjes is bevorderlijk op het vlak van vochtbestendigheid en kwantumefficiëntie. Thermische behandelingen werden voorgesteld in de literatuur, maar bij het gebruik van een fluoratmosfeer is voorzichtigheid geboden, aangezien er in contact met water gemakkelijk HF gevormd kan worden.

Een stabiele, efficiënte $K_2SiF_6:Mn^{4+}$-fosfor kan worden toegepast in verschillende verlichtingstoepassingen waaronder achtergrondverlichting voor beeldschermen en algemene verlichting. Voor beeldschermen worden de mogelijkheden voor $K_2SiF_6:Mn^{4+}$ vooral bedreigd door de ontwikkeling van stabiele, efficiënte, goedkope, niet-giftige quantum dots die een vergelijkbare smalle emissieband hebben. Voor verlichtingstoepassingen is $K_2SiF_6:Mn^{4+}$ een geschikte fosfor voor warmwitte ledverlichting door de kleurweergave en het lichtrendement te verbeteren. Een andere veelbelovende toepassing is de *remote*-fosforopstelling met een half-transparante fosforlaag die baat heeft bij de lage brekingsindex van K_2SiF_6 en ruimte laat voor een redelijk sterke absorptie van blauw licht met beperkte verliezen door verstrooiing.

List of acronyms

at%	atomic percent
BAM	$BaMgAl_{10}O_{17}$
BSE	backscattered electrons
CAM	$CaMgAl_{10}O_{17}$
CC	configurational coordinate
CCD	charge-coupled device
CCT	correlated color temperature
CF	crystal field
CFL	compact fluorescent lamp
CIE	Commision Internationale d'Éclairage
CL	cathodoluminescence
CQS	color quality scale
CRI	color rendering index
CRT	cathode ray tube
DFT	density functional theory
DOS	density of states
DRS	diffuse reflectance spectroscopy
$\mathbf{D}_{uv}$	distance to the Planckian locus
EDX	energy-dispersive X-rays
EPR	electron paramagnetic resonance
EQE	external quantum efficiency
ESRF	European Synchrotron Radiation Facility
EXAFS	extended X-ray absorption fine structure
FWHM	full width at half maximum
GE	General Electric
GGA	generalized gradient approximation
HSE	Heyd-Scuseria-Ernzerhof

HTHH	high temperature and high humidity
ICCD	intensified charge-coupled device
ICSD	Inorganic Crystal Structure Database
IQE	internal quantum efficiency
IR	infrared
LDA	local density approximation
LED	light-emitting diode
LER	luminous efficiency of the radiation
NIST	National Institute of Standards and Technology
NOA	Norland Optical Adhesive
NTSC	National Television System Committee
PBE	Perdew-Burke-Ernzerhof
pc-wLED	phosphor-converted white light-emitting diode
PL	photoluminescence
PTFE	polytetrafluoroethylene
QD	quantum dot
QE	quantum efficiency
RGB	red, green and blue
RH	relative humidity
rt	room temperature
SAM	$SrMgAl_{10}O_{17}$
SCF	self-consistent field
SE	secondary electrons
SEM	scanning electron microscope
SMA	$SrMgAl_{30}O_{17\pm\delta}$:$Mn^{4+}$
UV	ultra-violet
wLED	white light-emitting diode
wt%	weight percent
XAS	X-ray absorption spectroscopy
XANES	X-ray absorption near edge structure
XRD	X-ray diffraction
YAG:Ce	$Y_3Al_5O_{12}$:Ce^{3+}
ZPL	zero-phonon line

Examination committee

Chairman

Prof. dr. Maarten Baes	Department of Physics and Astronomy, Ghent University

Supervisors

Prof. dr. Philippe Smet	Department of Solid State Sciences, Ghent University
Prof. dr. Dirk Poelman	Department of Solid State Sciences, Ghent University

Other members of the examination committee

Prof. dr. Freddy Callens	Department of Solid State Sciences, Ghent University
Prof. dr. Klaartje De Buysser	Department of Chemistry, Ghent University
Dr. Anna Kaczmarek	Department of Chemistry, Ghent University
Dr. Paul Leblans	Agfa Healthcare
Prof. dr. Youri Meuret	Department of Electrical Engineering, KU Leuven

Publications

Papers in international, peer reviewed journals

- **K_2SiF_6:Mn^{4+} as a red phosphor for displays and warm-white LEDs: a review of properties and perspectives**
  Heleen F. Sijbom, Reinert Verstraete, Jonas J. Joos, Dirk Poelman and Philippe F. Smet
  Optical Materials Express, 7(9) 3332–3365 (2017)

- **K_2MnF_6 as a precursor for saturated red fluoride phosphors: the struggle for structural stability**
  Reinert Verstraete, Heleen F. Sijbom, Katleen Korthout, Dirk Poelman, Christophe Detavernier and Philippe F. Smet
  Journal of Materials Chemistry C, 5(41) 10761–10769 (2017)

- **Oxidation and luminescence quenching of Europium in $BaMgAl_{10}O_{17}$ blue phosphors**
  Lucia Amidani, Katleen Korthout, Jonas J. Joos, Marte van der Linden, Heleen F. Sijbom, Andries Meijerink, Dirk Poelman, Philippe F. Smet and Pieter Glatzel
  Chemistry of Materials, 29(23) 10122–10129 (2017)

- **Luminescent behavior of the K_2SiF_6:Mn^{4+} red phosphor at high fluxes and at the microscopic level**
  Heleen F. Sijbom, Jonas J. Joos, Lisa I. D. J. Martin, Koen Van den Eeckhout, Dirk Poelman and Philippe F. Smet
  ECS Journal of Solid State Science and Technology, 5(1) R3040–R3048 (2016)

Contributions at international conferences

- **Red fluoride phosphors for remote phosphor LED applications**
  Heleen F. Sijbom, Lisa I. D. J. Martin, Dirk Poelman and Philippe F. Smet
  7th International symposium on Optical Materials (ISOM-7), Lyon, France, 29/02/2016-04/03/2016

- **Rare earths for phosphor development: the final frontier?**
  Dirk Poelman, Olivier Q. De Clercq, Jesse H. Bouman, Heleen F. Sijbom, Jonas J. Joos, Katleen Korthout, Kevin Braeckmans and Philippe F. Smet
  Rare Earths 2016, Sapporo, Japan, 05/06/2016-10/06/2016

- **K_2SiF_6:Mn^{4+} as a red phosphor for remote phosphor LEDs**
  Heleen F. Sijbom, Koen Van den Eeckhout, Dirk Poelman and Philippe F. Smet
  EuroDisplay 2015, Ghent, Belgium, 21/09/2015-23/09/2015

- **K_2SiF_6:Mn^{4+} as a red phosphor for remote phosphor LEDs**
  Heleen F. Sijbom, Koen Van den Eeckhout, Dirk Poelman and Philippe F. Smet
  4th International conference on the Physics of Optical Materials and Devcies (ICOM 2015), Budva, Montenegro, 31/08/2015-04/09/2015

- **Mapping of thermal quenching and luminescence lifetimes in phosphors at the microscopic level**
  Philippe F. Smet, Heleen F. Sijbom and Dirk Poelman
  International Workshop on Luminescent Materials 2013 (LumiMat 2013), Kyoto, Japan, 14/11/2013-15/11/2013

Contributions at national conferences

- **Accelerated aging testing of phosphors in remote wLED configuration**
  Reinert Verstraete, Heleen F. Sijbom, Dirk Poelman and Philippe F. Smet
  9th Belgian Crystallography Symposium (BCS-9), Brussels, Belgium, 26/10/2016

- **K_2SiF_6:Mn^{4+} as a red phosphor for warm white LEDs**
  Heleen F. Sijbom, Koen Van den Eeckhout, Dirk Poelman and Philippe F. Smet
  Belgian Physical Society: General Scientific Meeting 2015 (BPS 2015), Liège, Belgium, 13/05/2015

- **Hybrid remote phosphors for white LEDs**
  Sofie Abé, Jonas J. Joos, Dorian Dupont, Heleen F. Sijbom, Yolanda Justo Zarraquiños, Mickaël Tessier, Koen Van den Eeckhout, Guido Huybrechts, Philippe F. Smet and Zeger Hens
  NB Photonics annual meeting 2014, Ghent, Belgium, 08/09/2014

Bibliography

[1] E. N. Harvey and L. Marton: *A history of luminescence*, The American Philosophical Society (1957).

[2] W. M. Yen, S. Shionoya and H. Yamamoto, editors: *Phosphor handbook*, CRC Press, Boca Raton, FL, 2nd edition (2006).

[3] G. Blasse and B. C. Grabmeier: *Luminescent materials*, Springer-Verlag Berlin Heidelberg (1994).

[4] Nobel Media AB: The 2014 Nobel Prize in Physics - press release (2014).

[5] Y. Narukawa, M. Ichikawa, D. Sanga, M. Sano and T. Mukai: White light emitting diodes with super-high luminous efficacy. *Journal of Physics D: Applied Physics* 43 (35), 354 002 (2010).

[6] R. W. G. Hunt: Spectral luminous efficiency functions, in M. A. Kriss, editor, *The reproduction of colour*, 678–679, John Wiley & Sons Ltd, 6 edition (2005).

[7] Radiocommunication Sector of ITU (ITU-R): Parameter values for ultra-high definition television systems for production and international programme exchange, Technical report, International Telecommunication Union (2015).

[8] P. F. Smet, A. B. Parmentier and D. Poelman: Selecting conversion phosphors for white light-emitting diodes. *Journal of The Electrochemical Society* 158 (6), R37–R54 (2011).

[9] E. F. Schubert, T. Gessmann and J. K. Kim: *Light-emitting diodes*, Cambridge University Press (2005).

[10] J. H. Oh, H. Kang, Y. J. Eo, H. K. Park and Y. R. Do: Synthesis of narrow-band red-emitting K_2SiF_6:Mn^{4+} phosphors for a deep red monochromatic LED and ultrahigh color quality warm-white LEDs. *Journal of Materials Chemistry C* 3, 607–615 (2015).

[11] N. Avci, I. Cimieri, P. F. Smet and D. Poelman: Stability improvement of moisture sensitive CaS:Eu^{2+} micro-particles by coating with sol–gel alumina. *Optical Materials* 33 (7), 1032–1035 (2011).

[12] X. Piao, T. Horikawa, H. Hanzawa and K.-i. Machida: Characterization and luminescence properties of $Sr_2Si_5N_8$:Eu^{2+} phosphor for white light-emitting-diode illumination. *Applied Physics Letters* 88 (16), 2004–2007 (2006).

[13] K. Uheda, N. Hirosaki, Y. Yamamoto, A. Naito, T. Nakajima and H. Yamamoto: Luminescence properties of a red phosphor, $CaAlSiN_3$:Eu^{2+}, for white light-emitting diodes. *Electrochemical and Solid-State Letters* 9 (4), H22–H25 (2006).

[14] X. Luo, X. Fu, F. Chen and H. Zheng: Phosphor self-heating in phosphor converted light-emitting diode packaging. *International Journal of Heat and Mass Transfer* 58 (1-2), 276–281 (2013).

[15] I. U. Perera and N. Narendran: Understanding heat dissipation of a remote phosphor layer in an LED system. *Thermomechanical Phenomena in Electronic Systems -Proceedings of the Intersociety Conference* 186–192 (2014).

[16] I. U. Perera and N. Narendran: Thermal management of the remote phosphor layer in LED systems. *Proceedings of SPIE* 8835 (518), 883 504–883 507 (2013).

[17] J. J. Joos, K. W. Meert, A. B. Parmentier, D. Poelman and P. F. Smet: Thermal quenching and luminescence lifetime of saturated green $Sr_{1-x}Eu_xGa_2S_4$ phosphors. *Optical Materials* 34 (11), 1902–1907 (2012).

[18] K. W. Meert, V. A. Morozov, A. M. Abakumov, J. Hadermann, D. Poelman and P. F. Smet: Energy transfer in Eu^{3+} doped scheelites: use as thermographic phosphor. *Optics Express* 22 (S3), A961–A972 (2014).

[19] J. Botterman and P. F. Smet: Persistent phosphor $SrAl_2O_4$:Eu,Dy in outdoor conditions: saved by the trap distribution. *Optics Express* 23 (15), A868–A881 (2015).

[20] N. M. Avram and M. G. Brik: *Optical Properties of 3d-Ions in Crystals: Spectroscopy and Crystal Field Analysis*, Springer Berlin Heidelberg, Berlin, Heidelberg (2013).

[21] T. Takahashi and S. Adachi: Mn^{4+}-activated red photoluminescence in K_2SiF_6 phosphor. *Journal of The Electrochemical Society* 155 (12), E183–E188 (2008).

[22] M. G. Brik and A. M. Srivastava: On the optical properties of the Mn^{4+} ion in solids. *Journal of Luminescence* 133 (2013), 69–72 (2013).

[23] M. G. Brik, S. J. Camardello and A. M. Srivastava: Influence of covalency on the Mn^{4+} $^2E_g \rightarrow {}^4A_{2g}$ emission energy in crystals. *ECS Journal of Solid State Science and Technology* 4 (3), R39–R43 (2014).

[24] H. F. Sijbom, J. J. Joos, L. I. D. J. Martin, K. Van den Eeckhout, D. Poelman and P. F. Smet: Luminescent behavior of the K_2SiF_6:Mn^{4+} red phosphor at high fluxes and at the microscopic level. *ECS Journal of Solid State Science and Technology* 5 (1), R3040–R3048 (2016).

[25] J. J. Joos: *Designing Phosphors for LEDs: An experimental and theoretical perspective*, Phd, Ghent University (2017).

[26] B. Henderson and G. Imbusch: *Optical spectroscopy of inorganic solids*, Oxford University Press (1989).

[27] Z. Bryknar, V. Trepakov, Z. Potůček and L. Jastrabík: Luminescence spectra of $SrTiO_3$:Mn^{4+}. *Journal of Luminescence* 87, 605–607 (2000).

[28] G. Kemeny and C. H. Haake: Activator center in magnesium fluorogermanate phosphors. *The Journal of Chemical Physics* 33 (3), 783–789 (1960).

[29] Y. K. Xu and S. Adachi: Properties of Na_2SiF_6:Mn^{4+} and Na_2GeF_6:Mn^{4+} red phosphors synthesized by wet chemical etching. *Journal of Applied Physics* 105 (1), 013 525 (2009).

[30] P. H. M. Uylings, A. J. J. Raassen and J. F. Wyart: Energies of *N* equivalent electrons expressed in terms of two-electron energies and independent three-electron parameters: a new complete set of orthogonal operators : II. Application to $3d^N$ configurations. *Journal of Physics B: Atomic Molecular Physics* 17, 4103–4126 (1984).

[31] C. E. Schäffer and C. K. Jørgensen: The nephelauxetic series of ligands corresponding to increasing tendency of partly covalent bonding. *Journal of Inorganic and Nuclear Chemistry* 8, 143–148 (1958).

[32] C. K. Jørgensen: *Modern aspects of ligand field theory*, North-Holland Pub. Co, New York (1971).

[33] B. Han, B. W. Wessels and M. P. Ulmer: Optical investigation of electronic states of Mn^{4+} ions in p-type GaN. *Applied Physics Letters* 86 (4), 1–4 (2005).

[34] F. Karel, J. Pastrňák and J. Rosa: Thermoluminescent measurements of the trap level spectrum in AlN:Mn^{4+} phosphors. *Czechoslovak Journal of Physics* 19 (8), 974–982 (1969).

[35] V. Baslon, J. P. Harris, C. Reber, H. E. Colmer, T. A. Jackson, A. P. Forshaw, J. M. Smith, R. A. Kinney and J. Telser: Near-infrared $^2E_g \longrightarrow {}^4A_{2g}$ and visible LMCT luminescence from a molecular *bis*-(tris(carbene)borate) manganese(IV) complex. *Canadian Journal of Chemistry* 95 (5), 547–552 (2017).

[36] M. G. Brik, S. J. Camardello, A. M. Srivastava, N. M. Avram and A. Suchocki: Spin-forbidden transitions in the spectra of transition metal ions and nephelauxetic effect. *ECS Journal of Solid State Science and Technology* 5 (1), R3067–R3077 (2016).

[37] M. G. Brik and A. M. Srivastava: Ab initio studies of the structural, electronic, and optical properties of K_2SiF_6 single crystals at ambient and elevated hydrostatic pressure. *Journal of The Electrochemical Society* 159 (6), J212–J216 (2012).

[38] R. Kasa and S. Adachi: Red and deep red emissions from cubic K_2SiF_6:Mn^{4+} and hexagonal K_2MnF_6 synthesized in HF/$KMnO_4$/KHF_2/Si solutions. *Journal of The Electrochemical Society* 159 (4), J89–J95 (2012).

[39] R. Hoshino, T. Nakamura and S. Adachi: Synthesis and photoluminescence properties of $BaSnF_6$:Mn^{4+} red phosphor. *ECS Journal of Solid State Science and Technology* 5 (3), R37–R43 (2016).

[40] L.-l. Wei, C. C. Lin, M.-h. Fang, M. G. Brik, S.-F. Hu, H. Jiao and R.-s. Liu: A low-temperature co-precipitation approach to synthesize fluoride phosphors K_2MF_6:Mn^{4+} (M = Ge, Si) for white LED applications. *Journal of Materials Chemistry C* 3, 1655–1660 (2015).

[41] S. Adachi and T. Takahashi: Direct synthesis of K_2SiF_6:Mn^{4+} red phosphor from crushed quartz schist by wet chemical etching. *Electrochemical and Solid-State Letters* 12 (2), J20–J23 (2009).

[42] T. Arai and S. Adachi: Excited states of $3d^3$ electrons in K_2SiF_6:Mn^{4+} red phosphor studied by photoluminescence excitation spectroscopy. *Japanese Journal of Applied Physics* 50 (9), 092 401 (2011).

[43] A. Paulusz: Efficient Mn (IV) emission in fluorine coordination. *Journal of The Electrochemical Society* 120 (7), 942–947 (1973).

[44] M. Novita and K. Ogasawara: Comparative study of multiplet structures of Mn^{4+} in K_2SiF_6, K_2GeF_6, and K_2TiF_6 based on first-principles configuration–interaction calculations. *Japanese Journal of Applied Physics* 51, 022 604 (2012).

[45] M. H. Du: Chemical trends of Mn^{4+} emission in solids. *Journal of Materials Chemistry C* 2 (14), 2475–2481 (2014).

[46] Q. Shao, L. Wang, L. Song, Y. Dong, C. Liang, J. He and J. Jiang: Temperature dependence of photoluminescence spectra and dynamics of the red-emitting K_2SiF_6:Mn^{4+} phosphor. *Journal of Alloys and Compounds* 695, 221–226 (2017).

[47] A. Lazarowska, S. Mahlik, M. Grinberg, C. C. Lin and R.-S. Liu: Pressure effect on the zero-phonon line emission of Mn^{4+} in K_2SiF_6. *The Journal of Chemical Physics* 143 (13), 134 704 (2015).

[48] S. Adachi, H. Abe, R. Kasa and T. Arai: Synthesis and properties of hetero-dialkaline hexafluorosilicate red phosphor $KNaSiF_6:Mn^{4+}$. *Journal of The Electrochemical Society* 159 (2), J34–J37 (2012).

[49] Y. K. Xu and S. Adachi: Photoluminescence and raman scattering spectra in $(NH_4)_2XF_6:Mn^{4+}$ (X = Si, Ge, Sn, and Ti) red phosphors. *Journal of The Electrochemical Society* 159 (1), E11–E17 (2012).

[50] Y. K. Xu and S. Adachi: Properties of Mn^{4+}-activated hexafluorotitanate phosphors. *Journal of The Electrochemical Society* 158 (3), J58–J65 (2011).

[51] F. Tang, Z. Su, H. Ye, M. Wang, X. Lan, D. L. Phillips, Y. Cao and S. Xu: A set of manganese ion activated fluoride phosphors ($A_2BF_6:Mn^{4+}$, A = K, Na, B = Si, Ge, Ti): synthesis below 0 °C and efficient room-temperature photoluminescence. *Journal of Materials Chemistry C* 4 (40), 9561–9568 (2016).

[52] T. Takahashi and S. Adachi: Synthesis of $K_2SiF_6:Mn^{4+}$ red phosphor from silica glasses by wet chemical etching in $HF/KMnO_4$ solution. *Electrochemical and Solid-State Letters* 12 (8), J69–J71 (2009).

[53] H.-D. Nguyen, C. C. Lin and R.-S. Liu: Waterproof alkyl phosphate coated fluoride phosphors for optoelectronic materials. *Angewandte Chemie International Edition* 54 (37), 10 862–10 866 (2015).

[54] M. Novita, T. Honma, B. Hong, A. Ohishi and K. Ogasawara: Study of multiplet structures of Mn^{4+} activated in fluoride crystals. *Journal of Luminescence* 169, 594–600 (2016).

[55] K. Ogasawara, T. Ishii, I. Tanaka and H. Adachi: Calculation of multiplet structures of Cr^{3+} and V^{3+} in α-Al_2O_3 based on a hybrid method of density-functional theory and the configuration interaction. *Physical Review B* 61 (1), 143–161 (2000).

[56] V. Bachmann, C. Ronda and A. Meijerink: Temperature quenching of yellow Ce^{3+} luminescence in YAG:Ce. *Chemistry of Materials* 21 (10), 2077–2084 (2009).

[57] S. Leyre, E. Coutino-Gonzalez, J. J. Joos, J. Ryckaert, Y. Meuret, D. Poelman, P. F. Smet, G. Durinck, J. Hofkens, G. Deconinck and P. Hanselaer: Absolute determination of photoluminescence quantum efficiency using an integrating sphere setup. *Review of Scientific Instruments* 85 (12), 123 115 (2014).

[58] Y. N. Wu, C. H. Cheng and Z. X. Xiong: Enhancement of blue emission via upconversion in solid-state synthesized hexagonal $NaYF_4:Ln^{3+}$. *Key Engineering Materials* 368-372, 398–401 (2008).

[59] P. Yang, G. Q. Yao and J. H. Lin: Energy transfer and photoluminescence of $BaMgAl_{10}O_{17}$ co-doped with Eu^{2+} and Mn^{2+}. *Optical Materials* 26 (3), 327–331 (2004).

[60] L. Meng, L. Liang and Y. Wen: Deep red phosphors $SrMgAl_{10}O_{17}:Mn^{4+}$, M (M = Li^+, Na^+, K^+, Cl^-) for warm white light emitting diodes. *Journal of Materials Science: Materials in Electronics* 25 (6), 2676–2681 (2014).

[61] V. Singh, V. Natarajan and D.-k. Kim: Combustion synthesis and luminescence properties of $MgSrAl_{10}O_{17}:Mn^{2+}$ and $BaAl_2O_4:Mn^{4+}$. *Radiation Effects and Defects in Solids* 163 (3), 199–206 (2008).

[62] S. R. Jansen, J. W. de Haan, L. J. M. van de Ven, R. Hanssen, H. T. Hintzen and R. Metselaar: Incorporation of nitrogen in alkaline-earth hexaaluminates with a β-alumina- or a magnetoplumbite-type structure. *Chemistry of Materials* 9 (7), 1516–1523 (1997).

[63] N. Iyi and M. Gobbels: Crystal structure of the new magnetoplumbite-related compound in the system $SrO-Al_2O_3-MgO$. *Journal of Solid State Chemistry* 122 (1), 46–52 (1996).

[64] R. Cao, K. N. Sharafudeen and J. Qiu: Enhanced luminescence in $SrMgAl_xO_{17\pm\delta}:yMn^{4+}$ composite phosphors. *Spectrochimica Acta Part A: Molecular and Biomolecular Spectroscopy* 117 (2014), 402–5 (2014).

[65] R. Cao, H. Xue, X. Yu, F. Xiao, D. Wu and F. Zhang: Luminescence properties and synthesis of $SrMgAl_{10}O_{17}:Mn^{4+}$ red phosphor for white light-emitting diodes. *Journal of Nanoscience and Nanotechnology* 16 (4), 3489–3493 (2016).

[66] B. Wang, H. Lin, F. Huang, J. Xu, H. Chen, Z. Lin and Y. Wang: Non-rare-earth $BaMgAl_{10-2x}O_{17}$:$x$$Mn^{4+}$,$x$$Mg^{2+}$: a narrow-band red phosphor for use as a high-power warm w-LED. *Chemistry of Materials* 28 (10), 3515–3524 (2016).

[67] A. Tomita, T. Sato, K. Tanaka, Y. Kawabe, M. Shirai, K. Tanaka and E. Hanamura: Luminescence channels of manganese-doped spinel. *Journal of Luminescence* 109 (1), 19–24 (2004).

[68] A. M. Srivastava and W. W. Beers: Luminescence of Mn^{4+} in the distorted perovskite Gd_2MgTiO_6. *Journal of The Electrochemical Society* 143 (9), 6–9 (1996).

[69] S. Geschwind, P. Kisliuk, M. P. Klein, J. P. Remeika and D. L. Wood: Sharp-line fluorescence, electron paramagnetic resonance, and thermoluminescence of Mn^{4+} in αAl_2O_3. *Physical Review* 126 (5), 1684–1686 (1962).

[70] S. Tigga, N. Brahme and D. P. Bisen: Photoluminescence and mechanoluminescence investigation of bluish-green afterglow $SrMgAl_{10}O_{17}$:Ce^{3+} phosphor. *Journal of Materials Science: Materials in Electronics* 28 (6), 4750–4757 (2017).

[71] Y. Zorenko, T. Zorenko, V. Gorbenko, V. Savchyn, T. Voznyak, K. Fabisiak, G. Zhusupkalieva and A. Fedorov: Luminescent properties of Al_2O_3:Ce single crystalline films under synchrotron radiation excitation. *Optical Materials* 59, 141–144 (2016).

[72] H. Sakamoto and T. Hitomi: Sensitized luminescence in Mn-activated alkaline earth aluminate phosphors. *Japanese Journal of Applied Physics* 6 (11), 1315–1325 (1967).

[73] J. Lu, Y. Pan, J. Wang, X. Chen, S. Huang and G. Liu: Reduction of Mn^{4+} to Mn^{2+} in $CaAl_{12}O_{19}$ by co-doping charge compensators to obtain tunable photoluminescence. *RSC Advances* 3 (14), 4510–4513 (2013).

[74] G. Tamulaitis, P. Duchovskis, Z. Bliznikas, K. Breive, R. Ulinskaite, A. Brazaityte, A. Novičkovas and A. Žukauskas: High-power light-emitting diode based facility for plant cultivation. *Journal of Physics D: Applied Physics* 38 (17), 3182–3187 (2005).

[75] G. D. Massa, H. H. Kim, R. M. Wheeler and C. A. Mitchell: Plant productivity in response to LED lighting. *HortScience* 43 (7), 1951–1956 (2008).

[76] S. Adachi and T. Takahashi: Direct synthesis and properties of K_2SiF_6:Mn^{4+} phosphor by wet chemical etching of Si wafer. *Journal of Applied Physics* 104 (2), 023 512 (2008).

[77] T. Hadjersi: Oxidizing agent concentration effect on metal-assisted electroless etching mechanism in HF-oxidizing agent-H_2O solutions. *Applied Surface Science* 253 (9), 4156–4160 (2007).

[78] W. Massa: Fluorides: solid-state chemistry, in *Encyclopedia of Inorganic Chemistry*, John Wiley & Sons Ltd, Chichester, UK (2006).

[79] J. Olchowka, M. Suta and C. Wickleder: Green synthesis of A_2SiF_6 (A=Li-Cs) nanoparticles using ionic liquids as solvents and as fluorine sources: a simple approach without HF. *Chemistry - A European Journal* 23 (50), 12 092–12 095 (2017).

[80] L. Huang, Y. Zhu, X. Zhang, R. Zou, F. Pan, J. Wang and M. Wu: HF-free hydrothermal route for synthesis of highly efficient narrow-band red emitting phosphor $K_2Si_{1-x}F_6$:xMn^{4+} for warm white light-emitting diodes. *Chemistry of Materials* 28 (5), 1495–1502 (2016).

[81] H. F. Sijbom, R. Verstraete, J. J. Joos, D. Poelman and P. F. Smet: K_2SiF_6:Mn^{4+} as a red phosphor for displays and warm-white LEDs: a review of properties and perspectives. *Optical Materials Express* 7 (9), 3332–3365 (2017).

[82] T. Nakamura, Z. Yuan and S. Adachi: Micronization of red-emitting K_2SiF_6:Mn^{4+} phosphor by pulsed laser irradiation in liquid. *Applied Surface Science* 320 (2014), 514–518 (2014).

[83] H.-D. Nguyen, C. C. Lin, M.-H. Fang and R.-S. Liu: Synthesis of Na_2SiF_6:Mn^{4+} red phosphors for white LED applications by co-precipitation. *Journal of Materials Chemistry C* 2 (48), 10 268–10 272 (2014).

[84] J. E. Murphy, F. Garcia-Santamaria, A. A. Setlur and S. Sista: PFS, K_2SiF_6:Mn^{4+}: the red-line emitting LED phosphor behind GE's Tri-Gain Technology™platform. *SID Symposium Digest of Technical Papers* 46 (1), 927–930 (2015).

[85] J. E. Murphy, A. A. Setlur, F. Garcia, R. J. Lyons, A. I. Chowdhury, N. Karkada and P. K. Nammalwar: Color stable red-emitting phosphors. *US Patent* 8906724 B2 (2014).

[86] J. E. Murphy: Processes for preparing color stable manganese-doped phosphors. *US Patent* 2015/0054400 A1 (2015).

[87] J. Zhuang, Z. Xia, H. Liu, Z. Zhang and L. Liao: The improvement of moisture resistance and thermal stability of $Ca_3SiO_4Cl_2$:Eu^{2+} phosphor coated with SiO_2. *Applied Surface Science* 257 (9), 4350–4353 (2011).

[88] R. J. Lyons, A. A. Setlur, A. R. Deshpande and L. S. Grigorov: Color stable manganese-doped phosphors. *US Patent* 8252613 B1 (2012).

[89] L. Lv, X. Jiang, S. Huang, X. Chen and Y. Pan: The formation mechanism, improved photoluminescence and LED applications of red phosphor K_2SiF_6:Mn^{4+}. *Journal of Materials Chemistry C* 2 (20), 3879–3884 (2014).

[90] J. W. Moon, B. G. Min, J. S. Kim, M. S. Jang, K. M. Ok, K.-Y. Han and J. S. Yoo: Optical characteristics and longevity of the line-emitting K_2SiF_6:Mn^{4+} phosphor for LED application. *Optical Materials Express* 6 (3), 782–792 (2016).

[91] U. Happek, A. A. Setlur and J. J. Shiang: Inverse bottleneck in Eu^{2+}-Mn^{2+} energy transfer. *Journal of Luminescence* 129 (12), 1459–1463 (2009).

[92] A. A. Setlur, J. J. Shiang and U. Happek: Eu^{2+}-Mn^{2+} phosphor saturation in 5 mm light emitting diode lamps. *Applied Physics Letters* 92 (8), 081 104 (2008).

[93] F. Garcia-Santamaria, J. E. Murphy, A. A. Setlur and S. P. Sista: Concentration quenching in K_2SiF_6:Mn^{4+} phosphors. *ECS Journal of Solid State Science and Technology* 7 (1), R3030–R3033 (2018).

[94] H. Bode, H. Jenssen and F. Bandte: Über eine neue Darstellung des Kalium-hexafluoromanganats(IV). *Angewandte Chemie* 65 (11), 304–304 (1953).

[95] R. D. Peacock: Some fluorine compounds of the transition metals, in F. A. Cotton, editor, *Progress in Inorganic Chemistry*, volume II, Interscience Publishers (1960).

[96] S. Ebnesajjad: *Introduction to fluoropolymers*, William Andrew Publishing (2013).

[97] A. Pfeil: The emission of hexafluoromanganates(IV). *Spectrochimica Acta Part A: Molecular Spectroscopy* 26 (6), 1341–1343 (1970).

[98] A. M. Black and C. D. Flint: Excitation and luminescence spectra of dipotassium hexafluoromanganate(IV). *Journal of the Chemical Society, Dalton Transactions* 0, 977–981 (1974).

[99] R. Verstraete, H. F. Sijbom, K. Korthout, D. Poelman, C. Detavernier and P. F. Smet: K_2MnF_6 as a precursor for saturated red fluoride phosphors: the struggle for structural stability. *Journal of Materials Chemistry C* 5 (41), 10 761–10 769 (2017).

[100] H. Zhu, C. C. Lin, W. Luo, S. Shu, Z. Liu, Y. Liu, J. Kong, E. Ma, Y. Cao, R.-S. Liu and X. Chen: Highly efficient non-rare-earth red emitting phosphor for warm white light-emitting diodes. *Nature communications* 5, 4312 (2014).

[101] A. A. Setlur, E. V. Radkov, C. S. Henderson, J.-H. Her, A. M. Srivastava, N. Karkada, M. S. Kishore, N. P. Kumar, D. Aesram, A. R. Deshpande, B. Kolodin, S. G. Ljudmil and U. Happek: Energy-efficient, high-color-rendering LED lamps using oxyfluoride and fluoride phosphors. *Chemistry of Materials* 22 (13), 4076–4082 (2010).

[102] J. Frayret, A. Castetbon, G. Trouve and M. Potin-Gautier: Solubility of $(NH_4)_2SiF_6$, K_2SiF_6 and Na_2SiF_6 in acidic solutions. *Chemical Physics Letters* 427 (4-6), 356–364 (2006).

[103] L. Xi, Y. Pan, S. Huang and G. Liu: Mn^{4+} doped $(NH_4)_2TiF_6$ and $(NH_4)_2SiF_6$ micro-crystal phosphors: synthesis through ion exchange at room temperature and their photoluminescence properties. *RSC Advances* 6 (80), 76 251–76 258 (2016).

[104] Y. Zhu, J. Yu, Y. Liu, M. G. Brik, L. Huang, T. Xuan and J. Wang: Photoluminescence properties of a novel red fluoride K_2LiGaF_6:Mn^{4+} nanophosphor. *RSC Advances* 7 (49), 30 588–30 593 (2017).

[105] L. Wang, X. Wang, T. Kohsei, K.-i. Yoshimura, M. Izumi, N. Hirosaki and R.-J. Xie: Highly efficient narrow-band green and red phosphors enabling wider color-gamut LED backlight for more brilliant displays. *Optics Express* 23 (22), 28 707–28 717 (2015).

[106] J.-H. Ha, S.-Y. Song, G.-B. Kim, J.-I. Sim and S.-W. Choi: Light-emitting device. *US Patent* 2016/0141457 A1 (2015).

[107] Y. Ooyabu, H. Ito and T. Naito: Reflecting resin sheet, light emitting diode device and producing method thereof. *US Patent* 2012/0262054 A1 (2012).

[108] Y. Ooyabu, H. Fujii, T. Nakamura and H. Ito: Component for light-emitting device, light-emitting device and producing method thereof. *US Patent* 2012/0012875 A1 (2012).

[109] H. Sakuta, Y. Satou, N. Kijima and B. Hong: White light emitting device and lighting device. *US Patent* 8890403 B2 (2014).

[110] Y. Ooyabu, T. Nakamura, H. Fujii and H. Ito: Light-emitting device. *US Patent* 8916893 B2 (2014).

[111] Y. Ooyabu, T. Nakamura, H. Fujii and H. Ito: Phosphor ceramic and light-emitting device. *US Patent* 8664678 B2 (2014).

[112] H. Sakuta, Y. Kohara and Y. Satou: Semiconductor light-emitting device, semiconductor light-emitting system and illumination fixture. *US Patent* 8779455 B2 (2014).

[113] J. Meyer, V. Weiler and P. J. Schmidt: Lighting device with light source and wavelength converting element. *US Patent* 9175214 B2 (2015).

[114] Y. S. Park and H. J. Hahm: Light emitting device, backlight unit and display apparatus. *US Patent* 2015/0301259 A1 (2015).

[115] V. Weiler, P. J. Schmidt and H.-H. Bechtel: LED-based device with wide color gamut. *US Patent* 2014/068440 A1 (2014).

[116] M. Mitani and H. Katayama: Silicone resin sheet, producing method thereof, encapsulating sheet, and light emitting diode device. *US Patent* 8569792 B2 (2013).

[117] R. A. Talewar, C. P. Joshi and S. V. Moharil: Enhancing the photovoltaic performance of CdTe/CdS solar cell via luminescent downshifting using K_2SiF_6:Mn^{4+} phosphors, in *AIP Conference Proceedings*, 1731, 140019 (2016).

[118] Z. Zhong, X. Wang, J. Zhang, H. Zhong and J.-B. Han: Optical detection of magnetic field with Mn^{4+}:K_2SiF_6 phosphor from room to liquid helium temperatures. *Applied Physics Letters* 110 (21), 212 405 (2017).

[119] H. C. Cheng, S. T. Wu and I. Ben-David: Five-primary-color LCDs. *Journal of Display Technology* 6 (1), 3–7 (2010).

[120] X. Zhang, H.-C. Wang, A.-C. Tang, S.-Y. Lin, H.-C. Tong, C.-Y. Chen, Y.-C. Lee, T.-L. Tsai and R.-S. Liu: Robust and stable narrow-band green emitter: an option for advanced wide-color-gamut backlight display. *Chemistry of Materials* 28 (23), 8493–8497 (2016).

[121] S. Abé, J. J. Joos, L. I. D. J. Martin, Z. Hens and P. F. Smet: Hybrid remote quantum dot/powder phosphor designs for display backlights. *Light: Science & Applications* 6 (6), e16 271 (2017).

[122] M. D. Tessier, D. Dupont, K. De Nolf, J. De Roo and Z. Hens: Economic and size-tunable synthesis of InP/ZnE (E = S, Se) colloidal quantum dots. *Chemistry of Materials* 27 (13), 4893–4898 (2015).

[123] J. R. Oh, H. K. Park, J. H. Oh, T. Kouh and Y. Rag Do: Highly efficient full-color display based on blue LED backlight and electrochromic light-valve coupled with front-emitting phosphors. *Optics Express* 19 (17), 16 022–16 031 (2011).

[124] Y. S. Cho, D. Kim, Y. J. Lee, H. Yang and Y. D. Huh: Preparation and photoluminescence properties of red-emitting $Gd_2(MoO_4)_3$:Eu phosphors for a three-band white LED. *Bulletin of the Korean Chemical Society* 31 (10), 2992–2994 (2010).

[125] Y. Yang, Y. Zheng, W. Cao, A. Titov, J. Hyvonen, J. R. Manders, J. Xue, P. H. Holloway and L. Qian: High-efficiency light-emitting devices based on quantum dots with tailored nanostructures. *Nature Photonics* 9, 1–9 (2015).

[126] K. Yoshimura, H. Fukunaga, M. Izumi, M. Masuda, T. Uemura, K. Takahashi, R.-J. Xie and N. Hirosaki: White LEDs using the sharp β-SiAlON:Eu phosphor and Mn-doped red phosphor for wide-color gamut display applications. *Journal of the Society for Information Display* 24 (7), 449–453 (2016).

[127] B.-E. Yeo, Y.-S. Cho and Y.-D. Huh: Synthesis and photoluminescence properties of a red-emitting phosphor, K_2SiF_6:Mn^{4+}, for use in three-band white LED applications. *Optical Materials* 51 (2016), 50–55 (2016).

[128] J. H. Oh, H. Kang, M. Ko and Y. R. Do: Analysis of wide color gamut of green/red bilayered freestanding phosphor film-capped white LEDs for LCD backlight. *Optics Express* 23 (15), A791–A804 (2015).

[129] F. Zhang, H. Zhong, C. Chen, X. Wu and X. Hu: Brightly luminescent and color-tunable colloidal $CH_3NH_3PbX_3$ (X=Br , I , Cl) quantum dots: potential alternatives for display technology. *ACS Nano* 9 (4), 4533–4542 (2015).

[130] G. Yang, Q. Fan, B. Chen, Q. Zhou and H. Zhong: Reprecipitation synthesis of luminescent $CH_3NH_3PbBr_3$/$NaNO_3$ nanocomposites with enhanced stability. *Journal of Materials Chemistry C* 4 (48), 11 387–11 391 (2016).

[131] H. Huang, Q. Xue, B. Chen, Y. Xiong, J. Schneider, C. Zhi, H. Zhong and A. L. Rogach: Top-down fabrication of stable methylammonium lead halide perovskite nanocrystals by employing a mixture of ligands as coordinating solvents. *Angewandte Chemie International Edition* 56 (32), 9571–9576 (2017).

[132] S. Lou, T. Xuan, C. Yu, M. Cao, C. Xia, J. Wang and H. Li: Nanocomposites of $CsPbBr_3$ perovskite nanocrystals in an ammonium bromide framework with enhanced stability. *Journal of Materials Chemistry C* 5, 7431–7435 (2017).

[133] Y. Ohno: Color rendering and luminous efficacy of white LED spectra, in *SPIE Fourth International Conference on Solid State Lighting*, volume 5530, 88–98 (2004).

[134] Y. Ohno: Spectral design considerations for white LED color rendering. *Optical Engineering* 44 (11), 111 302 (2005).

[135] W. Davis and Y. Ohno: Toward an improved color rendering metric, in I. T. Ferguson, J. C. Carrano, T. Taguchi and I. E. Ashdown, editors, *Proceedings of SPIE*, volume 5941, 59 411G–59 411G–8 (2005).

[136] Q. Zhou, Y. Zhou, Z. Wang, Y. Liu, G. Chen, J. Peng, J. Yan and M. Wu: Fabrication and application of non-rare earth red phosphors for warm white-light-emitting diodes. *RSC Advances* 5 (103), 84 821–84 826 (2015).

[137] Z. Wang, Y. Zhou, Z. Yang, Y. Liu, H. Yang, H. Tan, Q. Zhang and Q. Zhou: Synthesis of K_2XF_6:Mn^{4+} (X=Ti, Si and Ge) red phosphors for white LED applications with low-concentration of HF. *Optical Materials* 49 (2015), 235–240 (2015).

[138] P. Arunkumar, Y. H. Kim, H. J. Kim, S. Unithrattil and W. B. Im: Hydrophobic organic skin as a protective shield for moisture-sensitive phosphor-based optoelectronic devices. *ACS Applied Materials & Interfaces* 9 (8), 7232–7240 (2017).

[139] L. Lv, X. Jiang, Y. Pan, G. Liu and S. Huang: Luminescence properties and thermal stability of a red phosphor $ZnSiF_6{\cdot}6H_2O$:Mn^{4+} synthesized by the one-step hydrothermal method. *Journal of Luminescence* 152 (2014), 214–217 (2014).

[140] C. Liao, R. Cao, Z. Ma, Y. Li, G. Dong, K. N. Sharafudeen and J. Qiu: Synthesis of K_2SiF_6:Mn^{4+} phosphor from SiO_2 powders via redox reaction in HF/$KMnO_4$ solution and their application in warm-white LED. *Journal of the American Ceramic Society* 96 (11), 3552–3556 (2013).

[141] F. Baur, F. Glocker and T. Jüstel: Photoluminescence and energy transfer rates and efficiencies in Eu^{3+} activated $Tb_2Mo_3O_{12}$. *Journal of Materials Chemistry C* 3 (9), 2054–2064 (2015).

[142] D. Luo, L. Wang, S. W. Or, H. Zhang and R.-J. Xie: Realizing superior white LEDs with both high R9 and luminous efficacy by using dual red phosphors. *RSC Advances* 7 (42), 25 964–25 968 (2017).

[143] J. J. Joos, J. Botterman and P. F. Smet: Evaluating the use of blue phosphors in white LEDs: the case of $Sr_{0.25}Ba_{0.75}Si_2O_2N_2{:}Eu^{2+}$. *Journal of Solid State Lighting* 1 (1), 6 (2014).

[144] A. A. Setlur, R. J. Lyons, J. E. Murphy, N. Prasanth Kumar and M. Satya Kishore: Blue light-emitting diode phosphors based upon oxide, oxyhalide and halide hosts. *ECS Journal of Solid State Science and Technology* 2 (2), R3059–R3070 (2012).

[145] A. Setlur, M. Brewster, F. Garcia, M. C. Hill, R. Lyons, J. Murphy, T. Stecher, S. Stoklosa, S. Weaver, U. Happek, D. Aesram and A. Deshpande: Optimized phosphors for warm white LED light engines, Technical report, GE Global Research (2012).

[146] C.-C. Tsai, W.-C. Cheng, J.-K. Chang, L.-Y. Chen, J.-H. Chen, Y.-C. Hsu and W.-H. Cheng: Ultra-high thermal-stable glass phosphor layer for phosphor-converted white light-emitting diodes. *Journal of Display Technology* 9 (6), 427–432 (2013).

[147] J. Meyer, V. Weiler, M. Heidemann and H.-H. Bechtel: Wavelength converting screen for a lighting device. *WO Patent* 2012131533(A1) (2012).

[148] G. Khanarian: Rubber toughened and optically transparent blends of cyclic olefin copolymers. *Polymer Engineering and Science* 40 (12), 2590–2601 (2000).